

Synthesis and characterisation of  
novel layered electrode materials for  
sodium-ion batteries

Lancaster  
University



**Joel Canhoto Cardoso**

**This thesis was submitted for the degree in  
Doctor in Philosophy**

**Supervised by Dr Nuria Tapia Ruiz**

**October 2024**



*“Regina cæli, lætare, Alleluia  
Quia quem meruisti portare, Alleluia  
Resurrexit, sicut dixit, Alleluia  
Ora pro nobis Deum, Alleluia”*

*Unknown author circa, 12<sup>th</sup> century*



# Declaration

This thesis has not been submitted to support an application for another degree at this or any other university. It is the result of my work and includes nothing that is the outcome of work done in collaboration except where specifically indicated. Many of the ideas in this thesis were the product of a discussion with my supervisor Dr Nuria Tapia Ruiz.

The Faraday Institution financially through NEXGENNA, financially supported the research presented within this thesis; however, the author declares no conflicts of interest.

Joel Mário Canhoto Cardoso, MSc

Lancaster University, UK



# Abstract

This thesis explores the development of new materials for sodium-ion battery (NIBs) electrodes. The transfer of some energy storage capacity from lithium-ion batteries (LIBs) to alternative technologies is crucial to address the growing demand for lithium, which is not adequately supported by known reserves. By mitigating some of the forecasted supply constraints, NIBs offer a viable and cost-effective alternative, especially as the demand for high energy and power density in electrical energy storage applications continues to rise. However, the lack of high capacity and high cycle life electrode materials for NIBs is still limiting the implementation of this technology.

In this thesis, we attempt to tackle these limitations by exploring novel approaches to enhance both cathode and anode materials for NIBs: In Chapter 3 (i), the effects of calcium pillaring and dual calcium pillaring combined with fluorination on *O3*-type sodium and iron oxides as cathodes are studied. With this aim,  $\alpha$ -NaFeO<sub>2</sub> was doped at 2, 3 and 5 % with calcium. For the dual calcium and fluorine-doping,  $\alpha$ -NaFeO<sub>2</sub>, doping corresponded to 2, 3 and 5 % calcium-doping and 4, 6 and 10 % fluorine-doping. The structure and electrochemical performance of these materials were characterised. Chapter 4 (ii) investigates the impact of transition metal substitution on *P2*-type sodium, manganese, and nickel oxides as cathodes. In this chapter, the structure, electrochemical performance and stability of Na<sub>0.67</sub>Mn<sub>0.8</sub>Ni<sub>0.15</sub>Ti<sub>0.05</sub>O<sub>2</sub>, Na<sub>0.67</sub>Mn<sub>0.8</sub>Ni<sub>0.15</sub>Fe<sub>0.05</sub>O<sub>2</sub> and, Na<sub>0.67</sub>Mn<sub>0.8</sub>Ni<sub>0.15</sub>Cu<sub>0.05</sub>O<sub>2</sub> was characterised. Finally, Chapter 5 (iii) focuses on titanate, lanthanum titanate, and yttrium-based perovskite oxides as anodes. With this aim, NaLaTiO<sub>4</sub> and NaYTiO<sub>4</sub> were synthesised, structurally and electrochemically characterised.

To confirm the general structures of the materials, this thesis employs X-ray diffraction (XRD), scanning electron microscopy (SEM), energy-dispersive spectroscopy (EDS), <sup>23</sup>Na nuclear magnetic resonance (NMR), and diffuse reflectance spectroscopy. The

electrochemical response is then studied using galvanostatic cycling, cyclic voltammetry, the galvanostatic intermittent titration technique, and electrochemical impedance spectroscopy. Finally, *operando* XRD techniques are applied to unravel the sodium insertion and desorption mechanisms when possible, and *ex-situ* XRD is used where *operando* methods are not feasible.

In Chapter 3, the synthesis of pristine, calcium-doped and dual calcium and fluorine-doped  $\alpha$ -NaFeO<sub>2</sub> was achieved with a small amount of impurity. The addition of Ca<sup>2+</sup> to the structure causes the unit cell to contract due to the increased electrostatic forces of Ca<sup>2+</sup> and O<sup>2-</sup>, compared with Na<sup>+</sup> and O<sup>2-</sup>. Dual doping with calcium and fluorine causes an expansion of the unit cell due to the decrease of electrostatic forces between the alkali metals and F<sup>-</sup>. The calcium-doping at 5 % has resulted in an increase of capacity retention from 41 % to 77 % after 100 cycles, however, with 68 % of the initial capacity of the pristine material. With dual calcium and fluorine doping with 5 and 10 %, respectively, the capacity retention was 79 % after 100 cycles, with 84 % of the initial capacity of the pristine material.

In Chapter 4, Na<sub>0.67</sub>Mn<sub>0.8</sub>Ni<sub>0.15</sub>Ti<sub>0.05</sub>O<sub>2</sub>, Na<sub>0.67</sub>Mn<sub>0.8</sub>Ni<sub>0.15</sub>Fe<sub>0.05</sub>O<sub>2</sub> and, Na<sub>0.67</sub>Mn<sub>0.8</sub>Ni<sub>0.15</sub>Cu<sub>0.05</sub>O<sub>2</sub> showed negligible changes in the size of the unit cell, due to the similar ionic radii of nickel, titanium, iron and copper in the structure. All materials except Na<sub>0.67</sub>Mn<sub>0.8</sub>Ni<sub>0.15</sub>Ti<sub>0.05</sub>O<sub>2</sub> showed good air and water stability. The initial capacity of Na<sub>0.67</sub>Mn<sub>0.8</sub>Ni<sub>0.15</sub>Ti<sub>0.05</sub>O<sub>2</sub>, Na<sub>0.67</sub>Mn<sub>0.8</sub>Ni<sub>0.15</sub>Fe<sub>0.05</sub>O<sub>2</sub> and, Na<sub>0.67</sub>Mn<sub>0.8</sub>Ni<sub>0.15</sub>Cu<sub>0.05</sub>O<sub>2</sub> was 102, 111 and 136 mA h g<sup>-1</sup>, respectively. Capacity retention was 44, 89 and 88 % after 200 cycles.

In Chapter 5, NaLaTiO<sub>4</sub> and NaYTiO<sub>4</sub> showed little to no activity as anodes for NIB, contrary to when these materials are used in anodes for LIB. This is likely due to the large Na<sup>+</sup> volume, compared to Li<sup>+</sup>.

# Acknowledgements

I would like to express my deepest gratitude to my supervisor, Dr Nuria Tapia Ruiz, for giving me the opportunity to become a research student and for her guidance and patience throughout my PhD studies. I extend my thanks to Dr Robert Crewe and Dr Layla Mahdi at the University of Liverpool for taking the TEM micrographs of the layered perovskite oxides, and to Dr Wei Zhixuan from the Justus Liebig University – Gießen for measuring the sodium diffusion rate of the layered perovskite oxides using EIS. I also appreciate the support of Dr Pierre-Olivier Autran, the beamline scientist at ESFR, who assisted me during *operando* XRD experiments on  $\alpha$ -NaFeO<sub>2</sub> and layered perovskites and Dr Gabriel Pérez García for ISIS, for the help on synchrotron data analysis. My colleagues in the Tapia Ruiz Group deserve special thanks for their teamwork and assistance both in and outside the lab. I am particularly grateful to Jack Fitzpatrick, Hannah Lynn, Beth Murdock, Sarah McKinney, Alexandra Michail, and Dr Li Zhang. Also, to my friends and colleagues, Joel Cabañero Jr., Chuxin Yue, YingLin Liao, Chen Chen Wang and Alexis Manche from the University of St Andrews, that I had the privilege to meet at the NEXGENNA consortium meetings for their friendship and technical advice.

I want to express my appreciation to Dr Begoña Silván for her specific support in Chapter 3, Dr Sidra Jamil for her help in Chapter 4, and Dr Sara Costa for her assistance in Chapter 5.

The first two years of my PhD studies were conducted at the Department of Chemistry at Lancaster University. I am sincerely grateful to this department for allowing me to carry out my research activities in their facilities. Special thanks go to Dr Nathan Halcovich for sharing his expertise with XRD measurements and technical knowledge about the diffractometer, to Dr Sara Baldock for taking all the SEM micrographs of my perovskite oxides and the pristine  $\alpha$ -NaFeO<sub>2</sub>, and to David Rochester and Helen Quirk for helping find

Joel Canhoto Cardoso

my way in the department during the 2020 lockdowns. I also appreciate the support from Dr Bin Wang for his clear and energetic instruction on *ex-situ* and *operando* XRD.

The last two years of my PhD studies were spent at the Department of Chemistry at Imperial College London. I am deeply grateful to the department and the school for allowing me to use their facilities and for their support in accessing equipment and providing counselling. Special thanks to Dr Mahmoud Ardakani for his support in taking the micrographs of the doped  $\alpha$ -NaFeO<sub>2</sub> and the materials in Chapter 4. I would also like to thank the master's students I co-supervised with Dr Sidra Jamil, Ding Ding and Arun Ramanathan, for all the insights I gained through our collaboration. Also, to Ding Ding, thank you for the help with Python which facilitated some data analyses. My sincere appreciation goes to Dr Michael Ray and Hanah Shire for their advice and support and Professor Rob Davies for extra thesis writing and preparation guidance.

Finally, I would like to thank my family and friends, both in the UK and Portugal, who lifted my spirits when things were tough. Special thanks to my good friends João, Ana, Telma, Ania, Jordan, and Sanch. I also appreciate the wonderful people I met at the Lancaster Cathedral Choir. I will always be thankful to have met all these amazing people. Thank you all with all my heart and soul!

Joel

# List of contents

Declaration .....	v
Abstract .....	vii
Acknowledgements .....	ix
List of contents .....	xi
List of figures .....	xvii
List of tables .....	xxix
1. Introduction .....	1
1.1. Environmental impact of carbon dioxide emissions .....	4
1.2. Geopolitical impact of fossil fuels .....	6
1.3. Renewable energy .....	10
1.4. Energy storage .....	11
1.5. Rechargeable batteries .....	12
1.5.1. Lithium-ion batteries .....	13
1.5.2. Sodium-ion Batteries .....	17
1.6. Cathode materials .....	20
1.6.1. Transition-metal oxides .....	24
1.7. Anodes .....	30

1.7.1. Titanates – Na <sub>2</sub> Ti <sub>3</sub> O <sub>7</sub> .....	32
1.8. References .....	39
2. Introduction .....	49
2.1 Solid-state synthesis .....	53
2.1.1. Synthesis of iron-rich O <sub>3</sub> -type layered oxides .....	54
2.1.2 Synthesis of manganese-rich P <sub>2</sub> -type transition metal oxides .....	55
2.1.3. Synthesis of layered perovskite oxides .....	56
2.2. Characterisation methods .....	56
2.2.1. Powder X-ray diffraction .....	56
2.2.2. Scanning Electron Microscopy .....	58
2.2.3. Energy dispersive X-ray spectroscopy .....	60
2.2.4 Transmission Electron Microscopy .....	60
2.2.5. Electronic spectroscopy .....	62
2.2.4. Solid-state nuclear resonance .....	64
2.3. Electrochemical characterisation .....	65
2.3.1. Electrolyte preparation .....	65
2.3.2. Fabrication of electrodes .....	66
2.3.3. Coin cell assembly .....	67
2.3.4. Galvanostatic measurements .....	68
2.3.5. Cyclic-voltammetry .....	70

2.3.6. Galvanostatic intermittent titration technique .....	72
2.3.7. Electrochemical Impedance Spectroscopy .....	73
2.4. Synchrotron techniques .....	75
2.4.1. Operando X-ray diffraction .....	77
2.5. References .....	80
3. Effect of calcium and dual calcium-fluorine doping on O <sub>3</sub> -type $\alpha$ -NaFeO <sub>2</sub> as cathodes for sodium-ion batteries .....	85
3.1. Calcium as pillaring agent .....	88
3.2. Doping on cathode materials .....	90
3.2.1. Anionic dopants .....	91
3.3. Synthesis optimisation and characterisation .....	94
3.3.1. $\alpha$ -NaFeO <sub>2</sub> synthesis optimisation .....	96
3.3.2. Structure .....	99
3.3.3. Morphology and composition .....	115
3.4. Electrochemical performance .....	117
3.4.1 Optimisation of cycling window .....	117
3.4.2. Galvanostatic measurements .....	121
3.4.3. Cyclic-voltammetry .....	141
3.4.4. Galvanostatic intermittent titration technique .....	149
3.4.5. Operando X-ray diffractometry .....	149

3.5. Conclusion .....	140
3.6. References .....	146
4. Transition-metal doping in manganese-rich P2-type layered oxides .....	151
4.1. P2-type transition metal layered oxides .....	154
4.2. Doping on cathode materials .....	156
4.3. Titanium, iron and copper as doping agents .....	159
4.4. Synthesis and characterisation .....	160
4.4.1. Synthesis .....	161
4.4.2. Rietveld refinements .....	163
4.4.3. Morphology and composition .....	169
4.4.4. Structural stability in contact with air and water .....	172
4.5. Electrochemical performance .....	176
4.5.1. Galvanostatic measurements .....	177
4.5.2. Cyclic-voltammetry .....	181
4.5.3. Galvanostatic intermittent titration technique .....	188
4.5.4. Ex-situ XRD diffraction .....	191
4.6. Conclusion .....	197
4.7. References .....	200
5. Layered perovskite oxides as anodes for LIBs and NIBs .....	209
5.1. Introduction .....	213

5.1.2. Titanium-based Perovskites .....	213
5.1.3. Layered Perovskites .....	218
5.2. Synthesis optimisation and characterisation .....	227
5.2.1. Calcination temperature optimisation .....	227
5.2.2. Sodium Excess Optimisation .....	229
5.2.3. Structure .....	231
5.2.4. Morphology and composition .....	235
5.2.6 Chemical deviation of structural sodium .....	238
5.2.6 Optic behaviour .....	239
5.3. Electrochemical performance versus lithium .....	241
5.3.1. Galvanostatic measurements .....	241
5.3.2. Cyclic-voltammetry .....	243
5.3.3. Structural changes during operation .....	245
5.4. Electrochemical performance versus sodium .....	246
4.1. Galvanostatic measurements .....	246
5.4.2. Cyclic-voltammetry .....	249
5.4.3. Carbon super-P electrochemical performance .....	250
5.4.4. Sodium mobility and diffusion coefficient by electrochemical impedance spectroscopy .....	253
5.5. Conclusion .....	257

5.6. References .....	259
6. Conclusion .....	267
6.1. Dual calcium and fluorine-doping in O <sub>3</sub> -type iron-rich transition layered oxides for cathodes for sodium-ion batteries .....	270
6.2. Transition-metal doping in manganese-rich P <sub>2</sub> -type layered oxides .....	272
6.3. Layered perovskite oxides as anodes for LIBs and NIBs .....	273
6.4. Future work .....	274
7. Annexes .....	277

## List of figures

Figure 1.1 – Evolution of the concentration of CO <sub>2</sub> in Earth's atmosphere from 1960 to today obtained from the National Aeronautics and Space Administration (NASA) [6].....	5
Figure 1.2 – Prediction of the world's energy demand partitioned in energy sources until the year 2050 obtained from the International Energy Outlook Report 2021. [4].....	6
Figure 1.3 – Countries with the largest oil reserves and the largest consumers of oil. [9].....	7
Figure 1.4 – Natural gas production in the EU and imports in 2020. [13].....	8
Figure 1.5 – Distribution of known lithium reserves and forecast of lithium production and demand from Benchmark Minerals Intelligence [43].....	14
Figure 1.6 – General scheme of a sodium-ion battery functioning. [61].....	18
Figure 1.7 - Relative energies of the electrolyte window, E <sub>g</sub> , and the relationship between electrochemical potentials of electrodes and the HOMO or LUMO of the electrolyte [23].....	19
Figure 1.8 – Schematic representation of a polyanionic compound (Adapted from Min <i>et al.</i> ) [71].....	21
Figure 1.9 – schematic representation of a Prussian blue analogue (Adapted from Jing <i>et al.</i> ) [73].....	22
Figure 1.10 – Schematic representation of the transition metal oxide .....	23
Figure 1.11 – Schematic representations of the O <sub>3</sub> , O <sub>2</sub> , P <sub>3</sub> and P <sub>2</sub> -type transition metal oxides the most common transition upon sodiation/desodiation [28].....	25
Figure 1.12 – Specific capacity versus working potential plot for materials having been reported to exhibit reversible sodium insertion and hence being potential electrode materials for sodium-ion cells.[117].....	29
Figure 1.13 – Schematic illustration of Na <sub>2</sub> Ti <sub>3</sub> O <sub>7</sub> obtained from VESTA software with the Materials Project database (mp-3488), where the yellow ball represents Na <sup>+</sup> ions, red represents oxygen and the TiO <sub>6</sub> octahedra are represented in blue.....	33
Figure 1.14 – In situ, X-ray diffraction study of a Na <sub>2</sub> Ti <sub>3</sub> O <sub>7</sub> /Na metal cell, cycled between 2.5 and 0.01 V at a C/50 rate [122].....	34

Figure 1.15 – Capacity versus cycle number for the reduction of a composite electrode containing $\text{Na}_2\text{Ti}_3\text{O}_7$ and 30% carbon black (blue curve) once the contribution from carbon black has been subtracted. The inset shows derivative curves for the first two cycles and the blank experiment containing only carbon black (in blue). [127].....	34
Figure 1.16 – (a) Charge/discharge curves of layered $\text{Na}_2\text{Ti}_3\text{O}_7$ (red) and $\text{Na}_2\text{Ti}_3\text{O}_7$ deposited on Ni-foam (blue); (b) Cycling performance at 20, 100, 200 and 400 $\text{mA h g}^{-1}$ ; Cyclic performance over 500 cycles at 50 $\text{mA g}^{-1}$ . [127].....	35
Figure 1.17 – XDR diffractograms of $\text{Na}_2\text{Ti}_3\text{O}_7$ power (in black), $\text{Na}_4\text{Ti}_3\text{O}_7$ after discharge (in red), three days after discharge (in blue), ten days after discharge (in green) [129] .....	36
Figure 2.1 – Schematic representation of a constructive interference under Bragg’s law [5]..	53
Figure 2.2 – Schematic representation of scanning electronic microscope components. [8].	55
Figure 2.3 – Schematic representation of a transmission electron microscopic [10].....	56
Figure 2.4 – Schematic illustration of the coin-cell components by order of assembly [24]..	63
Figure 2.5 – Schematic representation of a synchrotron facility .....	72
Figure 2.6 – Schematic representation of a modified coin cell with a glass window and its components [46].....	74
Figure 2.7 – Design of the holder used during the operando X-ray diffraction made by AutoCAD 2022.....	75
Figure 3.1 – Capacity over cycling of $\text{NaCrO}_2$ , pristine and 5 % calcium pillared (a) and fast-rate cycling of $\text{NaCrO}_2$ , pristine and 5 % calcium pillared (b), from Chen et al.....	83
Figure 3.2 – $\text{NaCrO}_2$ capacity evolution over cycling at various calcium-pillaring percentages (a) and capacity of $\text{NaCrO}_2$ at faster charge/discharge rates (b) from Laisa et al.....	83
Figure 3.3 – Capacity of $\text{NaCoO}_2$ , pristine, 2, 5, 7 and 10 % calcium-pillaring rate over cycling (a) and $\text{NaCoO}_2$ , pristine and 7 % at faster charge/discharge rates.....	84
Figure 3.4 – Cycling stability of undoped and F-doped NFM over 70 cycles at a scan rate of 150 $\text{mA g}^{-1}$ (a) and O 1s band binding energy of undoped and F-doped NFM (b).....	84

Figure 3.5 – cyclic-voltammetry curves at a scan rate of $0.1 \text{ mV s}^{-1}$ of undoped NFM and 1 % F-doped NFM (a) and the relationship of peak current ( $i_p$ ) and the square root of scan rate ( $v^{1/2}$ ) of all NFM (b).....	88
Figure 3.6 - Cycling performance of $\text{Na}_{0.67-x}\text{Ca}_x\text{Ni}_{0.33}\text{Mn}_{0.67}\text{O}_{2-2x}\text{F}_{2x}$ ( $x = 0, 0.01, 0.03$ and $0.05$ ) cycled at 1C in the voltage range of 2.0–4.3 V. (a) Comparison of cycling performance of $\text{Na}_{0.67}\text{Ni}_{0.33}\text{Mn}_{0.67}\text{O}_2$ cathodes doped with Ca, F and $\text{CaF}_2$ cycled at 1C in the voltage range of 2.0–4.3 V (b) [6].....	90
Figure 3.7 – X-ray diffractograms of the samples synthesised at temperatures of 650, 670, and 680 °C with the standards of $\alpha\text{-NaFeO}_2$ , $\beta\text{-NaFeO}_2$ , $\text{CaCO}_3$ , $\text{Na}_2\text{CO}_3$ and $\text{Fe}_3\text{O}_4$ obtained from ICSD. [19] The peaks attributed only to the $\alpha\text{-NaFeO}_2$ phase are indicated with an asterisk (*) and those attributed only to the $\text{Na}_2\text{CO}_3$ phase are indicated with a plus sign (+).....	92
Figure 3.8 – X-ray diffractograms of the samples synthesised at temperatures of 630 °C for 10, 15, and 20 hours, with a two-step synthesis of 15+10 hours and a three-step synthesis of 15+5+5 hours with the standards of $\alpha\text{-NaFeO}_2$ , $\beta\text{-NaFeO}_2$ , $\text{CaCO}_3$ , $\text{Na}_2\text{CO}_3$ and $\text{Fe}_3\text{O}_4$ obtained from ICSD. [19] The peaks attributed to any of the precursors are indicated with a plus sign (+) .....	93
Figure 3.9 – X-ray diffractograms of the $\alpha\text{-Na}_{0.90}\text{Ca}_{0.05}\text{FeO}_2$ (C5NFO), $\alpha\text{-Na}_{0.96}\text{Ca}_{0.02}\text{FeO}_2$ (C2NFO) and $\alpha\text{-Na}_{0.94}\text{Ca}_{0.03}\text{FeO}_2$ (C3NFO) (a) and (C5NFOF), $\alpha\text{-Na}_{0.96}\text{Ca}_{0.02}\text{FeO}_{1.96}\text{F}_{0.04}$ (C2NFOF) and $\alpha\text{-Na}_{0.94}\text{Ca}_{0.03}\text{FeO}_{1.94}\text{F}_{0.06}$ (C3NFOF) (b) compared with the standards of $\alpha\text{-NaFeO}_2$ , $\beta\text{-NaFeO}_2$ , $\text{CaCO}_3$ , $\text{Na}_2\text{CO}_3$ , $\text{CaF}_2$ , $\text{NaF}$ and $\text{Fe}_3\text{O}_4$ obtained from ICSD. [19] .....	94
Figure 3.10 - Rietveld refinement of pristine $\alpha\text{-NaFeO}_2$ .....	95
Figure 3.11 – $\alpha\text{-NaFeO}_2$ (left) and $\beta\text{-NaFeO}_2$ (right) structures drawn with VESTA where the oxygen is marked in red, iron in brown and sodium in yellow .....	96
Figure 3.12 - Rietveld refinement of pristine $\alpha\text{-Na}_{0.96}\text{Ca}_{0.02}\text{FeO}_2$ .....	97
Figure 3.13 - Rietveld refinement of pristine $\alpha\text{-Na}_{0.94}\text{Ca}_{0.03}\text{FeO}_2$ .....	99
Figure 3.14 - Rietveld refinement of pristine $\alpha\text{-Na}_{0.9}\text{Ca}_{0.05}\text{FeO}_2$ .....	110

Figure 3.15 – Structure of $\text{Na}_{(1-2x)}\text{Ca}_x\text{FeO}_2$ drawn with VESTA where the oxygen is marked in red, iron in brown, sodium in yellow and calcium in blue .....	102
Figure 3.16 – (0 0 3) plain distance variation with $\text{Ca}_{2+}$ -doping of NFO .....	103
Figure 3.17 – Rietveld refinement of pristine $\alpha\text{-Na}_{0.96}\text{Ca}_{0.02}\text{FeO}_{1.96}\text{F}_{0.04}$ .....	104
Figure 3.18 – Rietveld refinement of pristine $\alpha\text{-Na}_{0.94}\text{Ca}_{0.03}\text{FeO}_{1.94}\text{F}_{0.06}$ .....	105
Figure 3.19 – Rietveld refinement of pristine $\alpha\text{-Na}_{0.9}\text{Ca}_{0.05}\text{FeO}_{1.9}\text{F}_{0.1}$ .....	107
Figure 3.20 – Idealised structure of $\text{Na}_{(1-2x)}\text{Ca}_x\text{FeO}_{(2-2x)}\text{F}_{2x}$ drawn with VESTA where the oxygen is marked in red, iron in brown, sodium in yellow, calcium in blue and fluorine is on dark grey .....	108
Figure 3.21 – (0 0 3) plain distance variation with $\text{Ca}^{2+}$ and $\text{F}^-$ -doping of NFO.....	109
Figure 3.22 – image of a SEM microscopy of pristine $\alpha\text{-NaFeO}_2$ at a $\times 6000$ amplification (left) and elemental analysis from EDS of $\alpha\text{-NaFeO}_2$ (right) .....	110
Figure 3.23– image of a SEM microscopy of pristine $\alpha\text{-Na}_{0.9}\text{Ca}_{0.05}\text{FeO}_2$ at a $\times 6000$ amplification (left) and elemental analysis from EDS of $\alpha\text{-NaFeO}_2$ (right).....	110
Figure 3.24– image of a SEM microscopy of pristine $\alpha\text{-Na}_{0.9}\text{Ca}_{0.05}\text{FeO}_{1.8}\text{F}_{0.1}$ at a $\times 6000$ amplification (left) and elemental analysis from EDS of $\alpha\text{-NaFeO}_2$ (right).....	111
Figure 3.25 – Capacity over cycling of $\alpha\text{-NaFeO}_2$ at potential windows from 2.5-3.5, 2.5-3.8 and 2.5-4.0 V vs $\text{Na}^+/\text{Na}$ (a) and galvanostatic curves of $\alpha\text{-NaFeO}_2$ at potential windows from 2.5-3.5, 2.5-3.8 and 2.5-4.0 V vs $\text{Na}^+/\text{Na}$ (b).....	112
Figure 3.26 – Cyclic-voltammetry of $\alpha\text{-NaFeO}_2$ at 2.5-3.5 (a), 2.0-3.8 (b) and 2.0-4.0 V vs $\text{Na}^+/\text{Na}$ .....	113
Figure 3.27 – Relative rate of iron migration related to the sodium content (left) and phase conversion during charge and degradation at higher potential (right) in $\alpha\text{-NaFeO}_2$ .....	114

Figure 3.28 – Capacity and Coulombic efficiency over cycling in NFO, C <sub>3</sub> NFO and C <sub>5</sub> NFO (a), mid-potential over cycling in NFO, C <sub>3</sub> NFO and C <sub>5</sub> NFO (b), galvanostatic curves of the 2nd cycle of NFO, C <sub>3</sub> NFO and C <sub>5</sub> NFO (c) and, cycling at faster rates of NFO, C <sub>3</sub> NFO and C <sub>5</sub> NFO (d) .....	115
Figure 3.29 - Capacity and Coulombic efficiency over cycling in NFO, C <sub>3</sub> NFOF and C <sub>5</sub> NFOF (a), mid-potential over cycling in NFO, C <sub>3</sub> NFOF and C <sub>5</sub> NFOF (b), galvanostatic curves of the 2nd cycle of NFO, C <sub>3</sub> NFOF and C <sub>5</sub> NFOF (c) and, cycling at faster rates of NFO, C <sub>3</sub> NFOF and C <sub>5</sub> NFOF (d) .....	117
Figure 3.30 - Cyclic-voltammetry at 0.1 mV s <sup>-1</sup> over 5 cycles (a) and cyclic-voltammetry at the 2nd cycle at a scan rate of 0.1, 0.2, 0.5 and 1.0 mV s <sup>-1</sup> (b) of NFO .....	119
Figure 3.31 – Maxima of the anodic and the cathodic peaks at different scan rates, related to $v^{1/2}$ with the cathodic and anodic linear regressions .....	120
Figure 3.32 - Cyclic-voltammetry of C <sub>3</sub> NFO (a) and C <sub>5</sub> NFO (b) at 0.1 mV s <sup>-1</sup> over 10 cycles and cyclic-voltammetry at the 2nd cycle at a scan rate of 0.1, 0.2, 0.5 and 1.0 mV s <sup>-1</sup> of C <sub>3</sub> NFO (c) and C <sub>5</sub> NFO (d) .....	121
Figure 3.33 - Maxima of the anodic and the cathodic peaks at different scan rates, related to $v^{1/2}$ with the cathodic and anodic linear regressions of C <sub>3</sub> NFO (left) and C <sub>5</sub> NFO (right) .....	122
Figure 3.34 - Cyclic-voltammetry of C <sub>3</sub> NFOF (a) and C <sub>5</sub> NFOF (b) at 0.1 mV s <sup>-1</sup> over 10 cycles and cyclic-voltammetry at the 2nd cycle at a scan rate of 0.1, 0.2, 0.5 and 1.0 mV s <sup>-1</sup> of C <sub>3</sub> NFOF (c) and C <sub>5</sub> NFOF (d) .....	123
Figure 3.35 - Maxima of the anodic and the cathodic peaks at different scan rates, related to $v^{1/2}$ with the cathodic and anodic linear regressions of C <sub>3</sub> NFOF (left) and C <sub>5</sub> NFOF (right) .....	124
Figure 3.36 – GITT of NFO and diffusion rate versus potential .....	126
Figure 3.37 – GITT of C <sub>3</sub> NFO and diffusion rate versus potential .....	127
Figure 3.38 – GITT of C <sub>5</sub> NFO and diffusion rate versus potential .....	128
Figure 3.39 – GITT of C <sub>3</sub> NFOF and diffusion rate versus potential .....	129
Figure 3.40 – GITT of C <sub>5</sub> NFOF and diffusion rate versus potential .....	130

Figure 3.41 – Heat map of the diffraction peaks (0 0 3) (a), (0 0 6), (1 0 1) and (0 1 2) (b), (0 1 4) (c) and, (2 0 2) (d) .....	132
Figure 3.42 – Illustration of the phase change caused by O <sup>2-</sup> repulsion, caused by the depletion of sodium in the alkali-metal layer (a) and the contraction of the transition metal layer caused by Jahn-Teller distortion of Fe(IV) .....	133
Figure 4.1 – Illustration of the sodium ion pathway in an O <sub>3</sub> and P <sub>2</sub> -type structure [4]	149
Figure 4.2 – Illustration of a honeycomb type Na <sup>+</sup> /□ ordering (i), a diamond type Na <sup>+</sup> /□ ordering (ii), a row type Na <sup>+</sup> /□ ordering (iii) and a large zigzag type Na <sup>+</sup> /□ ordering (iv) [14].....	150
Figure 4.3 – Comparison between the first discharge galvanostatic curve of P <sub>2</sub> -Na <sub>x</sub> CoO <sub>2</sub> (•) and P <sub>2</sub> -Na <sub>x</sub> Co <sub>0.67</sub> Ni <sub>0.33</sub> O <sub>2</sub> (•) [11].....	151
Figure 4.4 – Influence of Na content in the formation of an O <sub>3</sub> or P <sub>2</sub> -type structure (a) and influence of Mn and Ni content in the formation of an O <sub>3</sub> or P <sub>2</sub> -type structure, where the x-axis is the sodium content and the y-axis is the manganese content. [30], [31].....	156
Figure 4.5 – X-ray diffractograms of all NMNTO, NMNFO, and NMNCO are shown and compared with the O <sub>3</sub> -type and P <sub>2</sub> -type Na <sub>0.67</sub> Mn <sub>0.8</sub> Ni <sub>0.2</sub> O <sub>2</sub> obtained from ICSD [32].....	157
Figure 4.6 – Structure of Na <sub>0.67</sub> Mn <sub>0.8</sub> Ni <sub>0.2</sub> O <sub>2</sub> obtained with VESTA where oxygen is represented in red, sodium is represented in yellow, manganese is represented in purple and nickel is represented in dark grey.....	158
Figure 4.7 – Rietveld refinement of P <sub>2</sub> -NMNTO.....	159
Figure 4.8– Rietveld refinement of P <sub>2</sub> -NMNFO.....	160
Figure 4.9– Rietveld refinement of P <sub>2</sub> -NMNCO.....	162
Figure 4.10 – SEM image of NMNTO taken at a magnification of ×6500 (a), EDS elemental analysis (b).....	163
Figure 4.11 – SEM image of NMNFO taken at a magnification of ×6500 (a), EDS elemental analysis (b).....	164

Figure 4.12 - SEM image of NMNTO taken at a magnification of $\times 6500$ (a), EDS elemental analysis (b).....	164
Figure 4.13 - X-ray diffractograms of NMNTO before being put in contact with air or water, after one hour, 1 week, 2 weeks and one month in air and 1 hour stirring in water.....	166
Figure 4.14 - diffractogram of the P2-type $\text{Na}_{0.67}\text{MnO}_2$ compared with the hydration phase (birnessite) and buserite as well as, a diagram illustrating the hydration and degradation process of $\text{Na}_{0.67}\text{MnO}_2$ [41], [42].....	167
Figure 4.15 - X-ray diffractograms of NMNFO before being put in contact with air or water, after one hour, 1 week, 2 weeks and one month in air and 1 hour stirring in water.....	168
Figure 4.16 - X-ray diffractograms of NMNTO before being put in contact with air or water, after one hour, 1 week, 2 weeks and one month in air and 1 hour stirring in water.....	169
Figure 4.17 – Redox potentials of various transition metals, compared with the $\text{O}_2 + \text{H}_2\text{O} + 2\cdot\text{e}^- + 2\cdot\text{OH}^-$ .adapted from [3], and built with information from [28], [42]–[48].....	170
Figure 4.18 – Capacity over 200 cycles of NMNTO, NMNFO and NMNCO (a), evolution of mean-potential over 200 cycles of NMNTO, NMNFO and NMNCO (b), galvanostatic curves of the 1st cycle of NMNTO, NMNFO and NMNCO (c), rate capability of NMNTO, NMNFO and NMNCO at 0.1, 0.2, 0.5, 1, 2, 5 and 10 C (d).....	171
Figure 4.19 – lattice distortion of P2-type $\text{Na}_x\text{Mn}_{(1-y)}\text{M}_y\text{O}_2$ , where M = Li, Mg, Ni, Ti, Al, V, Co, Fe, Cr and Mn upon charge [53].....	173
Figure 4.20 – galvanostatic curves of the 1 <sup>st</sup> , 2 <sup>nd</sup> , 80 <sup>th</sup> , 120 <sup>th</sup> , and 200 <sup>th</sup> cycles of NMNTO (a), NMNFO (b) and NMNCO (c) .....	174
Figure 4.21 – Cyclic-voltammogram of NMNTO at $0.1 \text{ mV s}^{-1}$ over 5 cycles (a) and the 2nd cycles of NMNTO at 0.1, 0.2, 0.5 and $1.0 \text{ mV s}^{-1}$ (b).....	175
Figure 4.22 - Maxima of the anodic and the cathodic peaks at different scan rates, related to $v_{1/2}$ with the cathodic and anodic linear regressions of NMNTO.....	176
Figure 4.23 – Cyclic-voltammogram of NMNFO at $0.1 \text{ mV s}^{-1}$ over 5 cycles (a) and the 2nd cycles of NMNFO at 0.1, 0.2, 0.5 and $1.0 \text{ mV s}^{-1}$ (b).....	177
Figure 4.24 - Maxima of the anodic and the cathodic peaks at different scan rates, related to $v_{1/2}$ with the cathodic and anodic linear regressions of NMNFO.....	178

Figure 4.25 - Cyclic-voltammogram of NMNCO at  $0.1 \text{ mV s}^{-1}$  over 5 cycles (a) and the 2nd cycles of NMNFO at  $0.1, 0.2, 0.5$  and  $1.0 \text{ mV s}^{-1}$  (b).....179

Figure 4.26 - Maxima of the anodic and the cathodic peaks at different scan rates, related to  $v^{1/2}$  with the cathodic and anodic linear regressions of NMNCO.....180

Figure 4.27 - galvanostatic curves of NMNTO during GITT analysis and the sodium diffusion coefficient versus potential.....182

Figure 4.28 - - galvanostatic curves of NMNFO during GITT analysis and the sodium diffusion coefficient versus potential.....183

Figure 4.29- galvanostatic curves of NMNCO during GITT analysis and the sodium diffusion coefficient versus potential .....184

Figure 4.30 – Ex-situ diffractograms of NMNTO at the pristine state, OCV, 3.0, 4.3, 4.5 and 2.0 V vs  $\text{Na}^+/\text{Na}$ , with detail of the peak (0 0 2) of NMNTO.....185

Figure 4.31 – Detail of the (0 0 2) peak of the ex-situ XRD analysis of the gradient  $\text{Co}^{3+}$  substituted P2-NaNMO electrode tested at various discharge/ charge states from Hou et al. [63].....186

Figure 4.32 -- Ex-situ diffractograms of NMNFO at the pristine state, OCV, 3.0, 4.3, 4.5 and 2.0 V vs  $\text{Na}^+/\text{Na}$ , with detail of the peak (0 0 2) of NMNFO.....187

Figure 4.33 - Operando XRD analysis of the  $\text{Na}_{0.67}\text{Fe}_{0.5}\text{Mn}_{0.5}\text{O}_2$  positive electrode (a) and schematic representation of the P2 to OP4 transition (b).....188

Figure 4.34 - Ex-situ diffractograms of NMNCO at the pristine state, OCV, 3.0, 4.3, 4.5 and 2.0 V vs  $\text{Na}^+/\text{Na}$ , with detail of the peak (0 0 2) of NMNCO.....189

Figure 5.1 – Schematic representation of  $\text{CaTiO}_3$  perovskite obtained from VESTA with Materials Project database (mp-5827) where the  $\text{TiO}_6$  octahedra are represented in grey-blue, the oxygen on the tips of the octahedra in red and calcium in green.....205

Figure 5.2 – Charge/discharge curves of  $\text{CaMnO}_3$  at  $0.1 \text{ A g}^{-1}$  in the 1<sup>st</sup>, 2<sup>nd</sup>, 3<sup>rd</sup>, 5<sup>th</sup> and 10<sup>th</sup> cycles at the current density of  $0.1 \text{ A g}^{-1}$ [26]..... 207

Figure 5.3 – (a) Phase structures of the pristine, after discharge and after 300 cycles of HEPO, and (b) enlargement of the diffractogram between  $2\theta$  values of  $30^\circ$  and  $35^\circ$  [27].....209

- Figure 5.4 – a) cycling performance and Coulombic efficiency of HEPO at 100 mA·g<sup>-1</sup> and (b) galvanostatic charge/discharge profiles of the selected cycles at the current density of 100 mA·g<sup>-1</sup> [27] .....210
- Figure 5.5 – Sketch of the idealised crystal structure of the n = 1, 2, 3, and N members of the perovskite-related layered homologous series A<sub>2</sub>[A<sub>m-1</sub>B<sub>m</sub>O<sub>3m+1</sub>] (RP phases) projected along with the a and b axes.[22].....212
- Figure 5.6 – Schematic representation of a Ruddlesden-Popper type layered perovskite obtained from VESTA with Materials Project database (mp-6514) where the titanium octahedra are represented in grey-blue, lanthanum in dark green, the oxygen on the tips of the octahedra in red and sodium in yellow.....213
- Figure 5.7 – Cycling performances to the 50th cycle at 0.2 C of NaLnTiO<sub>4</sub>, where Ln = Y, Tb, Gd, Eu, Sm, Nd, Pr, La [33].....214
- Figure 5.8 – (a) Galvanostatic discharge/charge voltage profiles of NaEuTiO<sub>4</sub> for the first three cycles at 100 mA·g<sup>-1</sup>, (b) Rate performance and Coulombic efficiency at various current densities ranging from 0.1 to – 4 A g<sup>-1</sup>. [35].....216
- Figure 5.9 – X-rays diffractograms of NaEuTiO<sub>4</sub> at four different charge states: Pristine; A – Discharge to 100 mA·h·g<sup>-1</sup>; B – Discharge to 0.01 V; C – Charge to 100 mA·h·g<sup>-1</sup> and; D – Charge to 3 V.[35].....217
- Figure 5.10 – XPS spectra of Eu and Ti of two electrode samples (pristine and after 1st discharge to 0.01 V [35].....217
- Figure 5.11 – X-ray diffractograms of the samples synthesised at temperatures of 800, 840, 900, and 1000 °C with the standards of NaLaTiO<sub>4</sub> and Na<sub>2</sub>La<sub>2</sub>Ti<sub>3</sub>O<sub>10</sub> obtained from ICSD. [36] The peaks attributed only to the Na<sub>2</sub>La<sub>2</sub>Ti<sub>3</sub>O<sub>10</sub> phase are indicated with an asterisk (\*)......220
- Figure 5.12 – X-ray diffractograms of the samples synthesised with an excess of 20, 30, 40, and 50 % sodium compared with the standards of NaLaTiO<sub>4</sub> and Na<sub>2</sub>La<sub>2</sub>Ti<sub>3</sub>O<sub>10</sub> obtained from ICSD. The peaks attributed only to the Na<sub>2</sub>La<sub>2</sub>Ti<sub>3</sub>O<sub>10</sub> phase are signalled with an asterisk (\*)......222
- Figure 5.13 – Rietveld fit of XRD data of NLTO. (+) corresponds to the observed data, the solid red line indicates the calculated profile and the solid blue line corresponds to the

difference between the two profiles. (|) indicate Bragg reflections of NaLaTiO<sub>4</sub> (ICSD 73323) and Na<sub>2</sub>La<sub>2</sub>Ti<sub>3</sub>O<sub>10</sub>.....224

Figure 5.14 – Rietveld fit of XRD data of Td-WTe2. (+) corresponds to the observed data, the solid red line indicates the calculated profile and the solid blue line corresponds to the difference between the two profiles. (|) indicate Bragg reflections of NaLaTiO<sub>4</sub> (ICSD 73323) and Na<sub>2</sub>La<sub>2</sub>Ti<sub>3</sub>O<sub>10</sub>.....225

Figure 5.15 – Schematic representation of NLTO (a) and NYTO (b), where sodium is represented in yellow, lanthanum in green, yttrium in grey, titanium in blue and oxygen in red.....227

Figure 5.16 – FESEM images of as-synthesised NLTO (a) and NYTO (b) after calcination at 800 °C for 12 hours.....228

Figure 5.17 – EDS mapping of Na, Ti, La, and O elements in the as-synthesised NLTO after calcination at 800 °C for 12h.....228

Figure 5.18 – EDS mapping of Na, Ti, Y, and O elements in the as-synthesised NYTO after calcination at 800 °C for 12h.....229

Figure 5.19 – TEM images of NLTO taken from the (1 1 0) taken at the University of Liverpool (a), TEM image of NLTO taken from the (1 0 0) from Xu, et al. (b), diagram of the material seen from the (1 1 0) (c) and, diagram for the material seen from the (1 0 0) (d).....230

Figure 5.20 – 2D <sup>23</sup>Na solid-state NMR of NaLaTiO<sub>4</sub> (a) and Na<sub>2</sub>La<sub>2</sub>Ti<sub>3</sub>O<sub>10</sub> (b).....231

Figure 5.21 – 2D <sup>23</sup>Na NMR of NaYTiO<sub>4</sub> (a) and Na<sub>2</sub>CO<sub>3</sub> (b).....231

Figure 5.22 – Diffuse reflectance spectra of NLTO (a) and NYTO (b) with the calculations of each material’s bandgaps marked in red.....233

Figure 5.23 – Capacity of NLTO (•) and NYTO (•) over 45 cycles at a 0.1 C rate and Coulombic efficiency of NLTO (⊕) and NYTO (⊕), over a potential window between 0.01 and 0.60 V vs Li<sup>+</sup>/Li.....234

Figure 5.24 – Galvanostatic curves of NLTO (a) and NLTO (b) at a 0.1 C rate over a potential window of 0.01 to 0.60 V vs Li<sup>+</sup>/Li with a detail on the 2nd cycle onwards shown in the inset .....235

Figure 5.25 – Cyclic-voltammetry of NLTO at 0.1 mV s <sup>-1</sup> (a) and at 1.0 mV s <sup>-1</sup> (b) over 10 cycles.....	236
Figure 5.26 – Cyclic-voltammetry of NYTO at 0.1 mV s <sup>-1</sup> (a) and 1.0 mV s <sup>-1</sup> (b) over 10 cycles.....	237
Figure 5.27 – Heatmap of the operando X-ray diffraction on NLTO, between 0.5 ≥ Q ≥ 2 Å <sup>-1</sup> (a) and NYTO, between 1.4 ≥ Q ≥ 2.2 Å <sup>-1</sup> . Electrochemical cycling occurred between 0.01 and 0.60 V vs Li <sup>+</sup> /Li.....	238
Figure 5.28 – Capacity of NLTO (•) and NYTO (•) over 80 cycles at a 0.1 C rate and Coulombic efficiency of NLTO (⊕) and NYTO (⊕), over a potential window between 0.01 and 2.50 V vs Na <sup>+</sup> /Na.....	239
Figure 5.29 – Galvanostatic curves of NLTO (a) and NLTO (b) at a 0.1 C rate over a potential window of 0.01 to 2.50V vs Na <sup>+</sup> /Na with a detail on the 2nd cycle onwards shown in the inset.....	240
Figure 5.30 – Capacity of NLTO (•) and NYTO (•) over 80 cycles at a 1 C rate (a), 2 C rate (b), and 5 C rate, as well as the respective Coulombic efficiency of NLTO (⊕) and NYTO (⊕) for each scan rate, over a potential window between 0.01 and 0.60 V vs Na <sup>+</sup> /Na.....	241
Figure 5.31 – Cyclic-voltammetry of NYTO (a) and NYTO (b) at 0.2 mV s <sup>-1</sup> over 10 cycles.....	242
Figure 5.32 – Galvanostatic curves of NLTO and NLTO compared with carbon super-P at a 0.1 C rate over a potential window of 0.01 to 2.50V vs Na <sup>+</sup> /Na (a) and NLTO and NYTO where the capacity is normalised to the mass of carbon super-P (b).....	243
Figure 5.33 – Cyclic-voltammetry of carbon super-P at 0.2 mV s <sup>-1</sup> over 10 cycles.....	244
Figure 5.34 – Nyquist plot of NLTO before (a) and after (b) activation between 1 MHz and 1 mHz and variation of conductivity before (c) and after (d) activation with the calculated activation energy for each step.....	245

Figure 5.35– Nyquist plot of NYTO before (a) and after (b) activation between 1 MHz and 1 mHz and variation of conductivity before (c) and after (d) activation.....246

Figure 5.36 – Potentiostatic curve of NYTO versus lithium with the area below 0.3 V shaded to illustrate the area inaccessible when cycling versus sodium (a) and schematic representation of  $\text{NaLnTiO}_4$  and  $\text{LiLnTiO}_4$  adapted from Hirano, et al. ....249

## List of tables

Table 1.1 – Available energy storage technologies, energy density, efficiency and lifetime [29]–[32].....	11
Table 1.2 – Comparison between the physical and electrical properties of lithium and sodium [60].....	17
Table 2.1 – List of precursors used in synthesising the iron-rich, O <sub>3</sub> -type layered materials, their suppliers, and purities.....	49
Table 2.2 – List of precursors used in synthesising manganese, P2-type materials, their suppliers and their purities.....	51
Table 2.3 – List of precursors used in synthesising the layered perovskite oxides, their suppliers, and purities.....	52
Table 3.1 – Cell parameters, goodness-of-fitness parameters and phase composition of NaFeO <sub>2</sub> , obtained from Rietveld refinements on lab XRD data.....	96
Table 3.2 - Cell parameters, goodness-of-fitness parameter and phase composition of $\alpha$ -Na <sub>0.96</sub> Ca <sub>0.02</sub> FeO <sub>2</sub> , obtained from Rietveld refinements.....	98
Table 3.3 - Cell parameters, goodness-of-fitness parameter and phase composition of $\alpha$ -Na <sub>0.94</sub> Ca <sub>0.03</sub> FeO <sub>2</sub> , obtained from Rietveld refinements.....	100
Table 3.4 - Cell parameters, goodness-of-fitness parameter and phase composition of $\alpha$ -Na <sub>0.90</sub> Ca <sub>0.05</sub> FeO <sub>2</sub> , obtained from Rietveld refinements.....	101
Table 3.5 - Cell parameters, goodness-of-fitness parameter and phase composition of $\alpha$ -Na <sub>0.96</sub> Ca <sub>0.02</sub> FeO <sub>1.6</sub> Fo <sub>.4</sub> , obtained from Rietveld refinements.....	104
Table 3.6 - Cell parameters, goodness-of-fitness parameter and phase composition of $\square$ -Na <sub>0.94</sub> Ca <sub>0.03</sub> FeO <sub>1.4</sub> Fo <sub>.6</sub> , obtained from Rietveld refinements.....	106
Table 3.7 - Cell parameters, goodness-of-fitness parameter and phase composition of $\square$ -Na <sub>0.94</sub> Ca <sub>0.03</sub> FeO <sub>1.4</sub> Fo <sub>.6</sub> , obtained from Rietveld refinements.....	107
Table 3.8 – Sodium diffusion rate at the cathode and anode, calculated with cyclic-voltammetry at different rates of NFO, C <sub>3</sub> NFO, C <sub>5</sub> NFO, C <sub>3</sub> NFOF and C <sub>5</sub> NFOF.....	125

Table 4.1 - Cell parameters, goodness-of-fitness parameters and phase composition of P2-NMNTO, obtained from Rietveld refinements on lab XRD data.....	159
Table 4.2 - Cell parameters, goodness-of-fitness parameters and phase composition of P2-NMNFO, obtained from Rietveld refinements on lab XRD data.....	161
Table 4.3 - Cell parameters, goodness-of-fitness parameters and phase composition of P2-NMNCO, obtained from Rietveld refinements on lab XRD data.....	162
Table 4.4 – Main emission peaks of all elements used in this chapter, adapted from the EDAX peak identification chart.....	165
Table 4.5 – Anodic and cathodic sodium diffusion rates of NMNTO, NMNFO, and NMNFO.....	181
Table 5.1 – Prices of some rare earth element oxides.....	215
Table 5.2 – Atomic positions, isotropic displacement parameters, occupancies, and reliability factors of NaLaTiO <sub>4</sub> determined by the Rietveld refinement method from the PXRD data acquired at room temperature.....	224
Table 5.3 – Atomic positions, isotropic displacement parameters, occupancies, and reliability factors of NaYTiO <sub>4</sub> determined by the Rietveld refinement method from the PXRD data acquired at room temperature.....	226



## List of acronyms

**2D** – Two-dimensional

**a.u.** – Arbitrary units

**CEI** – Cathode-electrolyte interphase

**CV** – Cyclic-voltammetry

**DEC** – Diethyl carbonate

**DFT** – Density functional theory

**EC** – Ethyl carbonate

**EDS** – Energy dispersive X-ray spectroscopy

**EIS** – Electrochemical impedance spectroscopy

**HEPO** – High entropy perovskite oxide

**HOMO** – Highest occupied molecular orbital

**ICL** – Irreversible charge loss

**LIB** – Lithium-ion battery

**LUMO** – Lowest unoccupied molecular orbital

**NIB** – Sodium-ion battery

**NFO** –  $\alpha$ -Sodium iron oxide

**NLTO** – Sodium lanthanum and titanium oxide

**NMNCO** – Sodium manganese nickel and copper oxide

**NMNFO** – Sodium manganese nickel and iron oxide

**NMNTiO** – Sodium manganese nickel and titanium oxide

**NMP** – N-methyl-2-pyrrolidone

**NYTiO** – sodium yttrium titanium oxide

**PBA** – Prussian-blue analogues

**PVDF** – Polyvinylidene Fluoride

**pXRD** – Powder X-ray diffraction

**SEI** – Solid-electrolyte interphase

**SEM** – Scanning electron microscopy

**SHE** – Standard hydrogen electrode ( $E^o = 0.00$  V)

**TEM** – Transmission electron microscopy

**TM** – Transition metal

**TMO** – Transition metal oxide

**XRD** – X-ray diffraction

**Z** – atomic number



# **1. Introduction**



1.	Introduction.....	1
1.1.	Environmental impact of carbon dioxide emissions.....	4
1.2.	Geopolitical impact of fossil fuels.....	6
1.3.	Renewable energy.....	10
1.4.	Energy storage.....	11
1.5.	Rechargeable batteries.....	12
1.5.1.	Lithium-ion batteries.....	13
1.5.2.	Sodium-ion Batteries.....	17
1.6.	Cathode materials.....	20
1.6.1.	Transition-metal oxides.....	24
1.7.	Anodes.....	30
1.7.1.	Titanates – $\text{Na}_2\text{Ti}_3\text{O}_7$ .....	31
1.8.	References.....	39

## 1.1. Environmental impact of carbon dioxide emissions

Modern societies increasingly depend on electronic devices, such as mobile phones, portable computers, electric/hybrid vehicles, tracking devices and portable medical equipment with internet connectivity. These technologies have seen enormous advances that have increased both the general quality of life and the communication and co-operation between geographically separated people. Also, the increase in the prices of fossil fuels, and the well-known effects of carbon emissions, caused a resurgence of electric mobility. The development of these technologies, including electric vehicles, increases the demand for high-performance portable power storage devices. [1], [2]

Throughout history, human societies have resorted to various energy sources to improve their quality of life and ensure sustainable development. Societies have required energy to meet their lighting, cooking, mobility, communication, heating, and manufacturing needs. For most of human history, the majority of energy was sourced from burning wood or other organic matter. The Industrial Revolution began at the end of the 18<sup>th</sup> century and extended through the 19<sup>th</sup> century. It was a period of radical industrialisation, technological advancements, and modernisation that predominantly relied on fossil fuels such as coal, petroleum, and natural gas. However, the widespread burning of fossil fuels leads to significant amounts of CO<sub>2</sub> emission, contributing to global warming and climate change. [3], [4] Furthermore, the rapid population increase, coupled with rising living standards, expanding economies, and digitalisation, has led to an explosive increase in CO<sub>2</sub> emissions. Consequently, the concentration of CO<sub>2</sub> in the atmosphere has risen to 427 ppm, reflecting an increase of 50 % from the pre-industrial era. [5] Figure 1.1 illustrates the evolution of atmospheric CO<sub>2</sub> concentration from 1960 to the present day.

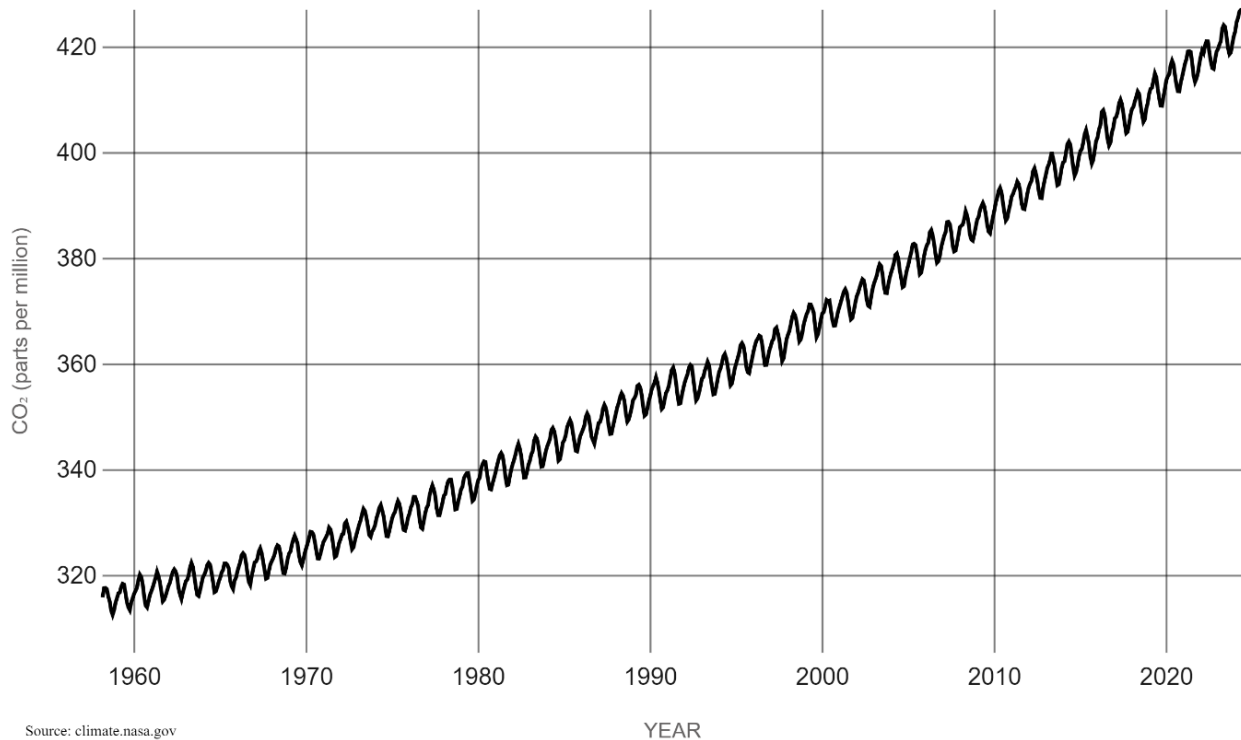


Figure 1.1 – Evolution of the concentration of CO<sub>2</sub> in Earth's atmosphere from 1960 to today obtained from the National Aeronautics and Space Administration (NASA) [6]

The International Energy Outlook 2023 report forecasts that energy consumption will keep increasing in all regions of the world due to economic and population growth. [5] Furthermore, the energy consumption in developing countries has exceeded that of the developed countries and is set to reach two-thirds of the global energy consumption expected for 2050 (739 quadrillion Btu). It is important to highlight that the crude oil reserves are expected to peak around 2030. [5] This means that part of the supply needed for the future is expected to be sourced from reservoirs not yet known. Henceforth, an increase in energy costs is expected, followed by an increase in geopolitical instability. In Figure 1.2, the forecast

of the world's energy consumption, obtained from the International Energy Outlook 2021 is shown. [4]

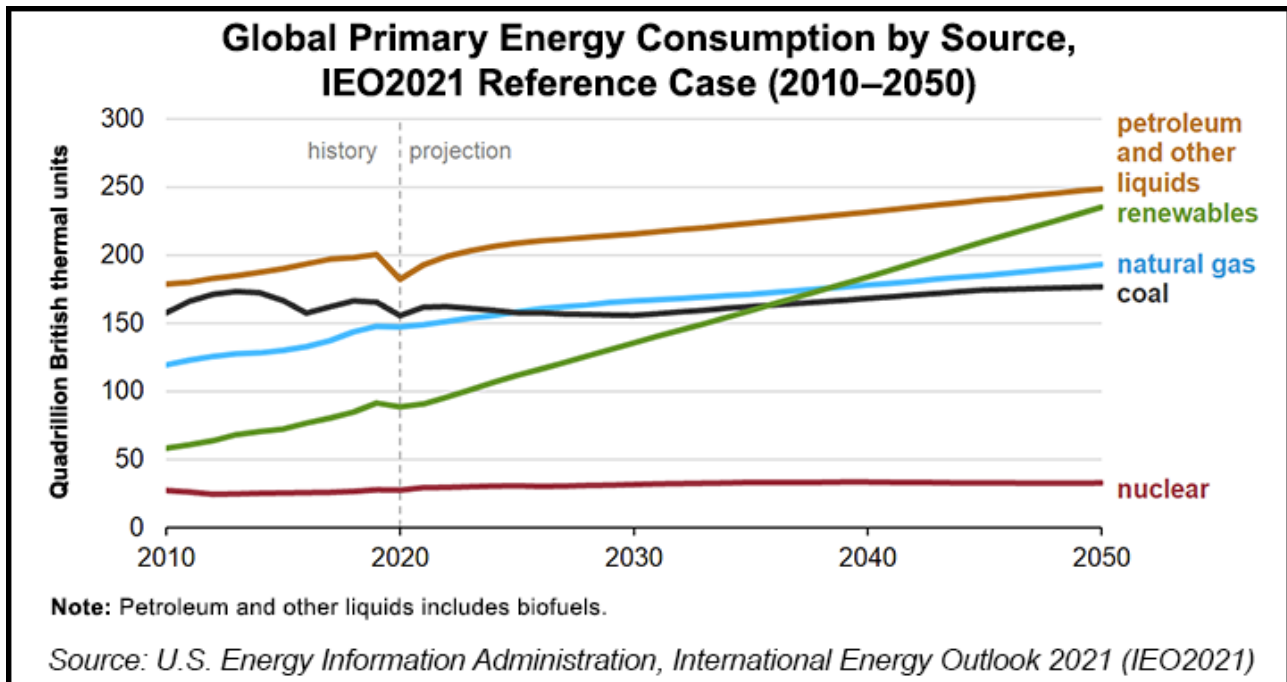


Figure 1.2 – Prediction of the world's energy demand partitioned in energy sources until the year 2050 obtained from the International Energy Outlook Report 2021. [4]

Nuclear energy can be a reliable base supplier of energy to the grid however, a series of disastrous accidents have brought up the many safety concerns of this source of energy. [7] In addition, the issue of safe disposal of nuclear waste is yet to be solved. [8]

## 1.2. Geopolitical impact of fossil fuels

The 20<sup>th</sup> century has staged numerous conflicts over energy. Some of the most notable are the Middle Eastern oil conflicts. The region's vast oil reserves have made it a focal point of international interest and intervention. Furthermore, some of the largest consumers of oil and fossil fuels do not have any reserves or demand more than what they can extract. [9] In

Figure 1.3, the map with the countries with the largest oil reserves and the countries who are the largest consumers of oil. [9]

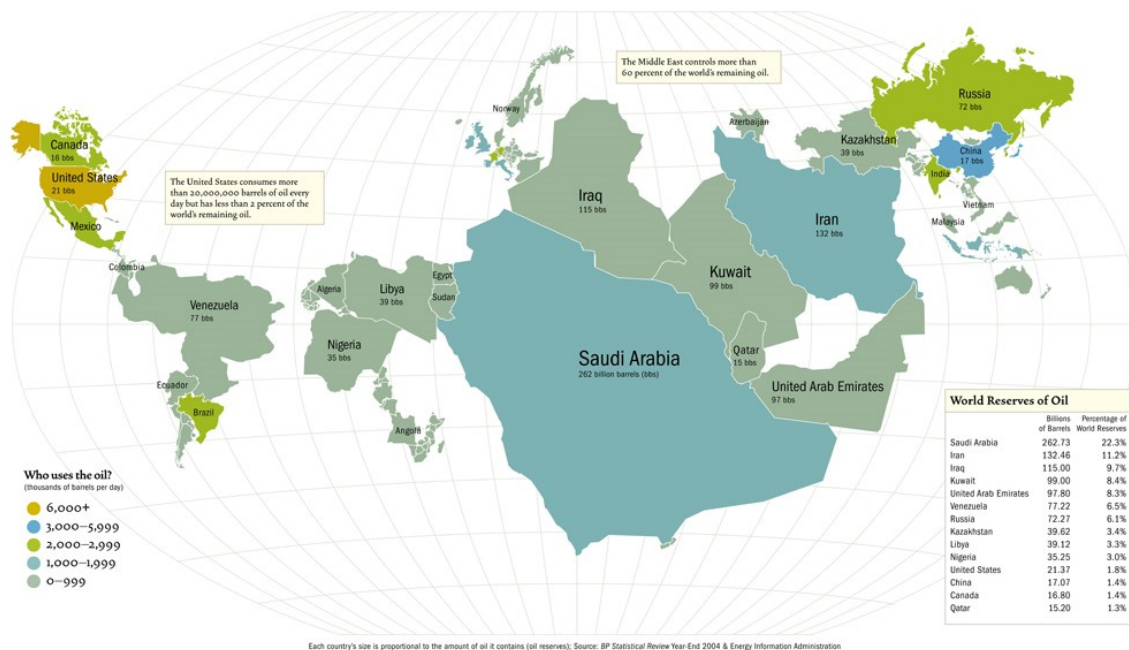


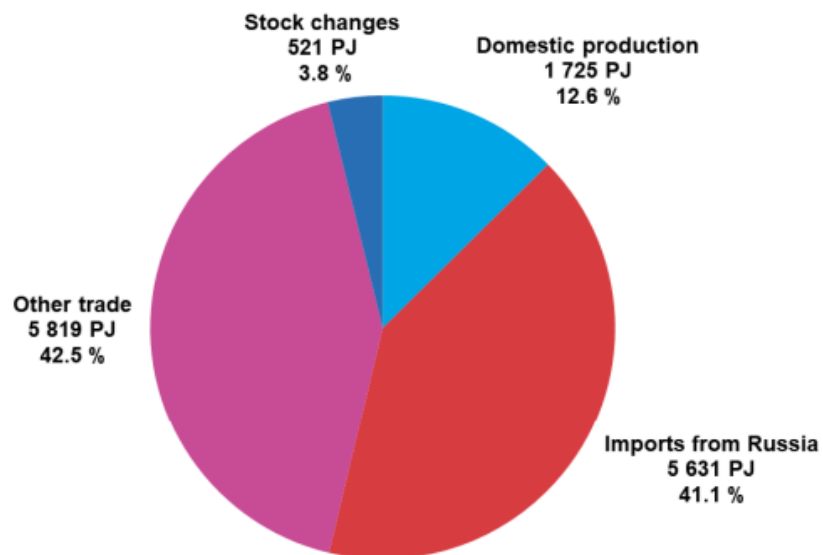
Figure 1.3 – Countries with the largest oil reserves and the largest consumers of oil. [9]

The oil embargo of 1973, where Arab oil producers restricted exports to countries supporting Israel, demonstrated the strategic leverage of oil. [10] This event not only led to an economic crisis in the West but also underscored the geopolitical power of oil-producing nations. [10]

The Gulf Wars further exemplify the link between fossil fuels and conflict. The 1990-91 Gulf War, prompted by Iraq's invasion of Kuwait, had underlying motives linked to oil control. [11] Similarly, the 2003 invasion of Iraq by the United States and its allies, though justified on grounds of weapons of mass destruction, was widely perceived as driven by the desire to secure oil resources. [12]

Beyond direct military conflicts, fossil fuels have incited numerous commercial wars. The control of oil and gas pipelines, for instance, has been a source of tension between Russia and Europe. [13] Russia's control over gas supplies and its pipeline infrastructure grants it significant political leverage over European nations, often resulting in political and economic standoffs. The 2006 and 2009 gas disputes between Russia and Ukraine are prime examples, where disagreements over prices and debts led to supply cuts, impacting several European countries dependent on Russian gas. [14] Figure 1.4 shows the natural gas production in the EU and imports in 2020 from Eurostat. [14]

**Natural gas: EU production, trade and imports, 2020**  
(in % and petajoules, PJ)



Source: Eurostat (including estimates for non-reported data)

eurostat 

Figure 1.4 – Natural gas production in the EU and imports in 2020. [13]

Economic dependencies on fossil fuels create vulnerabilities. Countries with abundant fossil fuel resources, like those in the Middle East, Russia, and Venezuela, wield significant influence. Conversely, nations reliant on imports, such as many in Europe and Asia, find

themselves susceptible to supply disruptions and price volatility. This dependency can shape foreign policies, often leading to alliances and enmities based on energy security needs.

The transition to renewable energy is poised to transform the geopolitical landscape dramatically. As nations shift towards wind, solar, and other renewable sources, the power dynamics centred around fossil fuels is expected to shift. [15] This transition holds several geopolitical implications:

**Reduction in Resource Conflicts:** Renewables are more evenly distributed globally compared to fossil fuels. Most countries have access to some form of renewable energy, whether it be solar, wind, hydro, or geothermal. This geographic dispersion reduces the likelihood of conflicts over resource control, as energy generation can become more localised. [16]

**Diminished Influence of Oil-Rich Nations:** Countries whose geopolitical power is tied to their fossil fuel reserves may see a reduction in their global influence. [17] As the world reduces its dependence on oil and gas, the strategic importance of regions like the Middle East may diminish, potentially leading to economic and political instability within those nations if they fail to diversify their economies. [17]

**New Economic Dependencies:** While renewables offer energy independence, they also create new dependencies. [18] The production of renewable energy technologies, such as solar panels and wind turbines, requires rare earth elements and other minerals. [18] Countries rich in these resources, like China, which currently dominates the supply chain for many renewable technologies, could gain significant geopolitical leverage. [19] This shift could lead to new forms of commercial competition and strategic alliances.

**Technological and Economic Shifts:** The transition to renewables involves significant technological advancements and economic restructuring. Countries leading in renewable technologies may gain economic and political advantages. [20] Innovations in energy storage,

grid infrastructure, and renewable generation will likely be the new arenas for geopolitical competition, as nations strive to become leaders in the next era of energy. [21]

The geopolitical impact of fossil fuels has been profound, driving wars and commercial conflicts, and shaping international relations. However, the ongoing energy transition to renewables heralds a potential reduction in resource-based conflicts and a reconfiguration of global power dynamics. While the move towards renewables promises a more sustainable and potentially more equitable energy landscape, it also introduces new geopolitical challenges and dependencies. As the world navigates this transition, the balance of power will shift, creating both opportunities and tensions in the quest for energy security and sustainability.

### **1.3. Renewable energy**

To avoid the impacts of CO<sub>2</sub> emissions on the environment, there has been an increasing effort to replace global energy sources with renewable sources while maintaining the global energy demand. The most common types of renewable energy sources may include wind, tidal, hydroelectric, biomass, geothermal, and photovoltaic. [22], [23] Increasing the use of renewable energy in the mix is expected to mitigate the effects of climate change and reduce the dependency on fossil fuels, which is crucial for regions where these resources do not exist. [22], [23] Many of these sources of energy are promising but, unfortunately, they are inherently intermittent which means, they do not have the same output throughout the day. [24] Energy demand, on the other hand, is relatively constant during the day. Energy sources like solar, tidal and hydroelectric are relatively predictable however, wind and waves are highly unpredictable. [25], [26] Having the possibility to store energy when it is produced so that it is available when required, could help to achieve higher penetration of renewable energy, reducing the period of the day when backup fossil sources have to be consumed. [27]

To this day, only a small percentage of energy can be stored. Therefore, the development of low-cost electrical energy storage systems is required.

#### 1.4. Energy storage

Currently, pumped hydroelectric is the most used in grid energy storage system, which stores 96 % of the total stored energy. [28] However, as shown in Table 1.1, there are a variety of systems with a higher energy density and conversion and efficiency values, such as batteries. [29]–[32] Lithium-ion batteries (LIBs) have a high energy density and high efficiency. [23] Since the beginning of the commercialisation of LIBs in 1991, these have been widely used as portable electronic devices and electric means of transportation.

Table 1.1 – Available energy storage technologies, energy density, efficiency and lifetime [29]–[32]

	<i>Energy density</i> ( $Wh\ kg^{-1}$ )	<i>Efficiency</i> (%)	<i>Lifetime</i>
<i>Pumped hydroelectric</i>	0.3-1.3	65-80	20-80 years
<i>Compressed air</i>	3.2-60	60-80	20-40 years
<i>Flywheel</i>	5-200	45-90	15-20 years
<i>Thermal energy storage</i>	10-200	40-70	4000 cycles
<i>Fuel-cell</i>	300-600	30-85	1000 cycles
<i>Capacitors</i>	0.05-5	85-95	$10^6$ cycles
<i>Pb-acid</i>	30-40	60-90	200-500 cycles
<i>Ni-Cd</i>	40-60	50-75	500 cycles
<i>Ni metal-hydrate</i>	75-100	60-80	300-500 cycles
<i>LIB</i>	100-250	70-95	500-1000 cycles

These systems are key enablers of energy storage for the electrical grid, as they allow the storage of electrical energy when it is produced. With these developments, several challenges to the energy systems and different technological solutions are required. Among

the various systems, batteries have gained ground in recent years, especially rechargeable batteries. [33] They are used in electric cars and portable devices such as mobile phones and laptops. The growing number of portable devices and their increasing power consumption make energy storage a limiting factor to their use. A typical battery in these devices lasts only a few hours. Hence, a longer lifetime of energy storage devices is required to meet the usage of portable devices. There are various types of rechargeable batteries such as Pb-acid, Ni-Cd, Ni-MH, Na-S, Li-ion, Na-ion, etc. [23], [34] For these reasons, they were originally used in portable applications such as laptops and mobile phones that became essential tools for society. [23], [34] One of the most important criteria for these devices is the weight and volume, where Li-ion batteries fulfil these requirements. Later, these batteries found use in hybrid electric vehicles (HEV) and battery electric vehicles (BEV).

### **1.5. Rechargeable batteries**

Rechargeable batteries are a type of electrochemical storage system that can store chemical energy and release electrical energy on demand. [34] These systems are known as secondary batteries because they can be recharged a significant number of times. Similarly, to non-rechargeable, or primary batteries, rechargeable batteries are composed of two electrodes connected by an electrolyte that is an ionic conductor but an electronic insulant. [34] The two electrodes have two different electrochemical potentials, which are related to their chemical composition. They are connected through an external electrical circuit that allows the transport of electrons from and electrode to the other, while ions are transported through the electrolyte. The energy density depends on the average potential between the two electrodes and their specific capacity. [35] During the charging process, the positive electrode or cathode is oxidised, releasing electrons that flow through the external circuit to the negative electrode or anode, which is reduced. [35] During the discharge process, electrons flow in the opposite direction while the negative electrode is oxidised, and the positive

electrode is reduced. The electrolyte allows the medium for internal ion flow between the electrodes.

The stored energy per unit of mass or volume that a battery can deliver is a function of the working potential of the battery and its capacity. The capacity is heavily dependent on the chemistry of the materials in the system. [36] Another important parameter is the specific power of the battery, which is defined as the power that can be delivered per unit mass in watts per kilogram ( $\text{W kg}^{-1}$ ). [37], [38] The factors that influence the specific power of a battery are:

- **Cell Chemistry** - Different battery chemistries have varying specific power capabilities.
- **Cooling and Thermal Management** - Efficient cooling systems are essential to maintain optimal battery temperatures during high-power discharges.
- **Electrode Design** - Electrodes with higher surface areas and rapid ion transport can enhance power delivery.
- **Packaging and Layout** - The arrangement of cells within the battery pack impacts heat dissipation and overall power delivery.

Some of the relevant properties of a rechargeable battery are its volumetric and gravimetric energy density and volumetric and gravimetric power density, as well as its good cycle life and rate performance.

### 1.5.1. *Lithium-ion batteries*

Lithium-ion batteries are among the most prominent candidates for energy storage applications requiring high energy density such as portable electronic devices, electric

vehicles, and stationary energy storage. [39] This is due to the low molecular weight of lithium ( $6.94 \text{ g mol}^{-1}$ ), and its small ionic radius (96 pm), enabling fast diffusion and a low redox potential ( $-3.04 \text{ V vs. SHE}$  – standard hydrogen electrode). [39] Most commercial lithium-ion batteries employ layered electrode materials and a liquid electrolyte solution of a lithium salt (*i.e.*,  $\text{LiPF}_6$ ,  $\text{LiBF}_4$  and  $\text{LiClO}_4$ ) dissolved in an organic solvent such as ethylene carbonate, propylene carbonate and dimethyl carbonate or a mixture of them. [40], [41] Since its commercialisation, billions of LIBs have been produced however, due to the use of some elements, whose exploration and extraction was proven not to be sustainable. [42] The increasing energy demand has caused an abrupt increase in the demand for lithium. [43] However, lithium is not evenly distributed in the Earth's crust and is concentrated in South America. Therefore, a peak of production is expected, leading to a significant rise in the production cost of this type of battery. [43] Adding to that, cobalt is an element widely used in cathode materials for LIBs and, is not only becoming scarce, but its exploration is also often associated with child slavery. [44] Figure 1.5 shows the distribution of the known lithium reserves and the forecast of lithium demand and production. [45], [43]

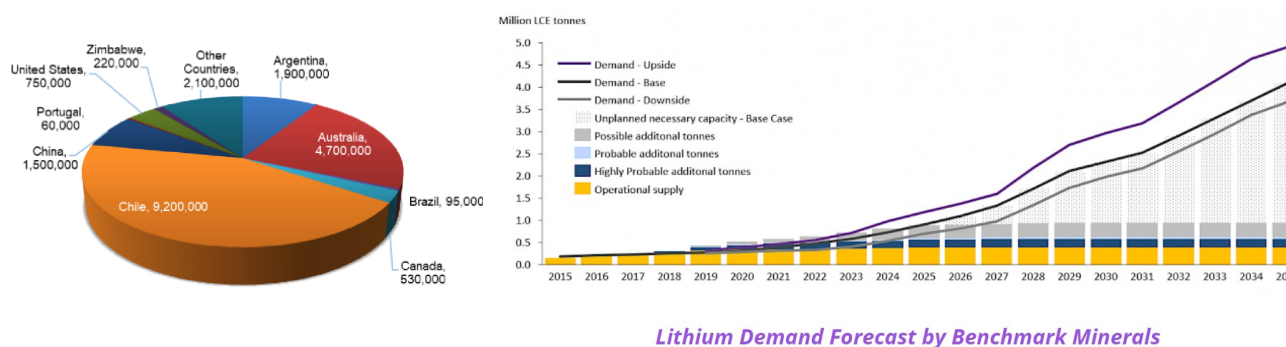


Figure 1.5 – Distribution of known lithium reserves and forecast of lithium production and demand from Benchmark Minerals Intelligence [43]

Furthermore, LIBs present various safety issues related to the flammable organic electrolytes that can react with the electrodes, potentially leading to explosions. [46] Finally,

early integrated life-cycle assessment estimations revealed that more than 400 kWh are needed to produce a 1 kWh LIB, resulting in the emission of 75 kg of CO<sub>2</sub>. [47] In comparison, to produce 1 kWh of electricity from coal combustion produces approximately 1 kg of CO<sub>2</sub>. In other words, under these conditions, batteries will only begin to have an environmental benefit after hundreds of cycles. [48]

Alternative storage systems need to be investigated to mitigate these issues. In this context, sodium-ion batteries have gained ground in recent years. The first reversible electrochemical sodium insertion at room temperature was demonstrated in 1980 using TiS<sub>2</sub> as the negative electrode, at the same period that LIBs started to be developed. [49]

However, the average discharge voltage was lower than 3 V, which favoured the abandonment of NIBs studies for LIBs, which had shown to be more promising at that time. [50] In addition, the lack of conditions and apparatuses such as electrolyte solution, binders, separators and gloveboxes were not adequate for handling sodium metal, dictating the abandonment of NIBs. [50]

The most commonly used energy storage system is the lithium-ion battery (LIB), due to its superior energy and power densities. [51] Given its low molecular weight and ionic radius, 6.94 g mol<sup>-1</sup> and 0.96 Å, respectively, lithium has a high diffusion rate. This contributes to its fast diffusion and low redox potential (-3.04 V *vs.* SHE). As a result, this technology is advantageous for the use of portable devices. These devices have also been investigated as in-site energy storage from renewable sources as a solution for their intermittent energy production. [52] In most renewable energy sources, the peak of production occurs in the hours of the day when the energy demand is at its lowest. On the other hand, when the power demand is at its highest, renewable energy production is usually, at its lowest, leading to the use of fossil fuels to bridge the gap. The use of batteries to store the excess energy produced

in off-peak hours, to be then released in time of higher consumption, could be beneficial for energy sustainability. [53]

Nonetheless, to consider this technology sustainable, one must consider the materials employed in these systems and their extracting/processing methods. [42], [54]. The price of lithium carbonate, one of the main sources of lithium, has risen from £5,300 per tonne in 2015 to £10,500 per tonne in 2019. [55], [56] Furthermore, the mining of lithium uses about 2000 m<sup>3</sup> of water per tonne, raising problems, especially in regions such as Argentina, Bolivia and Chile, also known as the Lithium Triangle, where water scarcity is an issue. [55] Adding to this fact, a typical lithium-ion battery uses a layered LiCoO<sub>2</sub> or Li<sub>0.33</sub>Mn<sub>0.33</sub>Co<sub>0.33</sub>O<sub>2</sub>-based cathode. [56] The current lithium-ion batteries cathodes constitute more than 20% of the batteries' overall cost, due to the high costs of cobalt (£24.00 per kg in February 2020), driving up the costs of production. [56]

The scientific community has turned to alternative storage technologies to mitigate the above-mentioned issues. Together with LIBs, sodium-ion batteries (NIBs) started to be studied in the late 1980s and were found to have a similar functioning mechanism. [54] Some companies have initiated studies on NIBs using sodium and lead alloys and P<sub>2</sub>-Na<sub>x</sub>CoP<sub>2</sub> as the cathode and the anode, respectively. [57] But, notwithstanding this, the average discharging potential was below 3 V, leading to the abandonment of this technology in favour of LIBs. Furthermore, the inadequacy of the existing electrolytes, binders or separators, as well as gloveboxes or other equipment to safely handle NIB, contributed to the cessation of all research in this area, at the time. Finally, the initial studies also indicated that the power density of sodium-based systems would be lower than that of lithium-based systems, given its higher atomic weight. [51], [58] Table 1.2, compares the main characteristics of lithium and sodium. [54], [59] In the later years, NIBs have attracted attention due to the higher natural abundance on Earth's crust and lower cost. [2] Additionally, LIBs present some safety

issues due to the use of flammable organic solvents that may react with the electrodes and lead to fires or even explosions. Knowing that coal is a less efficient source of energy, compared with petroleum and natural gas, batteries will only be sustainable after hundreds of cycles. This raises questions on the electrification of the automobile fleet justified by the reduction of greenhouse gases, knowing that the production and recycling of its components rely heavily on the emission of said gases. [60] Table 1.2 shows the physical and electric properties of lithium and sodium.

Table 1.2 – Comparison between the physical and electrical properties of lithium and sodium [60]

	Lithium	Sodium
Relative abundance (ppm)	20	23 600
Cost, carbonates (£/tonne)	4700	250
Cationic radius (Å)	0.76	1.02
Atomic weight (g mol <sup>-1</sup> )	6.9	23.0
Massic theoretical capacity (mA h g <sup>-1</sup> )	3861	1166
Volumic theoretical capacity (mA h cm <sup>-3</sup> )	2062	1131
Coordination preference	Octahedral, tetrahedral	Octahedral, prismatic

### 1.5.2. Sodium-ion Batteries

Given the analogous behaviour of NIBs regarding LIBs, the construction of both systems is relatively similar. In

Figure 1.6 a typical schematic of a NIB is presented. [20] Like LIBs, NIBs have a cathode-anode pair, an electrolyte and a porous separator, allowing the passage of Na<sup>+</sup> ions while preventing short-circuits. [61], [62] Typically, the cathodes consist of a transition metal oxide (*e.g.*, NaFeO<sub>2</sub>, NaFe<sub>0.5</sub>Mn<sub>0.5</sub>O<sub>2</sub>, NaFe<sub>0.5</sub>Co<sub>0.5</sub>O<sub>2</sub>, NaFe<sub>0.5</sub>Ni<sub>0.5</sub>O<sub>2</sub>, NaMnO<sub>2</sub>, *etc.*). [50], [62] The most common type of anode materials is carbon-based (*e.g.*, hard carbon, graphene,

*etc.*). [50], [62] The electrolyte is usually a sodium salt ( $\text{NaPF}_6$ ,  $\text{NaBF}_4$ ,  $\text{NaClO}_4$ , *etc.*) dissolved in an organic solvent or mixture of solvents (ethylene carbonate, propylene carbonate and dimethyl carbonate, *etc.*). [54], [61] Electrodes are deposited on a metallic current collector. The anode side current collector on LIBs anodes is usually copper, due to the possibility of lithium alloying with aluminium. [50], [59] In the case of NIBs, inexpensive aluminium can be used as the current collector in both electrodes, due to its immiscibility with sodium, contributing to a decrease in the overall cost of manufacture. [50] Figure 1.6 shows a schematic representation of a sodium-ion battery functioning. [61]

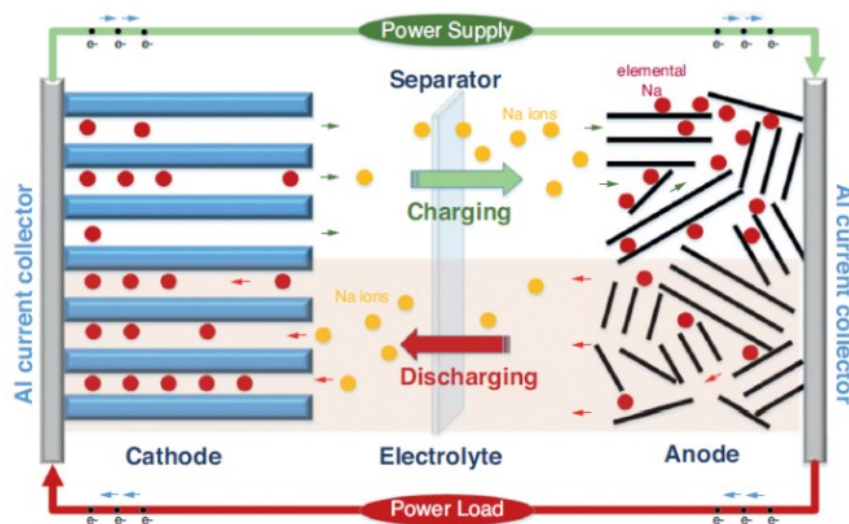


Figure 1.6 – General scheme of a sodium-ion battery functioning. [61]

In NIBs, sodium ions are transported between the cathode (positive electrode) and the anode (negative electrode) through the electrolyte. [61] During the charging process,  $\text{Na}^+$  is extracted from the cathode at a high potential,  $\mu_c$  (*e.g.*,  $\geq 3.0$  vs.  $\text{Na}^+/\text{Na}$ ), diffuses towards the anode usually at lower potentials,  $\mu_a$  (*e.g.*,  $\leq 1.0$  vs.  $\text{Na}^+/\text{Na}$ ). Electrons leave the cathode materials and, through the external circuit, associate with the anode material. [61] During discharge, the process occurs in the opposite direction.

The output potential of a battery cell will be dependent on the electrochemical potential difference between the cathode and the anode expressed as in Equation 1.1. [63]

$$V_{max} = \frac{\mu_a - \mu_c}{e} \quad \text{Equation 1.1}$$

Where  $\mu_a$  and  $\mu_c$  are the anode and the cathode electrochemical potential and  $e$ , is the magnitude of the electron charge. [63]

As shown in Figure 1.7, the materials composing the battery system should be chosen in a way that  $\mu_a$  lies below the LUMO of the electrolyte and the  $\mu_c$  above the HOMO. [22], [64]

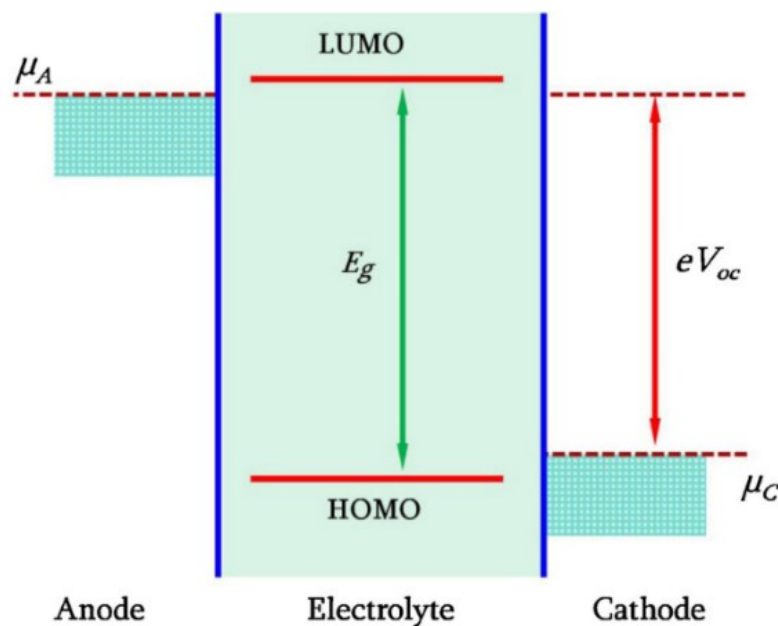


Figure 1.7 - Relative energies of the electrolyte window,  $E_g$ , and the relationship between electrochemical potentials of electrodes and the HOMO or LUMO of the electrolyte [23]

The electrochemical potential is involved in both energy and Na-ion transfer. The output potential of a battery is within the window limited by the HOMO and LUMO of a liquid electrolyte. [22], [64] If  $\mu_a$  is above the electrolyte LUMO the electrolyte will be reduced unless the anode-electrolyte reaction becomes impeded by the formation of a passivating

SEI – solid-electrolyte interphase – layer; likewise, if  $\mu_c$  situated below the HOMO, the electrolyte will be oxidised unless a passivating CEI (cathode-electrolyte interface) layer impedes the reaction. [22], [64]

## 1.6. Cathode materials

The cathode material is a crucial component in battery technology as it significantly influences the energy density, cycle life, and overall battery efficiency. [60], [65] For NIBs, the development of high-performance cathode materials is particularly challenging due to the larger ionic radius of sodium compared to lithium. [23], [44] This larger size leads to slower diffusion kinetics and greater structural strain during ion insertion and extraction, which can impact the stability and capacity of the cathode material. [44]

The exploration of various cathode materials for NIBs is therefore essential to overcome these challenges. Research focuses on optimising the structural stability, capacity, ion mobility, and electronic conductivity of these materials. The primary categories of cathode materials investigated for NIBs include polyanionic compounds, Prussian blue analogues (PBAs), and transition metal oxides. Each of these materials presents unique advantages and challenges, which are discussed in detail below. [66], [67]

Polyanionic compounds are composed of sodium, one or more transition metals, and an anion, typically a phosphate ( $\text{PO}_4^{3-}$ ) or a sulphate ( $\text{SO}_4^{2-}$ ). These compounds have attracted attention due to their robust structural stability and high working potential, which are beneficial for the performance and safety of NIBs. Examples include sodium iron phosphate ( $\text{NaFePO}_4$ ) and sodium vanadium phosphate ( $\text{Na}_2\text{V}_2(\text{PO}_4)_3$ ). [68], [69]

### Advantages:

- **Structural Stability:** The presence of polyanionic groups contributes to a more stable framework, which can withstand the volume changes during cycling. [70]

- **High Working Potential:** The strong inductive effects of the polyanionic groups lead to higher operating potentials, enhancing the energy density of the battery. [71]

### Challenges:

- **Limited Capacity:** Polyanionic compounds generally offer lower theoretical capacities compared to other cathode materials. [70], [71]
- **Restricted Ion Mobility:** The presence of large anionic groups can hinder the mobility of sodium ions, affecting the rate performance of the battery. [71]
- **Low Electronic Conductivity:** These compounds often suffer from poor electronic conductivity, necessitating the use of conductive additives or coatings to improve performance. [70]

In Figure 1.8, a schematic representation of a polyanionic compound cathode and its general sodium insertion/deinsertion equation is shown.

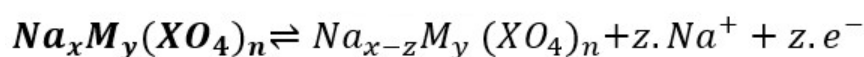
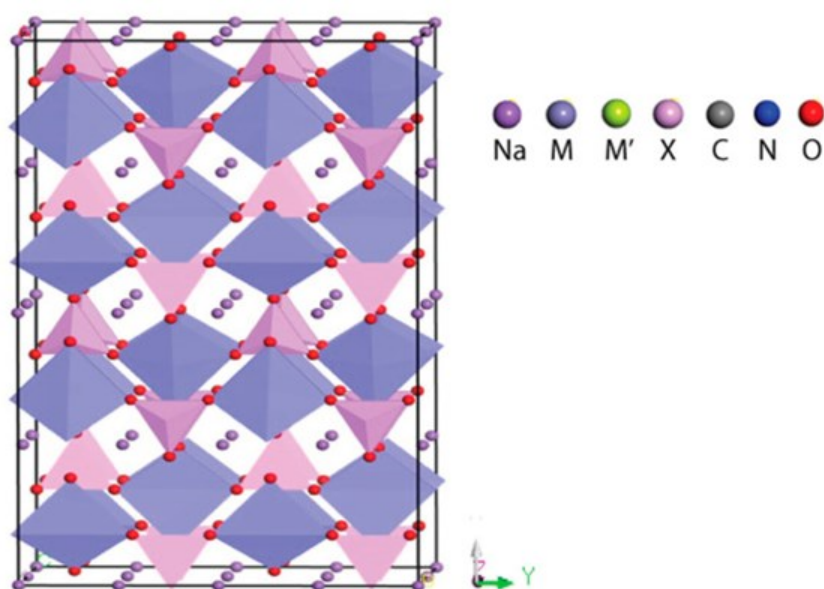


Figure 1.8 – Schematic representation of a polyanionic compound, where sodium is shown in purple, the transition metal is shown in blue, oxygen is shown in red, and the halogen is shown in pink (Adapted from Min et al. [72])

Prussian Blue Analogues are another class of promising cathode materials for NIBs. These compounds consist of sodium, one or more transition metals, and cyanometallate groups. They are known for their open framework structure, which facilitates sodium ion diffusion, increasing initial capacity and cyclability. [72] However, issues such as low electronic conductivity and the presence of interstitial water can degrade performance. [73], [74] Furthermore, interstitial water in PBAs can react with the electrolyte and anode, leading to degradation and reduced battery life. [74]

In Figure 1.9, a schematic representation of a Prussian blue analogue cathode and its general sodium insertion/deinsertion equation is shown.

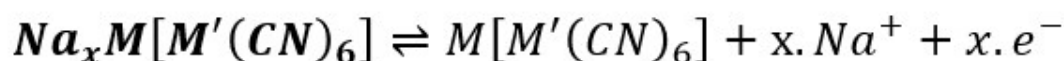
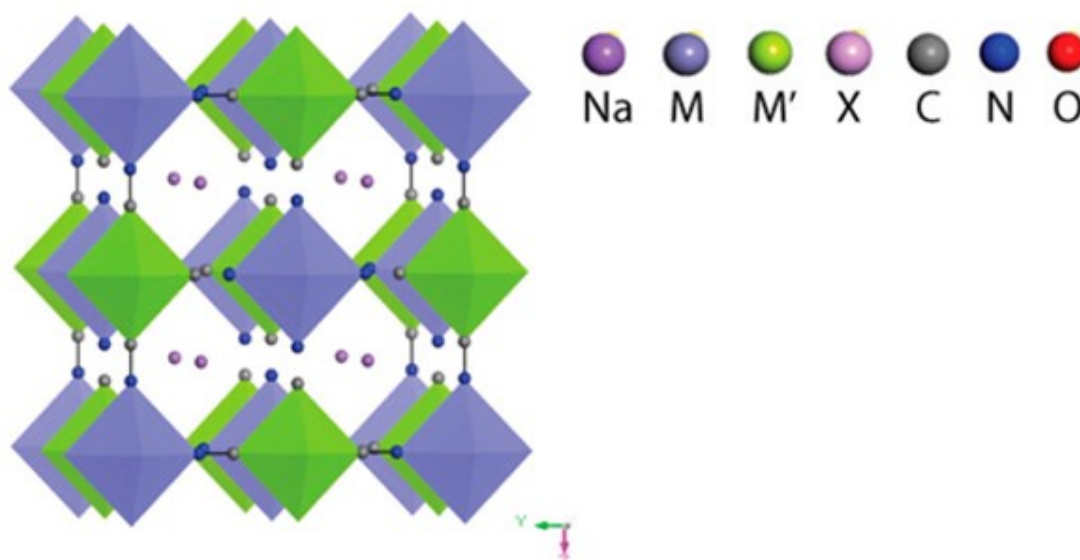


Figure 1.9 – schematic representation of a Prussian blue analogue, where sodium is shown in purple, the transition metal with a positive oxidation state is shown in blues, and the transition metal in a negative oxidation state is shown in green, nitrogen is shown in blue and carbon is shown in grey (Adapted from Jing et al.) [74]

Finally, transition metal oxides, particularly layered transition metal oxides, are a well-researched category of cathode materials for both LIBs and NIBs. These materials are

composed of sodium, one or more transition metals (such as cobalt, nickel, and manganese), and oxygen. Examples include  $\text{NaMO}_2$  ( $M = \text{Co, Ni, Mn, Fe}$ ). [59], [75]

### Advantages:

- **High Initial Capacity:** Layered transition metal oxides can deliver high initial capacities, making them attractive for high-energy-density applications. [76]
- **High Working Potential:** These materials can operate at high potentials, contributing to the overall energy density of the battery. [77]
- **Easy Synthesis:** The synthesis processes for transition metal oxides are relatively straightforward and scalable. [77]
- **Use of Abundant Elements:** It is possible to use non-toxic and abundant transition metals, such as manganese, to reduce costs and environmental impact. [66]

### Challenges:

- **Structural Instability:** These materials can suffer from structural instability during cycling due to the large volume changes associated with sodium ion insertion and extraction. [78]
- **Capacity Fading:** The high initial capacity can fade quickly over repeated cycles, which is a significant drawback for long-term applications. [79]
- **Ionic and Electronic Conductivity:** While generally better than polyanionic compounds and PBAs, transition metal oxides still face challenges with ion mobility and electronic conductivity. [80]

In Figure 1.10, a schematic representation of a transition metal oxide cathode and its general sodium insertion/deinsertion equation is shown

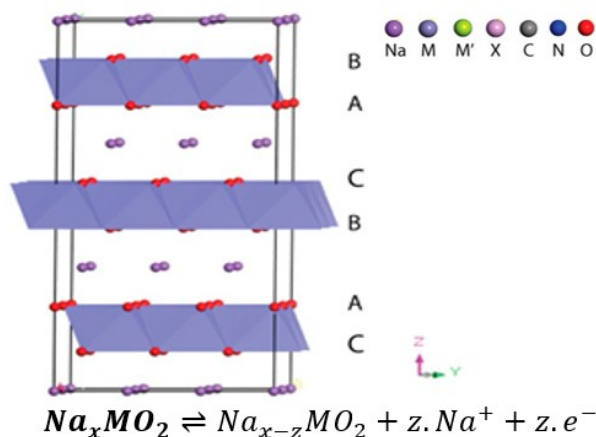


Figure 1.10 – Schematic representation of the transition metal oxide, where sodium is shown in purple, the transition metal is shown in blue, and the oxygen is shown in red

The search for optimal cathode materials for sodium-ion batteries is a dynamic and critical area of research. Each class of materials—polyanionic compounds, Prussian blue analogues, and transition metal oxides, offers unique advantages and faces specific challenges. Continued research and development are essential to address these challenges and harness the full potential of sodium-ion battery technology. By improving the performance of cathode materials, we can achieve higher capacities, longer cycle life, and better overall efficiency, paving the way for more sustainable and cost-effective energy storage solutions. [81][48]

Despite challenges like structural instability and capacity fading, the continued optimisation and engineering of transition metal oxides could lead to significant advancements in the performance and viability of sodium-ion batteries, making them a promising area of research in the quest for sustainable energy storage solutions.

### 1.6.1. Transition-metal oxides

Transition metal oxides (TMOs) are a key area of focus in the development of sodium-ion batteries due to their potential for high capacity and energy density. [82], [83] Within this

category, the specific structural types of layered transition metal oxides, namely  $O_2$ ,  $O_3$ ,  $P_2$ , and  $P_3$ , play a critical role in determining the electrochemical performance of NIBs. [84] The nomenclature of these types refers to the coordination environment of sodium ions within the crystal structure: "O" denotes octahedral coordination, while "P" denotes prismatic coordination. The accompanying number indicates the sequence of the oxygen layer stacking in the crystal lattice. [84] Understanding the characteristics of these structures is essential for optimising the performance of sodium-ion batteries. In Figure 1.11, a schematic representation of  $O_2$ ,  $O_3$ ,  $P_2$ , and  $P_3$ -type transition-metal oxides is shown. [85]

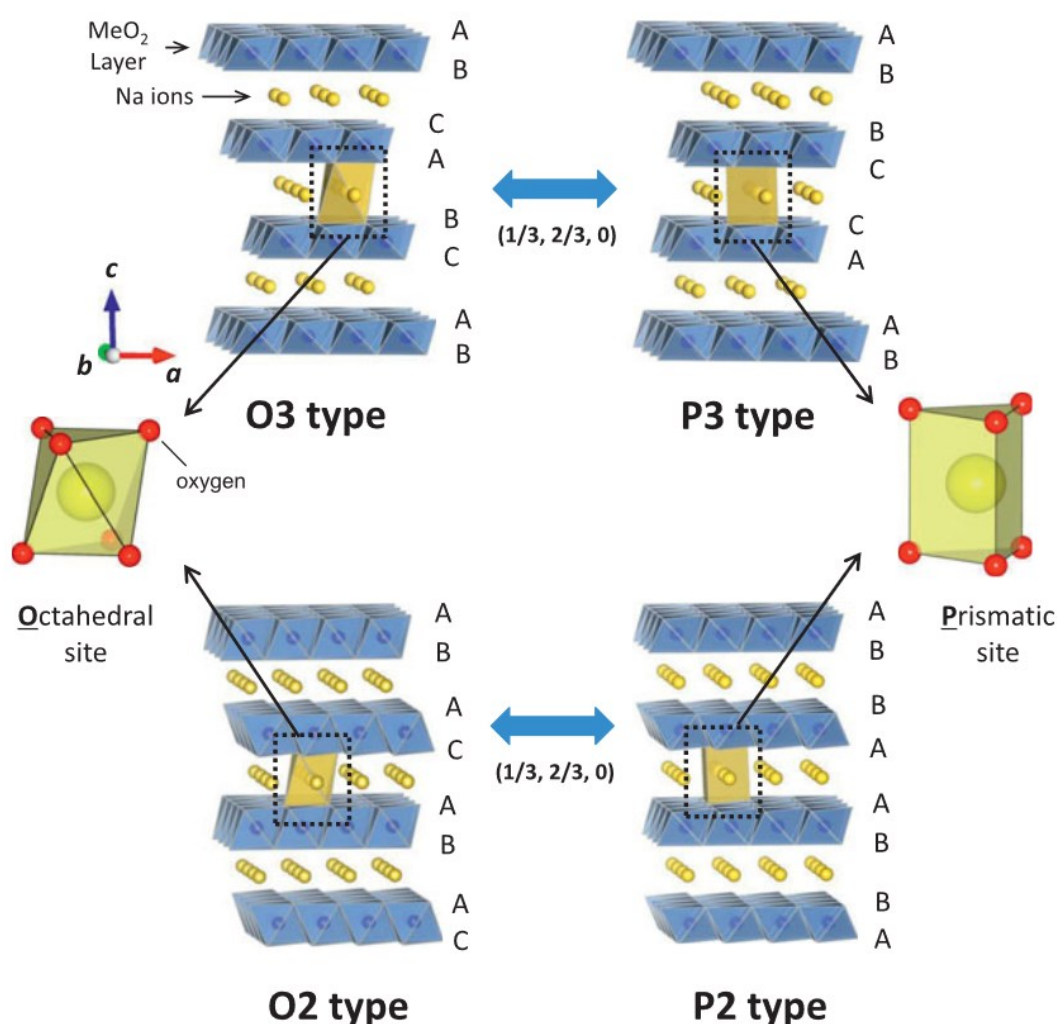


Figure 1.11 – Schematic representations of the  $O_3$ ,  $O_2$ ,  $P_3$  and  $P_2$ -type transition metal oxides the most common transition upon sodiation/desodiation [28]

$O_3$ -type transition metal oxides are characterised by their high sodium content and the arrangement of oxygen layers in an  $ABCABC$  sequence. [84], [85] This type of structure facilitates octahedral coordination for sodium ions, which can contribute to a high initial capacity due to the higher sodium content. However, this advantage comes with several drawbacks that impact the overall performance and practical application of these materials in NIBs.

#### **Advantages:**

- **High Initial Capacity:** The  $O_3$  structure allows for a high sodium content, which translates to a high initial capacity during the first few cycles of battery operation. [86]
- **Stability at High Sodium Content:** The structure can accommodate a large number of sodium ions, which is beneficial for energy density. [87]

#### **Disadvantages:**

- **Poor Performance:** Despite the high initial capacity,  $O_3$ -type TMOs often exhibit poor performance over prolonged cycling. This is due to structural instability and significant capacity fading. [87], [88]
- **Limited Sodium Mobility:** The octahedral coordination of sodium ions in the  $O_3$  structure can restrict ion mobility, leading to lower rate capabilities. [86]
- **Phase Transition:** During desodiation (removal of sodium ions),  $O_3$ -type TMOs tend to undergo a phase transition towards a  $P_3$ -type structure, particularly after 25% desodiation. This transition can introduce additional structural instability and performance degradation. [88]

$P_3$ -type transition metal oxides have a lower sodium content compared to  $O_3$ -type TMOs. [84] The oxygen layers in  $P_3$ -type structures are organised in an *ABBCCA* sequence, resulting in prismatic coordination for sodium ions. [84] This arrangement offers distinct electrochemical characteristics that can enhance the performance of sodium-ion batteries.

#### **Advantages:**

- **Higher Sodium Mobility:** The prismatic coordination in  $P_3$ -type structures facilitates better sodium ion mobility compared to the octahedral coordination in  $O_3$ -type structures. This enhances the rate capability and overall performance of the battery. [89]
- **Less Capacity Decay:**  $P_3$ -type TMOs generally exhibit less capacity decay, compared to  $O_3$ -type TMOs over cycling, making them more stable and reliable for long-term use. [90]
- **Structural Stability:** The  $P_3$  structure tends to be more stable during cycling, reducing the extent of phase transitions and associated performance losses. [89]

#### **Disadvantages:**

- **Lower Initial Capacity:** Compared to  $O_3$ -type TMOs,  $P_3$ -type TMOs have a lower initial capacity due to their reduced sodium content. [91]
- **Complex Synthesis:** Achieving a stable and high-performing  $P_3$  structure can be more challenging in terms of synthesis and material processing (*i.e.*, high temperature, aggressive synthesis conditions). [85]

$P_2$ -type transition metal oxides are similar to  $P_3$ -type TMOs in terms of advantages, with the oxygen layers arranged in an *ABBAAB* sequence. [84] This arrangement provides

prismatic coordination for sodium ions, contributing to several beneficial electrochemical properties. [92]

### Advantages:

- **High Sodium Mobility:** Like  $P_3$ -type TMOs,  $P_2$ -type TMOs offer high sodium ion mobility due to prismatic coordination, which enhances the rate capability. [79], [91]
- **Reduced Capacity Decay:**  $P_2$ -type structures exhibit less capacity decay, making them suitable for long-term cycling stability. [93], [94]
- **Structural Stability:** The  $ABBAAB$  oxygen layer arrangement provides a stable framework that can better accommodate the volume changes during cycling. [93], [95]

### Disadvantages:

- **Moderate Initial Capacity:**  $P_2$ -type TMOs have a moderate initial capacity, lower than  $O_3$ -type TMOs but comparable to  $P_3$ -type TMOs. [91]
- **Phase Transition:** During desodiation,  $P_2$ -type TMOs can transition to  $O_2$ -type structures, with oxygen layers reorganised in an  $ABACAB$  sequence. This phase transition can introduce instability and affect performance. [96]

$O_2$ -type transition metal oxides are typically formed from the desodiation of  $P_2$ -type TMOs. The oxygen layers in  $O_2$ -type structures are arranged in an  $ABACAB$  sequence, with octahedral coordination for sodium ions. [84]

### Advantages:

- **Work at high potentials:**  $O_2$ -type TMOs can operate at high potential, contributing to higher energy densities in sodium-ion batteries. [79]

**Disadvantages:**

- **Structural Instability:** The  $O_2$  structure can be less stable than  $P_2$  or  $P_3$  structures, leading to potential issues with long-term cycling and capacity retention. [79]

The various types of transition metal oxides offer distinct advantages and challenges for use in sodium-ion batteries. The choice of TMO structure can significantly influence the electrochemical performance, stability, and practical application of NIBs.  $O_3$ -type TMOs provide high initial capacity but suffer from poor long-term performance and sodium mobility. [86], [88]  $P_3$ -type and  $P_2$ -type TMOs, with their prismatic coordination and improved sodium mobility, offer more stable cycling and less capacity decay, though with slightly lower initial capacities. [89], [93], [97]  $O_2$ -type TMOs, while offering high potential operation, face challenges with structural stability and sodium content. [93] Continued research and development in optimising these structures and understanding their phase transitions are crucial for advancing sodium-ion battery technology and achieving sustainable, high-performance energy storage solutions.

Despite their challenges,  $O_3$ -type transition metal oxides may be worth exploring further due to their high initial capacity and potential for achieving high energy density. [86], [91] Their ability to accommodate a large number of sodium ions initially makes them attractive for applications where initial capacity is critical. [89] Furthermore, understanding and mitigating the phase transition to  $P_3$ -type structures during desodiation could unlock the potential for  $O_3$ -type TMOs to maintain higher performance over longer cycles. [86] Innovations in material engineering, such as doping and surface modifications, could enhance their stability and sodium mobility, making them a viable option for high-performance sodium-ion batteries.

## 1.7. Anodes

Despite the apparent simplicity of battery systems, the search for an anode material with appropriate anodic potential,  $\mu_a$ , a reversible capacity that can compete with those obtained in other systems, and structural stability remains a challenge. [98] Graphite is a common material in LIB anodes with a storage capacity of  $\approx 350 \text{ mA h g}^{-1}$  at  $\approx 0.1 \text{ V vs. Li/Li}^+$ . Unfortunately, sodium has an ionic radius of  $1.02 \text{ \AA}$  whereas the radius of lithium is  $0.76 \text{ \AA}$ . This difference is enough to hinder sodium intercalation due to the low flexibility of graphite layers. [50], [99] Figure 1.12 shows the working potential *versus* specific capacity of key anode materials.

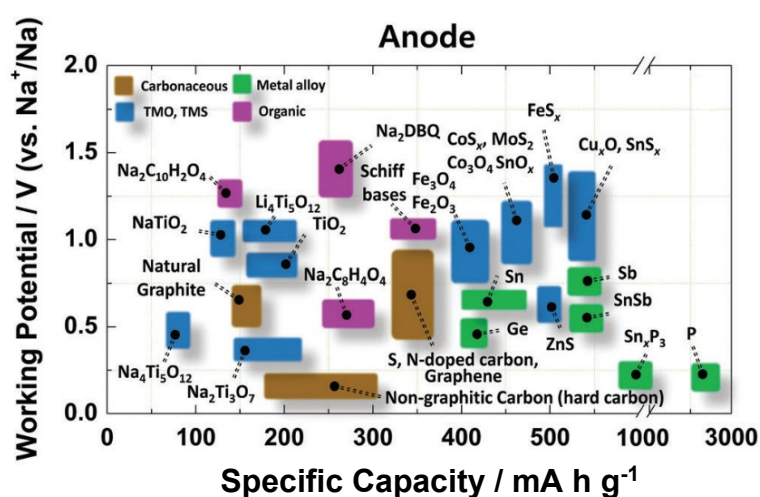
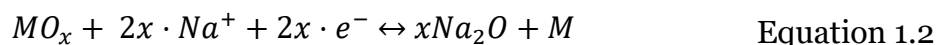


Figure 1.12 – Specific capacity versus working potential plot for materials having been reported to exhibit reversible sodium insertion and hence being potential electrode materials for sodium-ion cells.[100]

As mentioned earlier in this chapter, sodium ions have a larger radius than lithium. As a result, the mobility of sodium is lower than that of lithium, affecting the kinetics of the charge/discharge. Also, sodiated anode materials will forcibly have a lower massic charge/discharge capacity because of its higher atomic mass. [100] Hence, one of the main challenges in increasing NIB's performance is improving electrode performance. Research

on new anodes for NIB is separated according to the three mechanisms of sodiation/desodiation reaction: (1) insertion; (2) conversion; and (3) alloying. Most carbonaceous and titanium-based materials rely on an insertion mechanism. Although alloying anode materials have shown higher charge/discharge capacities, they present low cyclability, which is caused by the large increase and decrease in volume with the charge and discharge process, which leads to the formation of cracks and consequent degradation. [100], [101] Recent works investigated the application of transition metal oxides and sulphides, which rely on conversion reactions for sodiation/desodiation. [100]. In a conversion reaction, sodiation occurs by replacing one of the component elements with sodium, while the ionised element migrates to the electrolyte or intrinsic clusters. The general sodiation by conversion reaction is shown in Equation 1.2. [100]



Since the resurgence of NIB as a solution for a safe and reliable energy storage system, a wide number of materials based on transition metal oxides, especially, titanium oxides have appeared. These materials are relatively non-toxic, stable, and at the right conditions, can intercalate  $Na^+$  into their structure. [100]

Another material investigated for Na-ion batteries is  $Na_{0.66}(Li_{0.22}Ti_{0.78}O_2)$  showing a capacity of  $120 \text{ mA h g}^{-1}$  with an increase in the volume of 0.8 %. The average insertion/disinsertion potential is 0.7 V *vs.* Na/Na<sup>+</sup>. This material was shown to maintain 75 % of the initial capacity after 1200 cycles. [98]

Studies on sodium hexatitanate ( $Na_2Ti_6O_{13}$ ), found that this material can accommodate 0.85 mol per structure unit with minimal expansion. This material exhibits a discharge capacity of  $65 \text{ mA h g}^{-1}$  with a *plateau* around 0.8 V *vs.* Na/Na<sup>+</sup>. Intercalation

occurs with the reduction of Ti(IV) to Ti(III). This material has a good performance after the 3000<sup>th</sup> cycle at 20 °C. [104]

### 1.7.1. Titanates – $\text{Na}_2\text{Ti}_3\text{O}_7$

Sodium trititanate ( $\text{Na}_2\text{Ti}_3\text{O}_7$ ) has been the most widely studied anode for Na-ion batteries and the most successful. Interest in this material arose from its relatively low insertion potential of 0.3 V *vs.* Na/Na<sup>+</sup>. [105] This material is capable of intercalating two moles of Na<sup>+</sup> per cell unit, which results in a reversible capacity of 178 mA·h·g<sup>-1</sup>. The intercalation process occurs and Ti(IV) reduces the Ti(III), accompanied by the intercalation of Na<sup>+</sup>, forming  $\text{Na}_4\text{Ti}_3\text{O}_7$ . [106] Given their relatively high cyclability, high stability, and charge/discharge capacities approaching 200 mA·h·g<sup>-1</sup>, together with an interlayer space compatible with the insertion of Na<sup>+</sup> ions, layered sodiated transition metal oxides show good prospects as novel anodes for NIB. [105]

Titanates have attracted much attention for application in several electrochemical, photochemical, and photoelectrochemical applications. About a decade ago, it was found that  $\text{Na}_2\text{Ti}_3\text{O}_7$  has a relatively low average insertion potential of 3 V *vs.* Na/Na<sup>+</sup>. The structure of  $\text{Na}_2\text{Ti}_3\text{O}_7$  is composed of layers of titanium and oxygen octahedra ( $\text{Ti}_3\text{O}_7^{2-}$ ) with sodium ions in the interlayer space. The sodium in the interlayers can place itself in two crystallographic sites, with 9 or 7 coordination bonds with oxygen. [105]

In studies on  $\text{Na}_2\text{Ti}_3\text{O}_7$  from 2011, Seguttuvan *et al.* reported an intercalation potential of 0.2 V *vs.* Na<sup>+</sup>/Na and a deintercalation potential of 0.4 V *vs.* Na<sup>+</sup>/Na, the lowest compared to other transition metal oxides, resulting in a charge/discharge capacity of 178 mA·h·g<sup>-1</sup>. Upon reduction of Ti(IV) to Ti(III) at potentials around 0.3 V *vs.* Na<sup>+</sup>/Na, the increase of negative charge in the structure causes the intercalation of two moles of Na<sup>+</sup>. This process is highly reversible. [107]

As shown in Figure 1.13, layered  $\text{Na}_2\text{Ti}_3\text{O}_7$  structures are composed of layers of titanium and oxygen octahedra ( $\text{TiO}_6$ ) united by their edges with a covalent bond, giving this structure high stability. These covalent bonds result in the interaction between the  $3d$  orbitals of titanium and the  $2p$  orbitals of oxygen. The  $\text{Na}^+$  ions occupy the interlayer spaces, creating an ionic bond with the  $\text{TiO}_6$  system with a double negative charge. [108]

$\text{Na}_2\text{Ti}_3\text{O}_7$  has a wide bandgap of 3.0-3.2 eV meaning that more energy is needed to transfer an electron from the valence band to the conductive band. This has an impact on  $\text{Na}_2\text{Ti}_3\text{O}_7$  electrical conductivity and, therefore, makes the propagation of electrons throughout the structure slow. This compromises the sodiation/desodiation process, limiting the overall performance of this material as an anode for energy storage cells. To resolve this problem, there are usually two options: (1) creating fast paths of highly conductive materials to deliver charges near where the sodiation/desodiation process occurs; or (2) decreasing the band-gap of the material, facilitating the passage of electrons to the conductive band. To facilitate the passage of current,  $\text{Na}_2\text{Ti}_3\text{O}_7$  is commonly mixed with conductive carbon. [109]

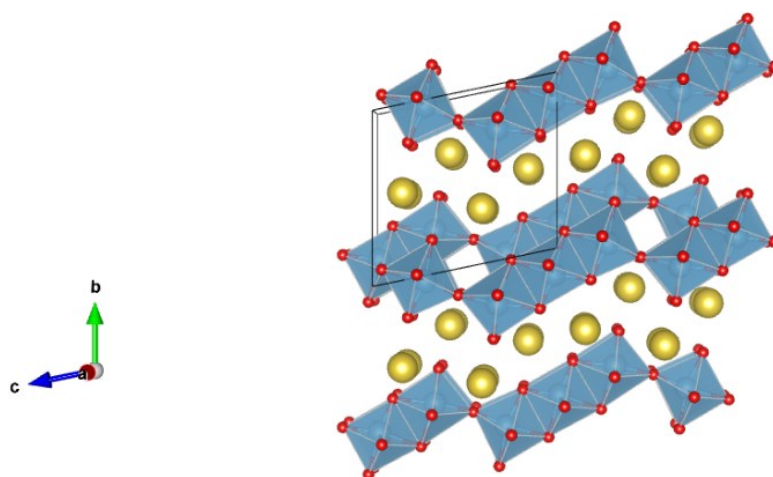


Figure 1.13 – Schematic illustration of  $\text{Na}_2\text{Ti}_3\text{O}_7$  obtained from VESTA software with the Materials Project database (mp-3488), where the yellow ball represents  $\text{Na}^+$  ions, red represents oxygen and the  $\text{TiO}_6$  octahedra are represented in blue

The redox process of the sodium titanate was followed by *in situ* XRD so that any changes in the structure could be observed. A structural change is observed during the *plateau* at 0.3 V vs. Na/Na<sup>+</sup>. [105], [108], [109] As can be observed in Figure 1.14, the peaks of the pristine phase tend to progressively disappear while the peak the peaks of the new sodiated phase emerge. As shown in Figure 1.14, the new phase is characterised by intense peaks  $2\theta$  values of 33.9, 39.2, and 40.2°. This newly formed phase has an estimated composition of Na<sub>4</sub>Ti<sub>3</sub>O<sub>7</sub>, confirming the insertion of two moles of Na<sup>+</sup> in the structure. [107]

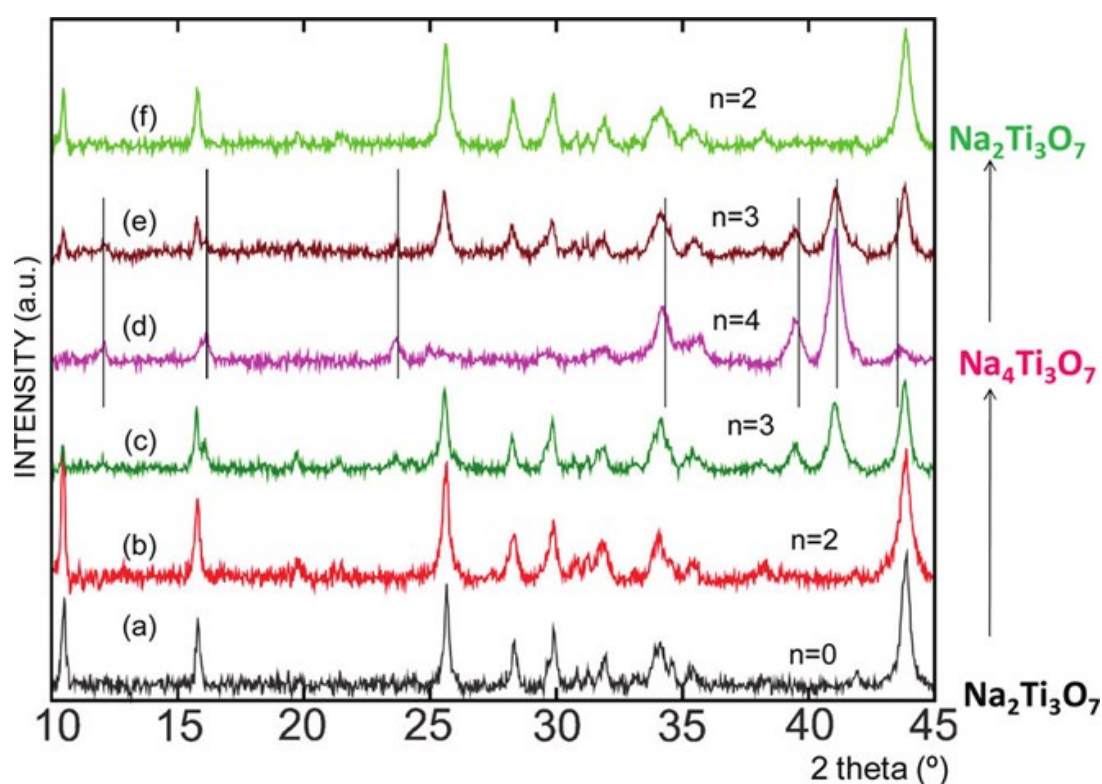


Figure 1.14 – *In-situ*, X-ray diffraction study of a Na<sub>2</sub>Ti<sub>3</sub>O<sub>7</sub>/Na metal cell, cycled between 2.5 and 0.01 V at a C/50 rate [105]

With reoxidation, the process is reversed and the amount of the Na<sub>2</sub>Ti<sub>3</sub>O<sub>7</sub> phase tends to reappear. At the end of this process, some traces of the sodiated phase can still be detected. Despite all attempts, the original structure with only two sodium ions intercalated was not obtained after cycling. [107]

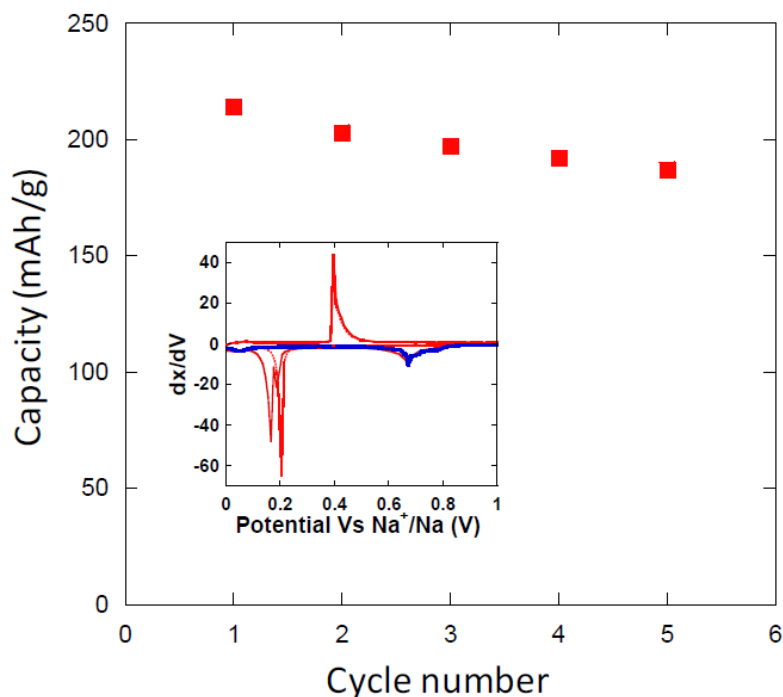


Figure 1.15 – Capacity versus cycle number for the reduction of a composite electrode containing  $\text{Na}_2\text{Ti}_3\text{O}_7$  and 30% carbon black (blue curve) once the contribution from carbon black has been subtracted. The inset shows derivative curves for the first two cycles and the blank experiment containing only carbon black (in blue). [110]

The CV analyses show a highly reversible  $\text{Na}^+$  storage process in  $\text{Na}_2\text{Ti}_3\text{O}_7$  during the charge/discharge process. As shown in Figure 1.15 the charge/discharge capacity is above  $200 \text{ mA h g}^{-1}$  with a slight decrease with cycling. [110] The differential cyclic-voltammogram was performed between  $0.01 \text{ V}$  and  $1 \text{ V}$ . The Super P Carbon black shows peaks at  $0.7 \text{ V}$ , from a reaction with the electrolyte. As shown in the differential cyclic-voltammograms, the oxidation peak occurs at  $0.4 \text{ V}$  and the reduction peak occurs at  $0.2 \text{ V}$ . [110]

A study by Chen *et al.*, aimed the increase the capacity by increasing the surface area, by depositing sodium titanate in nickel foam. To understand the electrochemical performance of the  $\text{Na}_2\text{Ti}_3\text{O}_7$  anode, the charge /discharge curve at  $20 \text{ mA}\cdot\text{g}^{-1}$  and the cycling performance at  $20, 50, 100, 200$  and  $400 \text{ mA g}^{-1}$  of  $\text{Na}_2\text{Ti}_3\text{O}_7$  and  $\text{Na}_2\text{Ti}_3\text{O}_7$  anode deposited on Ni-foam, acting a current fast path is presented in Figure 1.16. [110]

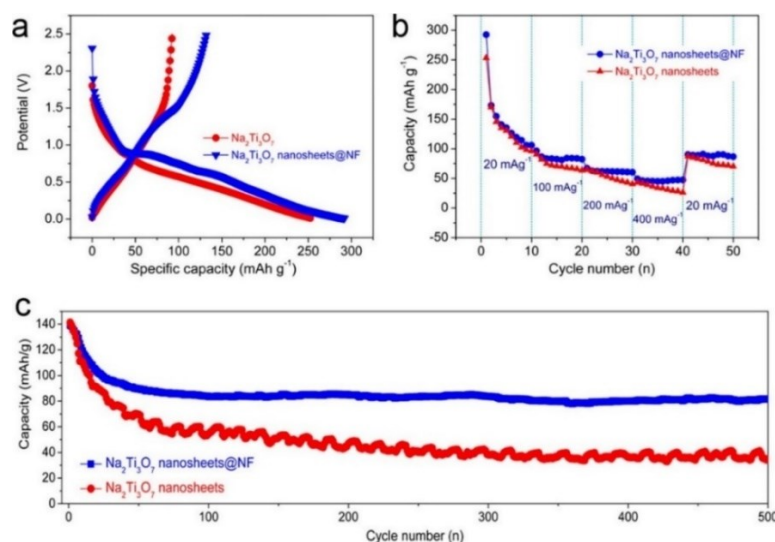


Figure 1.16 – (a) Charge/discharge curves of layered Na<sub>2</sub>Ti<sub>3</sub>O<sub>7</sub> (red) and Na<sub>2</sub>Ti<sub>3</sub>O<sub>7</sub> deposited on Ni-foam (blue); (b) Cycling performance at 20, 100, 200 and 400 mA h g<sup>-1</sup>; Cyclic performance over 500 cycles at 50 mA g<sup>-1</sup>. [110]

The tests carried out at 20 mA g<sup>-1</sup> show an initial capacity of Na<sub>2</sub>Ti<sub>3</sub>O<sub>7</sub>, deposited on aluminium foil, of 253.3 mA h g<sup>-1</sup> and for Na<sub>2</sub>Ti<sub>3</sub>O<sub>7</sub> deposited in Ni-foam of 300.2 mA h g<sup>-1</sup>. Due to the facilitated conduction of the generated current to the electrical circuit, the capacity of Na<sub>2</sub>Ti<sub>3</sub>O<sub>7</sub> deposited in Ni-foam is higher with a coulomb efficiency of 45.2 %. The capacity of Na<sub>2</sub>Ti<sub>3</sub>O<sub>7</sub> deposited in Ni-foam reaches 96.4, 67.2, and 50.3 mA h g<sup>-1</sup> at current densities of 100, 200, and 400 mA·g<sup>-1</sup> after the 10<sup>th</sup> cycle. The initial capacity of Na<sub>2</sub>Ti<sub>3</sub>O<sub>7</sub> in Ni-foam reaches 139.3 mA h g<sup>-1</sup> at a current density of 100 mA g<sup>-1</sup>. Initially, when cycling at 50 mA g<sup>-1</sup>, the capacity of Na<sub>2</sub>Ti<sub>3</sub>O<sub>7</sub> and Na<sub>2</sub>Ti<sub>3</sub>O<sub>7</sub> deposited in Ni-foam are close. After 500 cycles, the Na<sub>2</sub>Ti<sub>3</sub>O<sub>7</sub> deposited in Ni-foam reaches 81.7 mA h g<sup>-1</sup> representing a decay of 41.3 %. The capacity of the “pure” Na<sub>2</sub>Ti<sub>3</sub>O<sub>7</sub> decays to 34.4 mA h g<sup>-1</sup>, representing a decay of 82.61 %. [110]

One of the factors that compromise the cyclability of these materials, is the stability of the fully discharged state of sodium titanates (Na<sub>4</sub>Ti<sub>3</sub>O<sub>7</sub>). The electrostatic forces resulting from the extra Na<sup>+</sup> cause an increase of free Gibbs energy of the structure causing the structure's “self-relaxation” behaviour. When a titanate electrode is left fully discharged for

up to 10 days, the  $\text{Na}_4\text{Ti}_3\text{O}_7$  tends to desodiate back to a  $\text{Na}_2\text{Ti}_3\text{O}_7$ . Similarly to the study by Senguttuvan *et al.*, the  $(\bar{3} 0 2)$  and  $(1 0 4)$  peaks, characteristic of the sodiated  $\text{Na}_4\text{Ti}_3\text{O}_7$ , marked in Figure 1.17, tend to disappear, but some traces of the sodiated phase remain.

[111][112]

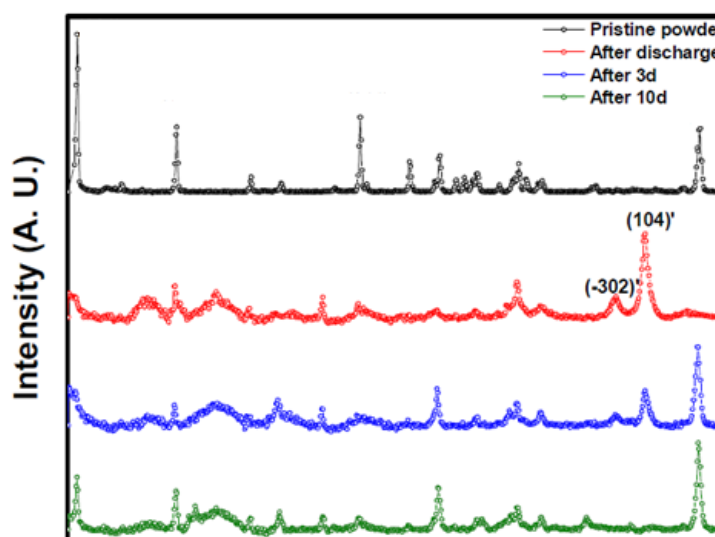


Figure 1.16 – XRD patterns of  $\text{Na}_2\text{Ti}_3\text{O}_7$  power (in black),  $\text{Na}_4\text{Ti}_3\text{O}_7$  after discharge (in red), three days after discharge (in blue), ten days after discharge (in green) [112]

According, to the data presented above, the fully sodiated structure ( $\text{Na}_4\text{Ti}_3\text{O}_7$ ) tends to relax back towards the pristine  $\text{Na}_2\text{Ti}_3\text{O}_7$  structure. [112] This structure relaxation hinders the battery cyclability and the capacity to hold on to a state of complete charge or discharge over long periods.[113]

A characteristic of several materials used as anodes in NIB, such as  $\text{Na}_2\text{Ti}_3\text{O}_7$ , is an unstable surface-electrolyte interface (SEI). [112] As described by Niemöler *et al.*, the SEI is a thin layer that forms on the surface of anode materials working at potentials below 1 V *vs.* sodium. [114] The formation of this layer is critical for the stability of the anode materials because it forms a passivation layer, assuring safe operation and long life for the battery system in general and preventing self-discharge. [115] [108] There is little consensus on the SEI composition and its mechanism of formation. [114] A consistent understanding is further

complicated by a large number of compounds found on cycles anode surfaces such as  $\text{Na}_2\text{CO}_3$ ,  $\text{Na}_2\text{O}$ , and other organic compounds. These compounds are suggested to originate from surface reactions between the products of reduction of the organic solvents or the counter ion of the electrolyte. [108] Hence, the formation of the SEI usually results in the use of part of the electrolyte in solution, resulting in irreversible charge loss (ICL). [115]

Due to its large importance on passivation and preservation of capacity, apart from being permeable to  $\text{Na}^+$ , the SEI layer should be resistant to cracking due to the material change of volume. [108], [114] The instability of these passivation layers usually results in the constant use of new electrolytes for the reformation of a new SEI layer, increasing the ICL. [108], [115]

The search for alternatives to titanates that do not self-relax is needed for the applicability of non-carbonaceous anodes in sodium-ion batteries

## 1.8. References

- [1] N. Nitta, F. Wu, J. T. Lee, and G. Yushin, “Li-ion battery materials: Present and future,” *Mater. Today*, vol. 18, no. 5, pp. 252–264, 2015, doi: 10.1016/j.mattod.2014.10.040.
- [2] K. Vignarooban *et al.*, “Current trends and future challenges of electrolytes for sodium-ion batteries,” *Int. J. Hydrogen Energy*, vol. 41, no. 4, pp. 2829–2846, 2016, doi: 10.1016/j.ijhydene.2015.12.090.
- [3] N. S. Lewis, “Powering the Planet,” *MRS Bull.*, vol. 32, no. 10, pp. 808–820, 2007, doi: 10.1557/mrs2007.168.
- [4] IEA, “World Energy Outlook 2021 日本語サマリー,” 2021.
- [5] “International Energy Outlook 2023 Narrative - IEO2023\_Narrative.”
- [6] D. Bolles, “Carbon Dioxide Vital Signs – Climate Change,” *SMD Content Editors*, 2023. <https://climate.nasa.gov/vital-signs/carbon-dioxide/?intent=121> (accessed Jul. 17, 2024).
- [7] G. Good, *The Security of Energy Supply and the Contribution of Nuclear Energy*, vol. 1, no. April. 2015.
- [8] M. Jacoby, “As nuclear waste piles up, scientists seek the best long-term storage solutions,” *Chemical & Engineering News*, p. 12, 2020.
- [9] J. Konrad, “Who Has The Oil? A Map of World Oil Reserves. – gCaptain,” 2010.
- [10] A. Zeidan, “Arab oil embargo,” *Encyclopaedia Britannica*. 2024.
- [11] J. Wharton, “What Caused The Gulf War?,” *Forces Net*, 2021.
- [12] C. Doherty and J. Kiley, “20 Years After Iraq War Began, a Look Back at U.S. Public Opinion | Pew Research Center,” Pew Research Center.
- [13] Eurostat, “Archive:EU energy mix and import dependency,” *Eurostat Stat. Explain.*, no. May, pp. 1–12, 2022.
- [14] S. Pirani, J. Stern, and K. Yafimava, *The Russo-Ukrainian gas dispute of January 2009: a comprehensive assessment*, vol. NG 27, no. February 2009. 2009.
- [15] Q. Hassan *et al.*, “The renewable energy role in the global energy Transformations,” *Renew. Energy Focus*, vol. 48, no. January, p. 100545, 2024, doi: 10.1016/j.ref.2024.100545.
- [16] I. Overland, J. Juraev, and R. Vakulchuk, “Are renewable energy resources more evenly distributed than fossil fuels?,” *Renew. Energy*, vol. 200, no. December 2021, pp. 379–386, 2022, doi: 10.1016/j.renene.2022.09.046.
- [17] F. F. Clairmont, *Cuba and Venezuela: The Nemeses of Imperialism*. 2007.
- [18] S. T. Huber and K. Steininger, “Critical sustainability issues in the production of wind and solar electricity generation as well as storage facilities and possible solutions,” *J. Clean. Prod.*, vol. 339, no. January, p. 130720, 2022, doi: 10.1016/j.jclepro.2022.130720.
- [19] Y. Ghorbani *et al.*, “The strategic role of lithium in the green energy transition: Towards

- an OPEC-style framework for green energy-mineral exporting countries (GEMEC),” *Resour. Policy*, vol. 90, no. January, p. 104737, 2024, doi: 10.1016/j.resourpol.2024.104737.
- [20] A. Raihan and A. Tuspekova, “Role of economic growth, renewable energy, and technological innovation to achieve environmental sustainability in Kazakhstan,” *Curr. Res. Environ. Sustain.*, vol. 4, no. December 2021, p. 100165, 2022, doi: 10.1016/j.crsust.2022.100165.
- [21] K. Westphal, “Global Energy Governance: Meeting the Challenge of the Energy Transition,” *The Geopolitics of Energy - Out with the old, in with the new?*, vol. Issue 26, no. 126. 2021.
- [22] G. L. Soloveichik, “Battery Technologies for Large-Scale Stationary Energy Storage,” *Annu. Rev. Chem. Biomol. Eng.*, vol. 2, pp. 503–530, 2011, doi: 10.1146/annurev-chembioeng-061010-114116.
- [23] B. Dunn, H. Kamath, and J.-M. Tarascon, “Electrical Energy Storage for the Grid: A Battery of Choices System power ratings, module size.”
- [24] A. Azarpour, S. Suhaimi, G. Zahedi, and A. Bahadori, “A review on the drawbacks of renewable energy as a promising energy source of the future,” *Arab. J. Sci. Eng.*, vol. 38, no. 2, pp. 317–328, 2013, doi: 10.1007/s13369-012-0436-6.
- [25] M. J. Grubb, “The integration of renewable electricity sources,” *Energy Policy*, vol. 19, no. 7, pp. 670–688, 1991, doi: 10.1016/0301-4215(91)90100-3.
- [26] R. F. Nicholls-Lee and S. R. Turnock, *Tidal energy extraction: Renewable, sustainable and predictable*, vol. 91, no. 1. 2008.
- [27] D. Anderson and M. Leach, “Harvesting and redistributing renewable energy: On the role of gas and electricity grids to overcome intermittency through the generation and storage of hydrogen,” *Energy Policy*, vol. 32, no. 14, pp. 1603–1614, 2004, doi: 10.1016/S0301-4215(03)00131-9.
- [28] A. Blakers, M. Stocks, B. Lu, and C. Cheng, “A review of pumped hydro energy storage,” *Prog. Energy*, vol. 3, no. 2, 2021, doi: 10.1088/2516-1083/abeb5b.
- [29] I. Buchmann, “Battery University - What’s the Best Battery?,” *Www.Batteryuniversity.Com*. 2010.
- [30] S. Sabihuddin, A. E. Kiprakis, and M. Mueller, “A numerical and graphical review of energy storage technologies,” *Energies*, vol. 8, no. 1, pp. 172–216, 2015, doi: 10.3390/en8010172.
- [31] H. Chen, T. N. Cong, W. Yang, C. Tan, Y. Li, and Y. Ding, “Progress in electrical energy storage system: A critical review,” *Prog. Nat. Sci.*, vol. 19, no. 3, pp. 291–312, 2009, doi: 10.1016/j.pnsc.2008.07.014.
- [32] J. Green and P. Newman, “Disruptive innovation, stranded assets and forecasting: the rise and rise of renewable energy,” *J. Sustain. Financ. Invest.*, vol. 7, no. 2, pp. 169–187, 2017, doi: 10.1080/20430795.2016.1265410.
- [33] Z. Yang *et al.*, “Electrochemical energy storage for green grid,” *Chemical Reviews*, vol. 111, no. 5. pp. 3577–3613, May 11, 2011, doi: 10.1021/cr100290v.

- [34] M. Armand and J. M. Tarascon, “Building better batteries,” *Nature*, vol. 451, no. 7179, pp. 652–657, 2008, doi: 10.1038/451652a.
- [35] X. Wang and J. P. Zheng, “The Optimal Energy Density of Electrochemical Capacitors Using Two Different Electrodes,” *J. Electrochem. Soc.*, vol. 151, no. 10, p. A1683, 2004, doi: 10.1149/1.1787841.
- [36] G. G. Eshetu *et al.*, “Electrolytes and Interphases in Sodium-Based Rechargeable Batteries: Recent Advances and Perspectives,” *Adv. Energy Mater.*, vol. 10, no. 20, 2020, doi: 10.1002/aenm.202000093.
- [37] J. Xu *et al.*, “High-Energy Lithium-Ion Batteries: Recent Progress and a Promising Future in Applications,” *Energy Environ. Mater.*, vol. 6, no. 5, pp. 1–26, 2023, doi: 10.1002/eem2.12450.
- [38] “What do you mean by Specific Power of an EV Battery\_ - everything PE.” <https://www.everythingpe.com/community/what-do-you-mean-by-specific-power-of-an-ev-battery> (accessed Jul. 21, 2024).
- [39] M. M. Thackeray, C. Wolverton, and E. D. Isaacs, “Electrical energy storage for transportation - Approaching the limits of, and going beyond, lithium-ion batteries,” *Energy Environ. Sci.*, vol. 5, no. 7, pp. 7854–7863, 2012, doi: 10.1039/c2ee21892e.
- [40] J.-M. Tarascon and M. Armand, “Issues and challenges facing rechargeable lithium batteries,” 2001.
- [41] R. G. Houdeville, A. P. Black, A. Ponrouch, M. R. Palacín, and F. Fauth, “Operando Synchrotron X-ray Diffraction Studies on TiS<sub>2</sub>: The Effect of Propylene Carbonate on Reduction Mechanism,” *J. Electrochem. Soc.*, vol. 168, no. 3, p. 030514, Mar. 2021, doi: 10.1149/1945-7111/abeg83.
- [42] M. C. S. U.S. Geological Survey, “No Title.”
- [43] Y. Yang, E. G. Okonkwo, G. Huang, S. Xu, W. Sun, and Y. He, “On the sustainability of lithium ion battery industry – A review and perspective,” *Energy Storage Mater.*, vol. 36, no. October 2020, pp. 186–212, 2021, doi: 10.1016/j.ensm.2020.12.019.
- [44] B. Sayahpour, H. Hirsh, S. Parab, L. H. B. Nguyen, M. Zhang, and Y. S. Meng, “Perspective: Design of cathode materials for sustainable sodium-ion batteries,” *MRS Energy Sustain.*, vol. 9, no. 2, pp. 183–197, 2022, doi: 10.1557/s43581-022-00029-9.
- [45] “Why is now time for Lithium mining\_ – M i N M E T.” <https://minmet.com/blog/why-is-now-time-for-lithium-mining/> (accessed Jul. 18, 2024).
- [46] K. Deng *et al.*, “Nonflammable organic electrolytes for high-safety lithium-ion batteries,” *Energy Storage Mater.*, vol. 32, no. July, pp. 425–447, 2020, doi: 10.1016/j.ensm.2020.07.018.
- [47] F. Arshad *et al.*, “Life Cycle Assessment of Lithium-ion Batteries: A Critical Review,” *Resour. Conserv. Recycl.*, vol. 180, no. January, 2022, doi: 10.1016/j.resconrec.2022.106164.
- [48] D. Larcher and J. M. Tarascon, “Towards greener and more sustainable batteries for electrical energy storage,” *Nat. Chem.*, vol. 7, no. 1, pp. 19–29, 2015, doi:

10.1038/nchem.2085.

- [49] Z. Hu, “Transition metal sulfide and phosphide for high performance lithium and sodium storage Transition metal sulfide and phosphide for high performance lithium and sodium storage,” 2019.
- [50] N. Yabuuchi, K. Kubota, M. Dahbi, and S. Komaba, “Research development on sodium-ion batteries,” *Chem. Rev.*, vol. 114, no. 23, pp. 11636–11682, 2014, doi: 10.1021/cr500192f.
- [51] K. Kubota and S. Komaba, “Review—Practical Issues and Future Perspective for Na-Ion Batteries,” *J. Electrochem. Soc.*, vol. 162, no. 14, pp. A2538–A2550, 2015, doi: 10.1149/2.0151514jes.
- [52] N. Nitta, F. Wu, J. T. Lee, and G. Yushin, “Li-ion battery materials: present and future,” *Mater. Today*, vol. 18, no. 5, pp. 252–264, Jun. 2015, doi: 10.1016/J.MATTOD.2014.10.040.
- [53] J. Y. Lee, A. K. Ramasamy, K. H. Ong, R. Verayiah, H. Mokhlis, and M. Marsadek, “Energy storage systems: A review of its progress and outlook, potential benefits, barriers and solutions within the Malaysian distribution network,” *J. Energy Storage*, vol. 72, no. PB, p. 108360, 2023, doi: 10.1016/j.est.2023.108360.
- [54] J. Y. Hwang, S. T. Myung, and Y. K. Sun, “Sodium-ion batteries: Present and future,” *Chem. Soc. Rev.*, vol. 46, no. 12, pp. 3529–3614, 2017, doi: 10.1039/c6cs00776g.
- [55] A. Katwala, “The spiralling environmental cost of our lithium battery addiction,” *Wired*. 2018.
- [56] J. H. Kim, N. P. W. Pieczonka, and L. Yang, “Challenges and approaches for high-voltage spinel lithium-ion batteries,” *ChemPhysChem*, vol. 15, no. 10, pp. 1940–1954, 2014, doi: 10.1002/cphc.201400052.
- [57] M. S. Balogun, Y. Luo, W. Qiu, P. Liu, and Y. Tong, “A review of carbon materials and their composites with alloy metals for sodium ion battery anodes,” *Carbon N. Y.*, vol. 98, pp. 162–178, 2016, doi: 10.1016/j.carbon.2015.09.091.
- [58] M. S. Balogun, Y. Luo, W. Qiu, P. Liu, and Y. Tong, *A review of carbon materials and their composites with alloy metals for sodium ion battery anodes*, vol. 98. Elsevier Ltd, 2016.
- [59] M. D. Slater, D. Kim, E. Lee, and C. S. Johnson, “Sodium-ion batteries,” *Adv. Funct. Mater.*, vol. 23, no. 8, pp. 947–958, 2013, doi: 10.1002/adfm.201200691.
- [60] D. Kundu, E. Talaie, V. Duffort, and L. F. Nazar, “The emerging chemistry of sodium ion batteries for electrochemical energy storage,” *Angew. Chemie - Int. Ed.*, vol. 54, no. 11, pp. 3432–3448, 2015, doi: 10.1002/anie.201410376.
- [61] J. Tang, A. D. Dysart, and V. G. Pol, “Advancement in sodium-ion rechargeable batteries,” *Curr. Opin. Chem. Eng.*, vol. 9, pp. 34–41, 2015, doi: 10.1016/j.coche.2015.08.007.
- [62] B. Mortemard De Boisse *et al.*, “Intermediate honeycomb ordering to trigger oxygen redox chemistry in layered battery electrode,” *Nat. Commun.*, vol. 7, pp. 1–9, 2016, doi: 10.1038/ncomms11397.

- [63] S. Peng and P. R. Ilango, *Electrospinning of Nanofibers for Battery Applications*. 2020.
- [64] C. Y. Tang and Z. Yang, “Transmission Electron Microscopy (TEM),” *Membrane Characterization*. pp. 145–159, 2017, doi: 10.1016/B978-0-444-63776-5.00008-5.
- [65] M. H. Han, E. Gonzalo, G. Singh, and T. Ofilo Rojo, “A comprehensive review of sodium layered oxides: powerful cathodes for Na-ion batteries,” 2015, doi: 10.1039/c4ee03192j.
- [66] M. Chen, Q. Liu, S. W. Wang, E. Wang, X. Guo, and S. L. Chou, “High-Abundance and Low-Cost Metal-Based Cathode Materials for Sodium-Ion Batteries: Problems, Progress, and Key Technologies,” *Adv. Energy Mater.*, vol. 9, no. 14, pp. 1–41, 2019, doi: 10.1002/aenm.201803609.
- [67] Y. Gupta, P. Siwatch, R. Karwasra, K. Sharma, and S. K. Tripathi, “Recent progress of layered structured P<sup>2-</sup> and O<sup>3-</sup> type transition metal oxides as cathode material for sodium-ion batteries,” *Renew. Sustain. Energy Rev.*, vol. 192, no. December 2022, p. 114167, 2024, doi: 10.1016/j.rser.2023.114167.
- [68] P. Barpanda, L. Lander, S. I. Nishimura, and A. Yamada, “Polyanionic Insertion Materials for Sodium-Ion Batteries,” *Adv. Energy Mater.*, vol. 8, no. 17, pp. 1–26, 2018, doi: 10.1002/aenm.201703055.
- [69] J. Y. Hwang *et al.*, “Sodium and sodium-ion energy storage batteries,” *Chem. Soc. Rev.*, vol. 3, no. 3, pp. 1867–1875, 2019, doi: 10.1039/c5ta03181h.
- [70] C. Masquelier and L. Croguennec, “Polyanionic (phosphates, silicates, sulfates) frameworks as electrode materials for rechargeable Li (or Na) batteries,” *Chem. Rev.*, vol. 113, no. 8, pp. 6552–6591, 2013, doi: 10.1021/cr3001862.
- [71] H. Li, M. Xu, Z. Zhang, Y. Lai, and J. Ma, “Engineering of Polyanion Type Cathode Materials for Sodium-Ion Batteries: Toward Higher Energy/Power Density,” *Adv. Funct. Mater.*, vol. 30, no. 28, pp. 1–29, 2020, doi: 10.1002/adfm.202000473.
- [72] Y. Bai *et al.*, “Progress of Prussian Blue and Its Analogues as Cathode Materials for Potassium Ion Batteries,” *Eur. J. Inorg. Chem.*, vol. 26, no. 25, 2023, doi: 10.1002/ejic.202300246.
- [73] J. Hu *et al.*, “Interstitial Water Improves Structural Stability of Iron Hexacyanoferrate for High-Performance Sodium-Ion Batteries,” *ACS Appl. Mater. Interfaces*, vol. 14, no. 10, pp. 12234–12242, 2022, doi: 10.1021/acsami.1c23762.
- [74] B. Wang *et al.*, “Prussian Blue Analogs for Rechargeable Batteries,” *iScience*, vol. 3, pp. 110–133, 2018, doi: 10.1016/j.isci.2018.04.008.
- [75] B. Mortemard de Boisse *et al.*, “Highly Reversible Oxygen-Redox Chemistry at 4.1 V in Na<sub>4/7-x</sub>[□<sub>1/7</sub>Mn<sub>6/7</sub>]O<sub>2</sub> (□: Mn Vacancy),” *Adv. Energy Mater.*, vol. 8, no. 20, Jul. 2018, doi: 10.1002/aenm.201800409.
- [76] P. He, H. Yu, D. Li, and H. Zhou, “Layered lithium transition metal oxide cathodes towards high energy lithium-ion batteries,” *J. Mater. Chem.*, vol. 22, no. 9, pp. 3680–3695, 2012, doi: 10.1039/c2jm14305d.

- [77] J. L. Shi *et al.*, “High-Capacity Cathode Material with High Voltage for Li-Ion Batteries,” *Adv. Mater.*, vol. 30, no. 9, pp. 1–8, 2018, doi: 10.1002/adma.201705575.
- [78] Q. Liu *et al.*, “Sodium transition metal oxides: the preferred cathode choice for future sodium-ion batteries?,” *This J. is Cite this Energy Environ. Sci*, vol. 14, p. 158, 2021, doi: 10.1039/d0ee02997a.
- [79] H. Fu *et al.*, “Synergetic stability enhancement with magnesium and calcium ion substitution for Ni/Mn-based P2-type sodium-ion battery cathodes †,” 2022, doi: 10.1039/d1sc05715d.
- [80] Q. Mao *et al.*, “Mitigating the P2-O2 transition and Na + /vacancy ordering in Na 2/3 Ni 1/3 Mn 2/3 O 2 by anion/cation dual-doping for fast and stable Na + insertion/extraction †,” 2021, doi: 10.1039/d1ta01433a.
- [81] H. S. Hirsh, Y. Li, D. H. S. Tan, M. Zhang, E. Zhao, and Y. S. Meng, “Sodium-Ion Batteries Paving the Way for Grid Energy Storage,” *Adv. Energy Mater.*, vol. 10, no. 32, pp. 1–8, 2020, doi: 10.1002/aenm.202001274.
- [82] Q. Liu *et al.*, “Sodium transition metal oxides: The preferred cathode choice for future sodium-ion batteries?,” *Energy Environ. Sci.*, vol. 14, no. 1, pp. 158–179, 2021, doi: 10.1039/d0ee02997a.
- [83] L. Wang *et al.*, “Challenges of layer-structured cathodes for sodium-ion batteries Nanoscale Horizons Challenges of layer-structured cathodes for sodium-ion batteries,” *This J. is Cite this Nanoscale Horiz*, vol. 7, p. 338, 2022, doi: 10.1039/d1nh00585e.
- [84] C. Delmas, J. J. Braconnier, and P. Hagenmuller, “A new variety of LiCoO2 with an unusual oxygen packing obtained by exchange reaction,” *Mater. Res. Bull.*, vol. 17, no. 1, pp. 117–123, 1982, doi: 10.1016/0025-5408(82)90192-1.
- [85] D. Karabelli Kaus *et al.*, “Sodium-Based Batteries: In Search of the Best Compromise Between Sustainability and Maximization of Electric Performance,” *Front. Energy Res.*, vol. 8, 2020, doi: 10.3389/fenrg.2020.605129.
- [86] S. Zhao *et al.*, “REVIEW Open Access Research progresses in O3-type Ni/Fe/Mn based layered cathode materials for sodium ion batteries,” 2014, doi: 10.1007/s43979-023-00053-9.
- [87] S. Roberts, L. Chen, B. Kishore, C. E. J. Dancer, M. J. H. Simmons, and E. Kendrick, “Mechanism of gelation in high nickel content cathode slurries for sodium-ion batteries,” *J. Colloid Interface Sci.*, vol. 627, pp. 427–437, 2022, doi: 10.1016/j.jcis.2022.07.033.
- [88] E. Lee *et al.*, “New Insights into the Performance Degradation of Fe-Based Layered Oxides in Sodium-Ion Batteries: Instability of Fe3+/Fe4+ Redox in  $\alpha$ -NaFeO2,” *Chem. Mater.*, vol. 27, no. 19, pp. 6755–6764, Sep. 2015, doi: 10.1021/acs.chemmater.5b02918.
- [89] S. Y. Zhang *et al.*, “P3/O3 Integrated Layered Oxide as High-Power and Long-Life Cathode toward Na-Ion Batteries,” *Small*, vol. 17, no. 10, pp. 1–7, 2021, doi: 10.1002/smll.202007236.
- [90] H. Zhang *et al.*, “Long-Cycle-Life Cathode Materials for Sodium-Ion Batteries toward

- Large-Scale Energy Storage Systems,” *Adv. Energy Mater.*, vol. 13, no. 23, 2023, doi: 10.1002/aenm.202300149.
- [91] D. Pahari, A. Kumar, D. Das, and S. Puravankara, “P2-type  $\text{Na}_x\text{TmO}_2$  oxides as cathodes for non-aqueous sodium-ion batteries—Structural evolution and commercial prospects,” *Int. J. Energy Res.*, vol. 46, no. 15, pp. 21894–21927, 2022, doi: 10.1002/er.8543.
- [92] J. Feng *et al.*, “Stable Electrochemical Properties of Magnesium-Doped Co-Free Layered P2-Type  $\text{Na}_{0.67}\text{Ni}_{0.33}\text{Mn}_{0.67}\text{O}_2$  Cathode Material for Sodium Ion Batteries,” *ACS Sustain. Chem. Eng.*, vol. 10, no. 15, pp. 4994–5004, Apr. 2022, doi: 10.1021/ACSSUSCHEMENG.2C00197.
- [93] I. Abate *et al.*, “The Role of Metal Substitution in Tuning Anion Redox in Sodium Metal Layered Oxides Revealed by X-Ray Spectroscopy and Theory,” *Angew. Chemie - Int. Ed.*, vol. 60, no. 19, pp. 10880–10887, May 2021, doi: 10.1002/anie.202012205.
- [94] K. Kannan, M. Kouthaman, R. Subadevi, and M. Sivakumar, “Dual metal (Fe and Mg) substituted layered titanium-based P2 and O3-type negative electrodes for rechargeable sodium batteries,” 2023, doi: 10.1016/j.appt.2023.104038.
- [95] W. Kang *et al.*, “Copper substituted P2-type  $\text{Na}_{0.67}\text{Cu}_x\text{Mn}_{1-x}\text{O}_2$ : A stable high-power sodium-ion battery cathode,” *J. Mater. Chem. A*, vol. 3, no. 45, pp. 22846–22852, 2015, doi: 10.1039/c5ta06371j.
- [96] H. Ren, Y. Li, Q. Ni, Y. Bai, H. Zhao, and C. Wu, “Unraveling Anionic Redox for Sodium Layered Oxide Cathodes: Breakthroughs and Perspectives,” *Adv. Mater.*, vol. 34, no. 8, pp. 1–34, 2022, doi: 10.1002/adma.202106171.
- [97] W. Kong *et al.*, “Simultaneously tuning cationic and anionic redox in a P2- $\text{Na}_{0.67}\text{Mn}_{0.75}\text{Ni}_{0.25}\text{O}_2$  cathode material through synergic Cu/Mg co-doping  $^{\dagger}$ ,” 2019, doi: 10.1039/c9ta00968j.
- [98] M. M. Doeff, J. Cabana, and M. Shirpour, “Titanate Anodes for Sodium Ion Batteries,” *J. Inorg. Organomet. Polym. Mater.*, vol. 24, no. 1, pp. 5–14, 2014, doi: 10.1007/s10904-013-9977-8.
- [99] K. Tang, X. Yu, J. Sun, H. Li, and X. Huang, “Kinetic analysis on  $\text{LiFePO}_4$  thin films by CV, GITT, and EIS,” *Electrochim. Acta*, vol. 56, no. 13, pp. 4869–4875, 2011, doi: 10.1016/j.electacta.2011.02.119.
- [100] Y. Kim, K. H. Ha, S. M. Oh, and K. T. Lee, “High-capacity anode materials for sodium-ion batteries,” *Chem. - A Eur. J.*, vol. 20, no. 38, pp. 11980–11992, 2014, doi: 10.1002/chem.201402511.
- [101] F. Klein, B. Jache, A. Bhide, and P. Adelhelm, “Conversion reactions for sodium-ion batteries,” *Phys. Chem. Chem. Phys.*, vol. 15, no. 38, pp. 15876–15887, 2013, doi: 10.1039/c3cp52125g.
- [102] V. Chandrakala *et al.*, “Investigation of the morphology based properties of multidimensional titanate nanostructures for application as proficient photo anodes,” *Mater. Today Proc.*, vol. 9, pp. 217–236, 2019, doi: 10.1016/j.matpr.2019.02.154.
- [103] Y. Zhang *et al.*, “Titanate and titania nanostructured materials for environmental and

- energy applications: A review,” *RSC Adv.*, vol. 5, no. 97, pp. 79479–79510, 2015, doi: 10.1039/c5ra11298b.
- [104] A. Rudola, K. Saravanan, S. Devaraj, H. Gong, and P. Balaya, “Na<sub>2</sub>Ti<sub>6</sub>O<sub>13</sub>: A potential anode for grid-storage sodium-ion batteries,” *Chem. Commun.*, vol. 49, no. 67, pp. 7451–7453, 2013, doi: 10.1039/c3cc44381g.
- [105] P. Senguttuvan, M. R. Palacín, G. Rouse, V. Seznec, and J.-M. Tarascon, “Na<sub>2</sub>Ti<sub>3</sub>O<sub>7</sub>: Lowest Voltage Ever Reported Oxide Insertion Electrode for Sodium Ion Batteries,” *Chem. Mater.*, vol. 23, no. c, pp. 4109–4111, 2011, doi: 10.1021/cm202076g.
- [106] Z. Zhang *et al.*, “Continuous hydrothermal synthesis of extensive 2D sodium titanate (Na<sub>2</sub>Ti<sub>3</sub>O<sub>7</sub>) nano-sheets,” *Dalt. Trans.*, vol. 39, no. 3, pp. 711–714, 2010.
- [107] P. Senguttuvan, G. Rouse, V. Seznec, J. M. Tarascon, and M. R. Palacín, “Na<sub>2</sub>Ti<sub>3</sub>O<sub>7</sub>: Lowest voltage ever reported oxide insertion electrode for sodium ion batteries,” *Chem. Mater.*, vol. 23, no. 18, pp. 4109–4111, 2011, doi: 10.1021/cm202076g.
- [108] M. A. Muñoz-Márquez, M. Zarrabeitia, E. Castillo-Martínez, A. Eguía-Barrio, T. Rojo, and M. Casas-Cabanas, “Composition and evolution of the solid-electrolyte interphase in Na<sub>2</sub>Ti<sub>3</sub>O<sub>7</sub> electrodes for Na-Ion batteries: XPS and auger parameter analysis,” *ACS Appl. Mater. Interfaces*, vol. 7, no. 14, pp. 7801–7808, 2015, doi: 10.1021/acsami.5b01375.
- [109] L. Noerochim, A. Ma’rifatul Maghfiroh, Widyastuti, D. Susanti, S. Priyono, and B. Prihandoko, “High electrochemical performance of Li<sub>4</sub>Ti<sub>5</sub>O<sub>12</sub>/C synthesized by ball milling and direct flaming of acetylene gas as anode for lithium-ion battery,” *Ionics (Kiel)*, vol. 25, no. 11, pp. 5315–5322, 2019, doi: 10.1007/s11581-019-03084-4.
- [110] Z. Chen *et al.*, “Enhanced Cycle Stability of Na<sub>2</sub>Ti<sub>3</sub>O<sub>7</sub> Nanosheets Grown in Situ on Nickel Foam as an Anode for Sodium-Ion Batteries,” *Energy and Fuels*, 2020, doi: 10.1021/acs.energyfuels.9b04307.
- [111] C. Y. Xu *et al.*, “Molten salt synthesis of Na<sub>2</sub>Ti<sub>3</sub>O<sub>7</sub> and Na<sub>2</sub>Ti<sub>6</sub>O<sub>13</sub> one-dimensional nanostructures and their photocatalytic and humidity sensing properties,” *CrystEngComm*, vol. 15, no. 17, pp. 3448–3454, 2013.
- [112] J. Xu, C. Ma, M. Balasubramanian, and Y. S. Meng, “Understanding Na<sub>2</sub>Ti<sub>3</sub>O<sub>7</sub> as an ultra-low voltage anode material for a Na-ion battery,” *Chem. Commun.*, vol. 50, no. 83, pp. 12564–12567, 2014, doi: 10.1039/c4cc03973d.
- [113] G. Rouse, P. Senguttuvan, M. R. Palacín, J.-M. Tarascon, M. E. Arroyo-de Dompablo, and A. Ponrouch, “Rationalization of Intercalation Potential and Redox Mechanism for A<sub>2</sub>Ti<sub>3</sub>O<sub>7</sub> (A = Li, Na),” *Chem. Mater.*, vol. 25, no. 24, pp. 4946–4956, 2013.
- [114] A. Niemöller, P. Jakes, R. A. Eichel, and J. Granwehr, “In operando EPR investigation of redox mechanisms in LiCoO<sub>2</sub>,” *Chem. Phys. Lett.*, vol. 716, no. June 2018, pp. 231–236, 2019, doi: 10.1016/j.cplett.2018.12.022.
- [115] P. Verma, P. Maire, and P. Novák, “A review of the features and analyses of the solid electrolyte interphase in Li-ion batteries,” *Electrochim. Acta*, vol. 55, no. 22, pp. 6332–6341, 2010, doi: 10.1016/j.electacta.2010.05.072.

## **2. Methods**



2. Introduction.....	49
2.1 Solid-state synthesis.....	53
2.1.1. Synthesis of iron-rich O <sub>3</sub> -type layered oxides .....	53
2.1.2 Synthesis of manganese-rich P2-type transition metal oxides .....	54
2.1.3. Synthesis of layered perovskite oxides.....	55
2.2. Characterisation methods .....	56
2.2.1. Powder X-ray diffraction.....	56
2.2.2. Scanning Electron Microscopy .....	58
2.2.3. Energy dispersive X-ray spectroscopy.....	60
2.2.4 Transmission Electron Microscopy .....	60
2.2.5. Electronic spectroscopy .....	62
2.2.6. Solid-state nuclear resonance.....	64
2.3. Electrochemical characterisation .....	65
2.3.1. Electrolyte preparation .....	65
2.3.2. Fabrication of electrodes.....	66
2.3.3. Coin cell assembly.....	67
2.3.4. Galvanostatic measurements.....	68
2.3.5. Cyclic-voltammetry .....	70
2.3.6. Galvanostatic intermittent titration technique .....	72
2.3.7. Electrochemical Impedance Spectroscopy .....	73
2.4. Synchrotron techniques.....	75
2.4.1. Operando X-ray diffraction.....	77

2.5. References .....80

This chapter is an outline of the electrode active materials synthesis, electrode preparation, and cell construction procedures used throughout this work. The concepts and procedures behind each synthesis procedure or characterisation technique will be expounded. Any punctual change to the methodology will be announced in the corresponding chapters.

## 2.1 Solid-state synthesis

### 2.1.1. Synthesis of iron-rich O<sub>3</sub>-type layered oxides

The active materials studied in Chapter 3 are  $\alpha$ -NaFeO<sub>2</sub>,  $\alpha$ -Na<sub>(1-2x)</sub>Ca<sub>x</sub>FeO<sub>2</sub>, and  $\alpha$ -Na<sub>(1-2x)</sub>Ca<sub>x</sub>FeO<sub>(2-2x)</sub>. The reasoning for exploring these materials is explained in the corresponding chapter. The molar quantity of each precursor was weighed out to  $\pm 0.00001$  g in a fume cupboard. All the precursors were then mixed and hand-ground with an agate mortar and pestle until a homogeneous and fine black powder was obtained. The precursors used in this synthesis are presented in Table 2.1. This mixture was then turned into  $\approx 300$  mg pellets with a 10 mm diameter and 1 to 2 mm thickness by pressing them in a hydraulic press with the help of a 10 mm diameter die set at 16 MPa (equivalent to 5 tonnes).

Table 2.1 – List of precursors used in synthesising the iron-rich, O<sub>3</sub>-type layered materials, their suppliers, and purities.

Precursor	Supplier	Purity (%)
Na <sub>2</sub> CO <sub>3</sub>	Sigma-Aldrich	99.5
Fe <sub>3</sub> O <sub>4</sub>	Thermo-Fisher	97.0
CaCO <sub>3</sub>	Alfa-Aesar	99.5
CaF <sub>2</sub>	Alfa-Aesar	99.0

The conditions of synthesis, such as temperature and calcination duration optimisation for each material, fall within the scope of this thesis and will be discussed in detail for each material. The synthesis conditions of  $\text{NaFeO}_2$ ,  $\text{Na}_{(1-2x)}\text{Ca}_x\text{FeO}_2$ , and  $\text{Na}_{(1-2x)}\text{Ca}_x\text{FeO}_{(2-2x)}\text{F}_{2x}$  will be specifically addressed in Chapter 3. Following calcination in air, the pellets were carefully allowed to cool down to 150 °C before being transferred to a nitrogen-filled Unilab MBraun glovebox ( $\text{O}_2 < 0.5$  ppm;  $\text{H}_2\text{O} < 0.5$  ppm). Inside the glovebox, the pellets were ground into a fine powder, ensuring homogeneity, and then subjected to further characterisation techniques, such as powder X-ray diffraction (XRD), for detailed analysis.

### *2.1.2 Synthesis of manganese-rich P2-type transition metal oxides*

The active materials investigated in Chapter 4 are  $\text{Na}_{0.67}\text{Mn}_{0.8}\text{Ni}_{0.15}\text{Cu}_{0.05}\text{O}_2$ ,  $\text{Na}_{0.67}\text{Mn}_{0.8}\text{Ni}_{0.15}\text{Fe}_{0.05}\text{O}_2$ , and  $\text{Na}_{0.67}\text{Mn}_{0.8}\text{Ni}_{0.15}\text{Ti}_{0.05}\text{O}_2$ . A stoichiometric amount of each precursor was carefully weighed out to  $\pm 0.00001$  g in a fume cupboard, ensuring accuracy. The precursors utilised in the synthesis of these materials are detailed in Table 2.2. They were placed in zirconia-lined stainless-steel jars along with 5 mm zirconia-lined stainless-steel balls. The ball-to-powder ratio applied was 22.5:1, and 10 mL of ethanol was added to facilitate uniform mixing of the materials. The jars were then positioned in a planetary ball-mill (Fritsch Pulverisette 8). The mixing process was conducted at 400 rpm for 6 hours in 10-minute cycles with a 5-minute pause after each cycle to prevent overheating. The resulting powder was dried thoroughly in a drying cabinet set at 40 °C. This mixture was subsequently compressed into approximately 300 mg pellets, each with a 10 mm diameter and a thickness of 1 to 2 mm, by pressing them using a hydraulic press equipped with a 10 mm diameter die set to 16 MPa (equivalent to 5 tonnes of pressure).

Table 2.2 – List of precursors used in synthesising manganese-rich, *P2*-type materials, their supplier and their purity.

<b>Precursor</b>	<b>Supplier</b>	<b>Purity (%)</b>
<b>Na<sub>2</sub>CO<sub>3</sub></b>	Sigma-Aldrich	99.5
<b>Mn<sub>2</sub>O<sub>3</sub></b>	Sigma Aldrich	99
<b>NiO</b>	Alfa-Aesar	99
<b>Fe<sub>2</sub>O<sub>3</sub></b>	Alfa-Aesar	99.0
<b>TiO<sub>2</sub></b>	Sigma-Aldrich	99.7
<b>CuO</b>	Thermo-Fisher	97

The pellets were calcined in air, using a box furnace (Carbolite) for 12 hours at 1000 °C. After the syntheses, the pellets were allowed to cool down to 150 °C and transferred to a nitrogen-fill Unilab MBraun glovebox ( $O_2 < 0.5$  ppm;  $H_2O < 0.5$  ppm) and ground into a fine powder and proceeded into further characterisation (e.g., powder XRD).

### 2.1.3. *Synthesis of layered perovskite oxides*

The active materials studied in Chapter 5 are NaTiLaO<sub>4</sub> (NLTO) and NaTiYO<sub>4</sub> (NYTO). For the syntheses of these materials, the molar quantity of each precursor, shown in Table 2.3, was weighed out to  $\pm 0.00001$  g. All the precursors were mixed in zirconia-lined stainless-steel jars with 5 mm zirconia-lined stainless-steel balls. A ball-to-powder ratio was 22.5:1 and 10 mL of acetone was added to facilitate the mixture. The jars were placed in a planetary ball-mill (Fritsch Pulverisette 8). The mixing was conducted at 350 rpm for 8 h in 10 min cycles and 5 min pause each cycle. The resulting powder was dried in a drying cabinet at 40 °C. This mixture was then turned into  $\approx 300$  mg pellets with a 10 mm

diameter and 1 to 2 mm thickness by pressing them in a hydraulic press with the help of a 10 mm diameter die set at 16 MPa (equivalent to 5 tonnes).

Table 2.3 – List of precursors used in synthesising the layered perovskite oxides, their supplier, and purity.

Precursor	Supplier	Purity (%)
$\text{Na}_2\text{CO}_3$	Sigma-Aldrich	99.5
$\text{TiO}$	Thermo-Fisher	97.0
$\text{La}_2\text{O}_3$	Alfa-Aesar	99.9
$\text{Y}_2\text{O}_2$	Alfa-Aesar	99.9

The conditions of synthesis, e.g., temperature and calcination duration optimisation for NLTO and NYTO, fall within the scope of this thesis and this will be discussed for each material, and will be discussed in Chapter 5. After the syntheses, the pellets were allowed to cool down to room temperature and transferred to a nitrogen-fill Unilab MBraun glovebox ( $\text{O}_2 < 0.5$  ppm;  $\text{H}_2\text{O} < 0.5$  ppm) and ground into a fine powder and proceeded into further characterisation (e.g., powder XRD).

## 2.2. Characterisation methods

### 2.2.1. Powder X-ray diffraction

Powder X-ray diffraction is non-destructive, meaning that, the sample can be recovered and further analysed. This technique permits the analysis of crystalline phases, as long as the wavelength ( $\lambda$ ) of the X-rays is of the same order of magnitude as the spacing of the atomic planes ( $\approx 0.1$  to  $10 \text{ \AA}$ ). [1] The X-rays interact with the electron cloud of each atom, which interferes constructively or destructively with the material. [2] When the

interaction is destructive, no diffracted X-rays will be detected, and no useful information will be obtained. However, if the interaction is constructive, information regarding the crystal structure and chemical composition will be obtained. [3] In 1912, British scientists William Henry Bragg and Lawrence Bragg discovered a relationship that describes constructive interaction. [3] They discovered that constructive interference can only occur if the difference in atomic planes ( $\delta$ ) between two electromagnetic waves interacting with successive planes of atoms equals a whole integer ( $n$ ) of the wavelength ( $\lambda$ ). A schematic of this principle is shown in Figure 2.1. This principle is equated as in equation 2.1,

$$n\lambda = 2d_{hkl} \sin 2\theta \quad \text{Equation 2.1}$$

where  $n$ , is the whole integer, which usually takes the value of 1,  $\lambda$ , is the wavelength,  $\theta$ , is the angle formed by the incident X-ray wave and the scattering plane and  $d$  is the spacing between two planes defined by the Miller indices  $h$ ,  $k$ , and  $l$ , corresponding to the diffracting plane. [4]

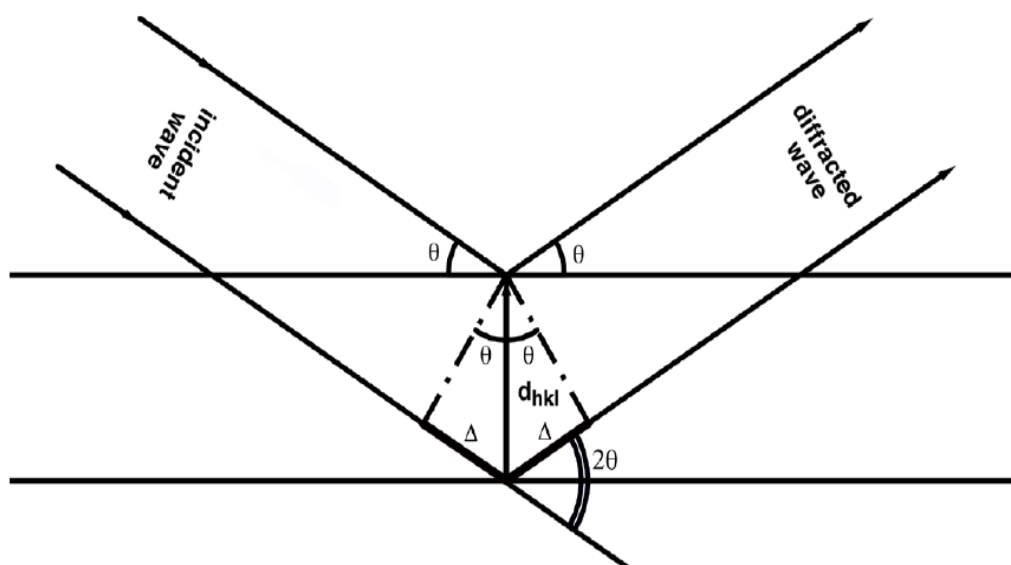


Figure 2.1 – Schematic representation of Bragg's law conditions [5]

During the experiments, X-rays were produced in a cathode-ray tube under vacuum. These are filtered through a monochromator, hitting the sample. The interaction of the incident X-rays with the sample atomic planes creates diffracted, transmitted, scattered, and absorbed beams. The degree of the diffracted beams depends on the arrangement of the atomic planes within the crystal lattice. The diffracted X-rays are detected, followed by processing, and counting that gives rise to the X-ray pattern. The obtained pXRD pattern is then compared to a reference diffractogram from a database. The most common is Materials Project and the International Center Diffraction Data (ICDD), formerly known as the Joint Committee on Powder Diffraction Standards (JCPDS). [6] The reference diffractogram displays various relevant information about a specific material such as  $d$ -spacing, relative intensity, and diffracting planes, among others. Rietveld refinements were conducted in all materials whose peak numbers were positions indicating the correct phase was obtained with a relatively low secondary phases and precursors peak count. In Chapters 3 and 4, Rietveld refinements were conducted using GSAS-II and in Chapter 5, Rietveld refinements were conducted using FullProf. [7], [8]

In this thesis, powder samples were analysed at room temperature using a Rigaku Miniflex 400 equipped with Cu  $K\alpha_1$  ( $\lambda = 1.54056 \text{ \AA}$ ) and Cu  $K\alpha_2$  ( $\lambda = 1.544390 \text{ \AA}$ ) radiation. A scan speed of  $0.01 \text{ }^\circ \text{ s}^{-1}$ , was used to record the PXRD patterns with  $2\theta$  between  $10$  and  $90 \text{ }^\circ$ . This piece of equipment is placed in a nitrogen-filled Unilab MBraun Eco glovebox ( $\text{O}_2 < 0.5 \text{ ppm}$ ;  $\text{H}_2\text{O} < 0.5 \text{ ppm}$ ).

### 2.2.2. Scanning Electron Microscopy

Scanning electron microscopy (SEM) is a powerful tool for characterising the morphology of a material. During the experiment, electrons are generated from a source and emitted either by heating a source material to high temperatures (thermionic

emission) or by using an electric field (field emission). The free electrons are accelerated through a sequence of condenser lenses, forming a beam that goes to an area of interest of the specimen. The interaction of the electron beam with the specimen produces secondary, backscattered, Auger electrons and X-rays. These are collected by various detectors in the specimen chamber and images are formed. [9] A schematic representation of the components of a scanning electronic microscope is shown in Figure 2.2.

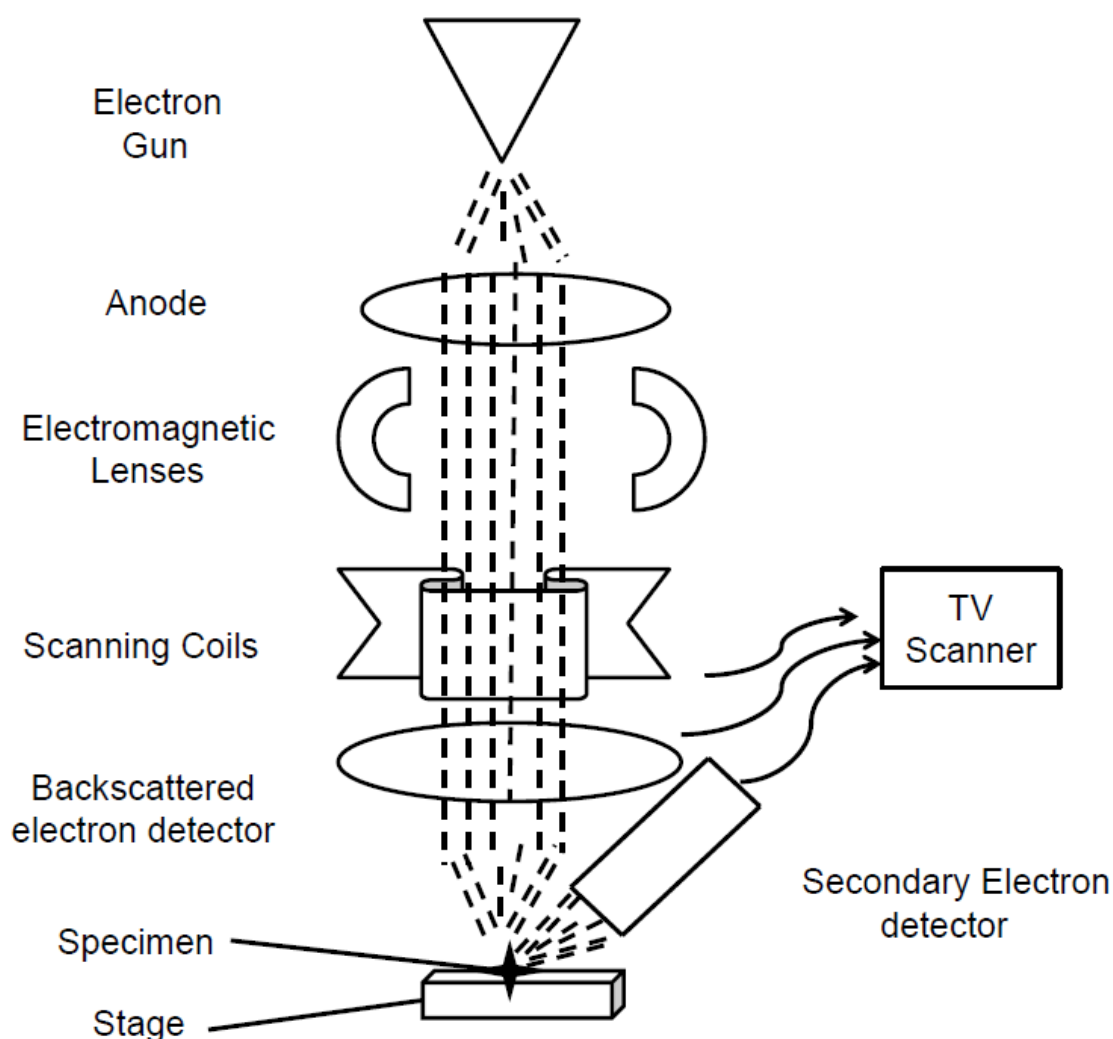


Figure 2.2 – Schematic representation of scanning electronic microscope components. [10]

In this thesis, SEM was performed (JEOL JSM-7800F) to characterise the particle size and shape of the various synthesised materials, using an accelerating voltage of 5 kV

and a current of 5 mA. Often, a conductive coating of gold or carbon is needed for samples with lower conductivity. This was not necessary in this case.

Air-sensitive samples were mounted onto the stubs using conductive carbon tape inside an argon-filled glovebox ( $O_2 < 0.1$  ppm;  $H_2O < 0.1$  ppm) and sealed. Upon mounting the stub into the microscope and atmosphere evacuation, the contact with air and water was unavoidable but minimised.

### *2.2.3. Energy dispersive X-ray spectroscopy*

Energy dispersive X-ray spectroscopy (EDS) is an analytical technique that quantifies the chemical composition of a sample and the homogeneity of each element present. The information is based on the interaction of X-ray excitation and the sample surface. Since each element has a unique electronic structure, it is possible to characterise a sample with an electromagnetic emission spectrum. [9] The greatest limitation of this method arises when samples have very low concentrations of a certain element. The chemical composition was analysed with AZtecEnergy software coupled with SEM analysis, using an accelerating voltage of 20 kV and 0.5 mm spot size.

### *2.2.4 Transmission Electron Microscopy*

High-resolution transmission electron microscopy (HRTEM) is a technique that allows the assessment of crystal size, defects and orientation, surface structures, and morphology. Selected area electron diffraction (SAED) is the most commonly used HRTEM technique, as it allows the determination of diffraction images of single crystallites in various orientations. [11] During these measurements, a beam of electrons is emitted from an electron gun, accelerated by a high voltage electric field (200/300 kV), and bent by multiple electromagnetic lenses that focus the beam. The electron beam is transmitted through an ultra-thin sample (~ 100 nm thickness) and interacts with the atoms. The transmitted beam is

magnified and detected by a fluorescent screen or digital CD camera to form an image. A schematic representation of a transmission electron microscope is shown in Figure 2.3.

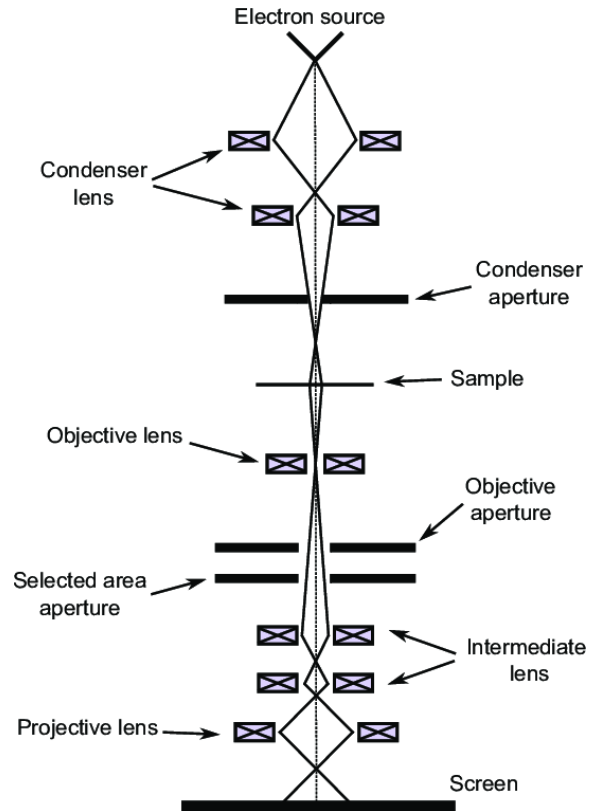


Figure 2.3 – Schematic representation of a transmission electron microscopic [12]

Four of the parameters that may affect the amount and scale of information that can be extracted from TEM and the quality of it: i) the resolving power of the microscope, ii) the energy spread of the electron beam, iii) the thickness of the sample and iv) the composition and stability of the sample. [13] Parameters i) and ii) are money dependent as the more expensive the better the microscope parameters. Average microscopes have a resolving power smaller than 0.3 nm and an energy spread in the range of several electron-volt which can be adapted to most of the samples analysed. [13] For the production of an image, an electron beam is required to be transmitted through the sample, usually less than 100 nm thick. The electron is produced in a tungsten filament or a lanthanum hexaborate crystal. This electron

is then accelerated in a vacuum, by a high potential electric field between 200 and 300 kV and focused by magnetic lenses, similar to SEM. [14] This technique requires the use of an electron beam that is transmitted through a specimen (usually less than 100 nm thick). The electron is usually produced in a tungsten wire shaped like a hairpin (filament) or a crystal of lanthanum hexaboride and accelerated under vacuum by a high voltage electric field (200 – 300 kV) away from the filament and focused by a magnetic lens. [14] The electrons that are transmitted through the sample are magnified by lenses and detected by a fluorescent screen/camera to form an image.

In this thesis, high-resolution transmission electron microscopy (HR-TEM) was performed using an EFTEM Jeol 2200 FS microscope (Jeol, Japan). A 200 keV acceleration voltage was used for measurement. Elemental maps and EDX spectra were acquired with SDD detector X-MaxN 80 TS from Oxford Instruments (England). Sample preparation was attained by drop-casting the suspension (1 mg mL<sup>-1</sup> in water) on a TEM grid (Cu; 200 mesh; Formvar/carbon) and dried at 60 °C for 12 h.

### *2.2.5. Electronic spectroscopy*

Electronic spectroscopy is a useful technique for the determination of the band gap of a material. Electronic spectroscopy relies on the absorption, scattering, diffraction, refraction, and reflection properties of the sample under analysis. For this, ultraviolet and visible lights with wavelengths between 200 and 780 nm are used. [15]

A UV-vis spectrometer's light source is a deuterium lamp, which emits light in the ultraviolet (UV) region, and a tungsten-halogen lamp, which emits light in the visible (vis) region. The mixed wavelength light beam is then guided through a monochromator and focused into the sample. The photons promote the electron in the sample to an excited state. If the energy for promoting an electron from the ground state to an excited state is lower than the energy of the incident photons, these will be absorbed by the sample, otherwise, they will be transmitted, reflected, refracted, or diffracted. [15] The light that is

not absorbed is detected by a multiplier or a photodiode and a spectrum of absorption of reflectance of light as a function of wavelength is generated. [16]

Electronic spectroscopy can be useful in determining the band gap of materials. The components of diffuse reflectance and specular reflectance can be used for that. Specular reflectance is the mirror-like reflection of the surface of a sample. Diffuse reflectance is when the surface of the sample reflects light in different directions, giving a matte appearance to the surface. The latter is of interest for the determination of the material's band gap. For the collection of diffuse reflectance information, an integrating sphere is coupled with the spectrometer.

In the thesis, this technique will be used to determine the band gap of some of the active materials. The measurements were carried out between 200 and 500 nm against a polytetrafluoroethylene standard. [17] The procedure of estimating the optical band gap is *via* fitting the experimentally determined absorption coefficient to the Tauc equation, which is a power-law expression in the form of Equation 2.2, where  $\alpha$  is the absorption coefficient, as a function of wavelength  $\alpha(\lambda)$ ,  $h$  is the Planck constant ( $6.62607015 \times 10^{34} \text{ m}^2 \text{ kg s}^{-1}$ ),  $E_g$  is the optical band gap of a semiconductor,  $\nu$  is the light frequency,  $A$  is the proportionality constant obtained from fitting and,  $n$  is the Tauc exponent. [16], [18]

$$(\alpha(\lambda)h\nu)^{1/n} = A(h\nu - E_g) \quad \text{Equation 2.2}$$

The Tauc coefficient,  $n$ , is typically chosen as one of four values, depending on the dominant transition in the material in the study:  $n = 1/2$  for direct allowed transitions,  $n = 3/2$  for direct forbidden transitions,  $n = 2$  for indirect allowed transitions and,  $n = 3$  for indirect forbidden transitions. [18] The energy band gap is obtained from the linear

extrapolation up to the energy axis, that is, the interception of the linear region with *the x-axis*.

[17]

## 2.2.. *Solid-state nuclear magnetic resonance*

Solid-state nuclear magnetic resonance (ssNMR) is a non-destructive analytical method used to study molecular structures, sample purity, and reaction mechanisms at the atomic level. [19] It is used as a complement to diffraction methods, providing information that is not readily available from these techniques, such as the presence of amorphous phases, low content of crystalline phases and local order. [20]

The principle behind NMR is that many nuclei have spin and have an angular momentum. This occurs when the nucleus of an atom contains unpaired protons or neutrons. Without the application of an electromagnetic field, these nuclear spins are oriented randomly due to thermal effects, and the oppositely oriented spin vectors cancel each other, leaving no net magnetisation. During the NMR experiment, a strong magnetic field is applied and the nuclei with spins are oriented either on the same or in opposite directions to the external magnetic field.

In NMR spectroscopy, the energy difference between the excited and ground states results from the Zeeman interaction between nuclear spins and magnetic field. From the Zeeman energy difference, the Larmor frequency can be obtained to produce the NMR spectrum. A 90 ° radiofrequency pulse is applied to flip the magnetisation out of alignment with the magnetic field,  $B_0$ . The Larmor precession of the magnetisation is then detected by the receiver coil in the NMR probe. As a result, information about the chemical environment of each nucleus can be derived from its resonant frequency. In general, the more electronegative the nucleus is, the higher the resonant frequency. [20]

The lack of extensive dynamics in the solid state means that NMR spectra of solid materials are strongly broadened by anisotropic interactions. However, more specialised

NMR techniques using “magic-angle spinning” can significantly reduce the broadening by averaging the anisotropic components of the NMR interactions. [20] By spinning the sample rapidly at an angle of  $54.74^\circ$  in relation to the applied magnetic field, a considerable improvement in resolution can be achieved. [21]

Among the diverse types of solid-state NMR,  $^{23}\text{Na}$  NMR has been used in this thesis.  $^{23}\text{Na}$  NMR is a medium-sensitivity nucleus that yields slightly broad lines over a moderate chemical shift range.  $^{23}\text{Na}$  presents a spin of  $3/2$ . The peak width increases with the asymmetry of the environment. The main use of sodium NMR is to determine the presence of sodium or the number of different chemical sites that it occupies, and this is sensitive to the local Na coordination. It presents a chemical shift range from  $-62$  to  $10$  ppm.

In this thesis, all solid-state  $^{23}\text{Na}$  NMR have been acquired using a 400 MHz Bruker Advance III HD WB spectrometer operating at a magnetic field of 9.4 T. Samples were loaded into a 3.2 mm outer-diameter zirconia rotor. The magic-angle spinning (MAS) rate was 20 and 10 kHz for  $^{23}\text{Na}$  NMR measurements, respectively. The recycle interval was set to at least  $5 \times T_1$  (as measured by a saturation recovery experiment).

## **2.3. Electrochemical characterisation**

Preparing a cell to be analysed is a three-step process. First, the active material was synthesised as a powder using a solid-state method. After obtaining a product with an acceptable purity, this powder was then converted into a solid electrode. These electrodes were then incorporated into a coin cell, using sodium metal as a counter electrode and an electrolyte.

### *2.3.1. Electrolyte preparation*

The electrolyte used in the electrochemical storage performance of the studied materials was prepared in the laboratory. Sodium hexafluorophosphate ( $\text{NaPF}_6$ )

(99 % Alfa Aesar, UK) was used as salt and a mixture of ethylene carbonate (EC) and diethyl carbonate (DEC) was used as the solvent (1:1 v/v%). All steps of the electrolyte solution preparation were conducted in an argon-filled glovebox ( $O_2 < 0.1$  ppm,  $H_2O < 0.1$  ppm). To prepare 20 mL of electrolyte solution, approximately 4 g of sodium hexafluorophosphate salt was weighed and dried at 60 °C under vacuum for no less than 8 hours. The following day, 3.359 g of  $NaPF_6$  was weighed into a glass vial containing a magnetic stirrer. 13.210 g of EC and 9.750 g of DEC were added to the same vial. The solution was left stirring in the argon-filled glovebox for 2 hours at 100 rpm and then for 10 days at 400 rpm. After this period, the vial was removed from stirring and left for 24 hours so that any undissolved solutes could precipitate. After decanting, the solution was transferred to an aluminium flask filled to a third of its capacity with 50 nm molecular sieves. The solution was left for at least three days before use so that any moisture could be adsorbed by the molecular sieves.

### 2.3.2. *Fabrication of electrodes*

The electrode components were mixed in an argon-filled glovebox ( $O_2 < 0.1$  ppm,  $H_2O < 0.1$  ppm). [22], [23] To prepare the negative solid electrode, this was combined with a binder and a Carbon Super-P (TOB machine, 99.6 %) as conductive additives in a weight ratio of 6:1:3, respectively. [24] The active material and the conductive additive were weighed and mixed with an agate mortar and pestle until full homogenisation and the mixture was placed in a polypropylene jar. The binder consisted of poly(vinylidene) fluoride (PVDF, Sigma-Aldrich, average molecular weight: 534.000 g mol<sup>-1</sup>) dissolved in N-methylpyrrolidone (NMP, Thermo-scientific, 99.5 %, extra dry, over molecular sieves) and was added as a solution to the beforementioned jar and the jar was isolated with PTFE (polytetrafluoroethylene) tape.

The active material, Carbon Super-P, and binder solution were mixed in a Thinky ARE-250 planetary centrifuge for 12 minutes in two 6-minute steps, at 1800 rpm, resulting in a homogeneous suspension. The resulting suspension was then coated in 100  $\mu\text{m}$  thick aluminium or 50  $\mu\text{m}$  thick copper foil using a 150  $\mu\text{m}$  doctor blade. The as-coated electrode was placed under a dynamic vacuum at 60  $^{\circ}\text{C}$  for 10 hours, to drive off the NMP solvent and any moisture.

The solid electrodes were cut into 10 mm disks ( $\approx 314 \text{ mm}^2$ ) for cell building and pressed at  $\approx 5 \text{ MPa}$  before being used for cell fabrication. All electrodes produced were weighed and labelled accordingly. The electrodes were labelled with an ethanol-based pen which, after testing *versus* unlabelled electrodes, was shown not to affect the electrochemical performance.

### 2.3.3. Coin cell assembly

In most of the electrochemical studies, a CR 2032-coin cell type was used. All cells were assembled in an argon-filled glovebox ( $\text{O}_2 < 0.1 \text{ ppm}$ ,  $\text{H}_2\text{O} < 0.1 \text{ ppm}$ ) using the as-prepared electrodes as the working electrodes and sodium-metal as a counter electrode. A porous glass microfibre separator (Whatman) was used to avoid contact between the electrodes. A schematic illustration of the coin cell assembly is shown in Figure 2.4.

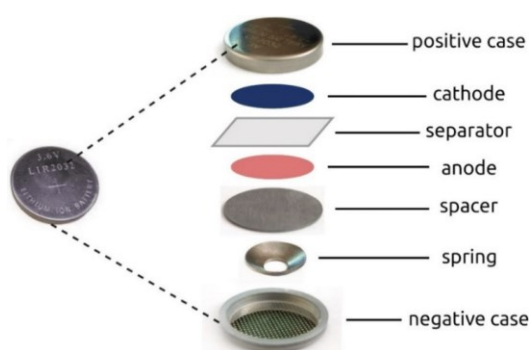


Figure 2.4 – Schematic illustration of the coin-cell components by order of assembly [25]

First, the working electrodes were placed on a positive cap, followed by a 20 mm glass fibre separator, which was tucked into the positive cap. After properly accommodating the separator into the positive cap, assuring the working electrode remains as centred as possible, 100  $\mu\text{L}$  of the electrolyte solution previously prepared was added on top of the glass fibre separator. After adding the electrolyte, a previously prepared and polished 15 mm diameter, and 0.

5 mm thickness sodium-metal disk was placed in the electrolyte-soaked glass fibre separator, followed by a 15 mm stainless steel disk. A spring and the negative cap were added and gently pressed to ensure all elements were properly aligned. The cell was finally closed using a crimper (TOBmachine) by pressing it at 100 psi.

#### 2.3.4. Galvanostatic measurements

Galvanostatic cycling or constant-current cycling is one of the most common electrochemical measurements performed on half-coin cells and assesses the performance of electrode material. The primary use of this technique is the determination of the specific capacity of an electrode material upon discharge and charge within a voltage range. In addition, properties such as Coulombic efficiency, capacity retention, and rate capabilities are easily investigated using galvanostatic cycling measurements. The rate at which the battery is cycled is normalized to the mass of active material. For the analysis of positive materials, the battery is first charged until it reaches the upper voltage cut off and then the current is reversed to charge until it reaches the lower voltage cut-off. This process is repeated over many cycles. The galvanostatic cycling data is typically plotted as a load curve with the specific capacity on the  $x$ -axis and voltage on the  $y$ -axis. The two main parameters recorded during cell cycling are time and voltage. The specific capacity ( $q$ ) is calculated from the product of time ( $t$ ) and current ( $I$ ) and normalized to the mass of active material ( $m$ ), as shown in Equation 2.3:

$$q = \frac{I \times t}{m} \quad \text{Equation 2.3}$$

In this thesis, the cycling performance of active materials was investigated at constant rates of 0.1 C and 2 C over 100 cycles. The C-rate is the cycling related to the theoretical capacity of the active material, for example, for a 1 C rate, the current applied will be able to extract the theoretical capacity in one hour. The expression used to calculate the theoretical capacity and the expression used to calculate the applied current are shown in Equations 2.4 and 2.5, respectively.

$$C^{theoretical} = \frac{n \times F \times 1000}{M \times 3600} (mA \text{ h } g^{-1}) \quad \text{Equation 2.4}$$

$$I = m^{active} \times C^{theoretical} \times CR \quad \text{Equation 2.5}$$

Where  $n$  corresponds to the number of electrons that are expected to be transferred per charge/discharge cycle per unit formula,  $F$  is the Faraday constant (96 485.3321 s A mol<sup>-1</sup>),  $M$  is the molecular weight of the active material,  $I$  is the applied current  $m^{active}$  is the mass of active materials,  $C^{theoretical}$  is the theoretical capacity and,  $CR$  is the C-rate desired for this experiment and. To convert the value from amp second per gram to miliamp second per gram the expression was multiplied by 1000 on the numerator and 3600 in the denominator.

In addition, the rate performance was investigated at different constant rates (0.1, 0.2, 1, 2, 5, 10, and 0.1 C), over 10 cycles at each rate. The cells were discharged and charged using an automatic battery tester system (Neware battery tester (China)). For the positive active materials, the performance was analysed between 2.0 and 3.5 V *vs.* Na<sup>+</sup>/Na, 2.0 and 3.8 V *vs.*

Na<sup>+</sup>/Na and 2.0 and 4.0 V *vs.* Na<sup>+</sup>/Na. For the negative active materials, the performance was analysed between 0.8 and 0.01 V *vs.* Li<sup>+</sup>/Li and 1.5 and 0.01 V *vs.* Na<sup>+</sup>/Na.

### 2.3.5. Cyclic-voltammetry

Cyclic voltammetry (CV) is an electrochemical technique commonly used to retrieve information on the electrochemical behaviour of electrode materials. [26] CV provides key information on the thermodynamics of redox reactions, the kinetics of electron-transfer reactions, and the stability of reaction products. During the experiment, the potential of the working electrode is measured against a reference electrode. For the characterisation of cathode materials, the potential increases linearly to the upper limit of the potential window in analysis, during the first cycle at a scan rate,  $\nu$ , (in mV s<sup>-1</sup>), and the redox reactions at the electrode/electrolyte interface are detected by measuring the resulting current. When the upper cut-off voltage is reached, the applied potential is reversed. For the anode materials, the inverse occurs.

Analysing a negative electrode, at the beginning of the cathodic scan, usually starting from the open circuit potential, the voltage is higher than the reduction potential, and only capacitive current flows (non-faradaic currents). As the voltage approaches the oxidation potential, the oxidation process starts. Hence, the diffusion process begins, consuming oxidised species at the electrode surface. The diffusion flux forms the cathodic current, which is proportional to the concentration gradient. As the scanning continues toward lower voltages, the surface concentration of oxidised species decreases while the flux increases. When the concentration of these species on the surface is exhausted, the flux reaches a peak. This peak corresponds to the cathodic peak current,  $I_{p,c}$ , occurring at a cathodic peak potential,  $E_{p,c}$ . Then, the current starts to decrease due to the depletion effect. During the opposite scan (anodic scan) the anodic peak current,  $I_{p,a}$ , and oxidation

potential,  $E_{p,a}$ , are obtained along with the increasing potential. [27] A diagram of a cyclic-voltammetry is shown in Figure 2.5.

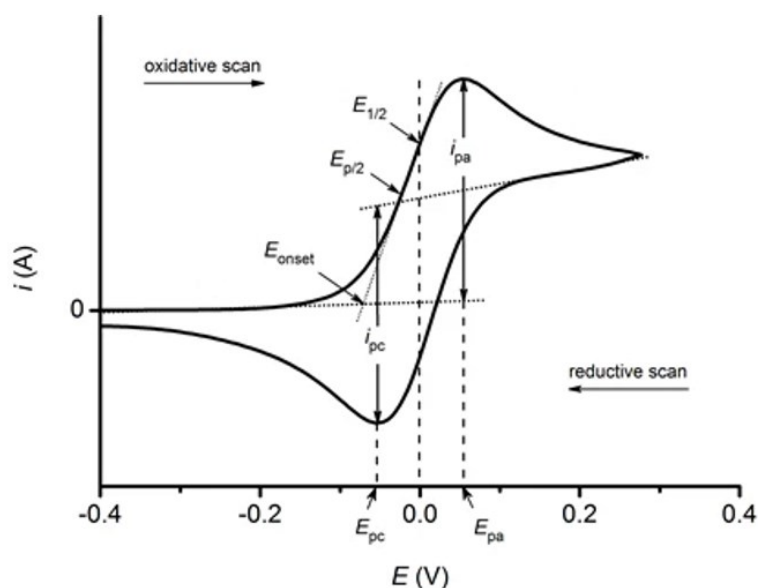


Figure 2.5 – Example of a diagram of a cyclic-voltammogram [28]

A qualitative comparison of the kinetics can be extracted from CV measurements such as the  $\text{Na}^+$  ion diffusion coefficient, by scanning an electrode material at different scan rates. The current peak values ( $I_p$ ) increase with increasing the scan rate ( $\nu$ ), normally following a linear trend of  $I_p$  vs.  $\nu^{1/2}$ .  $D(\text{Na}^+)$  ( $\text{cm}^2 \text{s}^{-1}$ ) is estimated by the Randles-Sevcik equation, shown in Equation 2.6. [29]

$$I_p = 0.4463zFAC \sqrt{\frac{zF\nu D_{CV}}{RT}} \quad \text{Equation 2.6}$$

where  $I_p$  is the peak current value (in mA),  $z$  is the number of exchanged electrons and it normally assumes the value of 1,  $F$  is the Faraday constant ( $96\,485 \text{ C mol}^{-1}$ ),  $A$  is the electrode geometric area (in  $\text{cm}^2$ ),  $C$  is the sodium ion concentration in the electrolyte (in  $\text{mol cm}^{-3}$ ),  $\nu$  is the scan rate (in  $\text{mV s}^{-1}$ ),  $R$  is the gas constant ( $8.314 \text{ J K}^{-1} \text{ mol}^{-1}$ ) and  $T$  is the

absolute temperature (in K). In this thesis, CV testing was based on two-electrode cells, in which sodium metal acts both as the reference and counter electrodes. The CV data was acquired on an Iviumstat instrument (Alvatek, UK) at different scan rates of, 0.1, 0.5, 0.2, and 1 mV s<sup>-1</sup>, over a voltage range of 2.0 – 3.5 V *vs.* Na<sup>+</sup>/Na for the positive active materials and 0.01 – 2.5 V *vs.* Na<sup>+</sup>/Na for the negative active materials.

### 2.3.6. Galvanostatic intermittent titration technique

The Galvanostatic Intermittent Titration Technique (GITT) is a method developed by Weppner and Huggins to measure the diffusion coefficient of an electrode material. [30] It consists of pulsing a low current through a battery cell for a certain period, followed by a rest period at open circuit potential until the voltage reaches equilibrium. This process is repeated during the entire discharge/charge process cycle of the battery. The Na<sup>+</sup> diffusion coefficient can be determined as follows in Equation 2.7, [30]

$$D_{GITT} = \frac{4}{l\tau} \left( \frac{m_B V_m}{M_B S} \right)^2 \left( \frac{\Delta E_S}{\Delta E_\tau} \right)^2 \quad \text{Equation 2.7}$$

where  $\tau$  is the period of the current pulse during charge or discharge for a constant current value,  $m_B$  is the mass of the electroactive material,  $M_B$  is its molecular weight,  $V_m$  is the molar volume,  $S$  is the total area of contact of the electrolyte with the electrode,  $\Delta E_S$  is the difference in the open circuit voltage measured at the end of the relaxation period for two successive steps,  $\Delta E_\tau$  is the difference in the cell voltage at the beginning and the end of the current pulse and  $l$  is the thickness of the electrode. The molar volume used in this equation was obtained from the X-ray diffraction. This equation can be only applied if there is a linear relationship of  $E_\tau$  with  $\tau^{1/2}$ . This technique gives accurate results only for

small stoichiometric changes and is strictly meant only for a vario-stoichiometric phase, meaning a solid solution mechanism. [31], [32]

In this thesis, GITT measurements were taken during the first charge-discharge cycle, where the composition of the electrode is still close to the pristine. A current pulse was applied for 10 minutes at a 0.1 C rate, followed by a relaxation period of 30 minutes.

### *2.3.7. Electrochemical Impedance Spectroscopy*

Electrochemical Impedance Spectroscopy (EIS) is a versatile technique that allows the non-destructive study of various electrochemical processes occurring within the electrolyte and at the electrode-electrolyte interface. In EIS, a small disturbance on the potential is applied ( $\pm 10$  to  $20$  mV), in a frequency window between  $1$  MHz to  $1$  mHz. [33] The electrical response of the system should be fitted to an equivalent circuit. For that, a knowledge of the system and what components may contribute to energy loss from impedance is required. [34] Limitation to the electron or ionic mobility and transfer mechanisms and other inner processes of the active material, as well as other rate-limiting mechanisms that hinder the charge transference processes can be identified via a Nyquist plot. [35] Classic impedance models highlight ionic diffusion as the major contributor to low performance, especially at higher rates. [36]

Furthermore, impedance measurements also account for any processes occurring in the electrode/electrolyte interface and those occurring at the electrode's bulk. This normally consists of capacitive and resistive phenomena. [35] The capacitive component of impedance corresponds to the accumulation of charge species near the surface of the electrode. The interchange of charge carriers between the two constituents at the interface is known as the charge transfer mechanism which consists of the insertion and extraction of charge carriers from the electrode. The charge transfer mechanism occurs by surpassing an interfacial potential barrier and therefore is dependent on the energetic properties of

the interface at a given charging state. The barrier crossing involving charge carriers is accompanied by an energy loss, which in electrical terms is modelled through a resistive element. Therefore, the interface is modelled with a  $C_{dl}$  in parallel with a charge transfer resistance  $R_{CT}$ . It is dependent on the voltage related to the charge state of the electrode, normally presenting a smaller value for sodiated electrodes. The combination of  $C_{dl}$  and  $R_{CT}$  corresponds to the characteristic  $\omega = 1/R_{CT}C_{dl}$ . In practical terms, the double-layer characteristic frequency is situated at  $\omega/2\pi < 1 \text{ kHz}$ , because it is usually observed that  $R_{CT} < 1 \text{ k}\Omega \text{ cm}^{-2}$ . [37]

The ionic conductivity of a solid-state electrolyte depends on the amount of mobile  $\text{Na}^+$  ions per volume and structural defect. [38], [39] Vacancies and interstitial ions are the most common structural defects, easily produced by substitution. The ionic conductivity in a crystalline solid-state electrolyte follows the Arrhenius equation, Equation 2.8. [40]

$$\sigma = \sigma_0 e^{-E_A/k_B T} \quad \text{Equation 2.8}$$

Where  $\sigma$  is the ionic conductivity,  $\sigma_0$  is the Arrhenius pre-exponential factor,  $T$  is the absolute temperature,  $E_A$  is the activation energy of diffusion, and  $k_B$  is the Boltzmann constant ( $1.380649 \times 10^{-23} \text{ m}^2 \text{ kg s}^{-2} \text{ K}^{-1}$ ). The conductivity is dependent on the diffusion energy barrier, temperature, and pre-exponential factor. The activation energy barrier reflects the energy required to go across bottlenecks. Increasing the concentration of mobile ions, decreasing the steric impediment, and constructing a continuous diffusion path, can be beneficial to reduce the activation energy and achieve a higher ionic conductivity. [41] The movement of ions through the material skeleton is usually temperature-dependent. [42]

The ionic conductivity measured by EIS, is the apparent conductivity that includes the contribution of both anions and cations which, knowing that only cations are mobile in our material, is enough to determine the ionic conductivity. [43] The transference number can be

measured using the steady-state current approach in the symmetric cells with non-blocking sodium metal electrodes with the material in the study in between these electrodes. The transference number can be determined by Equation 2.9.

$$t_+ = \frac{I_{ss}(\Delta V - I_0 R_0)}{I_0(\Delta V - I_{ss} R_{ss})} \quad \text{Equation 2.9}$$

Where the  $I_{ss}$  is the steady-state current,  $I_0$  is the initial current,  $R_0$  is the resistance at the initial  $R_{ss}$  is the resistance at the steady state, and  $\Delta V$  is the constant potential applied (generally  $\sim 10$  mV). [43]

In this thesis, EIS was measured was collected on an Iviumstat (Alvatek, UK) between 10 MHz and 5 mHz. The material was formed in an 80 mg pellet with a 10 mm diameter and 4 mm thickness. The studied material was subjected to an increasing temperature of 300 to 375 K, followed by a decreasing temperature from 375 to 300 K. This cycle was repeated two times to measure the conductivity before and after activation. The temperature was measured at 300, 305, 315, 325, 335, 345, 355, 365 and 375 K.

## 2.4. Synchrotron techniques

A synchrotron is a circular charged particle accelerator, usually electrons. It does this using a sequence of magnets that increase the speed of the particles to 99.9 % of the speed of light. The rapid movement of these charged particles produces exceptionally bright light, mainly in the X-ray range. The light intensity is in the range of 10 billion times the brightness of the Sun. [44]

The origins of synchrotrons can be traced back to 1873 when the theory of electromagnetism from James Clerk Maxwell revolutionised the understanding of light. Wilhelm Rontgen's 1895 discovery of X-ray light, followed by Charles Barkla's identification of X-rays as a tool for analysing gases in 1906. Max von Laue's 1912 revealed

that X-rays could reveal the structure of small matter and William Henry Bragg and Lawrence Bragg's 1913 formula for determining an object's structure through X-ray patterns further expanded the field. [44]

The first synchrotron, constructed in 1946, initially focused on studying high-energy particle collisions, like the Large Hadron Collider today. However, scientists noticed an unintended outcome: the production of exceptionally bright light. In 1956, experiments utilizing synchrotron light as a by-product began at Cornell in the USA. The trend grew, but dedicated synchrotron light sources did not emerge until 1980 when the UK built the world's first synchrotron dedicated to producing such light at Daresbury in Cheshire. [45]

Initially considered a nuisance, synchrotron light generated in the 1960s began to be viewed as a valuable tool for studying matter. The first-generation synchrotrons were primarily designed for high-energy particle physics, with synchrotron light experiments conducted incidentally. The shift occurred with second-generation synchrotrons, exclusively committed to synchrotron light production. The UK led this evolution with the construction of the first such facility in Daresbury in 1980. Third-generation synchrotrons distinguish themselves by employing insertion devices, and special magnet arrays causing electrons to wiggle, generating more intense and tuneable beams of light. [45] A general representation of a synchrotron facility is shown in Figure 2.6.

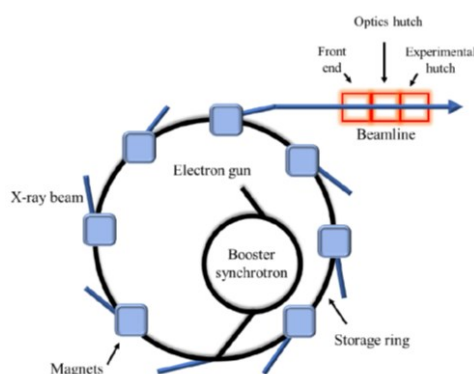


Figure 2.6 – Schematic representation of a synchrotron facility.

The components of synchrotron facilities are (i) an electron gun where the electrons are generated, (ii) a linear accelerator (or LinAc) and a booster which are made of a series of particle accelerators where electrons are filled and accelerated, and, (iii) a storage ring where the electrons travel close to the speed of light at an energy of 1.5 to 8 GeV. [45], [46] Particles maintain fixed energy as they are accelerated around the ring, right by a radio frequency alternating field in a microwave cavity. The movement of electrons creates a centrifugal acceleration generating electromagnetic radiation that covers a broad energy range. [46] The powerful magnets on the storage ring force the change of the electrons' path, leading to the loss of energy in the form of electromagnetic radiation. This electromagnetic radiation can be channelled out of the storage ring into the experimental station (known as beamlines), which is where the experiments occur and is accessible to scientists. [46] The beamlines contain (i) the optic hutch, where the light is filtered, (ii) the experiment hutch, where the experiment is carried out and the sample is measured, and (iii) the control cabin, where the experiment is controlled [45]

#### 2.4.1. *Operando X-ray diffraction*

The performance of a battery such as initial capacity or capacity retention is closely related to crystal structure of the electrode materials and how it evolves during the charge and discharge processes. Therefore, a good understanding of the structural changes that occur during the cell operation, such as lattice parameters, occupancy, or phase transition, is vital to understanding any deleterious transformations in the materials. For this, *operando* X-ray diffraction (*operando*-XRD) is a very powerful technique that provides information on any structural transformation occurring under cycling conditions. [47]

There are several advantages to using synchrotron-based XRD when compared to a conventional XRD. The higher intensity of synchrotron-based XRD, which is about 5 times

stronger than a conventional Cu-source, offers the opportunity to study the dynamic properties in a time-resolved manner, allowing the pin-pointing of each transformation to a time into the reaction or a certain potential. *Operando* experiments can be performed in a laboratory but, some issues may arise which can compromise the quality of the data collected especially, a high signal-to-noise ratio. [47]

All data was collected at the I15 beamline of the European Synchrotron Research Facility in Grenoble, France. A modified coin cell supplied by KIT, with a glass window transparent to X-rays, using an electrode of the active material in the study as the working electrode, lithium metal as a counter electrode for the negative electrodes, and sodium metal as the counter electrode for the positive electrodes. A schematic representation of the cells used in these experiments is shown in Figure 2.7. [48] Similar to the other electrochemical analysis, a solution of 1 M of  $\text{NaPF}_6$  in EC:DEC (1:1) was used during this session.

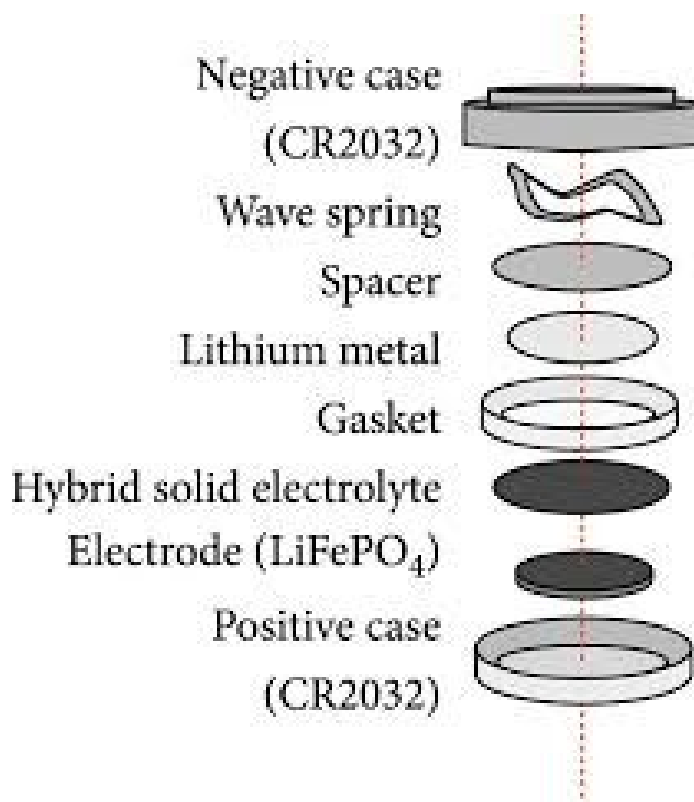


Figure 2.7 – Schematic representation of a modified coin cell with a glass window and its components [48]

The electrochemical data was acquired using an eight-channel potentiostat (Neware battery tester (China)) at a standard cycling rate of C/10 with a potential window of 0.01 to 2.0 V *vs.* Li<sup>+</sup>/Li for the negative electrodes and 2.5 to 3.5 V *vs.* Na<sup>+</sup>/Na for the positive electrodes. To allow the simultaneous collection of up to 5 cells, a holder was developed for this purpose with the necessary electric connections. A scheme of the holder is presented in Figure 2.8.

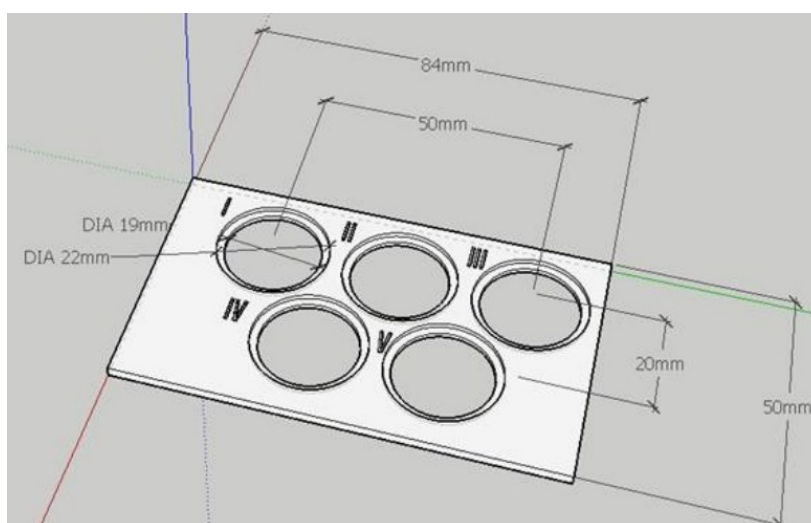


Figure 2.8 – Design of the holder used during the *operando* X-ray diffraction made by AutoCAD 2022

## 2.5. References

- [1] S. B. Das, Rasel; Ali, Eaqub; Abd Hamid, “CURRENT APPLICATIONS OF X-RAY POWDER DIFFRACTION - A REVIEW.,” *Rev. Adv. Mater. Sci.*, vol. 38, no. 2, pp. 69–109, 2014.
- [2] C. Giannini, M. Ladisa, D. Altamura, D. Siliqi, T. Sibillano, and L. De Caro, “X-ray Diffraction: A powerful technique for the multiple-length-scale structural analysis of nanomaterials,” *Crystals*, vol. 6, no. 8, pp. 1–22, 2016, doi: 10.3390/cryst6080087.
- [3] B. D. E. of X.-R. D. Cullity, *Elements of X-Ray Diffraction*, 1st ed. Reading, Massachusetts: , Cop. (ADDISON-WESLEY PUBLISHING COMPANY, 1956.
- [4] N. K. Thakral, R. L. Zanon, R. C. Kelly, and S. Thakral, “Applications of Powder X-Ray Diffraction in Small Molecule Pharmaceuticals: Achievements and Aspirations,” *J. Pharm. Sci.*, vol. 107, no. 12, pp. 2969–2982, 2018, doi: <https://doi.org/10.1016/j.xphs.2018.08.010>.
- [5] C. Stan, C. Beavers, M. Kunz, and N. Tamura, “X-Ray Diffraction under Extreme Conditions at the Advanced Light Source,” *Quantum Beam Sci.*, vol. 2, 2018, doi: 10.3390/qubs2010004.
- [6] “Home | ICSD,” *FIZ Karlsruhe GmbH*, 2024. <https://icsd.products.fiz-karlsruhe.de/> (accessed Apr. 10, 2024).
- [7] Edgewall Software, “GSAS-II - Crystallography Data Analysis Software.” .
- [8] J. Rodriguez-Carvajal, “Fullprof Homepage,” *Physica B*. 1993.
- [9] K. D. (UMIST) Vermon-Parr, “Microscopy : an introduction,” vol. 13, no. 4, pp. 40–44, 2000.
- [10] M. Tare, O. Puli, S. Oros, and A. Singh, “Drosophila adult eye model to teach Scanning Electron Microscopy in an undergraduate cell biology laboratory,” *Popul. Data Inf. Serv.*, vol. 92, pp. 174–180, 2009.
- [11] W. Zhou and H. F. Greer, “What Can Electron Microscopy Tell Us beyond Crystal Structures?,” *Eur. J. Inorg. Chem.*, vol. 2016, no. 7, pp. 941–950, 2016, doi: 10.1002/ejic.201501342.
- [12] N. Marturi, “Vision and visual servoing for nanomanipulation and nanocharacterization in scanning electron microscope.,” 2013.
- [13] J. Luxa *et al.*, “Layered Transition-Metal Ditellurides in Electrocatalytic Applications - Contrasting Properties,” *ACS Catal.*, vol. 7, no. 9, pp. 5706–5716, 2017, doi: 10.1021/acscatal.7b02080.

- [14] M. D. Hossain *et al.*, “The kinetics and potential dependence of the hydrogen evolution reaction optimized for the basal-plane Te vacancy site of MoTe<sub>2</sub>,” *Chem Catal.*, vol. 3, no. 1, p. 100489, 2023, doi: 10.1016/j.checat.2022.100489.
- [15] G. P. Holmes-Hampton, W. H. Tong, and T. A. Rouault, “Biochemical and Biophysical Methods for Studying Mitochondrial Iron Metabolism,” *Methods Enzymol.*, vol. 547, no. C, pp. 275–307, Jan. 2014, doi: 10.1016/B978-0-12-801415-8.00015-1.
- [16] F. Schmid, “Biological Macromolecules: UV-visible Spectrophotometry,” *Encycl. Life Sci.*, pp. 1–4, 2001, doi: 10.1038/npg.els.0003142.
- [17] A. B. Murphy, “Band-gap determination from diffuse reflectance measurements of semiconductor films, and application to photoelectrochemical water-splitting,” *Sol. Energy Mater. Sol. Cells*, vol. 91, pp. 1326–1337, 2007.
- [18] Ł. Haryński, A. Olejnik, K. Grochowska, and K. Siuzdak, “A facile method for Tauc exponent and corresponding electronic transitions determination in semiconductors directly from UV–Vis spectroscopy data,” *Opt. Mater. (Amst.)*, vol. 127, p. 112205, May 2022, doi: 10.1016/J.OPTMAT.2022.112205.
- [19] R. Darbeau, “Nuclear magnetic resonance (NMR) spectroscopy: A review and a look at its use as a probative tool in deamination chemistry,” *Appl. Spectrosc. Rev.*, vol. 41, no. 4, pp. 401–425, 2006, doi: 10.1080/05704920600726175.
- [20] M. Dračinský and P. Hodgkinson, “Solid-state NMR studies of nucleic acid components,” *RSC Adv.*, vol. 5, no. 16, pp. 12300–12310, 2015, doi: 10.1039/c4ra14404j.
- [21] H. Koller, G. Engelhardt, A. P. M. Kentgens, and J. Sauer, “<sup>23</sup>Na NMR spectroscopy of solids: Interpretation of quadrupole interaction parameters and chemical shifts,” *J. Physiol Chem.*, vol. 98, no. 6, pp. 1544–1551, 1994, doi: 10.1021/j100057a004.
- [22] W. Kang *et al.*, “Tunable Electrochemical Activity of P<sub>2</sub>-Na<sub>0.6</sub>Mn<sub>0.7</sub>Ni<sub>0.3</sub>O<sub>2-x</sub>F<sub>x</sub>Microspheres as High-Rate Cathodes for High-Performance Sodium Ion Batteries,” *ACS Appl. Mater. Interfaces*, vol. 13, no. 13, pp. 15333–15343, Apr. 2021, doi: 10.1021/acsami.1c02216.
- [23] M. Tabuchi and R. Kataoka, “Structure and Electrochemical Properties of  $\alpha$ -NaFeO<sub>2</sub> Obtained under Various Hydrothermal Conditions,” *J. Electrochem. Soc.*, vol. 166, no. 10, pp. A2209–A2214, 2019, doi: 10.1149/2.1411910jes.
- [24] S. H. Song, K. Ahn, M. G. Kanatzidis, J. A. Alonso, J. G. Cheng, and J. B. Goodenough, “Effect of an internal electric field on the redox energies of A<sub>1-x</sub>Ln<sub>x</sub>TiO<sub>4</sub>

- (A = Na or Li, Ln = y or Rare-Earth),” *Chem. Mater.*, vol. 25, no. 19, pp. 3852–3857, 2013, doi: 10.1021/cm401814z.
- [25] Y. Zhuo, “Investigation of nanostructured lithium-ion battery materials,” 2021.
- [26] N. Elgrishi, K. J. Rountree, B. D. McCarthy, E. S. Rountree, T. T. Eisenhart, and J. L. Dempsey, “A Practical Beginner’s Guide to Cyclic Voltammetry,” *J. Chem. Educ.*, vol. 95, no. 2, pp. 197–206, 2018, doi: 10.1021/acs.jchemed.7b00361.
- [27] L. W. Xia Huang, Zhiliang Wang, Ruth Knibbe, Bin Luo, Syed Abdul Ahad, Dan Sun, “Cyclic Voltammetry in Lithium–Sulfur Batteries—Challenges and Opportunities,” *Spec. Issue 3rd Int. Symp. Renew. Energy Technol.*, vol. 7, no. 8, 2019.
- [28] Ossila, “Cyclic Voltammetry Explained: Basic Principles & Set Up | Ossila.” .
- [29] K. Tang, X. Yu, J. Sun, H. Li, and X. Huang, “Kinetic analysis on LiFePO<sub>4</sub> thin films by CV, GITT, and EIS,” *Electrochim. Acta*, vol. 56, no. 13, pp. 4869–4875, 2011, doi: 10.1016/j.electacta.2011.02.119.
- [30] W. Weppner and R. A. Huggins, “Weppner, Determination of The Kinetic Parameters of Mixed-Conducting Electrodes and Application,” *High ion oxide cinduction*, vol. 124, no. 10, 1977.
- [31] W. Weppner and R. A. Huggins, “Determination of the Kinetic Parameters of Mixed-Conducting Electrodes and Application to the System Li<sub>3</sub>Sb,” *J. Electrochem. Soc.*, vol. 124, no. 10, p. 1569, 1977.
- [32] R. A. Huggins, *Advanced Batteries: Materials Science Aspects*, First. Boston, 2008.
- [33] Y. S. Su and A. Manthiram, “Lithium-sulphur batteries with a microporous carbon paper as a bifunctional interlayer,” *Nat. Commun.*, vol. 3, pp. 1–6, 2012, doi: 10.1038/ncomms2163.
- [34] R. Dugas, J. D. Forero-Saboya, and A. Ponrouch, “Methods and Protocols for Reliable Electrochemical Testing in Post-Li Batteries (Na, K, Mg, and Ca),” *Chem. Mater.*, no. Cv, 2019, doi: 10.1021/acs.chemmater.9b02776.
- [35] W. A. Khokhar *et al.*, “Impact of sintering temperature on the Al<sub>2</sub>O<sub>3</sub> electrolyte,” *Zeitschrift für Phys. Chemie*, vol. 237, no. 7, pp. 969–980, 2023, doi: doi:10.1515/zpch-2023-0240.
- [36] J. Song and M. Z. Bazant, “Effects of Nanoparticle Geometry and Size Distribution on Diffusion Impedance of Battery Electrodes,” *J. Electrochem. Soc.*, vol. 160, no. 1, pp. A15–A24, 2013, doi: 10.1149/2.023301jes.
- [37] Y. Lu, L. Li, Q. Zhang, Z. Niu, and J. Chen, “Electrolyte and Interface Engineering for Solid-State Sodium Batteries,” *Joule*, vol. 2, no. 9, pp. 1747–1770, 2018, doi:

- 10.1016/j.joule.2018.07.028.
- [38] N. J. J. de Klerk and M. Wagemaker, “No Title Diffusion Mechanism of the Sodium-Ion Solid Electrolyte Na<sub>3</sub>PS<sub>4</sub> and Potential Improvements of Halogen Doping,” *Chem. Mater.*, vol. 28, no. 9, pp. 3122–3160, 2016.
- [39] Z. Zhu, I.-H. Chu, Z. Deng, and S. P. Ong, “No Title Role of Na<sup>+</sup> Interstitials and Dopants in Enhancing the Na<sup>+</sup> Conductivity of the Cubic Na<sub>3</sub>PS<sub>4</sub> Superionic Conductor,” *Chem. Mater.*, vol. 27, no. 24, pp. 8318–8325, 2015.
- [40] H. Mehrer, *Diffusion in Solids: Fundamentals, Methods, Materials, Diffusion-Controlled Processes*, First. 2007.
- [41] J. C. Bachman *et al.*, “Inorganic Solid-State Electrolytes for Lithium Batteries: Mechanisms and Properties Governing Ion Conduction,” *Chem. Rev.*, vol. 116, no. 1, pp. 140–162, 2016.
- [42] J. L. Souquet, “Ionic Transport in Amorphous Solid Electrolytes,” *Annu. Rev. Mater. Res.*, vol. 11, 1981.
- [43] J. Evans, C. A. Vincent, and P. G. Bruce, “Electrochemical measurement of transference numbers in polymer electrolytes,” *Polymer (Guildf.)*, vol. 28, no. 13, pp. 2324–2328, 1987, doi: [https://doi.org/10.1016/0032-3861\(87\)90394-6](https://doi.org/10.1016/0032-3861(87)90394-6).
- [44] D. S. Chang, F. D. Lasley, I. J. Das, M. S. Mendonca, and J. R. Dynlacht, “Production and Properties of Radiation,” in *Basic Radiotherapy Physics and Biology*, Cham: Springer International Publishing, 2021, pp. 23–34.
- [45] “About Synchrotrons - Diamond Light Source,” 2022. <https://www.diamond.ac.uk/Home/About/FAQs/About-Synchrotrons.html>.
- [46] G. P. Williams, “A general review of synchrotron radiation, its uses and special technologies,” *Vacuum*, vol. 32, no. 6, pp. 333–345, 1982.
- [47] F. Lin *et al.*, “Synchrotron X-ray Analytical Techniques for Studying Materials Electrochemistry in Rechargeable Batteries,” *Chem. Rev.*, vol. 117, no. 21, pp. 13123–13186, 2017, doi: 10.1021/acs.chemrev.7b00007.
- [48] C. Li, “Supporting Information A quasi-intercalation reaction for fast sulfur redox kinetics in solid- state lithium-sulfur batteries.”



### **3. Effect of calcium and dual calcium-fluorine doping on $O_3$ -type $\alpha$ - $\text{NaFeO}_2$ as cathodes for sodium-ion batteries**



3. Effect of calcium and dual calcium-fluorine doping on O <sub>3</sub> -type α-NaFeO <sub>2</sub> as cathodes for sodium-ion batteries .....	85
3.1. Calcium as pillaring agent .....	87
3.2. Doping on cathode materials .....	90
3.2.1. Anionic dopants .....	91
3.3. Synthesis optimisation and characterisation .....	96
3.3.1. α-NaFeO <sub>2</sub> synthesis optimisation.....	96
3.3.2. Structure .....	99
3.3.3. Morphology and composition .....	115
3.4. Electrochemical performance .....	117
3.4.1 Optimisation of cycling window .....	117
3.4.2. Galvanostatic measurements .....	121
3.4.3. Cyclic-voltammetry .....	124
3.4.4. Galvanostatic intermittent titration technique.....	131
3.4.5. Operando X-ray diffractometry .....	138
3.5. Conclusion.....	140
3.6. References .....	146

### 3.1. Calcium as pillaring agent

The use of pillaring agents to enhance the performance of transition layered oxides in sodium-ion batteries has generated considerable interest. Among the various pillaring agents, calcium has emerged as a promising candidate due to its unique properties and benefits. [1], [2]

Calcium pillaring involves the incorporation of calcium ions into the interlayer spaces of O<sub>3</sub>-type transition metal oxides. This modification helps to stabilise the layered structure, preventing the collapse and phase transitions that typically occur during the charge and discharge cycles of the battery. [3] Calcium, being a divalent ion, offers strong electrostatic interactions with the oxygen atoms in the layers, which can significantly enhance the structural integrity of the material.

Recent studies have demonstrated the potential of calcium-pillared TMO in enhancing the electrochemical performance of NIBs. [4], [5] The introduction of calcium ions has been found to mitigate the effects of structural degradation, thereby maintaining higher performance over extended cycling. In Chen *et al.*, Calcium pillaring of NaCrO<sub>2</sub> was conducted. DFT studies concluded that calcium tends to substitute sodium in the sodium layer instead of the transition metal since the first is more energetically favourable. Due to a hindrance of the Na/vacancies ordering in the desodiation phase, the pillared material showed an improved cyclability and a smoothed galvanostatic curve. This is accompanied by a slight initial capacity loss. [4] Pillaring also improved NaCrO<sub>2</sub> air stability. In Figure 3.1, a capacity over cycling of pristine NaCrO<sub>2</sub> and 5 % Ca-pillared NaCrO<sub>2</sub> shows an improvement from the capacity after 500 cycles from 55 to 85 mA h g<sup>-1</sup>. There is also a noticeable improvement in the capacity at fast rates, especially at 20 C. [4]

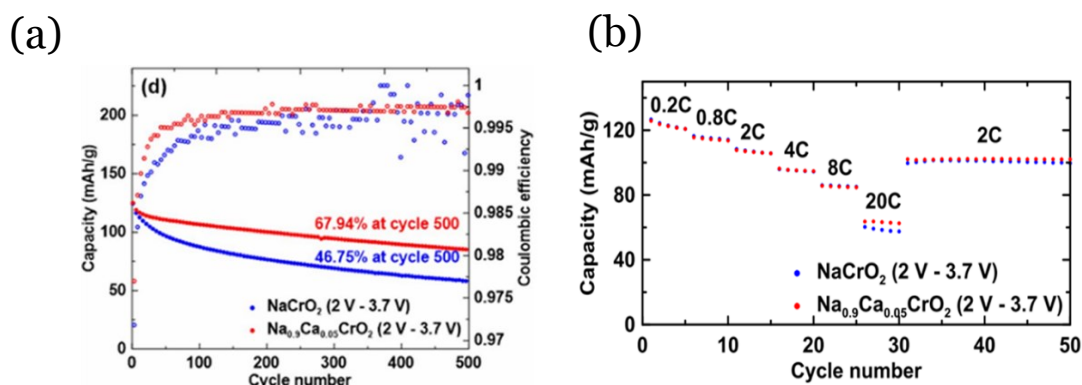


Figure 3.1 – (a) Capacity during cycling of NaCrO<sub>2</sub>, pristine and 5 % calcium pillared (b) and fast-rate cycling of NaCrO<sub>2</sub>, pristine and 5 % calcium pillared. [4]

In Laisa *et al* (2017), NaCoO<sub>2</sub> was pillared with calcium at percentages of 0.2, 0.5, 0.7, 1.0 and 3.0 %. [6] Calcium-pillaring shows an improvement of initial capacity and capacity retention from 0 to 0.7 % and a hindrance from 1.0 %, due to the deleterious effect calcium has on ion mobility. The calcium pillaring at 0.5 % has also a positive effect on the cyclability at faster rates. [6] In Figure 3.2, the capacity during cycling of NaCrO<sub>2</sub> at various pillaring percentages and pristine-NaCrO<sub>2</sub> and 0.5 % calcium pillared NaCrO<sub>2</sub> at various cycling rates. [6]

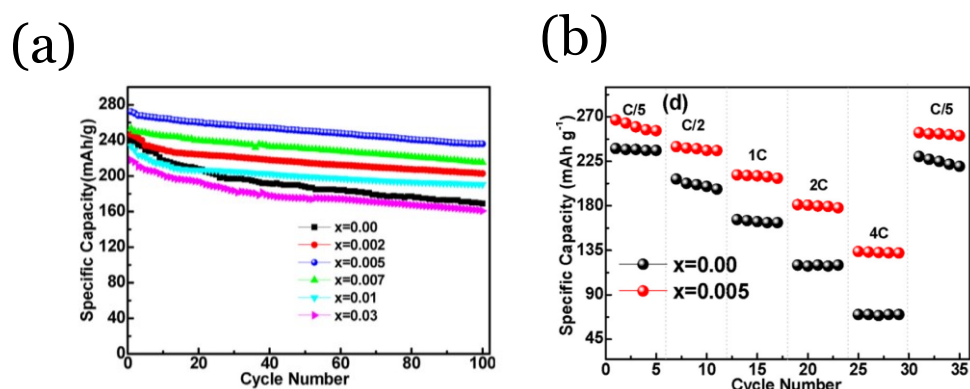


Figure 3.2 – (a) NaCrO<sub>2</sub> capacity evolution over cycling at various calcium-pillaring percentages (b) and capacity of NaCrO<sub>2</sub> at faster charge/discharge rates. [6]

In Han *et al* (2015), NaCoO<sub>2</sub>, 0 (A), 2 (B), 5 (C) 7 (D) and 10 (E) % Ca-doping was tested. [5] Those pillared at 2 and 5 % doping show a slight increase of initial capacity and a

little increase of cyclability. [5] On the other hand, those pillared at 7 and 10 % have a great decrease in the initial capacity but a big increase in capacity retention. [5] Has shown in Figure 3.2b, Ca-pillaring has a beneficial impact capacity at faster rates. In Figure 3.3, the capacity of NaCoO<sub>2</sub> calcium pillared at 0, 2, 5, 7 and 10 % is shown (a), as well as the capacity of the pristine NaCoO<sub>2</sub> and the 7 % calcium pillared NaCoO<sub>2</sub>. [5]

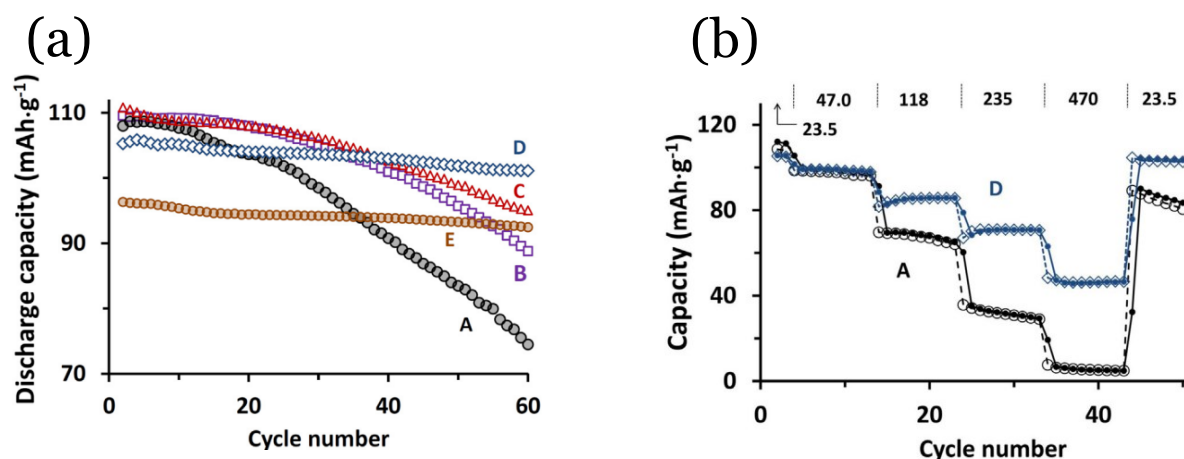


Figure 3.3 – Capacity of NaCoO<sub>2</sub>, pristine, 2, 5, 7 and 10 % calcium-pillaring rate over cycling (a) and NaCoO<sub>2</sub>, pristine and 7 % at faster charge/discharge rates

Calcium pillaring represents a valuable approach in the development of more robust and efficient transition metal oxides for sodium-ion batteries. By enhancing structural stability and sodium ion mobility, calcium pillars can significantly improve the durability and electrochemical performance of these materials. As research progresses, calcium-pillared materials may become a key component in the advancement of high-performance, sustainable energy storage solutions.

### 3.2. Doping on cathode materials

Doping in transition metal oxides is a critical strategy to enhance the capacity of cathodes in rechargeable batteries. [7]–[9] By introducing foreign atoms into the oxide lattice, one can significantly alter the electronic structure and ionic conductivity of the material. [7] This not only improves the overall energy storage capabilities but also enhances

the stability and lifespan of the cathode. For instance, doping sodium cobalt oxide with elements like nickel or manganese has been shown to increase capacity and thermal stability, making it a more viable option for high-performance applications. [7] This method has become a cornerstone in the development of advanced battery technologies, addressing the growing demand for more efficient and durable energy storage solutions.

### *3.2.1. Anionic dopants*

The introduction of anionic dopants into the cathode material. These dopants can either substitute for anions in the lattice or occupy interstitial sites. [10] Adding these elements to a material may enhance the electronic conductivity, ionic mobility, and structural stability of the cathode material. Common anionic dopants include halogens (e.g., fluorine, chlorine), chalcogens (e.g., sulfur, selenium), and pnictogens – group 15 of the periodic table (e.g., nitrogen, phosphorus). [10]

Anionic dopants alter the electronic structure of the host material, which can lead to improved electronic conductivity. For instance, the incorporation of fluorine (F<sup>-</sup>) into a transition metal oxide lattice can result in the formation of additional electronic states near the conduction band. [11] This facilitates the movement of electrons through the material, thereby enhancing its conductivity. [11] Improved electronic conductivity is crucial for the efficient operation of NIBs, as it reduces internal resistance and enhances the overall power output of the battery.

The introduction of anionic dopants can also improve the ionic mobility within the cathode material. By creating additional pathways or reducing the energy barriers for ion migration, anionic dopants can facilitate the movement of sodium ions during charge and discharge cycles. [10] For example, doping with sulphur (S<sup>2-</sup>) in a polyanionic compound can

lead to the formation of vacancies or interstitial sites that serve as conduits for sodium ion diffusion. [10] Enhanced ionic mobility contributes to better rate capability and higher capacity retention over multiple cycles.

One of the critical challenges in cathodes for NIBs is maintaining structural integrity during repeated charge-discharge cycles. [12] Volume changes associated with sodium ion insertion and extraction can lead to material degradation and capacity fade. [12] Anionic dopants can mitigate these effects by stabilising the crystal structure. For instance, chlorine (Cl<sup>-</sup>) doping in layered oxides can enhance the stability of the crystal lattice by reducing the distortion and strain associated with sodium ion intercalation. [13] This leads to improved cycle life and better overall battery performance.

Layered oxides are promising cathode materials due to their high capacity and good electrochemical performance. However, their structural stability and electronic conductivity are often inadequate for practical applications. [14] Fluorine doping has been shown to improve these properties significantly. [15] Studies have demonstrated that fluorine-doped Na<sub>x</sub>TMO<sub>2</sub> exhibits enhanced electronic conductivity, leading to higher power output. Additionally, the structural stability of the material is improved, resulting in better capacity retention over extended cycling. In Huang *et al.*, F doping of NaNi<sub>0.33(3)</sub>Fe<sub>0.033(3)</sub>Mn<sub>0.033(3)</sub>O<sub>2</sub> (NFM) was investigated. [16] In the study, NFM was cycled between 2.0 and 4.0 V *vs* Na<sup>+</sup>/Na, at a current density of 150 mA g<sup>-1</sup>. As seen in Figure 3.3, the undoped NFM can only retain approximately 60 mA h g<sup>-1</sup> after 70 cycles. In comparison, the 1 % F-doped NFM (NFM-F<sub>0.01</sub>) shows a superior capacity retention of 110 mA h g<sup>-1</sup> after 70 cycles. This occurs by the increase of the binding energy of oxygen and adjusting the Mn<sup>3+</sup>/Mn<sup>4+</sup>, shown in Figure 3.4, which helps in the stabilisation of the structure and prevents the release of O<sub>2</sub>. [16]

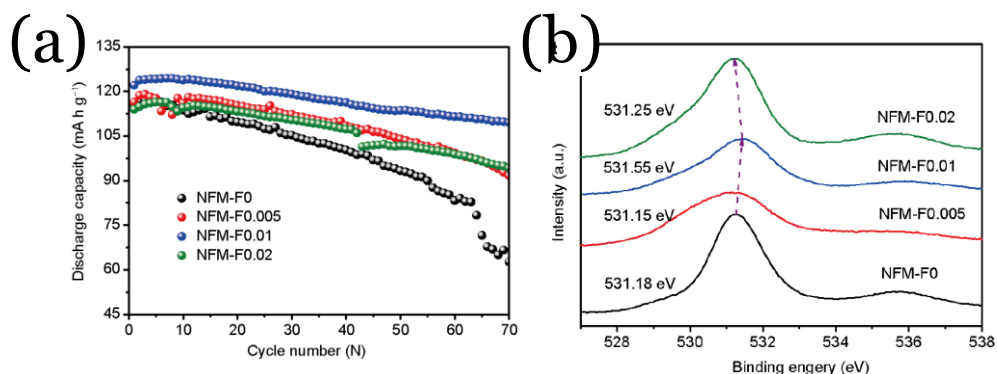


Figure 3.4 – Cycling stability of undoped and F-doped NFM over 70 cycles at a scan rate of 150 mA g<sup>-1</sup> (a) and O 1s band binding energy of undoped and F-doped NFM (b)

In Figure 3.5, shown the cyclic-voltammetry curves of undoped NFM and the 1 % fluorine-doped NFM in the potential range of 2.0 to 4.0 V *vs* Na<sup>+</sup>/Na at 0.1 mV s<sup>-1</sup> scan rate. The peaks observed at 2.85 and 3.05 V *vs* Na<sup>+</sup>/Na can be attributed to the Ni<sup>2+</sup>/Ni<sup>3+</sup> redox pair. The intensity of the peak of the doped materials is higher, indicating a lower polarisation, compared to the undoped material. [16] The Na<sup>+</sup> diffusion rate was measured by comparing the peak intensities of the cyclic-voltammetric measurements at various rates. The calculated Na<sup>+</sup> diffusion rate was calculated to be  $1.037 \times 10^{-12}$ ,  $3.076 \times 10^{-12}$ ,  $6.796 \times 10^{-12}$  and  $1.742 \times 10^{-12}$  cm<sup>2</sup> s<sup>-1</sup>, for the undoped, 0.5 %, 1 % and 2 % fluorine-doped NFM, respectively. [16]

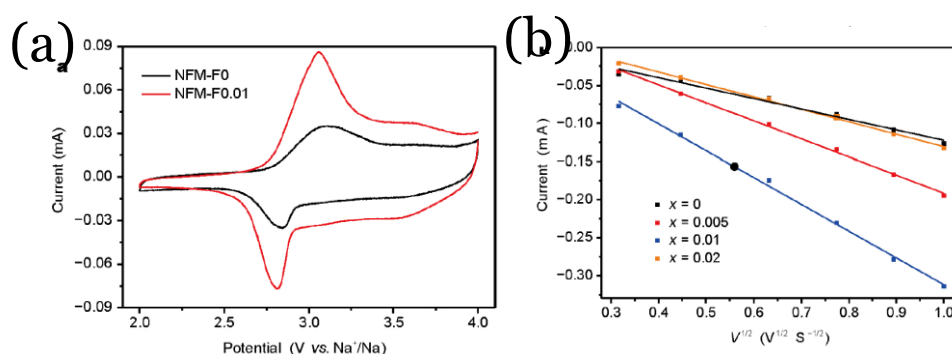


Figure 3.5 – cyclic-voltammetry curves at a scan rate of 0.1 mV s<sup>-1</sup> of undoped NFM and 1 % F-doped NFM (a) and the relationship of peak current (i<sub>p</sub>) and the square root of scan rate (v<sup>1/2</sup>) of all NFM (b) [16]

In this specific case (NFM), a further increase in the quantity of fluorine beyond 1 %, has a deleterious effect, related to the increase in Mn<sup>3+</sup> content, compared to Mn<sup>4+</sup> due to charge compensation. [16] It is known that the more Mn<sup>3+</sup> in the system, the better the performance achieved. However, an excess of Mn<sup>4+</sup> causes a rapid decrease in capacity with cycling due to deleterious Jahn-Teller distortions of Mn<sup>3+</sup>. [16]

Doping with F<sup>-</sup> may increase TM-O bond energy, reducing anionic reduction and increasing the material stability. Furthermore, F<sup>-</sup> increases the Na<sup>+</sup> diffusion by increasing the alkali-metal spacing and increasing the initial capacity of Na<sub>x</sub>TMO<sub>2</sub>. [16]

Anionic doping represents a powerful approach to enhancing the performance of cathode materials in sodium-ion batteries. [10], [15] By introducing negatively charged dopants, it is possible to improve the electronic conductivity, ionic mobility, and structural stability of the cathode. [10] Fluorine, sulfur, and chlorine are among the effective dopants that have shown promise in various cathode materials. [10] While challenges remain in optimising the doping process and understanding the underlying mechanisms, continued research in this area is likely to yield significant advancements in the development of high-performance sodium-ion batteries.

### *3.2.2. Double effect of calcium-pillaring and fluorine-doping*

The synergistic effect of calcium pillaring and fluorine doping in transition metal oxides holds great promise for enhancing the performance of cathodes in sodium-ion batteries. Calcium pillaring involves the insertion of calcium ions between the layers of the transition metal oxide structure, increasing the interlayer spacing and facilitating the diffusion of sodium ions. This structural modification improves ionic mobility and enhances the material's structural stability during repeated charge-discharge cycles. When combined with fluorine doping, which improves electronic conductivity and further stabilises the crystal lattice, the overall electrochemical performance of the cathode material can be significantly

enhanced. Fluorine doping introduces additional electronic states near the conduction band, boosting electronic conductivity and reducing internal resistance. This, coupled with the improved ionic pathways created by calcium pillaring, results in a cathode material that exhibits both high capacity and excellent rate capability. Furthermore, the dual approach of calcium pillaring and fluorine doping helps mitigate common issues such as structural degradation and capacity fade, leading to better cycle stability. The synergistic effect of these two modifications can thus produce a robust, high-performance cathode material, making sodium-ion batteries a more viable and competitive option for large-scale energy storage applications.

In Liu *et al.*, the *P2*-type cathode material  $\text{Na}_{0.67-x}\text{Ca}_x\text{Ni}_{0.33}\text{Mn}_{0.67}\text{O}_{2-2x}\text{F}_{2x}$  was constructed by tuning Na<sup>+</sup> and O-site co-doping with Ca<sup>2+</sup> and F<sup>-</sup>. [6] In Figure 3.6, the capacity of Ca and F-doped, as well as the comparison between the only Ca-doped or F-doped materials is shown. [6]

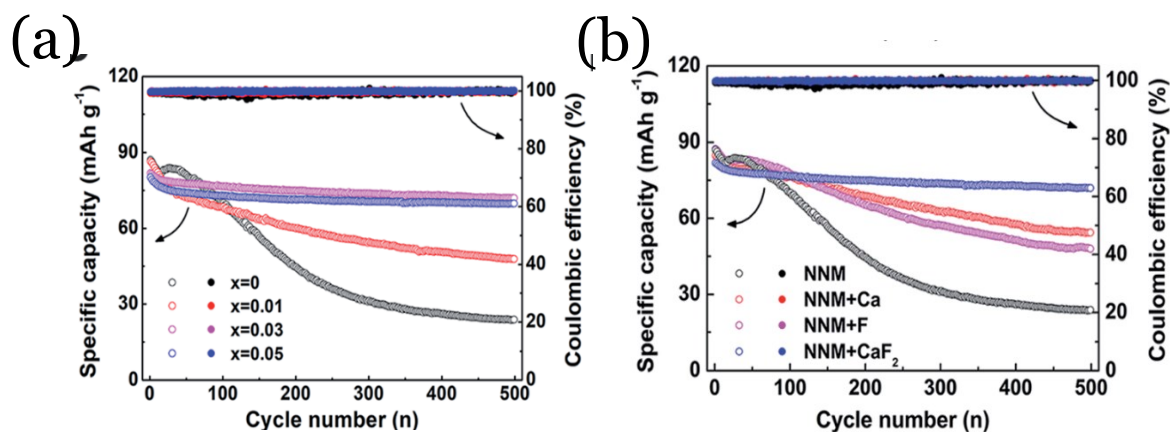


Figure 3.6 - Cycling performance of  $\text{Na}_{0.67-x}\text{Ca}_x\text{Ni}_{0.33}\text{Mn}_{0.67}\text{O}_{2-2x}\text{F}_{2x}$  ( $x = 0, 0.01, 0.03$  and  $0.05$ ) cycled at 1C in the voltage range of 2.0–4.3 V. (a) Comparison of cycling performance of  $\text{Na}_{0.67}\text{Ni}_{0.33}\text{Mn}_{0.67}\text{O}_2$  cathodes doped with Ca, F and  $\text{CaF}_2$  cycled at 1C in the voltage range of 2.0–4.3 V (b) [6]

The capacity retention of  $\text{Na}_{0.67-x}\text{Ca}_x\text{Ni}_{0.33}\text{Mn}_{0.67}\text{O}_{2-2x}\text{F}_{2x}$  ( $x = 0, 0.01, 0.03$  and  $0.05$ ) at the 500<sup>th</sup> cycle is 27.1%, 54.5%, 87.2% and 85.5%, respectively. This also demonstrates the superior cycling stability of Ca<sup>2+</sup> /F<sup>-</sup> co-doped cathodes. To unravel whether Ca<sup>2+</sup> or F<sup>-</sup> doping

is responsible for the improved cycling stability, the cathode doped with only Ca<sup>2+</sup> or F<sup>-</sup> ions was cycled at 1C as shown in Figure 3.6. The capacity retention was increased from 27.1% to 54.9% and 64.1% for 6 % F-doped and 3 % Ca-doped cathodes. The synergetic doping of Ca<sup>2+</sup> and F<sup>-</sup> can greatly enhance the cycling stability, which is much better than the effect of doping Ca<sup>2+</sup> or F<sup>-</sup> alone. [6]

### 3.3. Synthesis optimisation and characterisation

In this chapter, the synthesis of  $\alpha$ -NaFeO<sub>2</sub>,  $\alpha$ -Na<sub>0.94</sub>Ca<sub>0.03</sub>FeO<sub>2</sub>,  $\alpha$ -Na<sub>0.90</sub>Ca<sub>0.05</sub>FeO<sub>2</sub>,  $\alpha$ -Na<sub>0.94</sub>Ca<sub>0.03</sub>FeO<sub>1.94</sub>F<sub>0.06</sub> and,  $\alpha$ -Na<sub>0.90</sub>Ca<sub>0.05</sub>FeO<sub>1.9</sub>F<sub>0.1</sub> *via* the ceramic method was optimised to the environmental conditions and equipment available so that the material was obtained with the least number and number of secondary phases and impurities as possible. This was accomplished by manipulating the calcination temperature and calcination steps. The pristine material  $\alpha$ -NaFeO<sub>2</sub> was previously synthesised with a relatively low amount of impurities in Saurel *et al.* [17]

After synthesis, these materials were characterised structurally, morphologically, and chemically *via* X-ray diffractometry, scanning electron microscopy and energy-dispersive X-ray spectroscopy and, their electrochemical performance was studied and compared using galvanostatic charge and discharge methods, cyclic-voltammetry, galvanostatic intermittent titration technique and *operando* X-ray diffraction.

#### 3.3.1. $\alpha$ -NaFeO<sub>2</sub> synthesis optimisation

To obtain the  $\alpha$ -NaFeO<sub>2</sub> phase, belonging to the  $R\bar{3}m$  space group, the calcination temperature was first optimised. With this aim, the precursor mixture was calcined at 650, 670, and 680 °C for 15 hours. Further experimental details can be found in Section 2. In Figure 3.7, the diffractograms of the materials obtained from the calcination at 650, 670, and 680 °C are compared with a reference of  $\alpha$ -NaFeO<sub>2</sub> and some of the most common impurities

are reported in Saurel, *et al.* and Kataoka, *et al.* [17], [18] The reference material diffractograms were obtained from ICSD. [19]

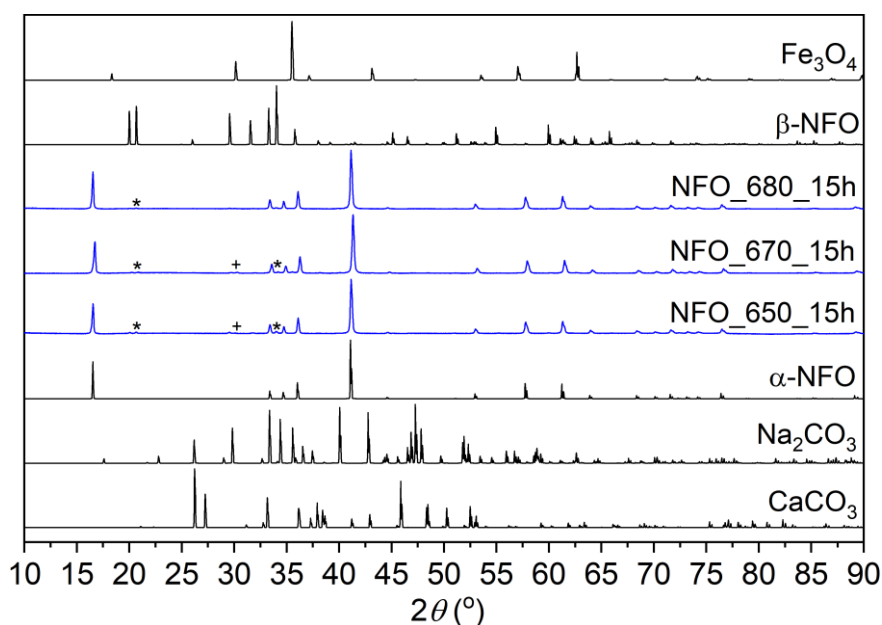


Figure 3.7. – X-ray diffractograms of the samples synthesised at temperatures of 650, 670, and 680 °C with the standards of  $\alpha$ -NaFeO<sub>2</sub>,  $\beta$ -NaFeO<sub>2</sub>, CaCO<sub>3</sub>, Na<sub>2</sub>CO<sub>3</sub> and Fe<sub>3</sub>O<sub>4</sub> obtained from the ICSD. [19] The peaks attributed only to the  $\beta$ -NaFeO<sub>2</sub> phase are indicated with an asterisk (\*) and those attributed only to the Na<sub>2</sub>CO<sub>3</sub> phase are indicated with a plus sign (+).

In all three iterations, the  $\alpha$ -NaFeO<sub>3</sub> phase is the main phase however, both the  $\beta$ -NaFeO<sub>2</sub> phase, and Na<sub>2</sub>CO<sub>3</sub>, the sodium source, are detected. The presence of unreacted precursor usually means that the energy supplied to the system was not enough to cause a complete reaction or that the limited exposure to air and moisture causes degradation. However, the  $\beta$ -NaFeO<sub>2</sub> is formed at high temperatures, meaning that there may be an overlap between the complete reaction of all the precursors and the formation of the high-temperature  $\beta$ -NaFeO<sub>2</sub> phase. Several studies indicate that the  $\beta$ -NaFeO<sub>2</sub> phase cannot be avoided. [20], [21] With this in mind, the decision was made to proceed with the material with the least number of impurities, which was the  $\alpha$ -NaFeO<sub>2</sub> synthesised at 680 °C.

The synthesis of the Ca-pillared  $\alpha$ -NaFeO<sub>2</sub> was not successful using the previous conditions hence, the synthesis of these materials had to be optimised. In Figure 3.8, the diffractograms of the materials obtained from the calcination at 630 °C are compared with a reference of  $\alpha$ -NaFeO<sub>2</sub> and some of the most common impurities such as  $\beta$ -NaFeO<sub>2</sub>, Na<sub>2</sub>CO<sub>3</sub>, CaCO<sub>3</sub>, and Fe<sub>3</sub>O<sub>4</sub>. The reference material diffractograms were obtained from ICSD. [19]

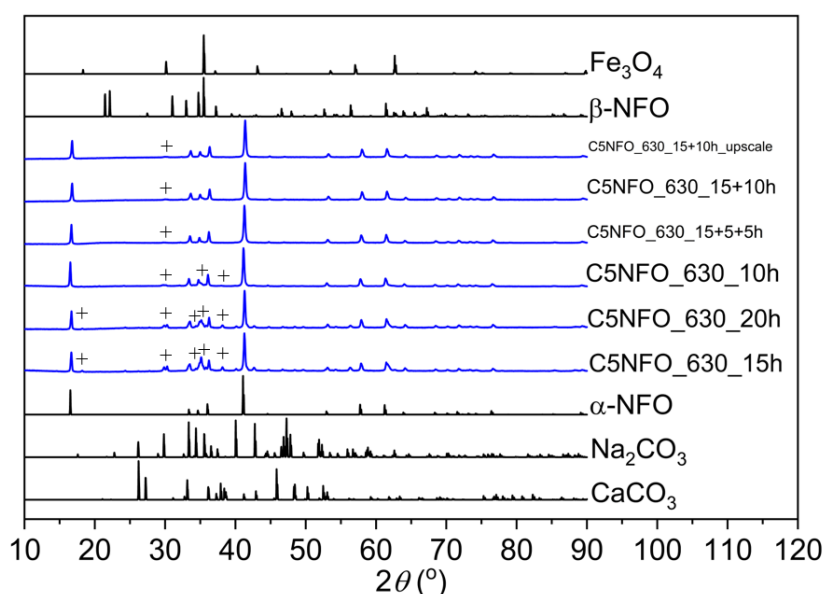


Figure 3.8 – X-ray diffractograms of the samples synthesised at temperatures of 630 °C for 10, 15, and 20 hours, with a two-step synthesis of 15+10 hours and a three-step synthesis of 15+5+5 hours with the standards of  $\alpha$ -NaFeO<sub>2</sub>,  $\beta$ -NaFeO<sub>2</sub>, CaCO<sub>3</sub>, Na<sub>2</sub>CO<sub>3</sub> and Fe<sub>3</sub>O<sub>4</sub> obtained from the ICSD. [19] The peaks attributed to any of the precursors are indicated with a plus sign (+).

The temperature was lowered to 630 °C from that used in the undoped material. The calcination of the precursor mixture for 15 hours resulted in a considerably high number of unreacted precursors. The increase of the calcination time to 20 hours, results in a higher amount of unreacted precursors. Reducing the calcination time to 10 hours did not promote the formation of a purer  $\alpha$ -Na<sub>0.90</sub>Ca<sub>0.05</sub>FeO<sub>2</sub> phase. To promote a better homogenisation of all elements, a two-step and three-step reaction was attempted. Both two-step 15+10 hours and three-step 15+5+5 hours resulted in a majority  $\alpha$ -Na<sub>0.90</sub>Ca<sub>0.05</sub>FeO<sub>2</sub> phase with a low

amount of secondary phase and unreacted precursors. For simplicity, the two-step synthesis at 630 °C for 15+10 hours instead of the three-step 15+5+5 h. The same synthetic procedure used in the  $\alpha$ -Na<sub>0.90</sub>Ca<sub>0.05</sub>FeO<sub>2</sub> (C5NFO) was successfully applied to calcium-pillared,  $\alpha$ -Na<sub>0.96</sub>Ca<sub>0.02</sub>FeO<sub>2</sub> (C2NFO) and  $\alpha$ -Na<sub>0.94</sub>Ca<sub>0.03</sub>FeO<sub>2</sub> (C3NFO) as well as, the calcium-doped and fluorinated  $\alpha$ -Na<sub>0.90</sub>Ca<sub>0.05</sub>FeO<sub>1.9</sub>F<sub>0.1</sub> (C5NFOF),  $\alpha$ -Na<sub>0.96</sub>Ca<sub>0.02</sub>FeO<sub>1.96</sub>F<sub>0.04</sub> (C2NFOF) and  $\alpha$ -Na<sub>0.94</sub>Ca<sub>0.03</sub>FeO<sub>1.94</sub>F<sub>0.06</sub> (C3NFOF). The diffractograms of these compounds are shown in Figure 3.9. Comparing all the material diffractograms, the higher the calcium concentration, the larger the concentration of calcium precursors, especially CaCO<sub>3</sub> for C2NFO and CaF<sub>2</sub> in C2NFOF. CaF<sub>2</sub> can also convert to NaF, which is detected in C2NFOF.

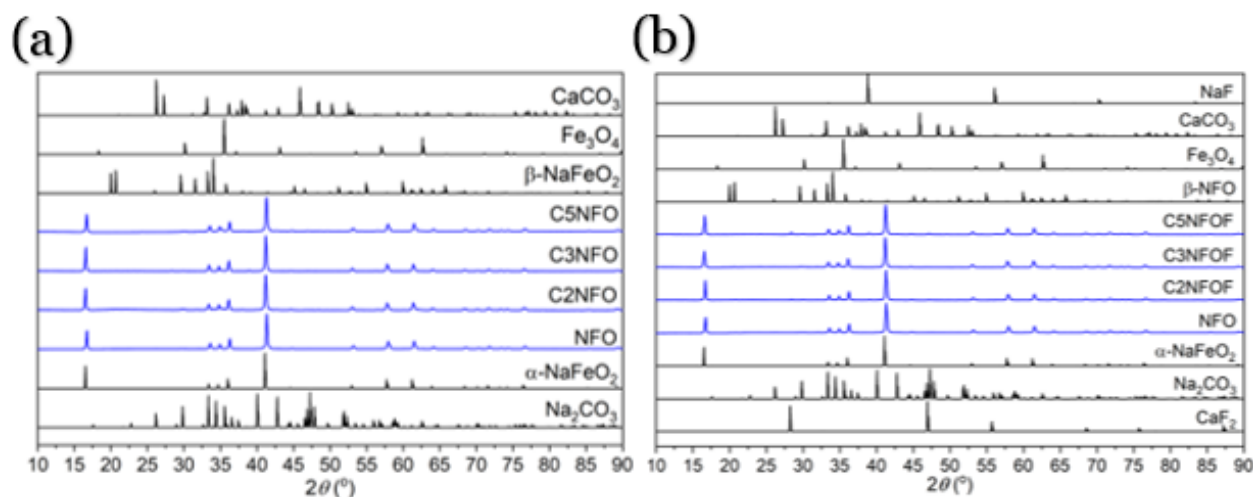


Figure 3.9 – X-ray diffractograms of the  $\alpha$ -Na<sub>0.90</sub>Ca<sub>0.05</sub>FeO<sub>2</sub> (C5NFO),  $\alpha$ -Na<sub>0.96</sub>Ca<sub>0.02</sub>FeO<sub>2</sub> (C2NFO) and  $\alpha$ -Na<sub>0.94</sub>Ca<sub>0.03</sub>FeO<sub>2</sub> (C3NFO) (a) and (C5NFOF),  $\alpha$ -Na<sub>0.96</sub>Ca<sub>0.02</sub>FeO<sub>1.96</sub>F<sub>0.04</sub> (C2NFOF) and  $\alpha$ -Na<sub>0.94</sub>Ca<sub>0.03</sub>FeO<sub>1.94</sub>F<sub>0.06</sub> (C3NFOF) (b) compared with the standards of  $\alpha$ -NaFeO<sub>2</sub>,  $\beta$ -NaFeO<sub>2</sub>, CaCO<sub>3</sub>, Na<sub>2</sub>CO<sub>3</sub>, CaF<sub>2</sub>, NaF and Fe<sub>3</sub>O<sub>4</sub> obtained from ICSD. [19]

### 3.3.2. Structure

The lattice parameters of  $\alpha$ -NaFeO<sub>2</sub> were obtained using Rietveld refinement (Figure 3.10). The refined parameters included the zero, lattice, and profile parameters, atomic positions, and isotropic displacement parameters ( $U_{iso}$ ). The lattice parameters were found to be  $a = b = 3.0231$  Å,  $c = 16.11257$  Å,  $\alpha = 90^\circ$ ,  $\beta = 90^\circ$  and  $\gamma = 90^\circ$ , which are in agreement

with the unit cell parameters reported in the literature. [17] The refined parameters can be found in Table 3.1. The goodness-of-fit,  $\chi^2$ , was found to be 10.62 and the R factors such as weighted profile R-factor,  $R_{wp}$ , and expected R-factor,  $R_{exp}$ , were found to be 2.967 and 1.643 %, respectively. In this case, the data was collected in a lab diffractometer in reflection mode using conventional Cu  $K\alpha_1$  and Cu  $K\alpha_2$  sources which influenced the goodness of the refinement. As expected, the material used for these and the following experiments has a purity of 97.1 wt% and an impurity of  $\beta$ -NaFeO<sub>2</sub>, corresponding to 2.9 wt% of the total amount of material.

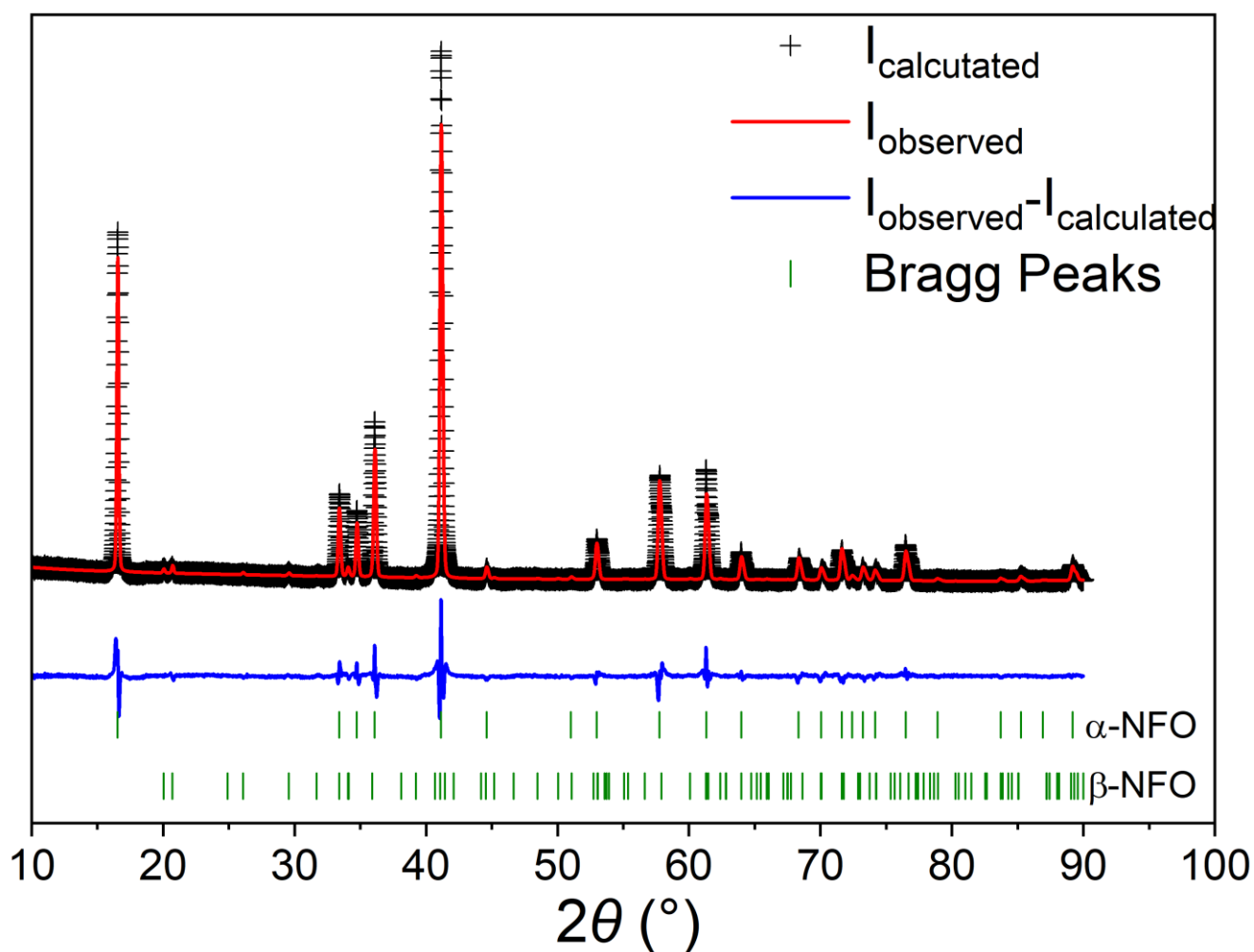


Figure 3.10 – Rietveld refinement of pristine  $\alpha$ -NaFeO<sub>2</sub>

Table 3.1 – Cell parameters, goodness-of-fitness parameters and phase composition of NaFeO<sub>2</sub>, obtained from Rietveld refinements on lab XRD data.

Atom	<i>x</i>	<i>Y</i>	<i>Z</i>	Multiplicity	Occupancy	<i>U</i> <sub>iso</sub> (Å <sup>2</sup> )
Na1	0.0000	0.0000	0.0000	3	0.9838(5)	0.0253(2)
Fe1	0.0000	0.0000	0.5000	3	0.9744(4)	0.0151(1)
O1	0.0000	0.0000	0.2355(6)	6	0.9878(4)	0.0386(3)

$\alpha$ -NaFeO<sub>2</sub> – space group  $R\bar{3}m$

$a = b = 3.023(1)$  Å;  $c = 16.1125(7)$  Å;  $\alpha = 90^\circ$ ;  $\beta = 90^\circ$ ;  $\gamma = 90^\circ$

$\chi^2 = 10.62$ ;  $R_{wp} = 2.967\%$ ;  $R_{exp} = 1.643\%$

%( $\alpha$ -NaFeO<sub>2</sub>) = 97.1 wt%; %( $\beta$ -NaFeO<sub>2</sub>) = 2.9 wt%

The structure of  $\alpha$ -NaFeO<sub>2</sub> and  $\beta$ -NaFeO<sub>2</sub> is illustrated in Figure 3.11. This figure shows an alternation between Na-O-Fe-O layers along the *c*-axis. On the other hand, the  $\beta$ -NaFeO<sub>2</sub> does not show any arrangement of FeO<sub>4</sub> and NaO<sub>4</sub> tetrahedra, comparable to the  $\alpha$ -phase. The  $\beta$ -NaFeO<sub>2</sub> belongs to the space group  $Pna2_1$ . [21]

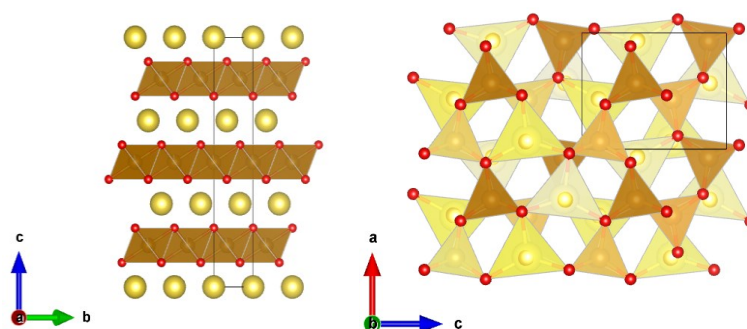


Figure 3.11 –  $\alpha$ -NaFeO<sub>2</sub> (left) and  $\beta$ -NaFeO<sub>2</sub> (right) structures drawn with VESTA where the oxygen is marked in red, iron in brown and sodium in yellow

The lattice parameters of  $\alpha$ -Na<sub>0.96</sub>Ca<sub>0.02</sub>FeO<sub>2</sub> were obtained using Rietveld refinement (Figure 3.12). The refined parameters included zero, lattice, and profile parameters, atomic

positions, and isotropic displacement parameters ( $U_{iso}$ ). The lattice parameters were found to be  $a = b = 3.02161 \text{ \AA}$ ,  $c = 16.09638 \text{ \AA}$ , and  $\alpha = \beta = \gamma = 90^\circ$ . These values agree with the unit cell parameters reported in the literature, and the presence of divalent Ca<sup>2+</sup> causes the  $c$ -axis length to decrease compared to pristine NFO. The refined parameters are detailed in Table 4.2.

The goodness-of-fit ( $\chi^2$ ) was 9.551, and the R factors, such as the weighted profile R-factor ( $R_{wp}$ ) and expected R factor ( $R_{exp}$ ), were 6.340% and 2.596%, respectively. Data collection was performed in reflection mode using conventional Cu K $\alpha$ 1 and Cu K $\alpha$ 2 sources, which influenced the refinement quality. The material used for these and subsequent experiments has a purity of 99.6 wt%, with an impurity of  $\beta$ -NaFeO<sub>2</sub> constituting 0.4 wt% of the total material.

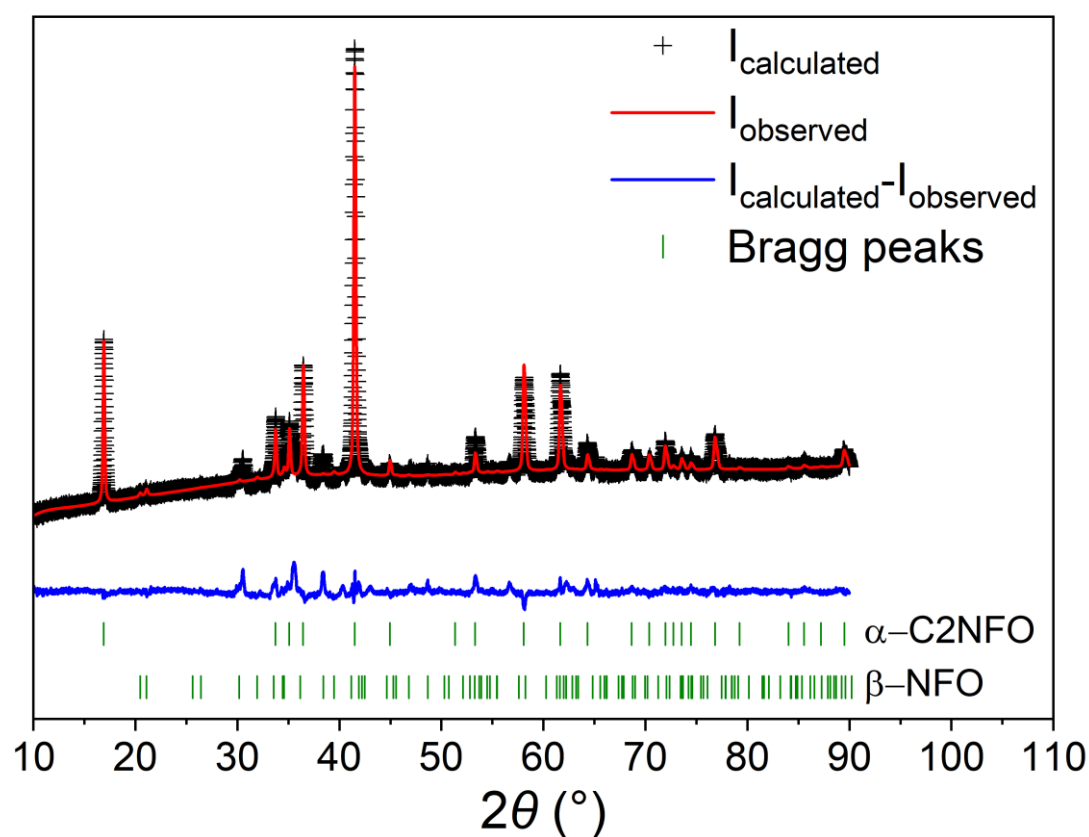


Figure 3.12 – Rietveld refinement of pristine  $\alpha$ -Na<sub>0.96</sub>Ca<sub>0.02</sub>FeO<sub>2</sub>

Table 3.2 - Cell parameters, goodness-of-fitness parameter and phase composition of  $\alpha$ -Na<sub>0.96</sub>Ca<sub>0.02</sub>FeO<sub>2</sub>, obtained from Rietveld refinements

Atom	<i>x</i>	<i>Y</i>	<i>Z</i>	Multiplicity	Occupancy	<i>U</i> <sub>iso</sub> (Å <sup>2</sup> )
<b>Na1</b>	0.0000	0.0000	0.0000	3	1.0029(8)	0.01267(1)
<b>Ca1</b>	0.0000	0.0000	0.0000	3	0.0263(2)	0.01267(1)
<b>Fe1</b>	0.0000	0.0000	0.5000	3	1.0049(6)	0.01267(1)
<b>O1</b>	0.0000	0.0000	0.2432(6)	6	0.9809(4)	0.02131(1)

$\alpha$ -Na<sub>0.96</sub>Ca<sub>0.02</sub>FeO<sub>2</sub> – space group  $R\bar{3}m$

$a = b = 3.0216(1)$  Å;  $c = 16.0963(8)$  Å;  $\alpha = 90^\circ$ ;  $\beta = 90^\circ$ ;  $\gamma = 90^\circ$

$\chi^2 = 9.551$ ;  $R_{wp} = 6.340$  %;  $R_{exp} = 2.596$  %

%( $\alpha$ -Na<sub>0.96</sub>Ca<sub>0.02</sub>FeO<sub>2</sub>) = 99.6 wt%; %( $\beta$ -NaFeO<sub>2</sub>) = 0.4 wt%

The lattice parameters of  $\alpha$ -Na<sub>0.94</sub>Ca<sub>0.03</sub>FeO<sub>2</sub> were determined using Rietveld refinement, as shown in Figure 3.13. The refined parameters included zero error, lattice and profile parameters, atomic positions, and isotropic displacement parameters (*U*<sub>iso</sub>). The lattice parameters were determined to be  $a = b = 3.02169$  Å,  $c = 16.13789$  Å, and  $\alpha = \beta = \gamma = 90^\circ$ , which demonstrates a high degree of precision. The detailed refined parameters are listed comprehensively in Table 4.4 for further reference.

The goodness-of-fit ( $\chi^2$ ) value was 15.41, with the weighted profile R-factor ( $R_{wp}$ ) and the expected R-factor ( $R_{exp}$ ) calculated to be 3.930 and 1.98 %, respectively. Data collection was conducted in reflection mode, utilising conventional Cu K<sub>α1</sub> and Cu K<sub>α2</sub> sources, which had a noticeable influence on the refinement's quality and accuracy.

The material used for this and subsequent experimental analyses exhibits a purity of 94.0 wt%, with minor impurities consisting of  $\beta$ -NaFeO<sub>2</sub> (4.06 wt%) and Ca<sub>2</sub>Fe<sub>2</sub>O<sub>5</sub> (1.40

wt%). Interestingly, the c-axis of C<sub>3</sub>NFO is larger compared to that of C<sub>2</sub>NFO, which is contrary to expectations given the higher Ca<sup>2+</sup> content present in the material. This unexpected discrepancy may be linked to the goodness-of-fit parameters affecting the structural simulation or an unanticipated excess of calcium in the precursor mixture. Additionally, the presence of Ca<sub>2</sub>Fe<sub>2</sub>O<sub>5</sub> suggests a potential deficiency of sodium and a reorganisation of calcium and iron atoms within the structure. This particular impurity is detected exclusively in C<sub>3</sub>NFO and is absent in samples with higher calcium content, a phenomenon that remains unexplained and warrants further investigation

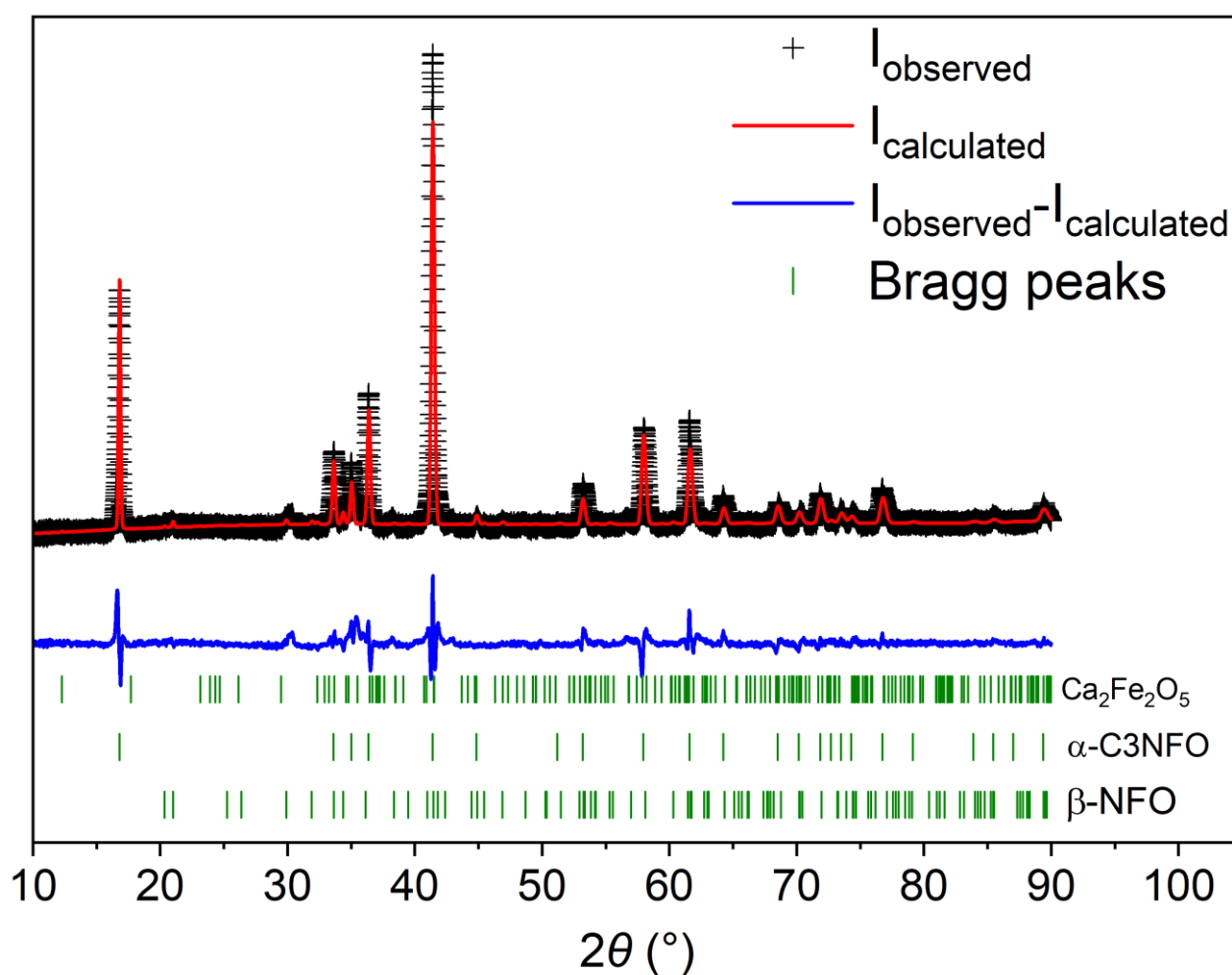


Figure 3.13 - Rietveld refinement of pristine  $\alpha\text{-Na}_{0.94}\text{Ca}_{0.03}\text{FeO}_2$

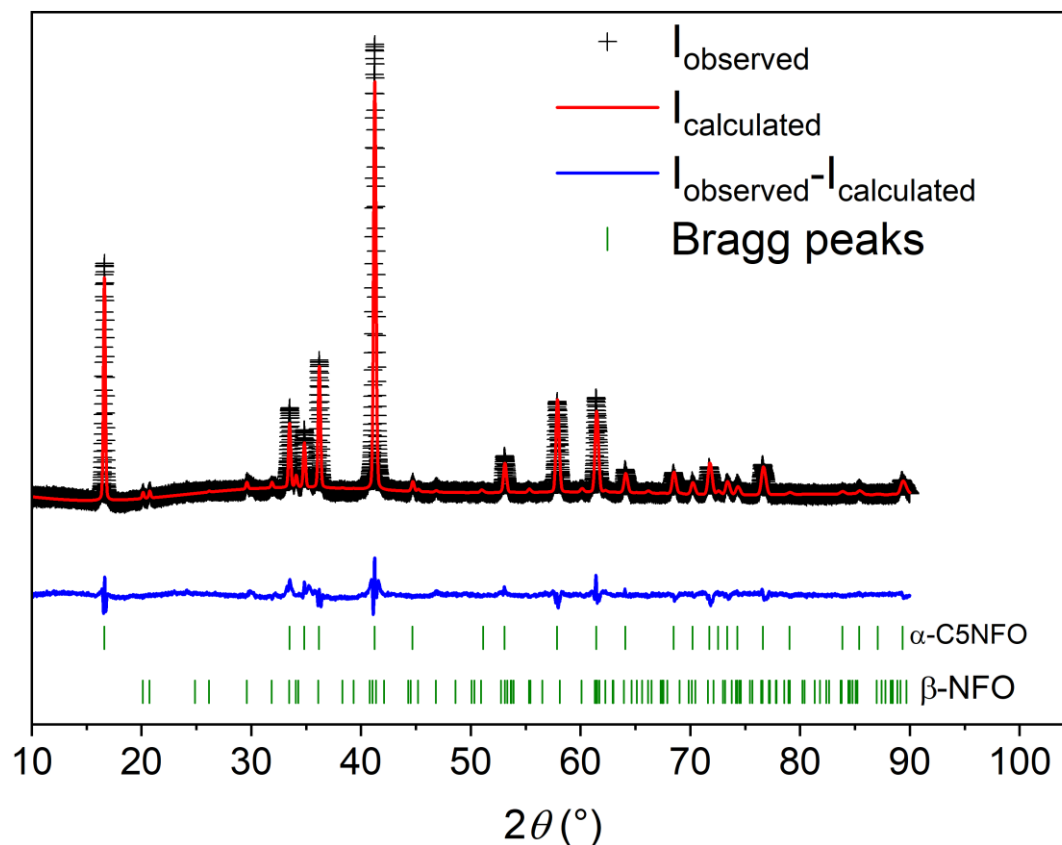
Table 3.3 - Cell parameters, goodness-of-fitness parameter and phase composition of  $\alpha$ -Na<sub>0.94</sub>Ca<sub>0.03</sub>FeO<sub>2</sub>, obtained from Rietveld refinements

Atom	X	y	Z	Multiplicity	Occupancy	$U_{iso}$ (Å <sup>2</sup> )
Na1	0.0000	0.0000	0.0000	3	0.9776(2)	0.01267(1)
Ca1	0.0000	0.0000	0.0000	3	0.0300(1)	0.01267(1)
Fe1	0.0000	0.0000	0.5000	3	0.9847(4)	0.01264(2)
O1	0.0000	0.0000	0.2372(3)	6	0.9919(2)	0.00645(3)

**$\alpha$ -Na<sub>0.94</sub>Ca<sub>0.03</sub>FeO<sub>2</sub> – space group  $R\bar{3}m$**   
 $a = b = 3.0216(9)$  Å;  $c = 16.1378(9)$  Å;  $\alpha = 90^\circ$ ;  $\beta = 90^\circ$ ;  $\gamma = 90^\circ$   
 $\chi^2 = 15.41$ ;  $R_{wp} = 3.930$  %;  $R_{exp} = 1.98$  %  
**%( $\alpha$ -Na<sub>0.94</sub>Ca<sub>0.03</sub>FeO<sub>2</sub>) = 94.0 wt%; %( $\beta$ -NaFeO<sub>2</sub>) = 4.06 wt%, Ca<sub>2</sub>Fe<sub>2</sub>O<sub>5</sub> = 1.40 wt%**

The lattice parameters of  $\alpha$ -Na<sub>0.90</sub>Ca<sub>0.05</sub>FeO<sub>2</sub> were determined using Rietveld refinement, as illustrated in Figure 3.14. The calculated lattice parameters are  $a = b = 3.02036$  Å,  $c = 16.06528$  Å, with  $\alpha = \beta = \gamma = 90^\circ$ , reflecting a high level of precision. These parameters are consistent with the unit cell dimensions reported in the literature, and the incorporation of dipositive Ca<sup>2+</sup> ions causes a reduction in the  $c$ -axis length compared to pristine NFO. Due to convergence issues encountered during the refinement, the occupancies were fixed to their expected theoretical values for reliability.

The goodness-of-fit ( $\chi^2$ ) value was 3.18, while the weighted profile R-factor ( $R_{wp}$ ) and expected R-factor ( $R_{exp}$ ) were calculated to be 1.673 and 1.254 %, respectively, indicating a satisfactory refinement quality. The material used for this and subsequent experimental investigations exhibits a purity of 94.7 wt%, with  $\beta$ -NaFeO<sub>2</sub> detected as a minor impurity constituting 5.30 wt% of the total material. This high level of purity ensures that the refined lattice parameters and other structural characteristics are representative of the primary phase and suitable for further analysis.

Figure 3.14 – Rietveld refinement of pristine  $\alpha$ - $\text{Na}_{0.90}\text{Ca}_{0.05}\text{FeO}_2$ Table 3.4 - Cell parameters, goodness-of-fitness parameter and phase composition of  $\alpha$ - $\text{Na}_{0.90}\text{Ca}_{0.05}\text{FeO}_2$ , obtained from Rietveld refinements

Atom	$x$	$Y$	$Z$	Multiplicity	Occupancy	$U_{iso}$ (Å <sup>2</sup> )
Na1	0.0000	0.0000	0.0000	3	1.0000(0)	0.01389(2)
Ca1	0.0000	0.0000	0.0000	3	0.0500(0)	0.00954(3)
Fe1	0.0000	0.0000	0.5000	3	1.0000(0)	0.00339(1)
O1	0.0000	0.0000	0.2357(1)	6	1.0000(0)	0.02169(2)

$\alpha$ - $\text{Na}_{0.90}\text{Ca}_{0.05}\text{FeO}_2$  – space group  $R\bar{3}m$

$a = b = 3.0203(6)$  Å;  $c = 16.0652(8)$  Å;  $\alpha = 90^\circ$ ;  $\beta = 90^\circ$ ;  $\gamma = 90^\circ$

$\chi^2 = 3.18$ ;  $R_{wp} = 1.673\%$ ;  $R_{exp} = 1.254\%$

%( $\alpha$ - $\text{Na}_{0.90}\text{Ca}_{0.05}\text{FeO}_2$ ) = 94.7 wt%; %( $\beta$ - $\text{NaFeO}_2$ ) = 5.30 wt%

The idealised structure of  $\alpha\text{-Na}_{(1-2x)}\text{Ca}_x\text{FeO}_2$  is illustrated in Figure 3.15. When replacing sodium for calcium, for each calcium ion added to the structure, two sodium ions are removed, resulting in a vacancy per calcium in the structure, resulting in the chemical formula of the calcium-pillared materials,  $\text{Na}_{(1-2x)}\text{Ca}_x\text{FeO}_2$ . This figure shows an alternation between (Na/Ca/□)-O-Fe-O layers along the *c*-axis. This is concomitant with the information in the literature. [21] One of the most significant impurities resulting from the calcination of  $\text{Na}_2\text{CO}_3$ ,  $\text{CaCO}_3$  and  $\text{Fe}_3\text{O}_4$  is  $\text{Ca}_2\text{Fe}_2\text{O}_5$  which belongs to the space group *Pcmn*, where Fe has 6 oxygens coordinated to it, in an octahedron, and Ca has 4 oxygens coordinated in a tetrahedron. Some of the oxygen molecules are shared with both Ca and Fe. [19]

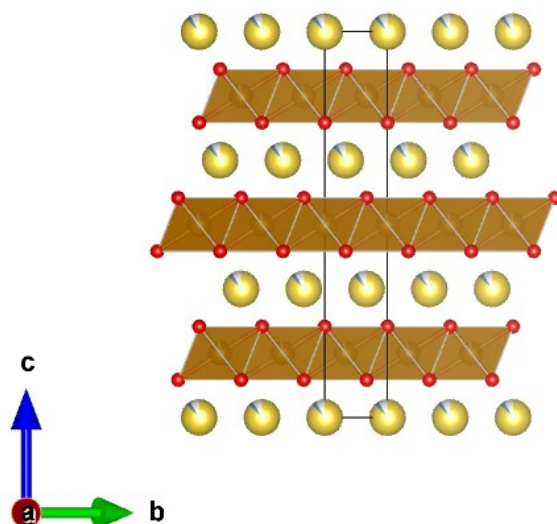


Figure 3.15 – Structure of  $\text{Na}_{(1-2x)}\text{Ca}_x\text{FeO}_2$  drawn with VESTA where the oxygen is marked in red, iron in brown, sodium in yellow and calcium in blue

With the replacement of two  $\text{Na}^+$  ions, there is a tendency for the distance between the (0 0 3) tends to decrease. This is due to the replacement of a monovalent ion with a bivalent ion. The ionic bond strength of a  $\text{Ca}^{2+}\text{-O}^{2-}$  is higher than that of  $\text{Na}^+\text{-O}^{2-}$  causing a contraction of the interlayer distance. We should take note of  $\text{C}_3\text{NFO}$ , which falls over the above-mentioned tendency (Figure 3.16). We should note that this material shows a  $\text{Ca}_2\text{Fe}_2\text{O}_5$  impurity, which may affect the calculations for structure optimisation and refinements.

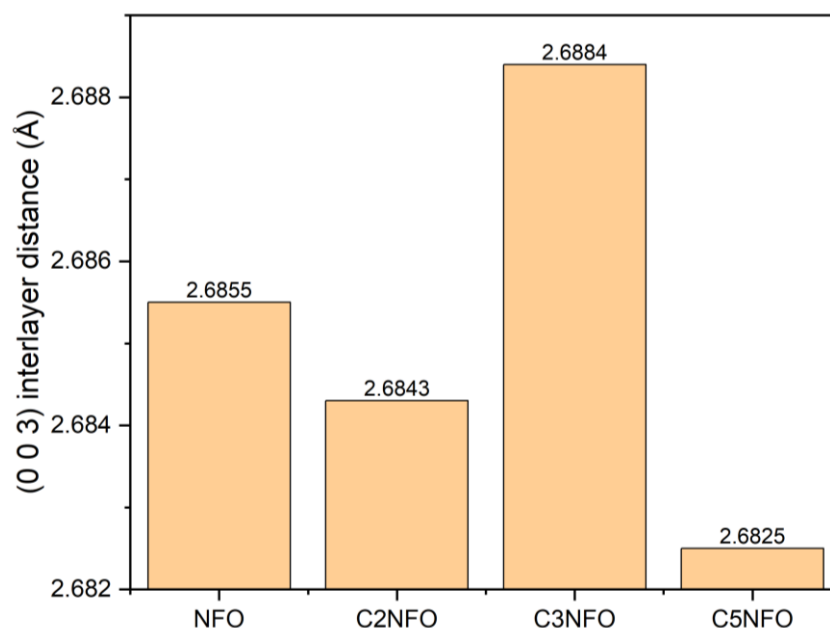
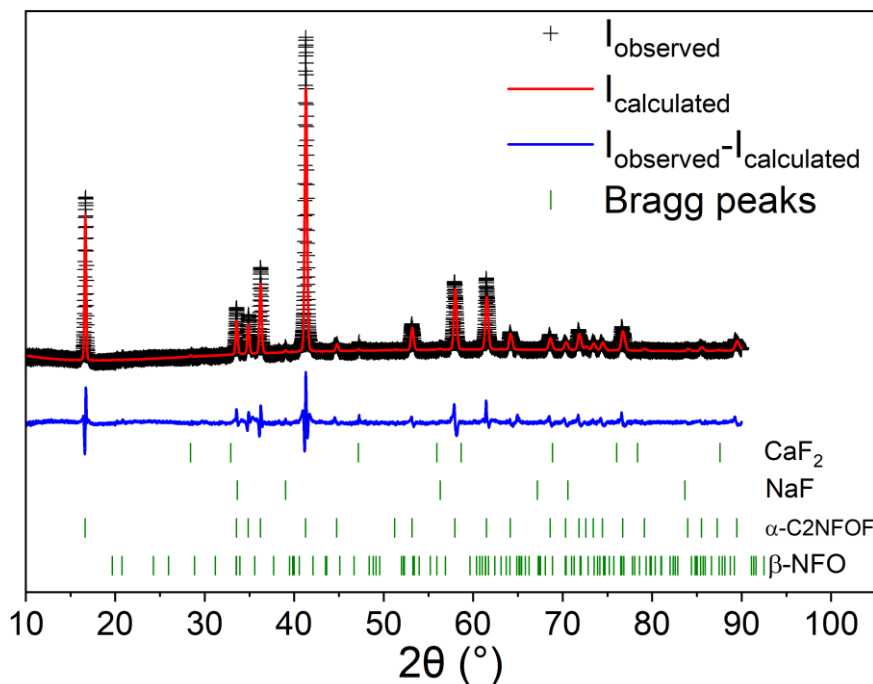


Figure 3.16 – (0 0 3) plane distance variation with Ca<sup>2+</sup>-doping of NFO

The lattice parameters of fluorinated  $\alpha$ -Na<sub>0.96</sub>Ca<sub>0.02</sub>FeO<sub>1.96</sub>F<sub>0.04</sub> were obtained using Rietveld refinement (Figure 3.17). The refined parameters included zero, lattice, and profile parameters, atomic positions, and isotropic displacement parameters ( $U_{iso}$ ). The lattice parameters were determined to be  $a = b = 3.01842 \text{ \AA}$ ,  $c = 16.07002 \text{ \AA}$ , and  $\alpha = \beta = \gamma = 90^\circ$ . These values are consistent with the expected results from replacing O<sup>2-</sup> with F<sup>-</sup>, as the  $c$ -axis length decreases compared to pristine NFO due to reduced electrostatic forces between Na<sup>+</sup>, Ca<sup>2+</sup>, and F<sup>-</sup>. Detailed refined parameters are listed in Table 4.5.

The goodness-of-fit ( $\chi^2$ ) was 7.78, while the weighted profile R-factor ( $R_{wp}$ ) and expected R factor ( $R_{exp}$ ) were 2.694% and 1.613%, respectively. Data collection was performed in reflection mode using conventional Cu K $\alpha_1$  and Cu K $\alpha_2$  sources, which influenced the refinement quality. The material used for these and subsequent experiments has a purity of 98.3 wt%, with impurities of  $\beta$ -NaFeO<sub>2</sub> at 0.2 wt%, NaF at 1.0 wt%, and CaF<sub>2</sub> at 0.6 wt% of the total material.

Figure 3.17 - Rietveld refinement of pristine  $\alpha\text{-Na}_{0.96}\text{Ca}_{0.02}\text{FeO}_{1.6}\text{F}_{0.04}$ Table 3.5 - Cell parameters, goodness-of-fitness parameter and phase composition of  $\alpha\text{-Na}_{0.96}\text{Ca}_{0.02}\text{FeO}_{1.6}\text{F}_{0.04}$ , obtained from Rietveld refinements

Atom	X	y	Z	Multiplicity	Occupancy	$U_{iso}$ (Å <sup>2</sup> )
Na1	0.0000	0.0000	0.0000	3	0.9668(3)	0.02988(4)
Ca1	0.0000	0.0000	0.0000	3	0.0595(2)	0.00270(2)
Fe1	0.0000	0.0000	0.5000(0)	3	1.0545(3)	0.00334(2)
O1	0.0000	0.0000	0.2360(1)	6	0.9145(3)	0.01054(3)
F1	0.0000	0.0000	0.2338(2)	6	0.0918(1)	0.09060(4)

$\alpha\text{-Na}_{0.96}\text{Ca}_{0.02}\text{FeO}_{1.92}\text{F}_{0.04}$  – space group  $R\bar{3}m$

$a = b = 3.0184(2)$  Å;  $c = 16.0700(2)$  Å;  $\alpha = 90^\circ$ ;  $\beta = 90^\circ$ ;  $\gamma = 90^\circ$

$\chi^2 = 7.78$ ;  $R_{wp} = 2.694$  %;  $R_{exp} = 1.613$  %

%( $\alpha\text{-Na}_{0.96}\text{Ca}_{0.02}\text{FeO}_{1.92}\text{F}_{0.04}$ ) = 98.3 wt%; %( $\beta\text{-NaFeO}_2$ ) = 0.2 wt%; %( $\text{NaF}$ ) = 1.0 wt%;

%( $\text{CaF}_2$ ) = 0.6 wt%

The lattice parameters were determined to be  $a = b = 3.01842 \text{ \AA}$ ,  $c = 16.07002 \text{ \AA}$ , and  $\alpha = \beta = \gamma = 90^\circ$ . These values agree with the unit cell parameters reported in the literature. Due to the replacement of O<sup>2-</sup> with F<sup>-</sup>, the  $c$ -axis length decreases compared to pristine NFO, a reduction attributed to the decreased electrostatic forces between Na<sup>+</sup>, Ca<sup>2+</sup>, and F<sup>-</sup>. However, the  $c$ -axis length is lower than that of C<sub>2</sub>NFOF, likely due to the higher Ca<sup>2+</sup> content, which increases electrostatic forces. Detailed refined parameters are listed in Table 4.6.

The goodness-of-fit ( $\chi^2$ ) was 2.90, while the weighted profile R-factor ( $R_{wp}$ ) and expected R factor ( $R_{exp}$ ) were 1.596% and 1.224%, respectively. Data collection was performed in reflection mode using conventional Cu K $\alpha_1$  and Cu K $\alpha_2$  sources, which influenced the refinement quality. The material used for these, and subsequent experiments has a purity of 99.8 wt%, with NaF and CaF<sub>2</sub> each constituting 0.1 wt% of the total material. Figure 3.18 shows a plot with the Rietveld refinement of  $\alpha$ -Na<sub>0.94</sub>Ca<sub>0.03</sub>FeO<sub>2</sub>

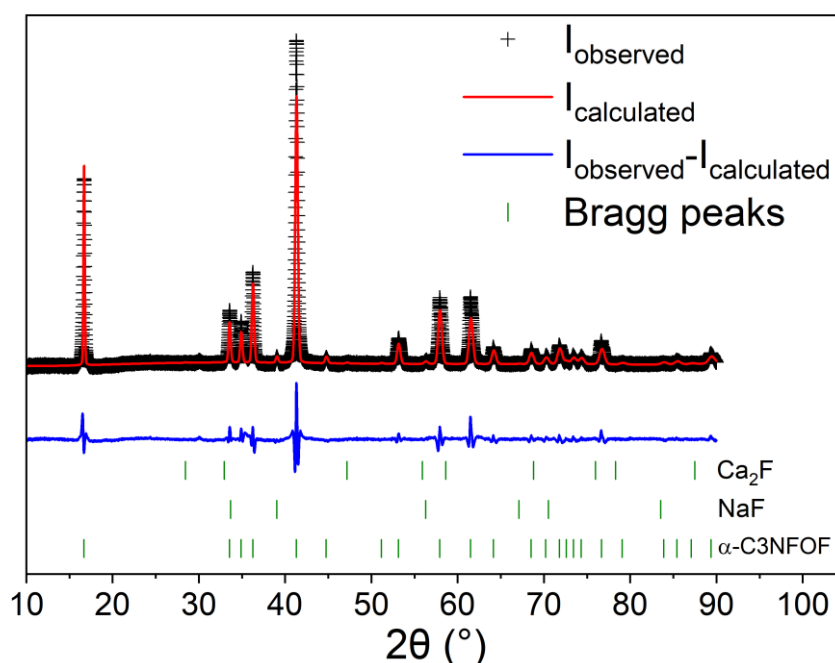


Figure 3.18 - Rietveld refinement of pristine  $\alpha$ -Na<sub>0.94</sub>Ca<sub>0.03</sub>FeO<sub>1.4</sub>F<sub>0.06</sub>

Table 3.6 - Cell parameters, goodness-of-fitness parameter and phase composition of  $\alpha$ -Na<sub>0.94</sub>Ca<sub>0.03</sub>FeO<sub>1.4</sub>F<sub>0.6</sub>, obtained from Rietveld refinements.

Atom	<i>x</i>	<i>y</i>	<i>Z</i>	Multiplicity	Occupancy	<i>U</i> <sub>iso</sub> (Å <sup>2</sup> )
<b>Na1</b>	0.0000	0.0000	0.0000	3	1.0423(5)	0.03702(3)
<b>Ca1</b>	0.0000	0.0000	0.0000	3	0.0320(3)	0.03840(2)
<b>Fe1</b>	0.0000	0.0000	0.5000(0)	3	0.9770(4)	0.00567(1)
<b>O1</b>	0.0000	0.0000	0.2354(2)	6	0.9150(2)	0.02141(2)
<b>F1</b>	0.0000	0.0000	0.2347(1)	6	0.0647(1)	0.00115(2)

**$\alpha$ -Na<sub>0.94</sub>Ca<sub>0.03</sub>FeO<sub>1.88</sub>F<sub>0.06</sub> – space group  $R\bar{3}m$**   
 $a = b = 3.0207(3)$  Å;  $c = 16.1029(5)$  Å;  $\alpha = 90^\circ$ ;  $\beta = 90^\circ$ ;  $\gamma = 90^\circ$   
 $\chi^2 = 2.90$ ;  $R_{wp} = 1.596\%$ ;  $R_{exp} = 1.224\%$   
**%( $\alpha$ -Na<sub>0.94</sub>Ca<sub>0.03</sub>FeO<sub>1.88</sub>F<sub>0.06</sub>) = 99.8 wt%; %(NaF) = 0.1 wt%; %(CaF<sub>2</sub>) = 0.1 wt%**

The lattice parameters of fluorinated  $\alpha$ -Na<sub>0.90</sub>Ca<sub>0.05</sub>FeO<sub>1.90</sub>F<sub>0.10</sub> were determined using Rietveld refinement, as shown in Figure 3.19. The refined parameters included zero error, lattice and profile parameters, atomic positions, and isotropic displacement parameters (*U*<sub>iso</sub>), ensuring a detailed and comprehensive analysis. The calculated lattice parameters were  $a = b = 3.02192$  Å,  $c = 16.13356$  Å, and  $\alpha = \beta = \gamma = 90^\circ$ , values that are in excellent agreement with the unit cell parameters reported in the literature.

The replacement of O<sup>2-</sup> with F<sup>-</sup> ions caused a noticeable decrease in the c-axis length compared to pristine NFO, attributed to the reduced electrostatic forces between Na<sup>+</sup>, Ca<sup>2+</sup>, and F<sup>-</sup>. This decrease in the c-axis length is consistent with the trend observed for materials with higher Ca<sup>2+</sup> content, which results in an increase in electrostatic forces within the crystal lattice. The detailed refined parameters for the structure are provided comprehensively in Table 4.7 for further reference.

The goodness-of-fit ( $\chi^2$ ) was 11.26, while the weighted profile R-factor ( $R_{wp}$ ) and expected R-factor ( $R_{exp}$ ) were 3.209% and 1.751%, respectively, demonstrating a reliable refinement with high-quality data. Data collection was carried out in reflection mode using conventional Cu K $\alpha_1$  and Cu K $\alpha_2$  sources, which significantly influenced the refinement quality due to their precise characteristics.

The material utilised for these and subsequent experimental studies exhibited a purity of 94.5 wt%, with minor impurities consisting of  $\beta$ -NaFeO<sub>2</sub> (0.8 wt%), NaF (3.5 wt%), and CaF<sub>2</sub> (1.2 wt%) of the total material. This high purity ensures that the refined lattice parameters accurately represent the primary phase, allowing for reliable comparisons and further characterisation.

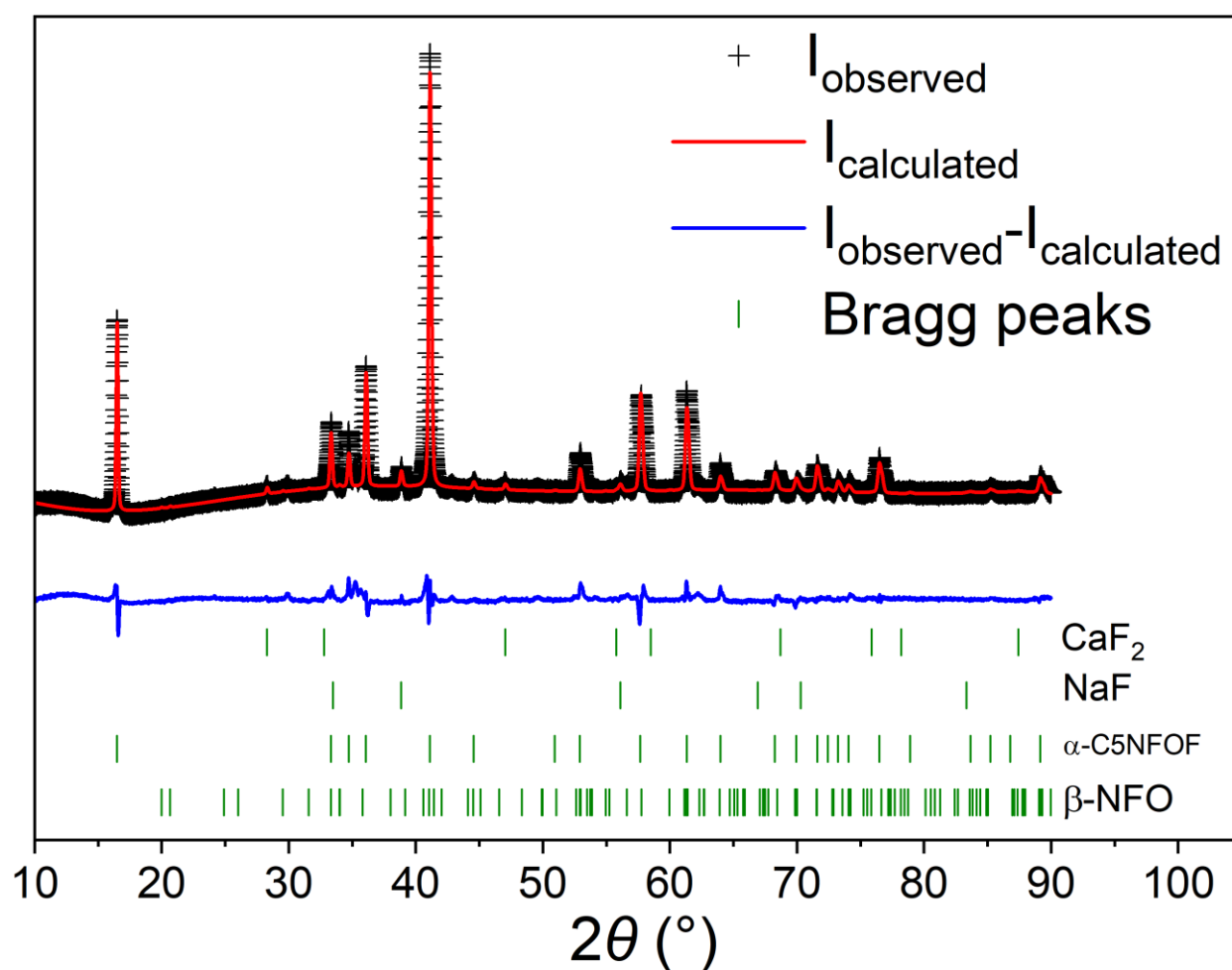


Figure 3.19 - Rietveld refinement of pristine  $\alpha$ -Na<sub>0.94</sub>Ca<sub>0.03</sub>Fe<sub>0.14</sub>Fo<sub>0.06</sub>

Table 3.7 - Cell parameters, goodness-of-fitness parameter and phase composition of  $\alpha$ -Na<sub>0.94</sub>Ca<sub>0.03</sub>FeO<sub>1.4</sub>F<sub>0.6</sub>, obtained from Rietveld refinements

Atom	<i>x</i>	<i>y</i>	<i>z</i>	Multiplicity	Occupancy	<i>U</i> <sub>iso</sub> (Å <sup>2</sup> )
Na1	0.0000	0.0000	0.0000	3	0.9000(1)	0.01267(0)
Ca1	0.0000	0.0000	0.0000	3	0.0506(2)	0.01267(0)
Fe1	0.0000	0.0000	0.5000(0)	3	0.8660(5)	0.01267(0)
O1	0.0000	0.0000	0.2385(3)	6	0.7323(4)	0.01267(0)
F1	0.0000	0.0000	0.2337(1)	6	0.1046(3)	0.01267(0)

**$\alpha$ -Na<sub>0.90</sub>Ca<sub>0.05</sub>FeO<sub>1.8</sub>F<sub>0.1</sub> – space group  $R\bar{3}m$**   
 $a = b = 3.0219(2)$  Å;  $c = 16.1335(6)$  Å;  $\alpha = 90^\circ$ ;  $\beta = 90^\circ$ ;  $\gamma = 90^\circ$   
 $\chi^2 = 11.26$ ;  $R_{wp} = 3.209$  %;  $R_{exp} = 1.751$  %  
 %( $\alpha$ -Na<sub>0.90</sub>Ca<sub>0.05</sub>FeO<sub>1.8</sub>F<sub>0.1</sub>) = 94.5 wt%; %( $\beta$ -NaFeO<sub>2</sub>) = 0.8 wt%; %(NaF) = 3.5 wt%;  
 %(CaF<sub>2</sub>) = 1.2 wt%

The idealised structure of  $\alpha$ -Na<sub>(1-2x)</sub>Ca<sub>x</sub>FeO<sub>(2-2x)</sub>F<sub>2x</sub> is illustrated in Figure 3.20. As in the case of  $\alpha$ -Na<sub>(1-2x)</sub>Ca<sub>x</sub>FeO<sub>2</sub>, when replacing sodium for calcium, for each calcium ion added to the structure, two sodium ions are removed, resulting in a vacancy per calcium, in the structure, resulting in the chemical formula of the calcium-pillared materials, Na<sub>(1-2x)</sub>Ca<sub>x</sub>□<sub>x</sub>FeO<sub>(2-2x)</sub>F<sub>2x</sub>. There is an indication that for each fluorine you replace only one oxygen. This may affect the oxidation state of the neighbouring iron atoms or form oxygen vacancies. This figure shows an alternation between (Na/Ca/□)-(O/F)-Fe-(O/F) layers along the *c*-axis.

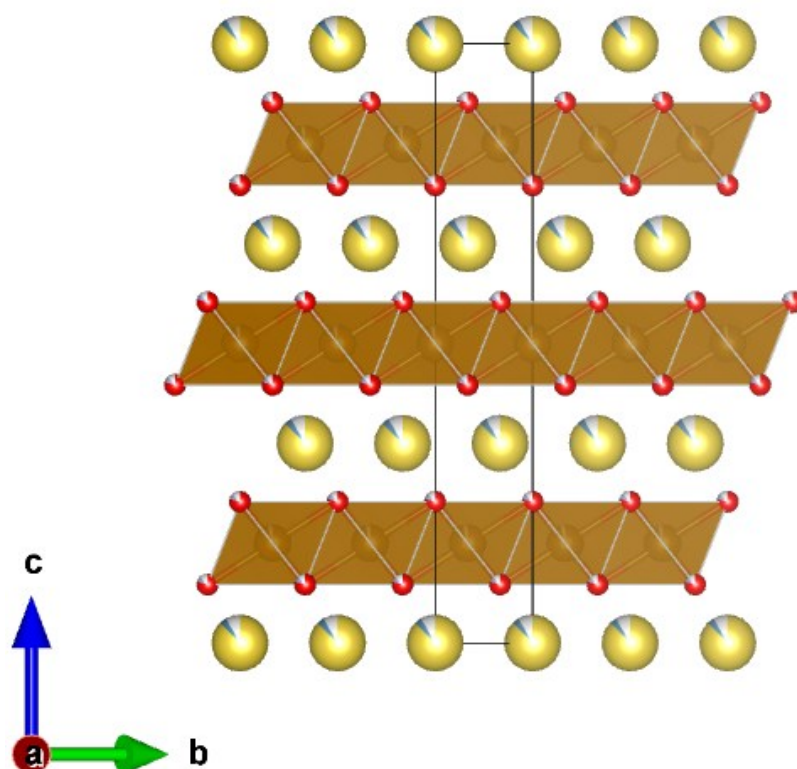


Figure 3.20 – Structure of  $\text{Na}_{(1-2x)}\text{Ca}_x\text{FeO}_{(2-2x)}\text{F}_{2x}$  drawn with VESTA where the oxygen is marked in red, iron in brown, sodium in yellow, calcium in blue and fluorine is on dark grey

We observe two competing phenomena with the dual substitution of two Na<sup>+</sup> ions for calcium and one O<sup>2-</sup> for one F<sup>-</sup> ion. On the one hand, the replacement of sodium with calcium leads to a reduction of the (0 0 3) interlayer distance due to the increased ionic bond strength. On the other hand, the replacement of O<sup>2-</sup> with F<sup>-</sup> is expected to cause an expansion of the interlayer distance (Figure 3.21), as the ionic bond strength of Na<sup>+</sup>-O<sup>2-</sup> is typically higher than that of Na<sup>+</sup>-F<sup>-</sup> due to differences in electrostatic forces.

Considering this information, at 2 calcium doping and 4 % fluorine doping, the dominant phenomenon is the contraction caused by the stronger electrostatic forces resulting from calcium substitution. However, as doping levels increase to 3 and 5 %, the reduction in electrostatic forces introduced by fluorine substitution becomes the larger contributor, leading to an expansion of the interlayer distance. This trend highlights the complex interplay

between calcium and fluorine doping in controlling the material's structural behaviour and interlayer spacing.

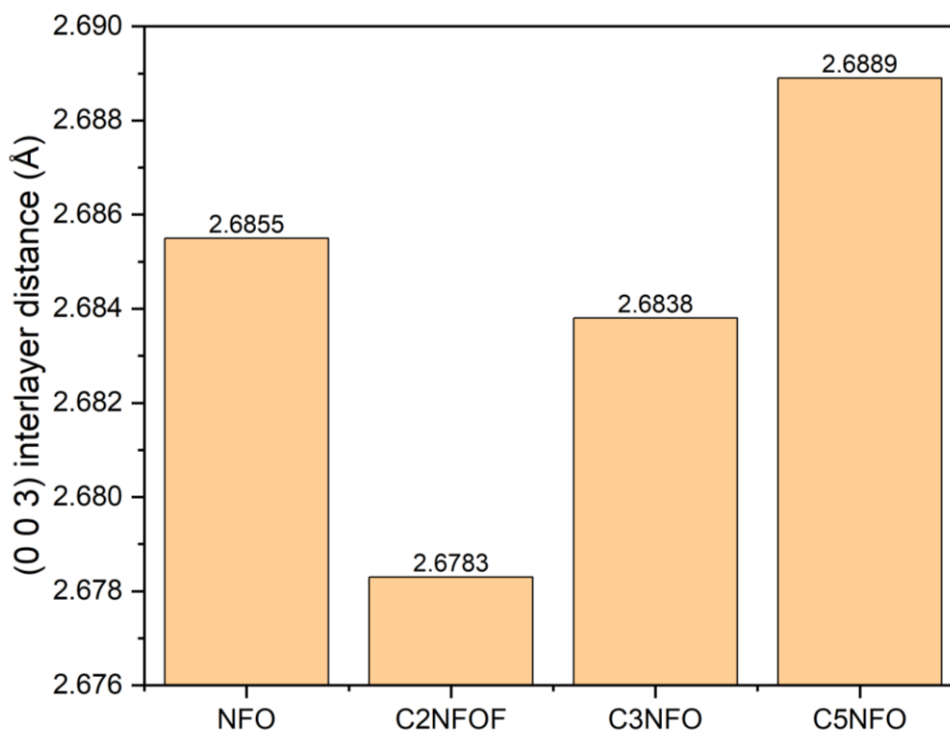


Figure 3.21 - (0 0 3) plain distance variation with Ca<sup>2+</sup> and F<sup>-</sup> -doping of NFO

### 3.3.3. Morphology and composition

To assess and compare the morphology of  $\alpha$ -NaFeO<sub>2</sub>, field emission electron microscopy (FESEM) was carried out. The morphology of  $\alpha$ -NaFeO<sub>2</sub> consists of highly agglomerated particles with approximately 500 nm diameter. This is in agreement with the previously reported data in the literature. [17], [18], [22] Elemental analysis with EDS, shown in Figure 3.22 confirms that Na, Fe, and O elements are present in the sample. These findings are consistent with those reported in the literature, in which the solid-state reaction method was used. [17], [18], [21]

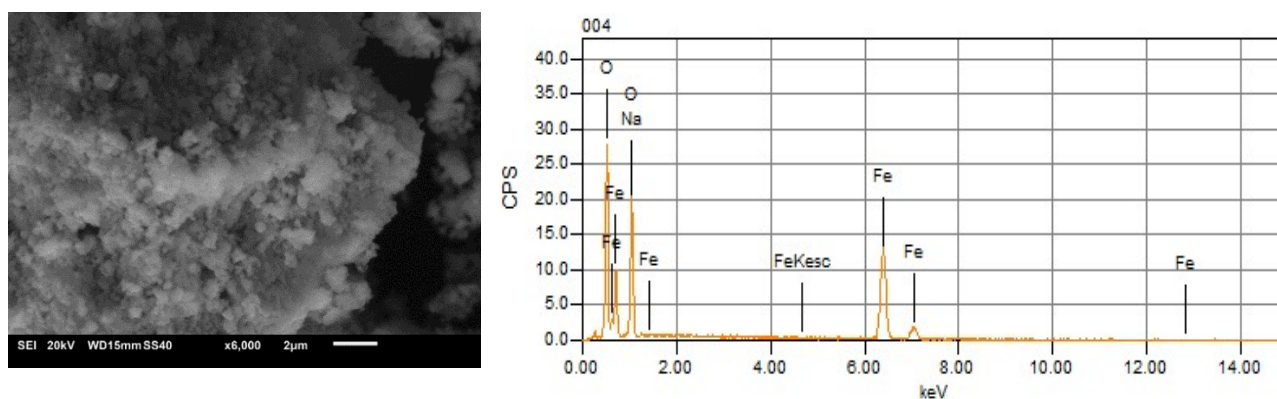


Figure 3.22 – image of a SEM microscopy of pristine  $\alpha$ -NaFeO<sub>2</sub> at a  $\times 6000$  amplification (left) and elemental analysis from EDS of  $\alpha$ -NaFeO<sub>2</sub> (right)

As in  $\alpha$ -NaFeO<sub>2</sub>, field emission electron microscopy (FESEM) was carried out on the  $\alpha$ -Na<sub>0.9</sub>Ca<sub>0.05</sub>FeO<sub>2</sub> and  $\alpha$ -Na<sub>0.90</sub>Ca<sub>0.05</sub>FeO<sub>1.90</sub>F<sub>0.10</sub> samples (Figure 3.23). The morphology of  $\alpha$ -Na<sub>0.9</sub>Ca<sub>0.05</sub>FeO<sub>2</sub> also consists of highly agglomerated spheres with approximately 500 nm diameter. This is in agreement with what was previously reported in the literature. Elemental analysis with EDS confirms that Na, Fe, Ca and O elements are present in the sample. These findings are consistent with what was expected after doping  $\alpha$ -NaFeO<sub>2</sub>, as calcium was added to the precursor mixture and no calcium anticipated losses.

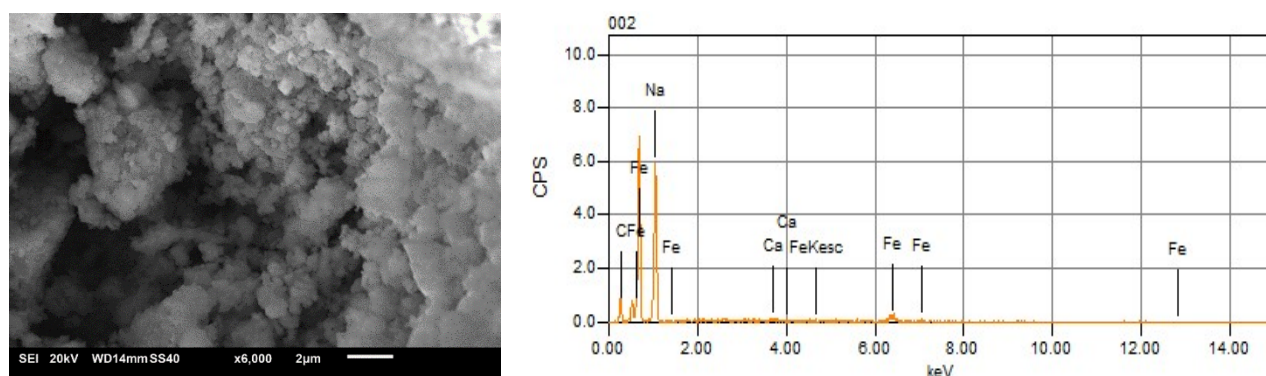


Figure 3.23 - Image of an SEM microscopy of pristine  $\alpha$ -Na<sub>0.90</sub>Ca<sub>0.05</sub>FeO<sub>2</sub> at a  $\times 6000$  amplification (left) and elemental analysis from EDS of  $\alpha$ -Na<sub>0.90</sub>Ca<sub>0.05</sub>FeO<sub>2</sub>

The morphology of  $\alpha$ -Na<sub>0.9</sub>Ca<sub>0.05</sub>FeO<sub>1.9</sub>F<sub>0.1</sub> consists of amorphous particles with approximately 2.5  $\mu$ m diameter, with larger blocks, probably caused by poor grinding

(Figure 3.24). Elemental analysis with EDS confirms that Na, Fe, Ca and O elements are present in the sample, but not F, probably due to overlap with the Fe peak. [23]

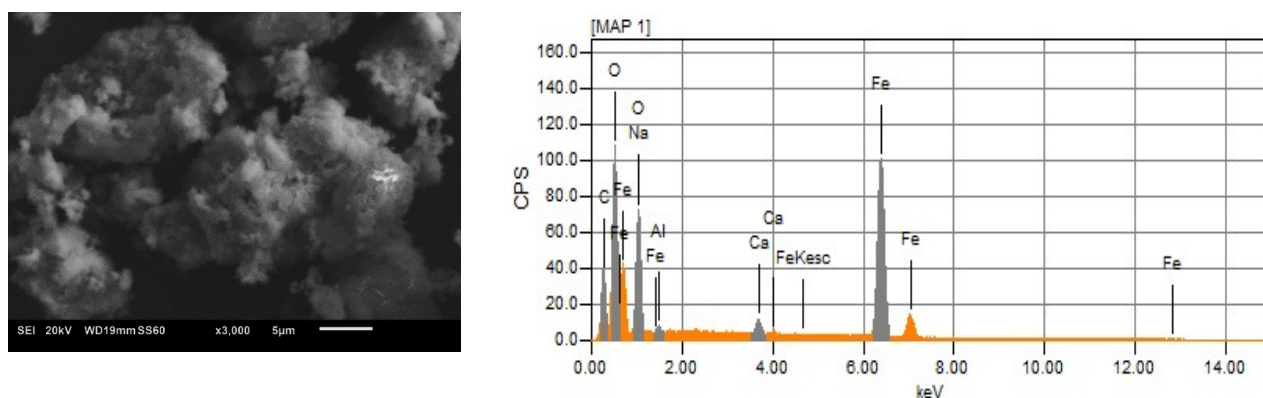


Figure 3.24 - Image of an SEM microscopy of pristine  $\alpha$ -Na<sub>0.90</sub>Ca<sub>0.05</sub>FeO<sub>1.9</sub>F<sub>0.1</sub> at a  $\times 6000$  amplification (left) and elemental analysis from EDS of  $\alpha$ -Na<sub>0.90</sub>Ca<sub>0.05</sub>FeO<sub>1.9</sub>F<sub>0.1</sub> (right)

### 3.4. Electrochemical performance

In the section, various electrochemical techniques were applied to investigate the electrochemical performance of  $\alpha$ -NaFeO<sub>2</sub> and all the calcium-pillared and fluorinated iterations as cathodes for sodium batteries. These included galvanostatic measurements, cyclic-voltammetry, *operando* X-ray diffraction, and galvanostatic intermittent titration technique. The composition of the electrodes was 80 wt% active material, 10 wt% carbon super-P conductor and, 9.9 wt% PVDF binder. The remaining 0.1 wt% is oxalic acid. Oxalic acid is added to the mixture to avoid the elimination reaction, which may form cross-links between the PVDF chains, causing gelation which affects the quality of the electrodes produced. A slurry pH higher than 8 promotes this H-F elimination reaction and the formation of cross-links. [24]

#### 3.4.1 Optimisation of cycling window

The selection and appropriate cycling conditions are crucial to ensure the stability of the components of the battery, especially the electrodes, avoiding any irreversible reactions. Specifically, for  $\alpha$ -NaFeO<sub>2</sub>, the electrochemical active transition metal pair is Fe(III)  $\rightleftharpoons$  Fe(IV)

and at a potential higher than 3.5 V *vs* Na<sup>+</sup>/Na, the capacity extracted from this material is not linked to the Fe(II)/Fe(IV) redox pair. [25] Electrodes were cycled on half-cells with sodium-metal as the counter electrode, from 2.0 to 3.5 V, 2.0 to 3.8 V, and 2.0 to 4.0 V *vs* Na<sup>+</sup>/Na at 0.1 C. The initial capacity was 91, 99 and 130 mA h g<sup>-1</sup> however, the capacity after 60 cycles becomes 50, 15 and 15 mA h g<sup>-1</sup> Figure 3.25).

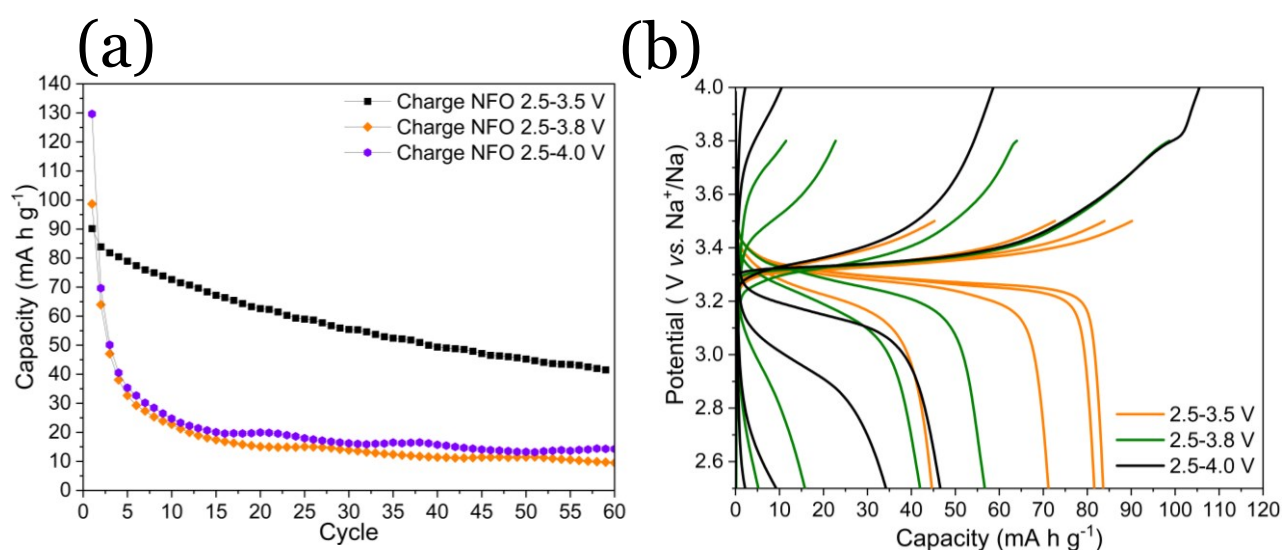


Figure 3.25 – Capacity over cycling of  $\alpha$ -NaFeO<sub>2</sub> at potential windows from 2.5-3.5, 2.5-3.8 and 2.5-4.0 V *vs* Na<sup>+</sup>/Na (a) and galvanostatic curves of  $\alpha$ -NaFeO<sub>2</sub> at potential windows from 2.5-3.5, 2.5-3.8 and 2.5-4.0 V *vs* Na<sup>+</sup>/Na (b)

Extending the potential window on which the cathode is cycled helps extract more capacity, however, this has a deleterious effect on the capacity retention. The initial capacity of NFO is 130, 99 and 91 mA h g<sup>-1</sup> for the potential range of 2.5-4.0, 2.5-3.8 and 2.5-4.0 V *vs* Na<sup>+</sup>/Na. At potential ranges of 2.5-3.8 and 2.5-4.0 V *vs* Na<sup>+</sup>/Na, the capacity rapidly falls to below 20 mA h g<sup>-1</sup>, probably related to irreversible oxygen oxidation, indicated in the *plateau* observed at approximately at 3.8 V *vs* Na<sup>+</sup>/Na. In Figure 3.26, the cyclic-voltammetry of  $\alpha$ -NaFeO<sub>2</sub> at different potential windows is shown

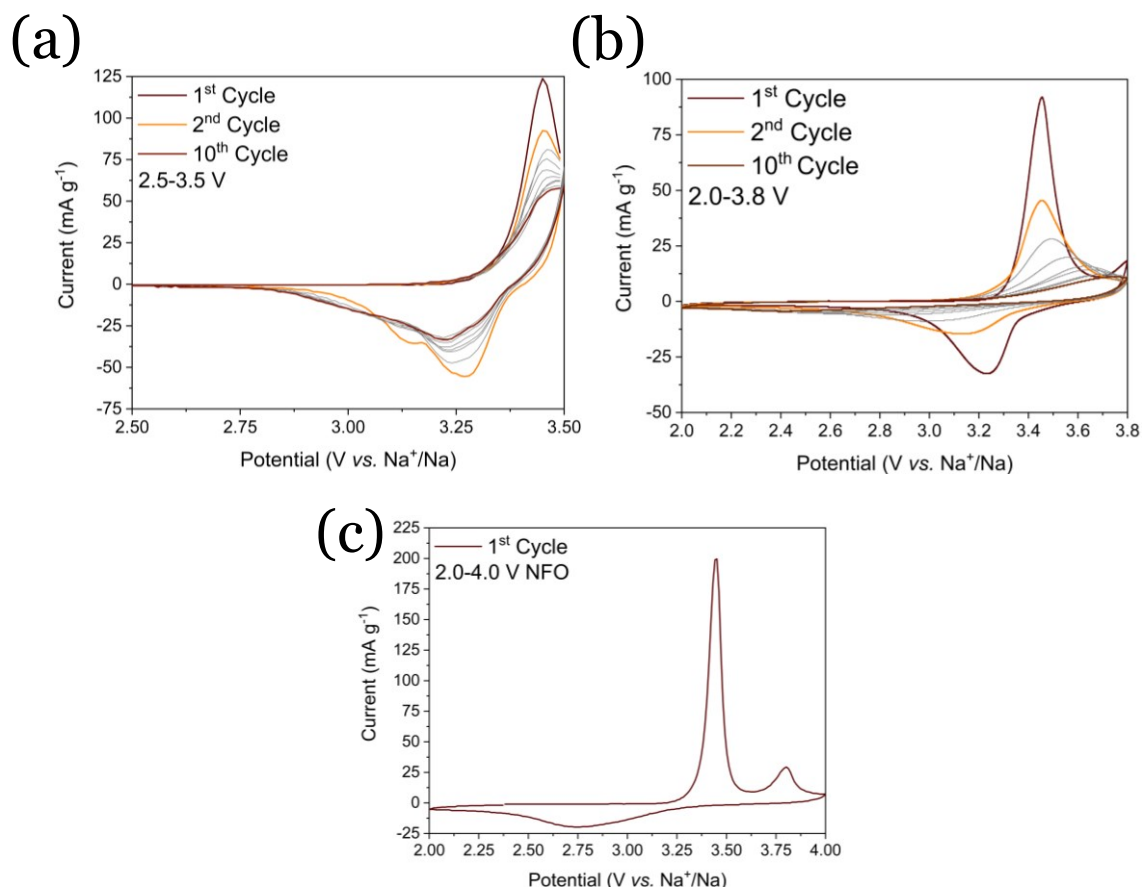


Figure 3.26 – Cyclic-voltammetry of  $\alpha$ -NaFeO<sub>2</sub> at 2.5-3.5 (a), 2.0-3.8 (b) and 2.0-4.0 V vs Na<sup>+</sup>/Na (c)

The cyclic-voltammetry done between 2.0 and 3.5 V vs Na<sup>+</sup>/Na shows one cathodic peak and two anodic peaks, all associated with the oxidation and reduction of Fe(III)  $\rightleftharpoons$  Fe(IV), respectively. [17] The duplication of the anodic is likely related to a two-step sodium insertion, or the existence of a meta-stable partially desodiated phase. [17], [18] From the second cycle to the tenth cycle, the intensity of the peaks tends to diminish, which is in accordance with some capacity loss observed in the galvanostatic measurements. The cyclic-voltammetry done between 2.0 and 3.8 V vs Na<sup>+</sup>/Na, shows the same peaks expected for the Fe(III)  $\rightleftharpoons$  Fe(IV) redox pair. However, from 3.7 V vs Na<sup>+</sup>/Na, there is an increase of the current on the cathodic, indicating an irreversible phenomenon occurring from this potential. This phenomenon has a nefarious effect on the material's capacity given that the following cycles show a poorer reversibility of the Fe(III)  $\rightleftharpoons$  Fe(IV) reaction with an impact on capacity

retention as observed in Figure 3.27b. Finally, the analysis run between 2.0 and 4.0 V vs Na<sup>+</sup>/Na, shows a strong peak at ~3.4 V vs Na<sup>+</sup>/Na, which was already attributed to the oxidation of Fe(III) to Fe(IV) however, its anodic counterpart appears at 2.75 V vs Na<sup>+</sup>/Na with a much lower current compared to other experimental condition, as seen in Figure 3.27c. This shows a very diminute capacity retention of  $\alpha$ -NaFeO<sub>2</sub> when cycled at these potentials. At this condition, we can also observe a cathodic peak with its maximum at ~3.8 V vs Na<sup>+</sup>/Na, without an anodic counterpart, similar to that that starts forming at 3.7 V vs Na<sup>+</sup>/Na. This is ascribed in the literature to irreversible iron migration, caused by oxygen oxidation ( $2\cdot\text{O}^{2-} \rightarrow \text{O}_2$ ). [17], [25], [26] In Figure 3.27, a proposal of the relative iron migration occurring in desodiation levels higher than  $x = 0.5$  by Saurel, *et al.* and a reaction diagram of the reversible sodiation and desodiation and the irreversible desodiation occurring at potential higher than 3.5 V vs Na<sup>+</sup>/Na or under contact with oxygen, water or carbon dioxide. [17], [26]

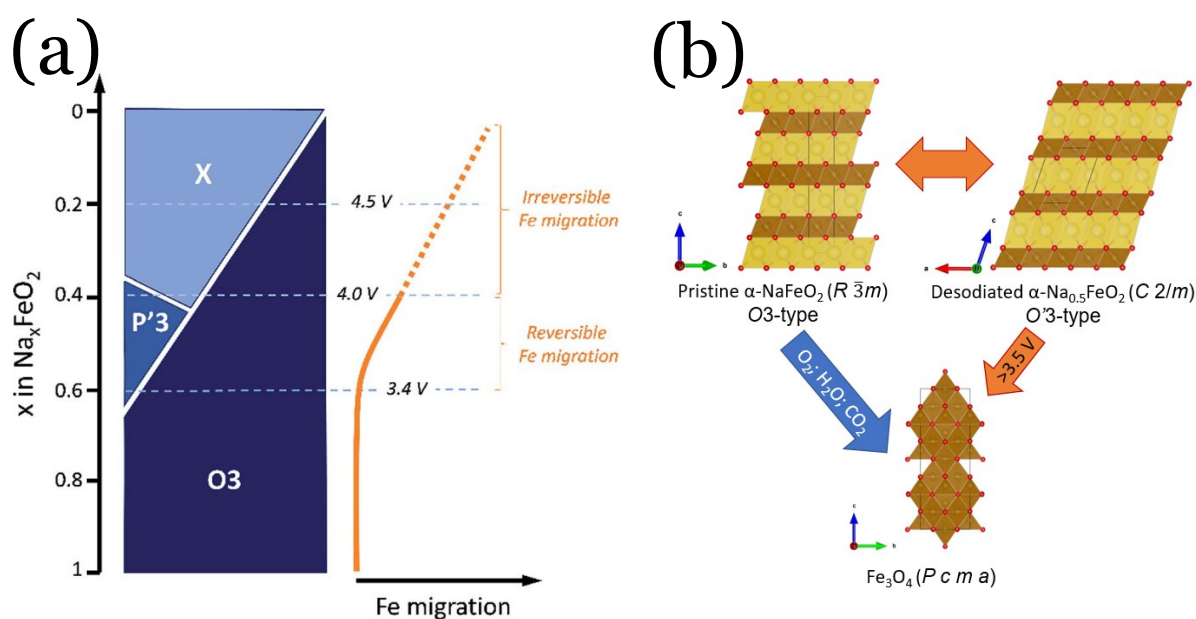


Figure 3.27 – Relative rate of iron migration related to the sodium content (a) and phase conversion during charge and degradation at higher potential (b) in  $\alpha$ -NaFeO<sub>2</sub> [17]

### 3.4.2. Galvanostatic measurements

The pristine and doped material were tested in coin cells from 2.0-3.5 V vs Na<sup>+</sup>/Na for 100 cycles at a cycling rate of 0.1 C and for 10 cycles at 0.1 C, 0.2 C, 0.5 C, 1 C, 2 C, 5 C, 10 C and back to 0.1 C, totalling 80 cycles. In Figure 3.28, The cycling performance, coulombic efficiency, mean potential, the first cycle potentiostatic curves and the cycling at different rates of NFO, C<sub>3</sub>NFO and C<sub>5</sub>NFO are shown.

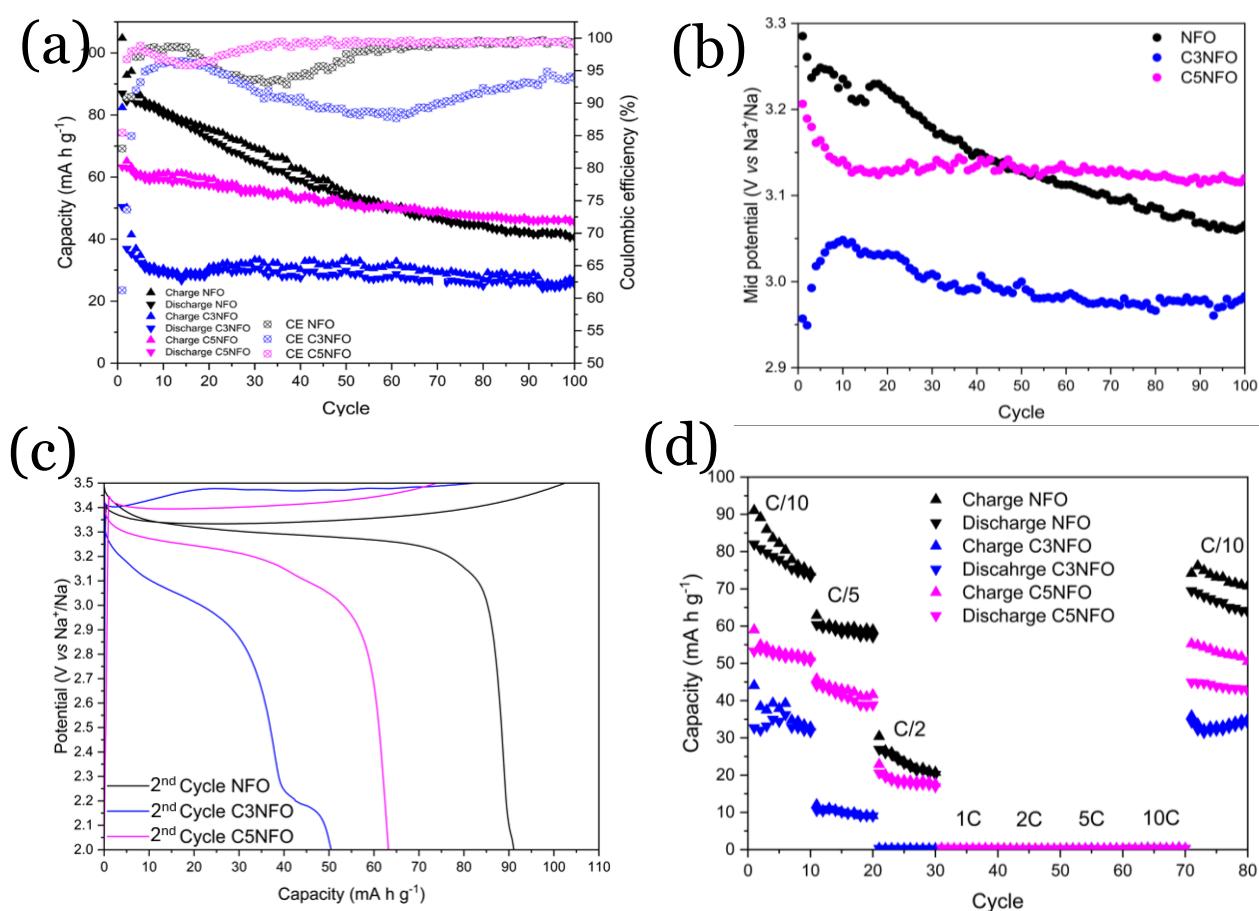
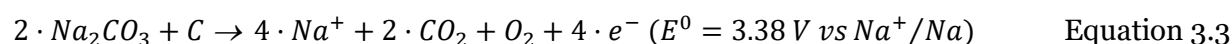
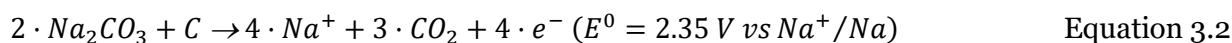


Figure 3.28 – Capacity and Coulombic efficiency over cycling in NFO, C<sub>3</sub>NFO and C<sub>5</sub>NFO (a), mid-potential over cycling in NFO, C<sub>3</sub>NFO and C<sub>5</sub>NFO (b), galvanostatic curves of the 2<sup>nd</sup> cycle of NFO, C<sub>3</sub>NFO and C<sub>5</sub>NFO (c) and, cycling at faster rates of NFO, C<sub>3</sub>NFO and C<sub>5</sub>NFO (d)

As observed in Figure 3.29a, the initial capacity of NFO, C<sub>3</sub>NFO and C<sub>5</sub>NFO is 105, 82 and 68 mA h g<sup>-1</sup>, which is what was expected since the initially available sodium decreases as the amount of calcium increases. In the following cycles, both NFO and C<sub>3</sub>NFO capacity

drastically decrease relatively quickly. This indicated that 3 % calcium pillaring may not be enough to stabilise the layers and increase capacity retention. When doping NFO with 5 % calcium doping, the capacity retention is higher than that of NFO and C<sub>3</sub>NFO so that the capacity of C<sub>5</sub>NFO surpasses the of pristine NFO after the 60<sup>th</sup> cycle. With the calcium doping, the mid-*plateau* tends to be more stable over 100 cycles and the 5 % doping shows a higher mid potential than the 3 %. This indicated that the 5 % doped material can deliver a higher energy than the 3 % doped in a more sustained manner than pristine material.

In Figure 3.29, The cycling performance, coulombic efficiency, mean potential, the second cycle potentiostatic curves and the cycling at different rates of NFO, C<sub>3</sub>NFOF and C<sub>5</sub>NFOF. The three materials show two *plateaux*, a main one at approximately 3.35 V *vs* Na<sup>+</sup>/Na and 3.25 V *vs* Na<sup>+</sup>/Na. Adding to that, C<sub>3</sub>NFO and C<sub>5</sub>NFO show an extra *plateau* at 2.2 V *vs* Na<sup>+</sup>/Na, probably related to the decomposition of Na<sub>2</sub>CO<sub>3</sub> which is in higher content in the doped materials than on the pristine materials. This Na<sub>2</sub>CO<sub>3</sub> content is not detected in the Rietveld refinement. This may come from interlayer sodium reactions with CO<sub>2</sub> at the particle surface, between structural measurements and cell assembly. [14] The sodium carbonate electrochemical decomposition equation, catalysed by carbon dioxide is shown in Equation 3.1, 3.2, and 3.3. [14]



Regarding these materials' performance at faster charge and discharge rates, at 3 % calcium-doping, shows a decrease in rate capability however at 5 % calcium-doping seems to allow better sodium conduction as it has a better rate capability. From 1 C to 10 C NFO and

C<sub>5</sub>NFO show no extractable capacity. This happens in C<sub>3</sub>NFO from 0.5 C to 10 C, where no capacity is extractable. Returning to a slower rate, all materials recover their extracted capacity, showing that these faster rates did not accelerated the degradation of any of the materials.

In Figure 3.29, The cycling performance, coulombic efficiency, mean potential, the first cycle potentiostatic curves and the cycling at different rates of NFO, C<sub>3</sub>NFOF and C<sub>5</sub>NFOF.

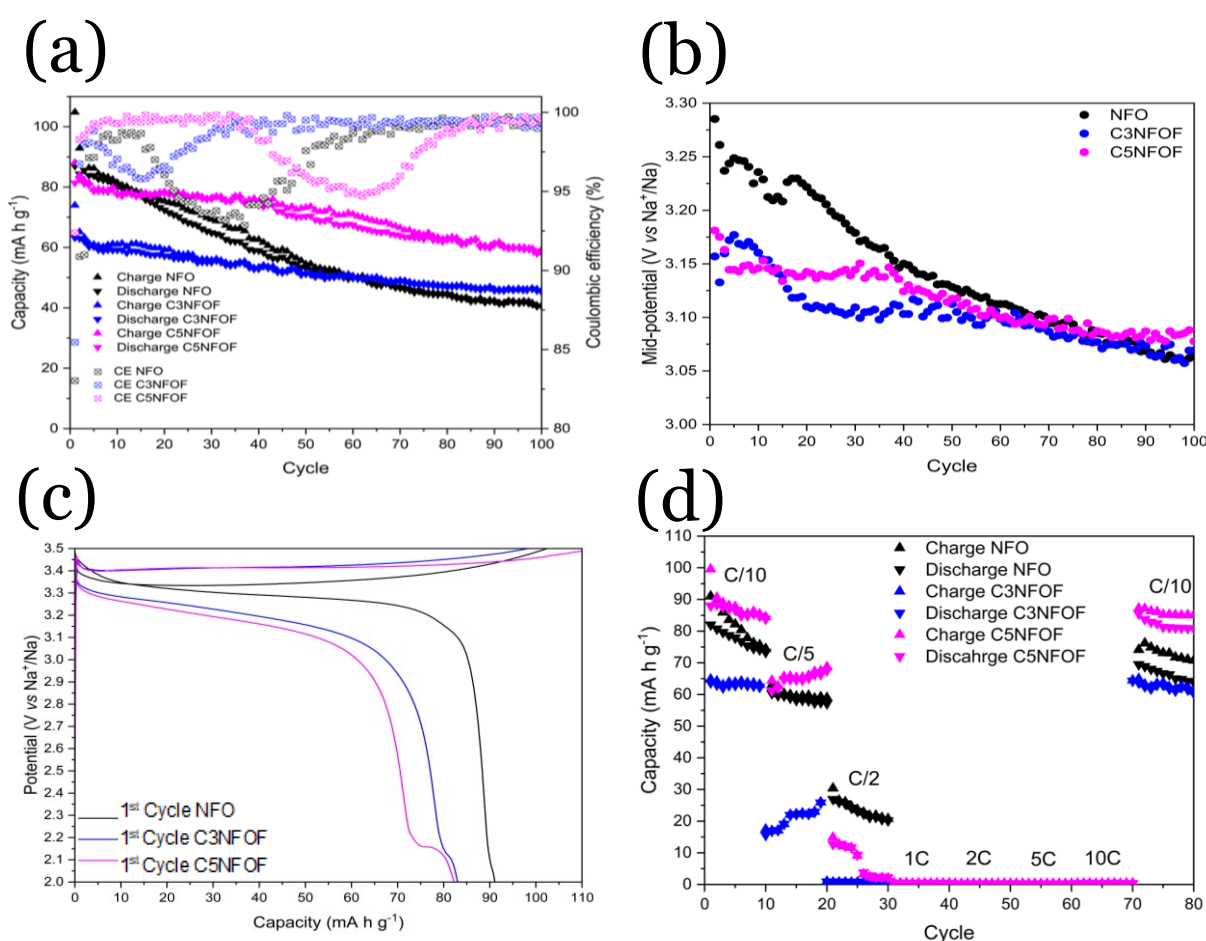


Figure 3.29 - Capacity and Coulombic efficiency over cycling in NFO, C<sub>3</sub>NFOF and C<sub>5</sub>NFOF (a), mid-potential over cycling in NFO, C<sub>3</sub>NFOF and C<sub>5</sub>NFOF (b), galvanostatic curves of the 2<sup>nd</sup> cycle of NFO, C<sub>3</sub>NFO and C<sub>5</sub>NFO (c) and, cycling at faster rates of NFO, C<sub>3</sub>NFOF and C<sub>5</sub>NFOF (d)

We can observe from Figure 3.29 that the initial capacity of NFO, C<sub>3</sub>NFOF and C<sub>5</sub>NFOF is 105, 68 and 89 mA h g<sup>-1</sup>, which, as in the case of the non-fluorinated compounds,

is what was expected since the initially available sodium decreases as the amount of calcium increases. On the following cycles, both C<sub>3</sub>NFOF and C<sub>5</sub>NFOF show a better capacity retention of the pristine material being that after 15 cycles for C<sub>5</sub>NFO and 60 cycles for C<sub>3</sub>NFOF, the capacity of the doped and fluorinated materials surpasses that of the pristine material. The three materials show two *plateaux*, a main one at approximately 3.35 V *vs* Na<sup>+</sup>/Na and 3.25 V *vs* Na<sup>+</sup>/Na. Adding to that, C<sub>3</sub>NFO and C<sub>5</sub>NFO show an extra *plateau* at 2.2 V *vs* Na<sup>+</sup>/Na, probably related to the decomposition of Na<sub>2</sub>CO<sub>3</sub> which may be in higher content in the doped materials than on the pristine materials. [14]

These materials' performance at faster charge and discharge rates, at 3 % calcium-doping and fluorinated, shows a decrease in rate capability however at 5 % calcium-doping allows better sodium conduction as it has a better rate capability, even better than the pristine materials. From 1 C to 10 C NFO and C<sub>5</sub>NFO show no extractable capacity. This happens in C<sub>3</sub>NFO from 0.5 C to 10 C, where no capacity is extractable. Such as in the case of the non-fluorinated materials, returning to a slower rate, all materials recover their extracted capacity, showing that these faster rates did not have a deleterious effect on the materials.

All the materials show a dip in the Coulombic efficiency from approximately 98 % to 95 %, followed by a full recuperation. This is probably related to a decrease in temperature in the analysis room during the building closure when the central heating was turned off.

### 3.4.3. Cyclic-voltammetry

Cyclic-voltammetry was run in all fluorinated and non-fluorinated calcium doping iterations at, 0.1, 0.2, 0.5, and 1.0 mV s<sup>-1</sup> for five cycles, to evaluate the stability and sodium diffusion. In Figure 3.30, the voltammogram of the first five cycles of pristine NFO at 0.1 mV s<sup>-1</sup> and the second cycles of all measured rates is shown.

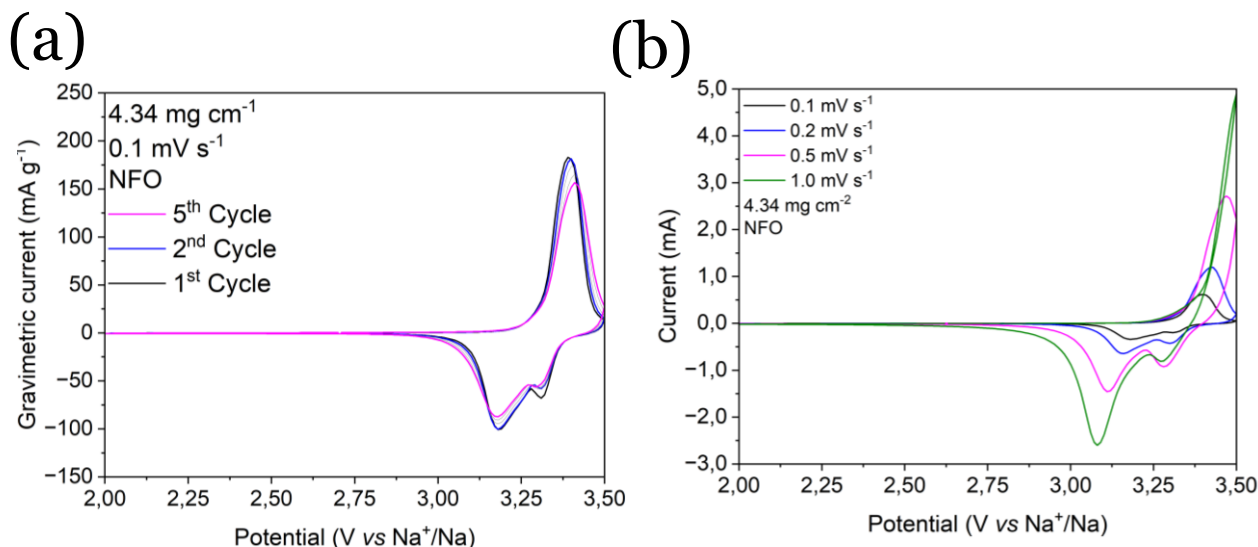


Figure 3.30 - Cyclic-voltammetry at  $0.1 \text{ mV s}^{-1}$  over 5 cycles (a) and cyclic-voltammetry at the 2<sup>nd</sup> cycle at a scan rate of  $0.1$ ,  $0.2$ ,  $0.5$  and  $1.0 \text{ mV s}^{-1}$  (b) of NFO

The voltammogram, measured at a scan rate of  $0.1 \text{ mV s}^{-1}$ , shows a small decay in the maximum anodic and cathodic currents with cycling, which aligns with the behaviour expected from the galvanostatic data. The voltammogram exhibits a cathodic peak at approximately  $\sim 3.35 \text{ V vs Na}^+/\text{Na}$  and two anodic peaks at  $\sim 3.30$  and  $\sim 3.20 \text{ V vs Na}^+/\text{Na}$ . These peaks are characteristic of the  $\text{Fe(III)} \rightleftharpoons \text{Fe(IV)}$  redox pair, which has an  $E^0$  of  $3.33 \text{ V vs Na}^+/\text{Na}$  and a  $\Delta E^0$  of  $0.10 \text{ V}$ . The  $\Delta E^0$  is defined as the separation between the cathodic and anodic peaks associated with the same redox reaction.

The presence of a double peak in the anodic scan suggests a two-step sodium insertion process. Cyclic voltammograms recorded at different scan rates still maintain an  $E^0$  of  $3.33 \text{ V vs Na}^+/\text{Na}$ , but the  $\Delta E^0$  increases to  $0.10$ ,  $0.20$ ,  $0.35$ , and  $0.45 \text{ V}$  for scan rates of  $0.1$ ,  $0.2$ ,  $0.5$ , and  $1.0 \text{ mV s}^{-1}$ , respectively. This behaviour is consistent with the mass transport limitations typically observed in such reactions. In Figure 3.31, the current maxima of each anodic and cathodic peak at different scan rates are plotted against the square root of the respective scan rate ( $v^{1/2}$ ), demonstrating the expected linear relationship.

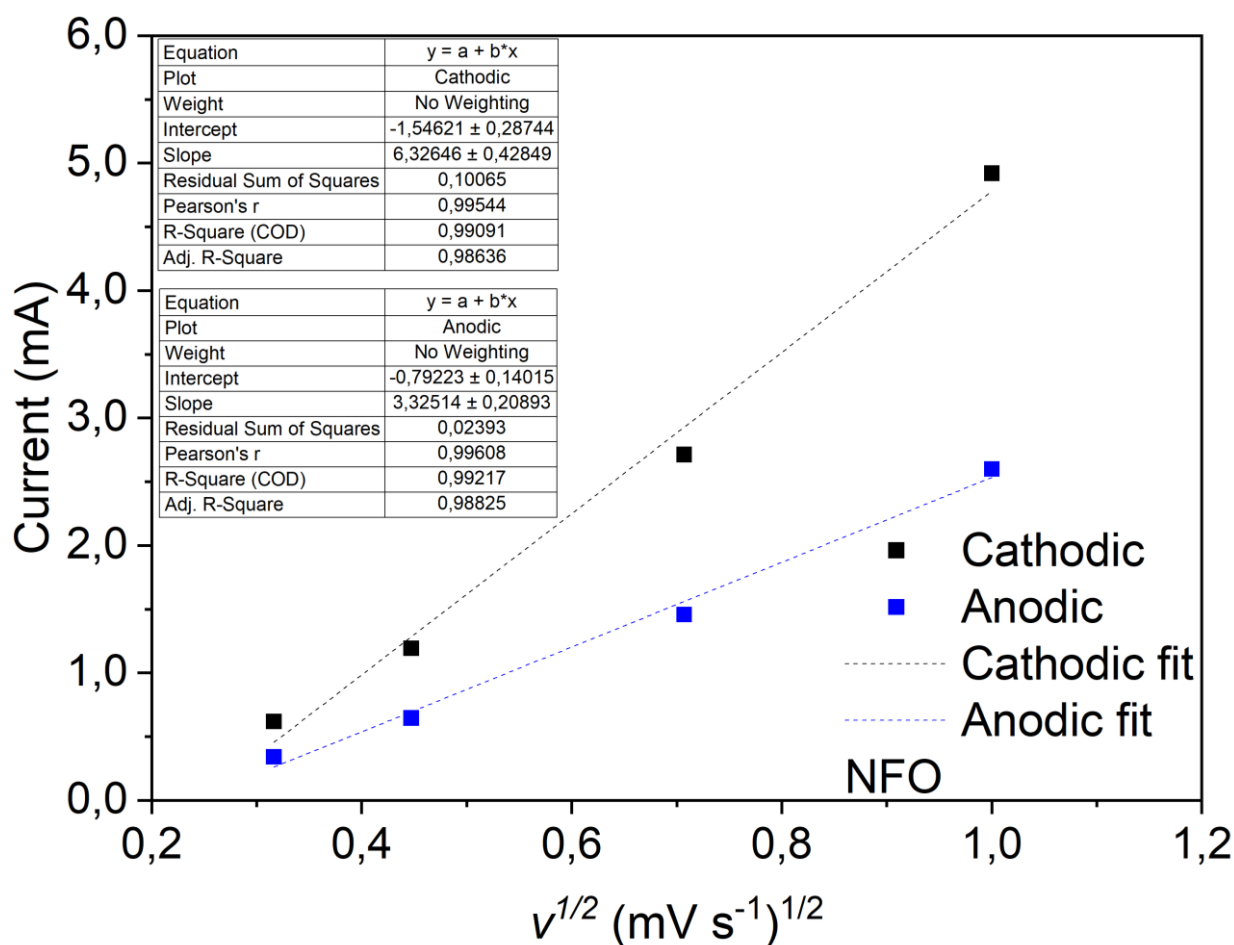


Figure 3.31 – Maxima of the anodic and the cathodic peaks at different scan rates, related to  $v^{1/2}$  with the cathodic and anodic linear regressions.

The anodic and the cathodic current maxima show a good correlation with the  $v^{1/2}$ , with a correlation coefficient, of  $r^2 = 0.99217$  and  $0.99061$ , respectively. The anodic and cathodic Na<sup>+</sup> diffusion coefficient was calculated using this method to be  $1.44887 \times 10^{-16} \text{ cm}^2 \text{ s}^{-1}$  and  $7.76232 \times 10^{-17} \text{ cm}^2 \text{ s}^{-1}$ , respectively.

In Figure 3.32, the voltammograms of C<sub>3</sub>NFO and C<sub>3</sub>NFOF at  $0.1 \text{ mV s}^{-1}$  for 10 cycles are shown. The voltammogram run at  $0.1 \text{ mV s}^{-1}$  shows a smaller decay of the maxima anodic and cathodic current with cycling when compared with the pristine NFO, which is concomitant with the information gathered from galvanostatic measurements. Adding to that, for both non-fluorinated and fluorinated 3 % calcium doping, the anodic scan only shows one peak instead of the two peaks in the anodic scan of the pristine material. This may

indicate a one-step reinsertion which may indicate a less stable desodiated phase, caused by the sodium/vacancies (Na<sup>+</sup>/□) disorder that promoted a better sodium reinsertion. [27]

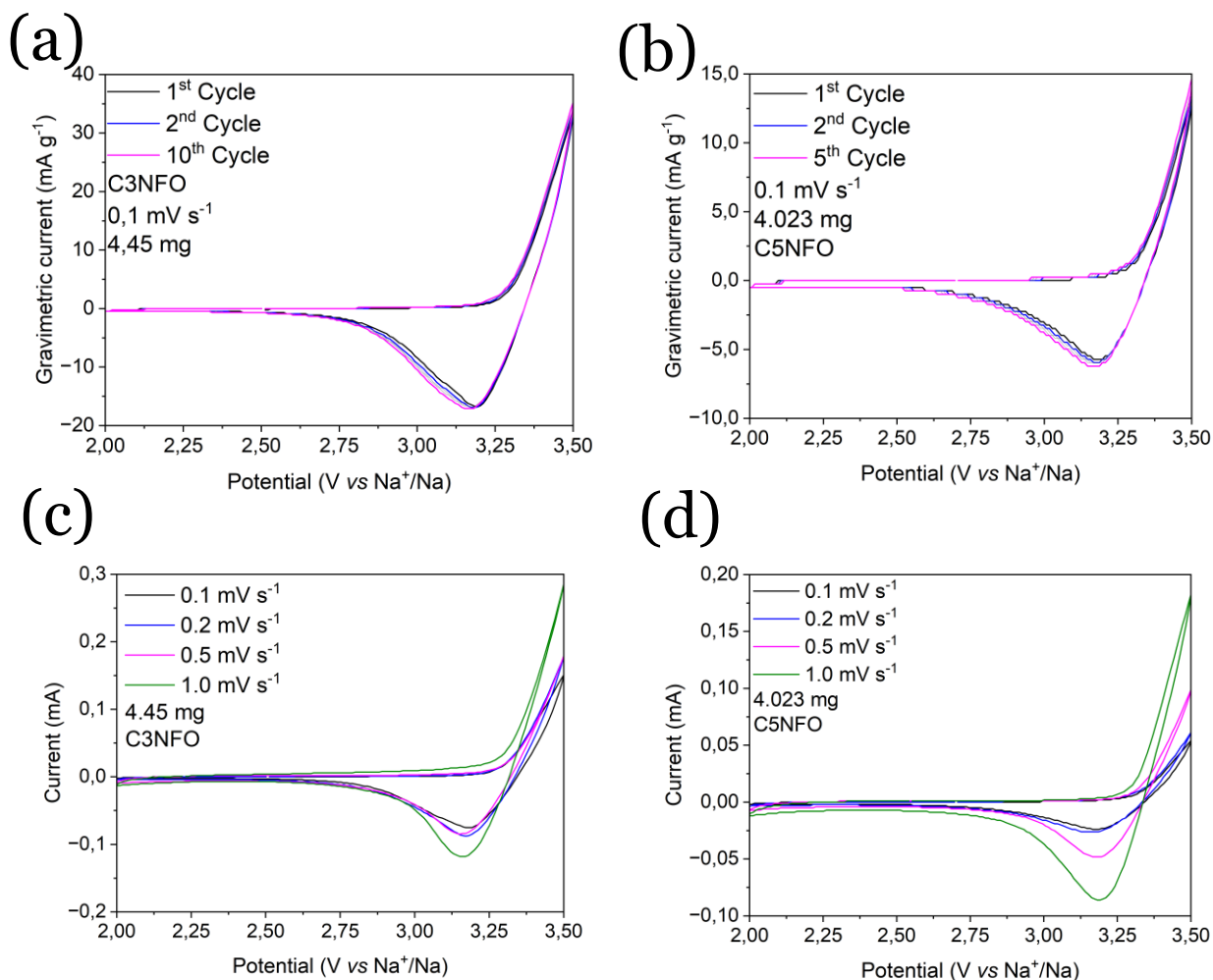


Figure 3.32 - Cyclic-voltammety of C<sub>3</sub>NFO (a) and C<sub>5</sub>NFO (b) at 0.1 mV s<sup>-1</sup> over 10 cycles and cyclic-voltammety at the 2<sup>nd</sup> cycle at a scan rate of 0.1, 0.2, 0.5 and 1.0 mV s<sup>-1</sup> of C<sub>3</sub>NFO (c) and C<sub>5</sub>NFO (d)

The cyclic voltammograms at different scan rates still maintain an  $E^o = 3.33$  V *vs* Na<sup>+</sup>/Na however an increasing  $\Delta E^o$ , which is the expected behaviour of the mass transport-dependent reaction. The  $\Delta E^o$  is also larger than that of the pristine NFO, which may indicate lower sodium mobility within the material structure, which is a known effect of calcium pillaring. [1] The  $\Delta E^o$  cannot be precisely measured because the cathodic peak is not complete in this potential range. The current of the anodic and cathodic peaks also increase at faster

rates which is an expected behaviour of redox reactions and can be used to measure the Na<sup>+</sup> diffusion. In Figure 3.33, the current maxima of each anodic and cathodic peak at different scan rates are compared with the square root of each scan rate,  $v^{1/2}$ .

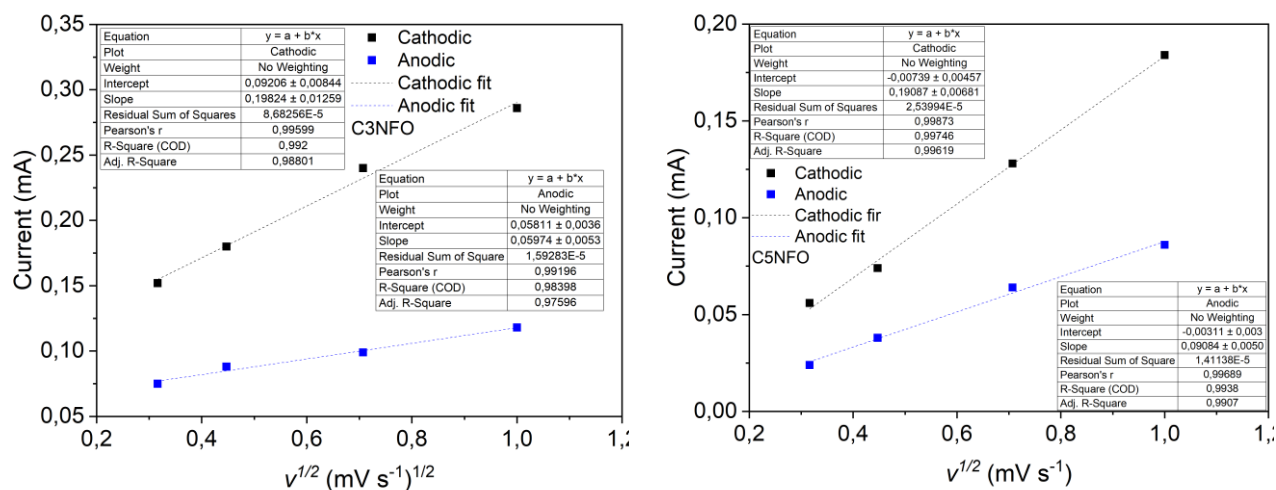


Figure 3.33 - Maxima of the anodic and the cathodic peaks at different scan rates, related to  $v^{1/2}$  with the cathodic and anodic linear regressions of C3NFO (left) and C5NFO (right)

The anodic and the cathodic current maxima show a good correlation with the  $v^{1/2}$ , with a correlation coefficient, of  $r^2 = 0.98398$  and  $0.992000$ , respectively, for C3NFO and  $r^2 = 0.9938000$  and  $0.99746$ , respectively for C3NFOF. The Na<sup>+</sup> diffusion coefficient in C3NFO was calculated using this method to be  $1.23599 \times 10^{-18} \text{ cm}^2 \text{ s}^{-1}$  and  $4.00259 \times 10^{-18} \text{ cm}^2 \text{ s}^{-1}$  for the anodic and cathodic, respectively. For C3NFOF the calculated Na<sup>+</sup> diffusion was calculated to be  $1.167221 \times 10^{-18} \text{ cm}^2 \text{ s}^{-1}$  and  $5.22447 \times 10^{-19} \text{ cm}^2 \text{ s}^{-1}$ . In Figure 3.34, the voltammograms of C5NFO and C5NFOF at  $0.1 \text{ mV s}^{-1}$  for 10 cycles are shown. The voltammogram run at  $0.1 \text{ mV s}^{-1}$  of the fluorinated material, shows less decay of the maximum anodic and cathodic current with cycling when compared with the pristine NFO, which is concomitant with the information gathered from galvanostatic measurements. Regarding the non-fluorinated sample, the decay is higher than all doped samples but less than that of the pristine material. Adding to that, for both non-fluorinated and fluorinated 5 % calcium doping, the anodic scan only shows one peak instead of the two peaks in the

anodic scan of the pristine material. This may indicate a one-step reinsertion which may indicate a less stable desodiated phase, caused by the sodium/vacancies (Na<sup>+</sup>/□) disorder that promoted better sodium reinsertion. [27]

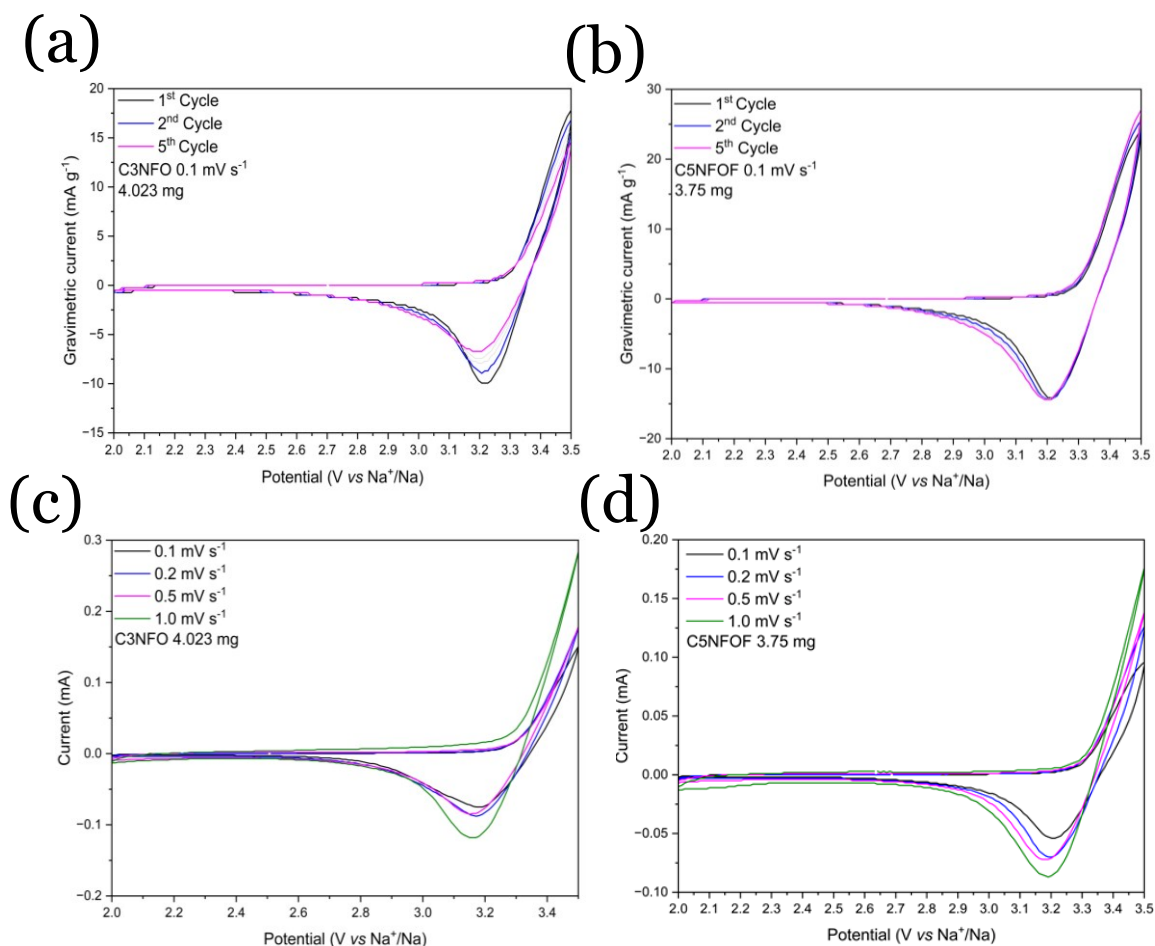


Figure 3.34 - Cyclic-voltammetry of C<sub>3</sub>NFOF (a) and C<sub>5</sub>NFOF (b) at 0.1 mV s<sup>-1</sup> over 10 cycles and cyclic-voltammetry at the 2<sup>nd</sup> cycle at a scan rate of 0.1, 0.2, 0.5 and 1.0 mV s<sup>-1</sup> of C<sub>3</sub>NFOF (c) and C<sub>5</sub>NFOF (d)

The anodic and the cathodic current maxima show a good correlation with the  $v^{1/2}$ , with a correlation coefficient, of  $r^2 = 0.94254$  and  $0.90147$ , respectively, for the anodic and the cathodic peaks of C<sub>5</sub>NFO and  $r^2 = 0.88243$  and  $0.94587$ , respectively for the anodic and cathodic peaks of C<sub>5</sub>NFOF. These correlation coefficients are too low for this method to be considered to have enough significance, which can be related to a higher  $\Delta E^0$  of the 5 % doped

samples that makes the cathodic peak uncomplete in the range of measurements of the cyclic-voltammograms in a way the cathodic maximum may not appear in this range.

Still, the Na<sup>+</sup> diffusion coefficient was calculated for these materials using this method, however, to be surer about these values, other methods such as galvanostatic intermittent titration technique (GITT), should be used. The Na<sup>+</sup> diffusion coefficient in C<sub>5</sub>NFO was calculated using this method to be  $1.78958 \times 10^{-18} \text{ cm}^2 \text{ s}^{-1}$  and  $3.90491 \times 10^{-18} \text{ cm}^2 \text{ s}^{-1}$  for the anodic and cathodic, respectively. For C<sub>5</sub>NFOF the calculated Na<sup>+</sup> diffusion was calculated to be  $9.4004 \times 10^{-19} \text{ cm}^2 \text{ s}^{-1}$  and  $2.41449 \times 10^{-18} \text{ cm}^2 \text{ s}^{-1}$  (Figure 3.35).

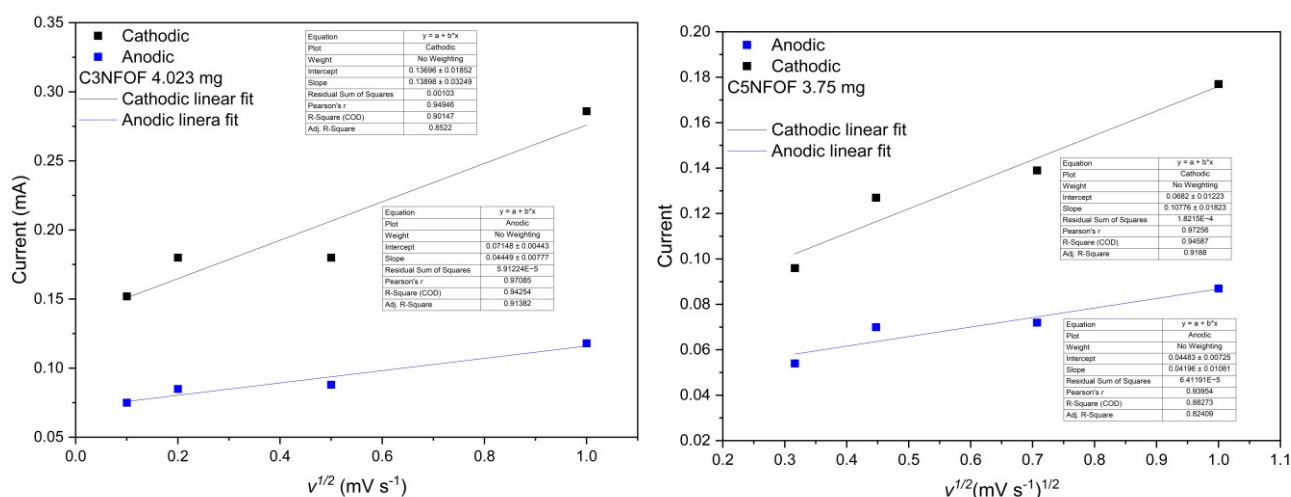


Figure 3.35 - Maxima of the anodic and the cathodic peaks at different scan rates, related to  $v^{1/2}$  with the cathodic and anodic linear regressions of C<sub>3</sub>NFOF (left) and C<sub>5</sub>NFOF (right)

Calcium doping at 3% (C<sub>3</sub>NFO) and its fluorinated version (C<sub>3</sub>NFOF) resulted in a single anodic peak, suggesting a one-step sodium reinsertion due to potential Na<sup>+</sup>/□ disorder. Both variants showed reduced current decay, indicating improved stability. However, the increased  $\Delta E^0$  suggested decreased sodium mobility due to calcium pillaring. The Na<sup>+</sup> diffusion coefficients for C<sub>3</sub>NFO were  $1.23599 \times 10^{-18} \text{ cm}^2 \text{ s}^{-1}$  (anodic) and  $4.00259$

$\times 10^{-18} \text{ cm}^2 \text{ s}^{-1}$  (cathodic), while for C<sub>3</sub>NFOF, they were  $1.167221 \times 10^{-18} \text{ cm}^2 \text{ s}^{-1}$  (anodic) and  $5.22447 \times 10^{-19} \text{ cm}^2 \text{ s}^{-1}$  (cathodic).

For 5% calcium doping (C<sub>5</sub>NFO and C<sub>5</sub>NFOF), the fluorinated variant exhibited the least current decay, indicating superior stability but, lower rate capability. Both displayed a single anodic peak, consistent with lower desodiated phase stability due to Na<sup>+</sup>/□ disorder. The lower correlation coefficients for these samples necessitate further analysis via methods like (GITT). The Na<sup>+</sup> diffusion coefficients for C<sub>5</sub>NFO were  $1.78958 \times 10^{-18} \text{ cm}^2 \text{ s}^{-1}$  (anodic) and  $3.90491 \times 10^{-18} \text{ cm}^2 \text{ s}^{-1}$  (cathodic) and for C<sub>5</sub>NFOF,  $9.4004 \times 10^{-19} \text{ cm}^2 \text{ s}^{-1}$  (anodic) and  $2.41449 \times 10^{-18} \text{ cm}^2 \text{ s}^{-1}$  (cathodic).

Overall, calcium pillaring reduces sodium mobility, while fluorine doping enhances stability and reduces current decay in NFO but, reduces the sodium diffusion rate, impacting in rate capability. Table 4.5, a table with all the results from the calculation of the diffusion coefficient of the pristine, non-fluorinated and fluorinated calcium-doped NFO.

Table 3.8 – Sodium diffusion rate at the cathode and anode, calculated with cyclic-voltammetry at different rates of NFO, C<sub>3</sub>NFO, C<sub>5</sub>NFO, C<sub>3</sub>NFOF and C<sub>5</sub>NFOF

	$D_{Na}(\text{NFO}) (\text{CM}^2 \text{ S}^{-1})$	$D_{Na}(\text{C}_3\text{NFO}) (\text{CM}^2 \text{ S}^{-1})$	$D_{Na}(\text{C}_5\text{NFO}) (\text{CM}^2 \text{ S}^{-1})$
<b>Cathodic</b>	$7.76232 \times 10^{-17}$	$4.00259 \times 10^{-18}$	$1.78958 \times 10^{-18}$
<b>Anodic</b>	$1.44887 \times 10^{-16}$	$1.23599 \times 10^{-18}$	$3.90491 \times 10^{-18}$
		$D_{Na}(\text{C}_3\text{NFOF}) (\text{cm}^2 \text{ s}^{-1})$	$D_{Na}(\text{C}_5\text{NFOF}) (\text{cm}^2 \text{ s}^{-1})$
<b>Cathodic</b>		$5.22447 \times 10^{-18}$	$2.41449 \times 10^{-19}$
<b>Anodic</b>		$1.167221 \times 10^{-18}$	$9.4004 \times 10^{-19}$

### 3.4.3. Galvanostatic intermittent titration technique

The galvanostatic intermittent titration technique was run for all calcium-pillared, fluorinated and non-fluorinated materials. These measurements were conducted at

potentials between 2.0 and 3.5 V *vs* Na<sup>+</sup>/Na. Current equivalent to a 0.1 C rate was applied for 10 minutes followed by a period of relaxation of 30 minutes, while the evolution of the potential was monitored. In Figure 3.36, the galvanostatic curves of NFO during GITT analysis and the sodium diffusion coefficient *versus* potential.

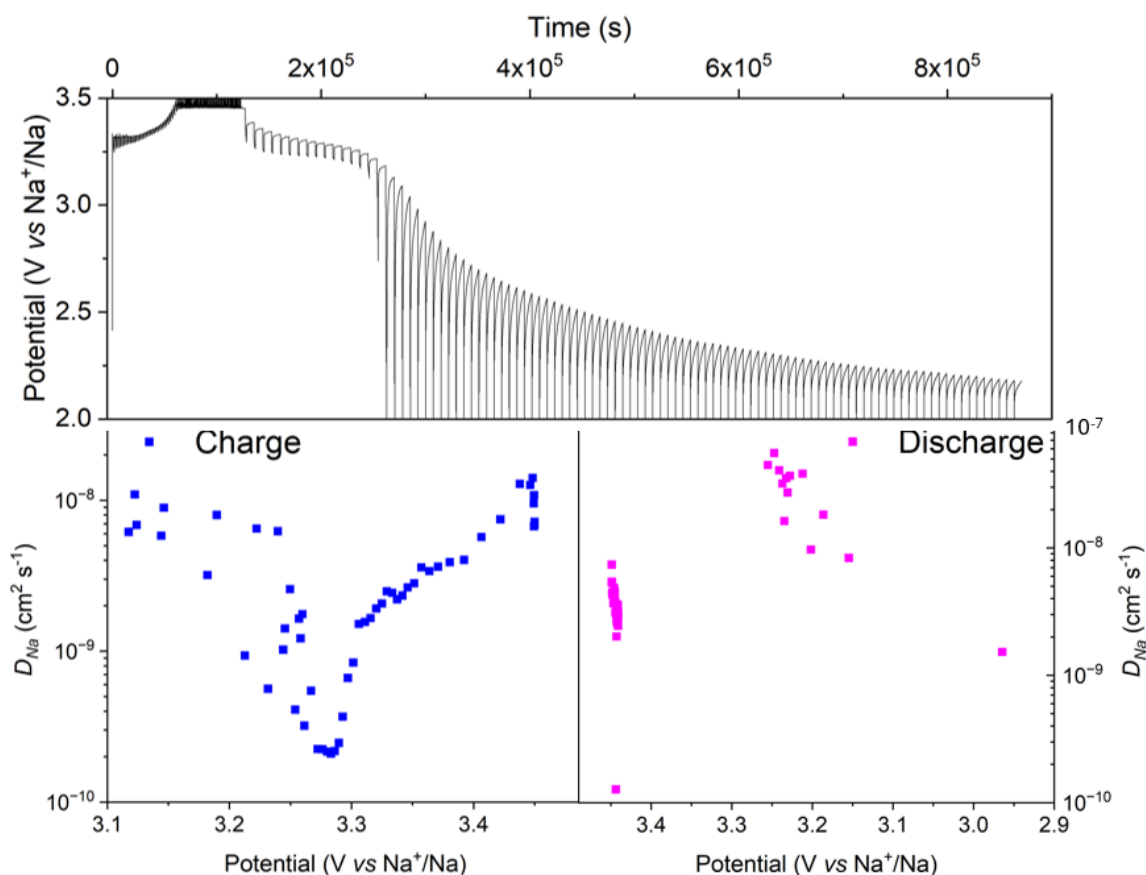


Figure 3.36 – GITT of NFO and diffusion rate versus potential

During charge, NFO shows a sodium diffusion coefficient between 10<sup>-8</sup> and 10<sup>-10</sup> cm<sup>2</sup> s<sup>-1</sup> with a minimum at approximately 3.3 V *vs* Na<sup>+</sup>/Na. During discharge, the sodium diffusion coefficient ranges between 10<sup>-10</sup> and 10<sup>-7</sup> cm<sup>2</sup> s<sup>-1</sup> with a maximum of approximately 3.2 V *vs* Na<sup>+</sup>/Na. This is a substantially higher diffusion coefficient when compared to that obtained from cyclic-voltammetry.

In Figure 3.37, the galvanostatic curves of C<sub>5</sub>NFO during GITT analysis and the sodium diffusion coefficient *versus* potential.

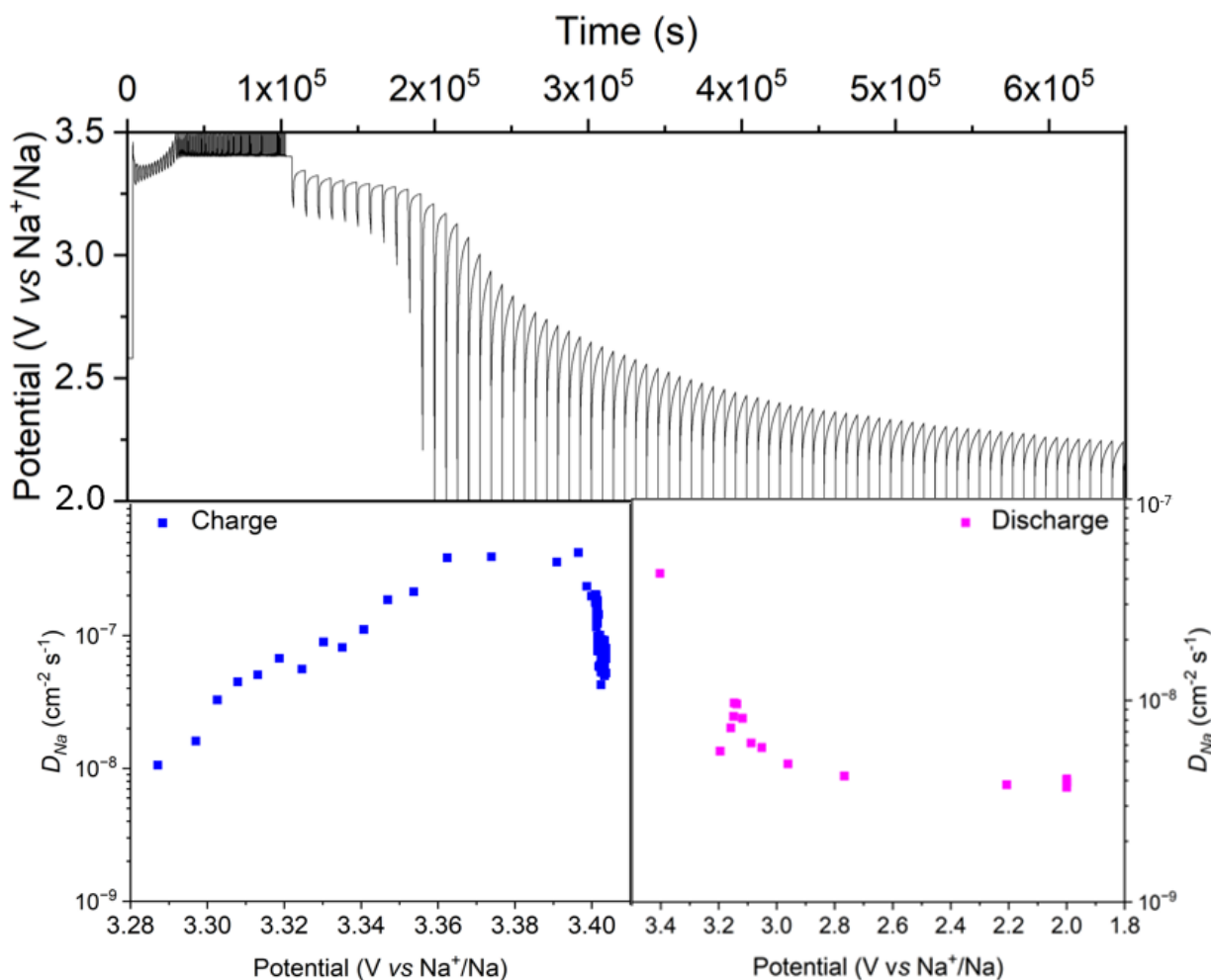


Figure 3.37 - GITT of C<sub>3</sub>NFO and diffusion rate versus potential

During charge, C<sub>3</sub>NFO shows a sodium diffusion coefficient between 10<sup>-6</sup> and 10<sup>-8</sup> cm<sup>2</sup> s<sup>-1</sup> with a minimum at approximately 3.3 V *vs* Na<sup>+</sup>/Na. During discharge, the sodium diffusion coefficient ranges between 10<sup>-7</sup> and 10<sup>-6</sup> cm<sup>2</sup> s<sup>-1</sup> with a maximum of approximately 3.2 V *vs* Na<sup>+</sup>/Na. This is a substantially higher diffusion coefficient when compared to that obtained from cyclic-voltammetry.

In Figure 3.38, the galvanostatic curves of C<sub>5</sub>NFO during GITT analysis and the sodium diffusion coefficient *versus* potential.

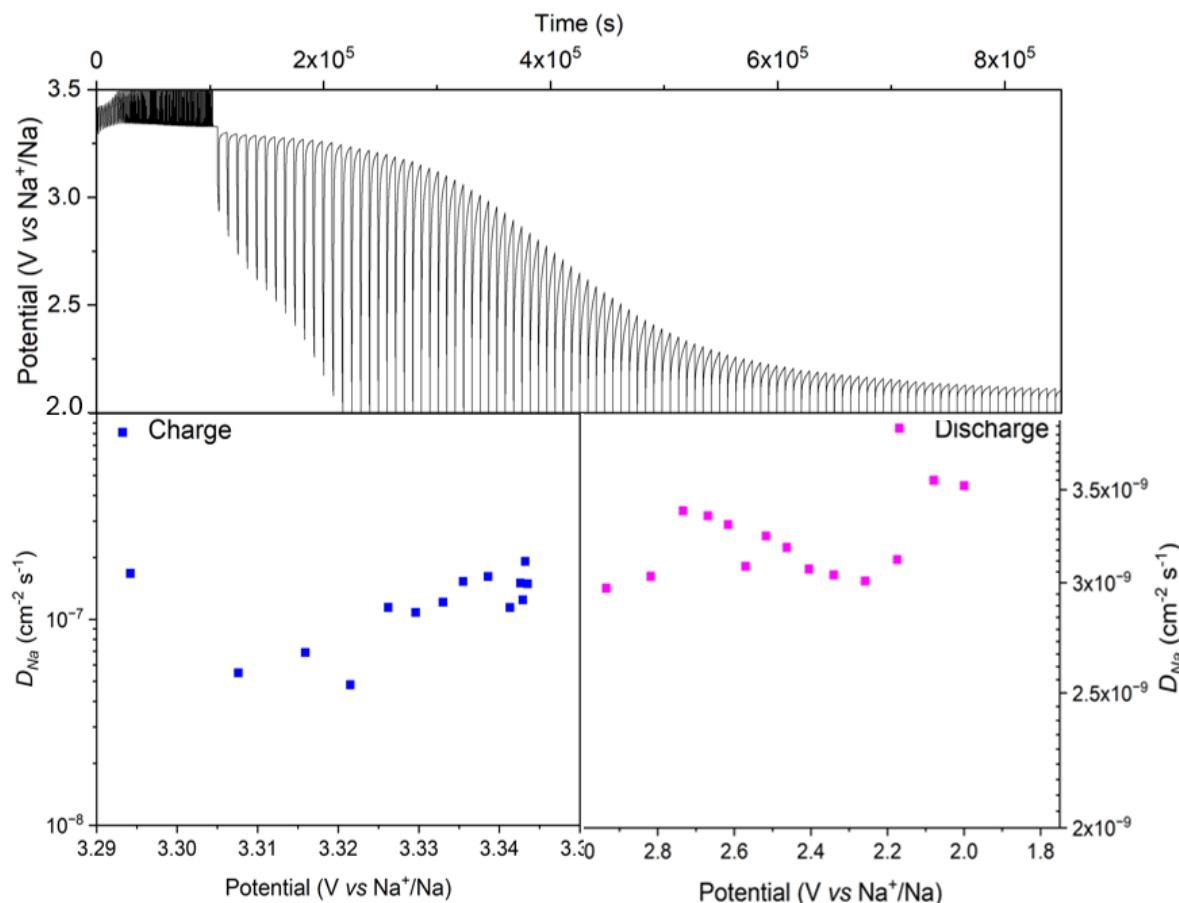


Figure 3.38 - GITT of C<sub>5</sub>NFO and diffusion rate versus potential

During charge, C<sub>5</sub>NFO shows a sodium diffusion coefficient between 10<sup>-6</sup> and 10<sup>-7</sup> cm<sup>2</sup> s<sup>-1</sup> with a minimum of approximately 3.32 V *vs* Na<sup>+</sup>/Na. During discharge, the sodium diffusion coefficient ranges between 3 × 10<sup>-9</sup> and 3.5 × 10<sup>-9</sup> cm<sup>2</sup> s<sup>-1</sup> with a maximum of approximately 2.7 V *vs* Na<sup>+</sup>/Na. This is a substantially higher diffusion coefficient when compared to that obtained from cyclic-voltammetry.

In Figure 3.39, the galvanostatic curves of C<sub>3</sub>NFOF during GITT analysis and the sodium diffusion coefficient *versus* potential.

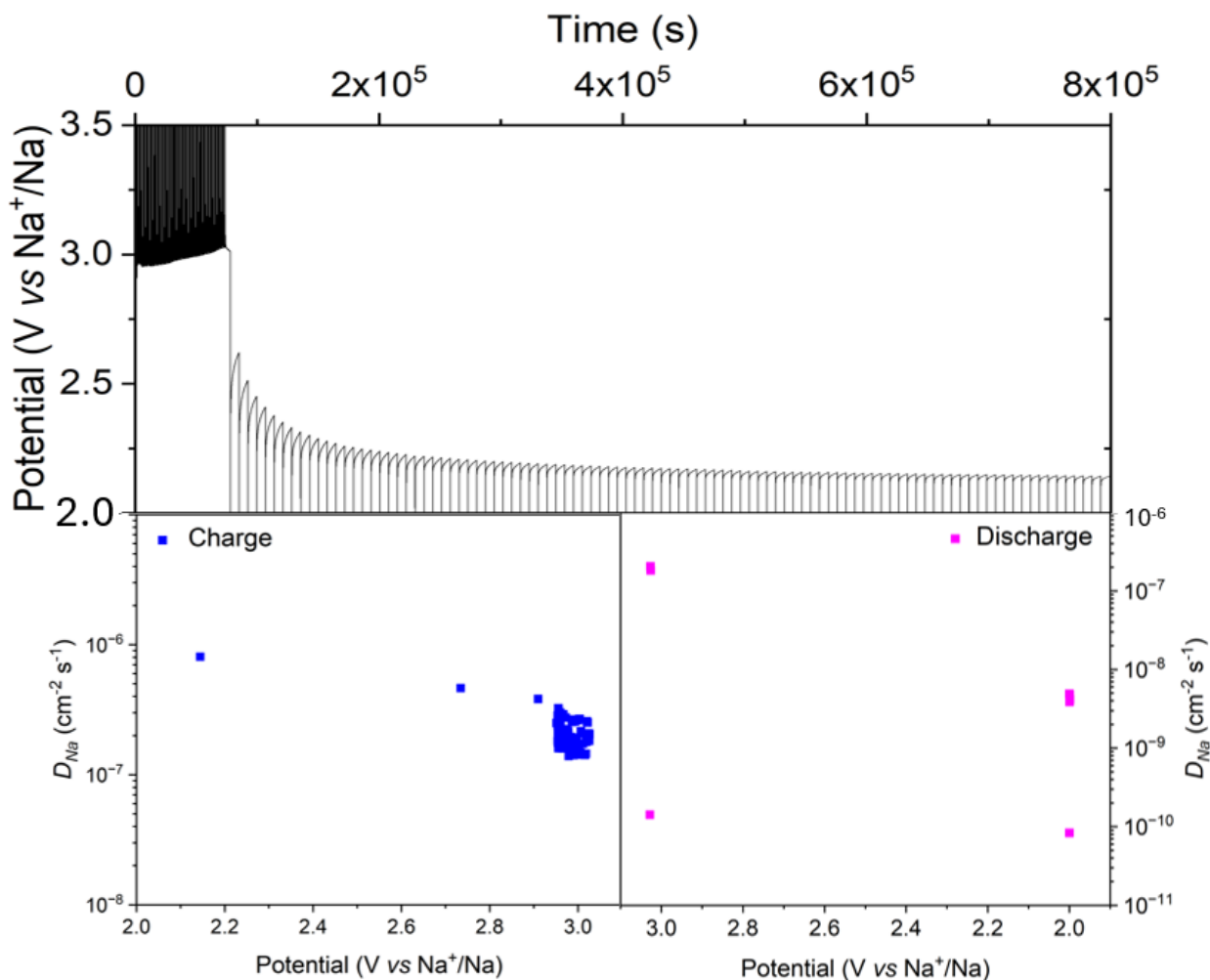


Figure 3.39 - GITT of C<sub>3</sub>NFOF and diffusion rate versus potential

During charge, C<sub>3</sub>NFOF shows a sodium diffusion coefficient between  $10^{-6}$  and  $10^{-7}$   $\text{cm}^2 \text{s}^{-1}$  with a minimum at approximately 3.0 V vs Na<sup>+</sup>/Na. During discharge, the sodium diffusion coefficient ranges between  $3 \times 10^{-10}$  and  $3.5 \times 10^{-6}$   $\text{cm}^2 \text{s}^{-1}$ . This is a substantially higher diffusion coefficient when compared to that obtained from cyclic-voltammetry.

In Figure 3.40, the galvanostatic curves of C<sub>5</sub>NFOF during GITT analysis and the sodium diffusion coefficient *versus* potential.

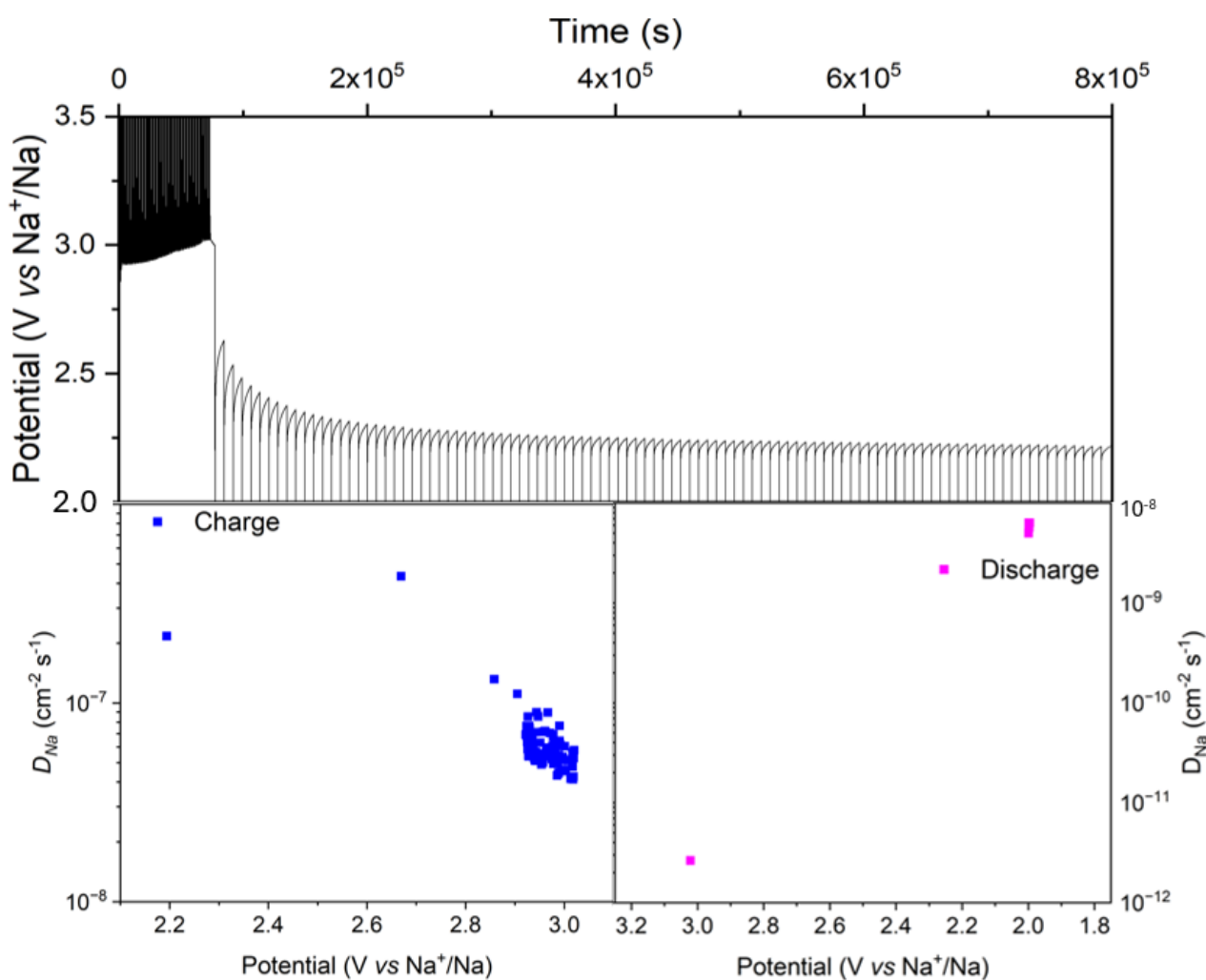


Figure 3.40 GITT of C<sub>5</sub>NFOF and diffusion rate versus potential

During charge, C<sub>5</sub>NFOF shows a sodium diffusion coefficient between  $10^{-6}$  and  $10^{-8}$   $\text{cm}^2 \text{s}^{-1}$  with a minimum at approximately 3.0 V vs Na<sup>+</sup>/Na. During discharge, the sodium diffusion coefficient ranges between  $3 \times 10^{-8}$  and  $3.5 \times 10^{-12}$   $\text{cm}^2 \text{s}^{-1}$ . This is a few orders of magnitude higher diffusion coefficient when compared to that obtained from cyclic voltammetry.

In section 3.4.2, where the sodium diffusion coefficient was measured using cyclic voltammetry at different scan rates, it tends to decrease with doping via fluorination. On the other hand, the values obtained from GITT exhibit the opposite trend.

In cyclic-voltammetry, the measured diffusion coefficient derived is often influenced by surface reactions and the kinetics of charge transfer at the electrode interface. [28] In opposition, GITT probes the bulk properties of the material more directly, particularly the solid-state diffusion within the material. [28] The decrease of diffusion of sodium detected in the CV may indicate that the doping is affecting the surface kinetics or the charge transfer processes at the electrode interface. The dopant could be creating surface defects or forming a passivation layer, thereby hindering the movement of ions or electrons at the surface. This may also correlate with the detection of different impurities in the doped materials.

The increase in the diffusion of sodium measured with GITT suggests that the doping is enhancing the bulk diffusion properties of the material. [29] The dopant might be increasing the number of available diffusion pathways or creating a more favourable environment for ion transport within the bulk material. [30]

The dopants could be affecting the surface and bulk properties differently. For instance, while the surface might become less conductive due to passivation or increased resistance, the bulk might benefit from increased disorder or defects that facilitate ion movement. Doping may be changing the dominant diffusion mechanism. [30] In the bulk, increased doping could lead to a higher concentration of defects, improving ionic mobility. However, at the surface, the same dopants and extra impurities may introduce barriers or bottlenecks for charge transfer. Finally, dopants may alter the interface and affect the formation of a CEI, perhaps by forming a resistive layer, which wouldn't significantly affect the bulk properties measured by GITT. [31]

In this case, conductivity measurements could provide more insight into how doping affects the overall electrical properties. Furthermore, other electrochemical techniques like electrochemical impedance spectroscopy (EIS) to get a more comprehensive understanding of the processes occurring at the electrode interface and within the bulk.

### 3.4.4. Operando X-ray diffractometry

Operando XRD diffractometry was performed on half-cell at a potential window of 2.0 – 3.5 V vs Na<sup>+</sup>/Na and the diffractograms were measured at  $Q$  values between 1 and 4.5 Å<sup>-1</sup>. The colourmaps were created using MATLAB® and in Figure 3.41, a detail of the heat map with  $Q$  between 1 and 1.3 Å<sup>-1</sup> for the (0 0 3) peak, 2.2 and 2.6 Å<sup>-1</sup> for the (0 0 6), (1 0 1) and (0 1 2) peaks, between 2.7 and 3.0 Å<sup>-1</sup> for the (0 1 4) peak, of the pristine phase, and between 3.7 and 4.05 Å<sup>-1</sup> for the (2 0 2) of the desodiated high potential phase.

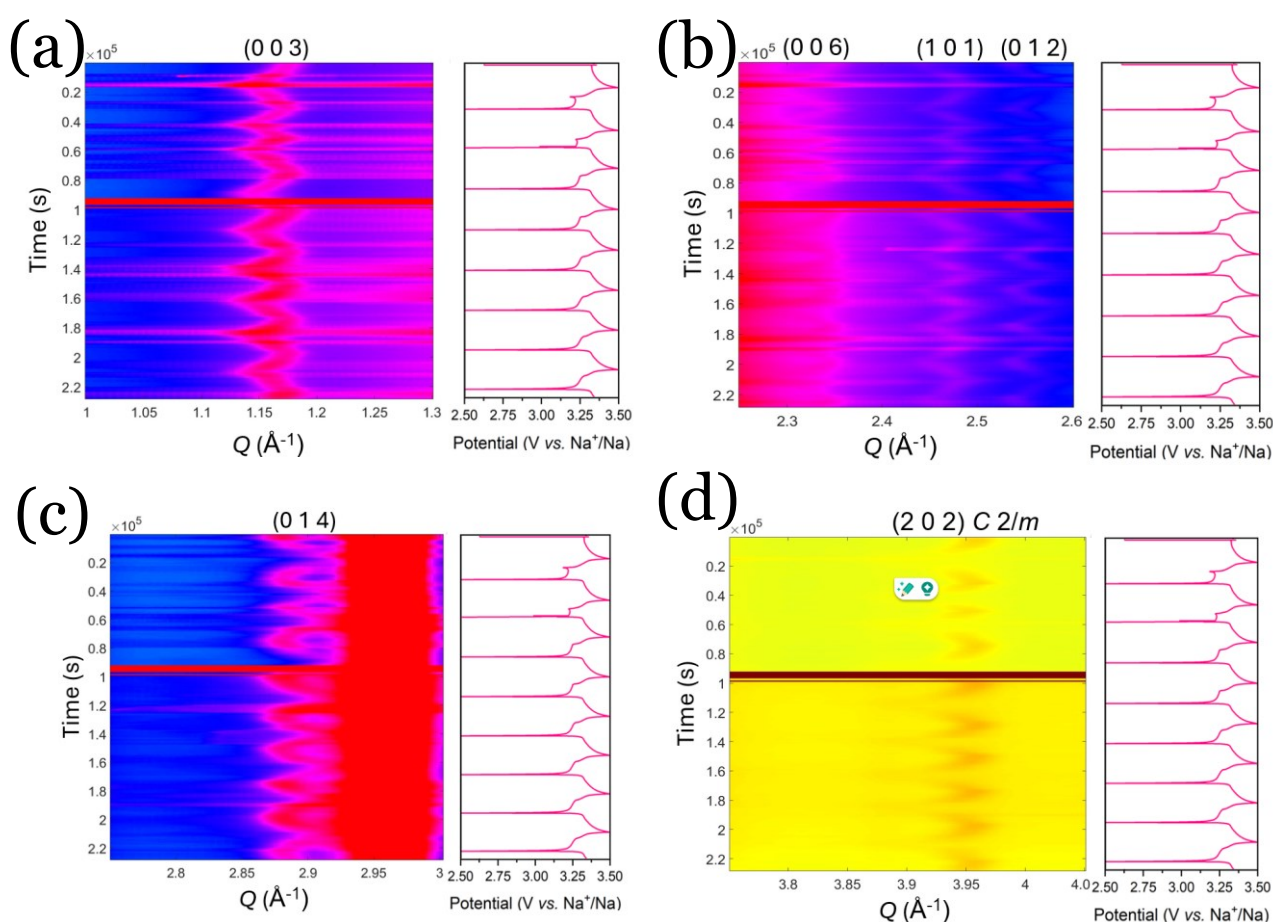


Figure 3.41 – Heat map of the diffraction peaks (0 0 3) (a), (0 0 6), (1 0 1) and (0 1 2) (b), (0 1 4) (c) and, the (2 0 2) peak of the desodiated phase (d)

The diffraction peaks (101) and (012) shift to higher angles, indicating a shortening of the in-plane cell parameters as sodium is extracted, as shown in Figure 3.42. This behaviour,

common in many O<sub>3</sub>-structured compounds, is due to increased electrostatic repulsion between oxygen atoms (increasing interlayer distance) and decreased repulsion between iron and sodium ions (decreasing in-plane distance) when sodium is extracted. A decrease of the peak associated with (0 0 3) moves to a lower degree, indicating an expansion of the alkali-metal layer due to O-O repulsion when Na<sup>+</sup> is removed from the structure. On the other hand, the peak to (0 0 6) moves to higher angles, indicating an expansion. These phenomena are illustrated in Figure 3.42.

A secondary phase emerges near half charge, appearing at a higher *Q* corresponding to a greater interlayer distance of 5.58 Å. This is similar to observations in other O<sub>3</sub>-type transition-metal layered oxides, where a biphasic transformation from O<sub>3</sub> to P<sub>3</sub> structure typically occurs. The slight distortion towards a P<sub>3</sub> phase, with the formation of an O'<sub>3</sub>-type secondary phase, is confirmed by the (003) and (104) peak intensity ratio of the P<sub>3</sub> phase, as well as the Na<sub>0.5</sub>FeO<sub>2</sub> (*C* 2/*m*) desodiated phase. During the second part of the charge, the (101), (012), and (104) reflections begin to shift to lower angles.

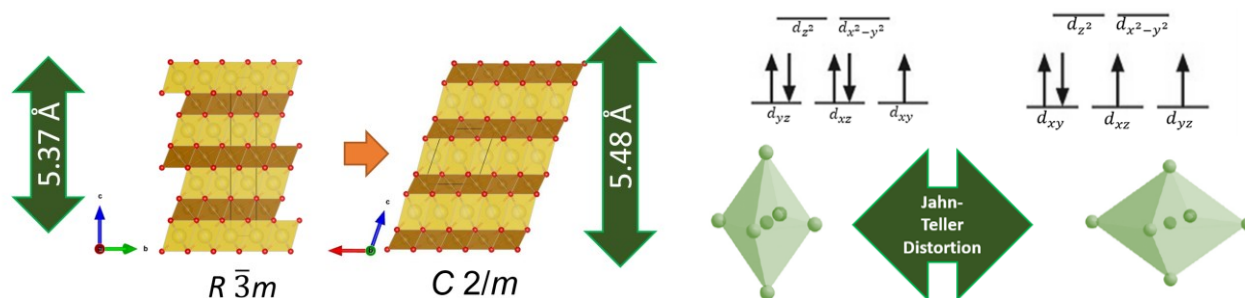


Figure 3.42 – Illustration of the phase change caused by O<sup>2-</sup> repulsion, caused by the depletion of sodium in the alkali-metal layer (a) and the contraction of the transition metal layer caused by Jahn-Teller distortion of Fe(IV)

Operando XRD on the doped samples was not run due to issues in producing a pure phase promptly in the case of the dual calcium and fluorine-doped sample and due to an accident in transportation for the calcium doped sample.

### 3.5. Conclusion

The synthesis and characterisation of a series of calcium-pillared and fluorinated variations of  $\alpha$ -NaFeO<sub>2</sub> have been meticulously optimised and thoroughly examined in this chapter. The primary focus was on achieving the purest possible materials with minimal secondary phases and impurities through the ceramic method, thereby enhancing their potential applicability in sodium-ion battery systems.

Despite the persistent presence of the  $\beta$ -NaFeO<sub>2</sub> phase and unreacted Na<sub>2</sub>CO<sub>3</sub>, the  $\alpha$ -NaFeO<sub>2</sub> phase synthesised at 680°C was selected for its relatively lower impurity levels. This optimisation process shows the complexity of achieving a pure  $\alpha$ -NaFeO<sub>2</sub> phase using ceramic synthesis, where a small amount of  $\beta$ -NaFeO<sub>2</sub> cannot be avoided. [22] The subsequent synthesis of calcium-doped and fluorinated variations required further adjustments, particularly lowering the calcination temperature to 630°C and employing multi-step calcination processes to enhance homogeneity and reduce unreacted precursors. The multi-step reactions, particularly the two-step 15+5 hours process, were instrumental in obtaining a purer  $\alpha$ -Na<sub>0.90</sub>Ca<sub>0.05</sub>FeO<sub>2</sub> phase. This method was successfully extended to other compositions, including  $\alpha$ -Na<sub>0.96</sub>Ca<sub>0.02</sub>FeO<sub>2</sub>,  $\alpha$ -Na<sub>0.94</sub>Ca<sub>0.03</sub>FeO<sub>2</sub>, and their fluorinated counterparts.

The structural characterisation using X-ray diffractometry and Rietveld refinement confirmed the successful synthesis of the desired phases. The refined lattice parameters were consistent with literature values, affirming the structural integrity of the synthesised materials. The purity levels, as indicated by the *R* factors and goodness-of-fit values, were satisfactory, though minor impurities like  $\beta$ -NaFeO<sub>2</sub> and Ca<sub>2</sub>Fe<sub>2</sub>O<sub>5</sub> were detected. Morphologically, field emission scanning electron microscopy (FESEM) revealed highly agglomerated spherical particles with diameters around 500 nm for the pristine and calcium-

doped  $\alpha$ -NaFeO<sub>2</sub>. The fluorinated variants, however, exhibited larger amorphous particles, potentially due to the challenges in grinding and homogenisation during synthesis. Energy-dispersive X-ray spectroscopy (EDS) confirmed the elemental composition, aligning well with the expected composition.

The electrochemical performance of these materials was tested using various techniques, including galvanostatic charge-discharge, cyclic voltammetry, *operando* X-ray diffraction, and galvanostatic intermittent titration technique. The pristine  $\alpha$ -NaFeO<sub>2</sub> showed a significant capacity fade upon cycling, particularly when cycled at higher potentials. This behaviour was attributed to irreversible iron migration and oxygen oxidation processes, which destabilise the material. The cyclic-voltammetry results further supported this, showing diminishing peak intensities and the onset of irreversible phenomena at higher potentials.

The calcium-doped and fluorinated variants exhibited improved electrochemical stability, with the fluorinated compounds showing particularly high purities and reduced impurity levels. These modifications helped mitigate some of the capacity fade issues observed in the pristine material, highlighting the beneficial effects of calcium and fluorine doping on the electrochemical performance.

The Rietveld refinement provided some information about the structural changes induced by calcium and fluorine doping. The incorporation of Ca<sup>2+</sup> ions led to a reduction in the *c*-axis length due to the dipositive nature of calcium, which was consistent across the series. The fluorination process further modified the lattice parameters, indicating a complex interplay between the electrostatic forces and the structural framework.

The electrochemical performance of pristine and calcium-doped NFO materials was comprehensively analysed through a series of tests, including cycling performance, coulombic efficiency, potentiostatic curves, and cyclic voltammetry. The pristine NFO, along

with its 3% and 5% calcium-doped variants, both with and without fluorination, exhibited distinct behaviours under various testing conditions.

The initial capacities of NFO, C<sub>3</sub>NFO, and C<sub>5</sub>NFO were 105, 82, and 68 mA h g<sup>-1</sup>, respectively. The reduction in initial capacity with increased calcium doping aligns with the anticipated decrease in available sodium. The rapid decline in capacity for NFO and C<sub>3</sub>NFO indicates that 3% calcium doping is insufficient to stabilise the layers and improve capacity retention. However, C<sub>5</sub>NFO displayed superior capacity retention, surpassing the pristine NFO after 60 cycles, suggesting that 5% calcium doping enhances the structural integrity and electrochemical performance of the material.

The stability of the mid-*plateau* over 100 cycles, along with the higher mid potential observed for the 5% doped material, implies a more sustained energy delivery capability. The observed stability and performance improvements with 5% calcium doping underscore its potential for practical applications where long-term performance and reliability are critical.

The materials' performance at varying charge and discharge rates revealed critical insights. While C<sub>3</sub>NFO exhibited a decrease in rate capability, C<sub>5</sub>NFO maintained better sodium conduction, reflecting its superior rate capability. At higher rates (1 C to 10 C), both NFO and C<sub>5</sub>NFO showed no extractable capacity, indicating that these faster rates did not adversely affect the materials' structural integrity, as they recovered their capacity upon returning to slower rates. Coulombic efficiency analysis showed a transient dip from approximately 98% to 95%, likely due to temperature fluctuations in the analysis room.

Cyclic voltammetry was conducted to evaluate the stability and sodium diffusion of all materials. The pristine NFO showed expected Fe(III) ⇌ Fe(IV) redox peaks, with a slight decay in anodic and cathodic currents over cycling. Calcium doping at 3% (C<sub>3</sub>NFO) and its fluorinated counterpart (C<sub>3</sub>NFOF) resulted in a single anodic peak, indicating a one-step sodium reinsertion process due to potential Na<sup>+</sup>/□ disorder. Both variants showed reduced

current decay, implying improved stability. However, increased  $\Delta E^o$  indicated decreased sodium mobility, attributed to calcium pillaring.

The Na<sup>+</sup> diffusion coefficients for C<sub>3</sub>NFO and C<sub>3</sub>NFOF were determined, with C<sub>3</sub>NFO showing  $1.23599 \times 10^{-18} \text{ cm}^2 \text{ s}^{-1}$  (anodic) and  $4.00259 \times 10^{-18} \text{ cm}^2 \text{ s}^{-1}$  (cathodic), while C<sub>3</sub>NFOF exhibited  $1.167221 \times 10^{-18} \text{ cm}^2 \text{ s}^{-1}$  (anodic) and  $5.22447 \times 10^{-19} \text{ cm}^2 \text{ s}^{-1}$  (cathodic). These values indicate that calcium doping while reducing surface sodium mobility, does not severely impair the overall performance.

For 5% calcium doping (C<sub>5</sub>NFO and C<sub>5</sub>NFOF), the fluorinated variant exhibited the least current decay, highlighting its superior stability. The lower correlation coefficients for these samples necessitate further analysis using methods like the galvanostatic intermittent titration technique (GITT). The Na<sup>+</sup> diffusion coefficients for C<sub>5</sub>NFO and C<sub>5</sub>NFOF were calculated, with C<sub>5</sub>NFO showing  $1.78958 \times 10^{-18} \text{ cm}^2 \text{ s}^{-1}$  (anodic) and  $3.90491 \times 10^{-18} \text{ cm}^2 \text{ s}^{-1}$  (cathodic), and C<sub>5</sub>NFOF exhibiting  $9.4004 \times 10^{-19} \text{ cm}^2 \text{ s}^{-1}$  (anodic) and  $2.41449 \times 10^{-18} \text{ cm}^2 \text{ s}^{-1}$  (cathodic).

GITT was employed to probe the bulk properties of the materials. The sodium diffusion coefficients measured through GITT were significantly higher compared to those obtained from cyclic voltammetry, suggesting that surface reactions and electrode interface kinetics significantly influence the diffusion coefficients derived from cyclic voltammetry. For instance, during charge, pristine NFO showed a sodium diffusion coefficient ranging from  $10^{-8}$  to  $10^{-10} \text{ cm}^2 \text{ s}^{-1}$ , whereas, during discharge, it ranged from  $10^{-10}$  to  $10^{-7} \text{ cm}^2 \text{ s}^{-1}$ . The higher diffusion coefficients measured via GITT indicate enhanced bulk diffusion properties, likely due to increased defect concentrations and disorder facilitated by calcium doping. These findings highlight the distinct impact of calcium and fluorine doping on surface and bulk properties, necessitating a multi-faceted approach to fully understand their effects on material performance.

*Operando* XRD diffractometry provided insights into the structural changes during cycling. The diffraction peaks associated with the pristine phase shifted, indicating in-plane cell parameter shortening and alkali-metal layer expansion due to sodium extraction. A secondary phase emerged near half charge, resembling a biphasic transformation from  $O_3$  to  $O'3$  structure, with slight distortions toward a  $P3$  phase. These structural transformations are consistent with increased electrostatic repulsion and decreased interlayer distance upon sodium extraction. The formation of an  $O'3$ -type secondary phase and  $\text{Na}_{0.5}\text{FeO}_2$  desodiated phase was observed, underscoring the complex structural dynamics of these materials during electrochemical cycling.

The comprehensive analysis of pristine and doped NFO materials highlights the intricate balance between surface and bulk properties, structural stability, and electrochemical performance. Calcium and fluorine doping offer promising avenues for enhancing the performance and longevity of NFO-based materials. However, the differing impacts on surface and bulk properties necessitate further investigation using advanced techniques such as electrochemical impedance spectroscopy (EIS) and conductivity measurements.

Future research should focus on optimising doping levels and exploring alternative dopants to achieve a harmonious balance between improved capacity retention, rate capability, and sodium diffusion. Additionally, in-depth studies on the formation and evolution of the cathode-electrolyte interface (CEI) could provide valuable insights into mitigating performance degradation and enhancing the overall stability of these materials.

In summary, this chapter has elucidated the effects of calcium and fluorine doping on the electrochemical performance of NFO materials. While calcium doping enhances structural stability and capacity retention, fluorine doping further improves stability and reduces current decay. The complex interplay between surface and bulk properties, as

revealed through cyclic voltammetry and GITT, underscores the need for a holistic approach to material design and optimisation. The insights gained from this study pave the way for developing high-performance sodium-ion batteries with enhanced durability and efficiency.

### 3.6. References

- [1] H. Fu *et al.*, “Synergetic stability enhancement with magnesium and calcium ion substitution for Ni/Mn-based P2-type sodium-ion battery cathodes †,” 2022, doi: 10.1039/d1sc05715d.
- [2] L. Zheng, J. C. Bennett, and M. N. Obrovac, “Stabilizing NaCrO<sub>2</sub> by Sodium Site Doping with Calcium,” *J. Electrochem. Soc.*, vol. 166, no. 10, pp. A2058–A2064, 2019, doi: 10.1149/2.1041910jes.
- [3] L. Ni *et al.*, “Available online 31,” *Nano Energy*, vol. 115, 2023, doi: 10.1016/j.nanoen.2023.108743.
- [4] Y. Wang, R. Xiao, Y. S. Hu, M. Avdeev, and L. Chen, “P2-Na<sub>0.6</sub>[Cr<sub>0.6</sub>Ti<sub>0.4</sub>]O<sub>2</sub> cation-disordered electrode for high-rate symmetric rechargeable sodium-ion batteries,” *Nat. Commun.*, vol. 6, pp. 1–9, 2015, doi: 10.1038/ncomms7954.
- [5] S. C. Han *et al.*, “Ca-doped Na<sub>x</sub>CoO<sub>2</sub> for improved cyclability in sodium ion batteries,” *J. Power Sources*, vol. 277, pp. 9–16, 2015, doi: 10.1016/j.jpowsour.2014.11.150.
- [6] Q. Mao *et al.*, “Mitigating the P2-O2 transition and Na + /vacancy ordering in Na<sub>2/3</sub>Ni<sub>1/3</sub>Mn<sub>2/3</sub>O<sub>2</sub> by anion/cation dual-doping for fast and stable Na + insertion/extraction †,” 2021, doi: 10.1039/d1ta01433a.
- [7] J. Feng *et al.*, “Stable Electrochemical Properties of Magnesium-Doped Co-Free Layered P2-Type Na<sub>0.67</sub>Ni<sub>0.33</sub>Mn<sub>0.67</sub>O<sub>2</sub> Cathode Material for Sodium Ion Batteries,” *ACS Sustain. Chem. Eng.*, vol. 10, no. 15, pp. 4994–5004, Apr. 2022, doi: 10.1021/ACSSUSCHEMENG.2C00197.
- [8] W. L. Pang *et al.*, “P2-type Na<sub>2/3</sub>Mn<sub>1-x</sub>Al<sub>x</sub>O<sub>2</sub> cathode material for sodium-ion batteries: Al-doped enhanced electrochemical properties and studies on the electrode kinetics,” *J. Power Sources*, vol. 356, pp. 80–88, 2017, doi: 10.1016/j.jpowsour.2017.04.076.

- [9] Y. Bai *et al.*, “Progress of Prussian Blue and Its Analogues as Cathode Materials for Potassium Ion Batteries,” *Eur. J. Inorg. Chem.*, vol. 26, no. 25, 2023, doi: 10.1002/ejic.202300246.
- [10] Y. Li, M. Chen, B. Liu, Y. Zhang, X. Liang, and X. Xia, “Heteroatom Doping: An Effective Way to Boost Sodium Ion Storage,” *Adv. Energy Mater.*, vol. 10, no. 27, pp. 1–36, 2020, doi: 10.1002/aenm.202000927.
- [11] C. D. Canestraro *et al.*, “Strong inter-conduction-band absorption in heavily fluorine doped tin oxide,” *Appl. Surf. Sci.*, vol. 255, no. 5 PART 1, pp. 1874–1879, 2008, doi: 10.1016/j.apsusc.2008.06.113.
- [12] W. Zuo, A. Innocenti, M. Zarrabeitia, D. Bresser, Y. Yang, and S. Passerini, “Layered Oxide Cathodes for Sodium-Ion Batteries: Storage Mechanism, Electrochemistry, and Techno-economics,” *Acc. Chem. Res.*, vol. 56, no. 3, pp. 284–296, 2023, doi: 10.1021/acs.accounts.2c00690.
- [13] B. Yang, A. G. Tamirat, D. Bin, Y. Yao, H. Lu, and Y. Xia, “Regulating Intercalation of Layered Compounds for Electrochemical Energy Storage and Electrocatalysis,” *Adv. Funct. Mater.*, vol. 31, no. 52, pp. 1–35, 2021, doi: 10.1002/adfm.202104543.
- [14] C. Tan *et al.*, “Unravelling the Complex Na<sub>2</sub>CO<sub>3</sub> Electrochemical Process in Rechargeable Na-CO<sub>2</sub> Batteries,” *Adv. Energy Mater.*, vol. 13, no. 13, pp. 1–11, 2023, doi: 10.1002/aenm.202204191.
- [15] L. Li *et al.*, “Retarded phase transition by fluorine doping in Li-rich layered Li<sub>1.2</sub>Mn<sub>0.54</sub>Ni<sub>0.13</sub>Co<sub>0.13</sub>O<sub>2</sub> cathode material,” *J. Power Sources*, vol. 283, pp. 162–170, 2015, doi: 10.1016/j.jpowsour.2015.02.085.
- [16] Q. Zhang *et al.*, “F-doped O<sub>3</sub>-NaNi<sub>1/3</sub>Fe<sub>1/3</sub>Mn<sub>1/3</sub>O<sub>2</sub> as high-performance cathode materials for sodium-ion batteries,” *Sci. China Mater.*, vol. 60, no. 7, pp. 629–636, 2017, doi: 10.1007/s40843-017-9045-9.

- [17] B. na SilvánSilv, E. Gonzalo, L. Djuandhi, N. Sharma, F. Fauth, and D. Saurel, “On the dynamics of transition metal migration and its impact on the performance of layered oxides for sodium-ion batteries: NaFeO<sub>2</sub> as a case study †,” 2018, doi: 10.1039/c8ta02473a.
- [18] M. Tabuchi and R. Kataoka, “ Structure and Electrochemical Properties of  $\alpha$ -NaFeO<sub>2</sub> Obtained under Various Hydrothermal Conditions ,” *J. Electrochem. Soc.*, vol. 166, no. 10, pp. A2209–A2214, 2019, doi: 10.1149/2.1411910jes.
- [19] “Home | ICSD,” *FIZ Karlsruhe GmbH*, 2024. <https://icsd.products.fiz-karlsruhe.de/> (accessed Apr. 10, 2024).
- [20] M. Kitta, T. Kojima, R. Kataoka, K. Yazawa, and K. Tada, “Realizing the Single-Phase Spinel-Type Sodium Titanium Oxide with the Li<sub>4</sub>Ti<sub>5</sub>O<sub>12</sub>-like Structure for Building Stable Sodium-Ion Batteries,” *ACS Appl. Mater. Interfaces*, vol. 12, no. 8, pp. 9322–9331, 2020, doi: 10.1021/acsami.9b21925.
- [21] E. Lee *et al.*, “New Insights into the Performance Degradation of Fe-Based Layered Oxides in Sodium-Ion Batteries: Instability of Fe<sup>3+</sup>/Fe<sup>4+</sup> Redox in  $\alpha$ -NaFeO<sub>2</sub>,” *Chem. Mater.*, vol. 27, no. 19, pp. 6755–6764, Sep. 2015, doi: 10.1021/acs.chemmater.5b02918.
- [22] J. Kugai, H. Mine, S. Seino, T. Nakagawa, T. A. Yamamoto, and H. Yamada, “Effects of sodium nitrate and heat treatment atmosphere on the synthesis of  $\alpha$ -NaFeO<sub>2</sub> layered oxide,” *Mater. Chem. Phys.*, vol. 249, Jul. 2020, doi: 10.1016/J.MATCHEMPHYS.2020.122948.
- [23] D. Yusupov *et al.*, “Fluorite Formation in Poplar Leaves (*Populus balsamifera* L.) in an HF-Polluted Area,” *Water, Air, Soil Pollut.*, vol. 232, 2021, doi: 10.1007/s11270-021-05279-w.
- [24] S. Roberts, L. Chen, B. Kishore, C. E. J. Dancer, M. J. H. Simmons, and E. Kendrick,

- “Mechanism of gelation in high nickel content cathode slurries for sodium-ion batteries,” *J. Colloid Interface Sci.*, vol. 627, pp. 427–437, 2022, doi: 10.1016/j.jcis.2022.07.033.
- [25] M. Fehse *et al.*, “The Fe<sup>4+</sup>/3<sup>+</sup> Redox Mechanism in NaFeO<sub>2</sub>: A Simultaneous Operando Nuclear Resonance and X-ray Scattering Study,” *Batter. Supercaps*, vol. 3, no. 12, pp. 1341–1349, Aug. 2020, doi: 10.1002/BATT.202000157.
- [26] M. Kim, H. Kim, M. Cho, and D. Kim, “Theoretical understanding of oxygen stability in Mn-Fe binary layered oxides for sodium-ion batteries,” *J. Mater. Chem. A*, pp. 11101–11109, 2022, doi: 10.1039/d2ta01747d.
- [27] R. J. Clément *et al.*, “Structurally stable Mg-doped P2-Na<sub>2</sub>/3Mn<sub>1</sub>-YMg<sub>y</sub>O<sub>2</sub> sodium-ion battery cathodes with high rate performance: Insights from electrochemical, NMR and diffraction studies,” *Energy Environ. Sci.*, vol. 9, no. 10, pp. 3240–3251, 2016, doi: 10.1039/c6ee01750a.
- [28] A. J. B. Larry R. Faulkner, *Electrochemical Methods: Fundamentals and Applications*, 2nd Editio. Wiley, 2000.
- [29] W. Wepner and R. A. Huggins, “Determination of the Kinetic Parameters of Mixed-Conducting Electrodes and Application to the System Li<sub>3</sub>Sb,” *J. Electrochem. Soc.*, vol. 124, no. 10, p. 1569, 1977.
- [30] B. Kang and G. Ceder, “Battery materials for ultrafast charging and discharging,” *Nature*, vol. 458, no. 7235, pp. 190–193, 2009, doi: 10.1038/nature07853.
- [31] M. Armand and J. M. Tarascon, “Building better batteries,” *Nature*, vol. 451, no. 7179, pp. 652–657, 2008, doi: 10.1038/451652a.



# **4. Transition-metal doping in manganese-rich *P2*-type layered oxides**



4. Transition-metal doping in manganese-rich <i>P2</i> -type layered oxides.....	151
4.1. <i>P2</i> -type transition metal layered oxides .....	154
4.2. Doping on cathode materials .....	156
4.3. Titanium, iron and copper as doping agents .....	159
4.4. Synthesis and characterisation .....	160
4.4.1. Synthesis .....	161
4.4.2. Rietveld refinements .....	163
4.4.3. Morphology and composition .....	169
4.4.4. Structural stability in contact with air and water .....	172
4.5. Electrochemical performance .....	176
4.5.1. Galvanostatic measurements.....	177
4.5.2. Cyclic-voltammetry .....	181
4.5.3. Galvanostatic intermittent titration technique.....	188
4.5.4. Ex-situ XRD diffraction.....	191
4.6. Conclusion.....	197
4.7. References .....	200

The importance of cathode research in sodium-ion batteries, and the various types of technologies and approaches were presented and compared in Chapter 3. Together with these, the reason for the investigation of transition-metal oxides, as well as the various types were discussed with their advantages and disadvantages. In this chapter, we aim to understand the advantages and limitations of *P2*-type transition-metal layered oxides and approaches to overcome them, such as doping with titanium, iron and copper, as well as the research conducted on some of these approaches.

#### 4.1. *P2*-type transition metal layered oxides

*P2*-type manganese transition metal oxides (NMNOs) have emerged as highly promising cathode materials for sodium-ion batteries. [1] The *P2* structure, characterised by its layered arrangement conducive to efficient sodium ion diffusion, provides an excellent framework for enhancing battery performance. [2] Incorporating nickel into these manganese-based oxides significantly boosts their electrochemical properties, making them suitable for high-performance NIBs. [3]–[5]

These materials are structured with alternating layers of sodium ions and transition metal oxides, a configuration that is particularly advantageous for sodium ion mobility, which is crucial for the battery's efficiency and stability. Regarding sodium mobility, *P2*-type phases tend to perform better than *O3*-type due to the existence of lower energy ionic conduction pathways. While in an *O3*-type phase, the sodium ion jumps from one octahedral coordination shell to the adjacent *via* crossing through the octahedral-tetrahedral sites, as illustrated in Figure 4.1. This imposes a relatively high activation energy barrier. [6] On the

other hand, in *P2*-type layered phases, sodium ions are coordinated in a tetrahedral shell, sharing rectangular faces and thus, providing easy passages for sodium transport, contributing to lower activation energy. [7] Adding to that, the presence of Jahn-Teller distortions of active cations or sodium/vacancy ( $\text{Na}^+/\square$ ) ordering will affect the activation barrier for sodium mobility. [7]

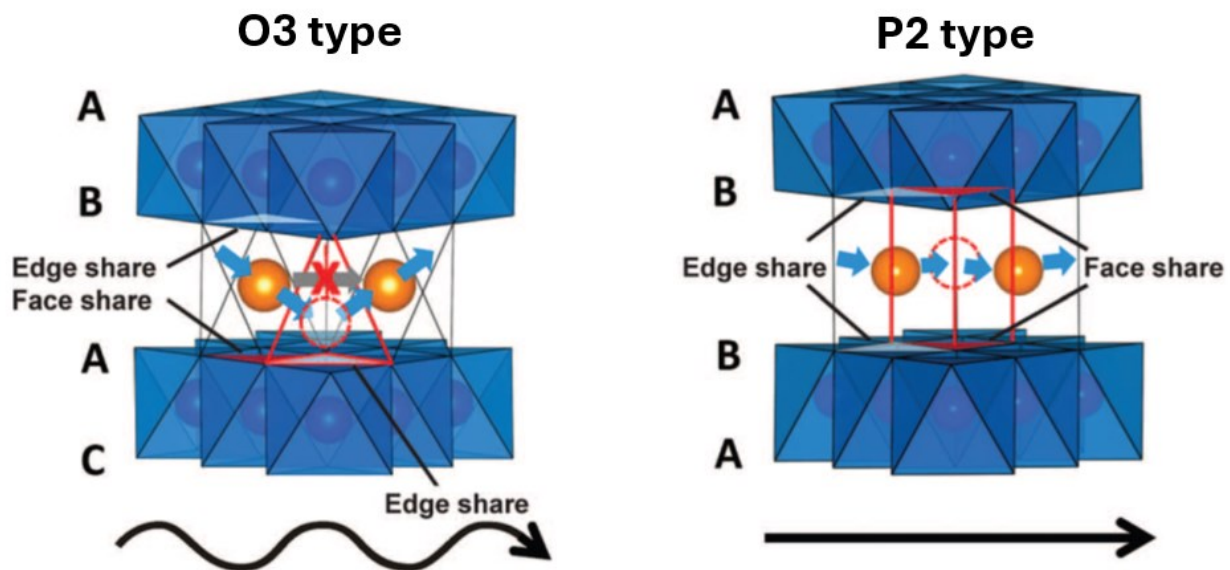


Figure 4.1 – Illustration of the sodium ion pathway in an O3 and P2-type structure [4]

Nickel, as an electrochemically active element, contributes to higher redox activity, and it usually undergoes a two-electron process, resulting in increased energy density. Moreover, nickel promotes a  $\text{Na}^+/\square$  disordering and promotes better ion mobility. [8] This is particularly significant given the tendency of manganese-based cathodes to undergo Jahn-Teller distortion, which can lead to structural degradation. [9] Nickel doping mitigates this issue, improving the material's stability and performance over long-term use. [10] The nickel content not only enhances the redox potential but also contributes to structural stability, resulting in improved battery performance. These properties are critical for the practical

application of NIBs, making nickel-doped *P2*-type NMNOs highly desirable for commercial energy storage solutions.

## 4.2. Doping on cathode materials

One of the primary effects of cationic dopants is the enhancement of structural stability. Manganese-rich cathodes often suffer from phase transitions and structural degradation during repeated charge-discharge cycles. [17] Dopants such as nickel, cobalt, magnesium, and aluminium can help stabilise the structure by mitigating the Jahn-Teller distortion associated with  $Mn^{3+}$  ions. [18], [19] Another significant impact of cationic doping is improved electrochemical performance.

*P2*-type manganese-rich layered transition metal oxides have gained attention due to their high capacity and favourable electrochemical properties. In *P2*-type structures, sodium ions occupy two distinct sites where they share the faces of the  $MO_6$  octahedra ( $Na_f$ ) or the edges ( $Na_e$ ) of the  $MO_6$  octahedra. [11] The relative occupation of the two sites is governed by the complex interaction between  $Na^+ - Na^+$  repulsion,  $Na^+ - M^+$  interaction, and *TM* charge ordering. [12] Ordering of  $Na^+/\square$  superstructures results in distinct potential *plateaux* in galvanostatic curves, resulting in lower  $Na^+$  diffusion coefficients, up to two orders of magnitude as well as reduced ionic transport. [13] This phenomenon results in a fast capacity loss during cycling. This behaviour is common in various *P2*-type transition metal oxides such as  $Na_xMnO_2$  and  $Na_xMn_{0.67}Ni_{0.33}O_2$ . [14]

The overall occupancy ratio between the two sodium sites leads to several distinct patterns of in-plane  $Na^+/\square$  ordering: (i) honeycomb, (ii) diamond, (iii) row, and (iv) large zigzag (Figure 4.2).

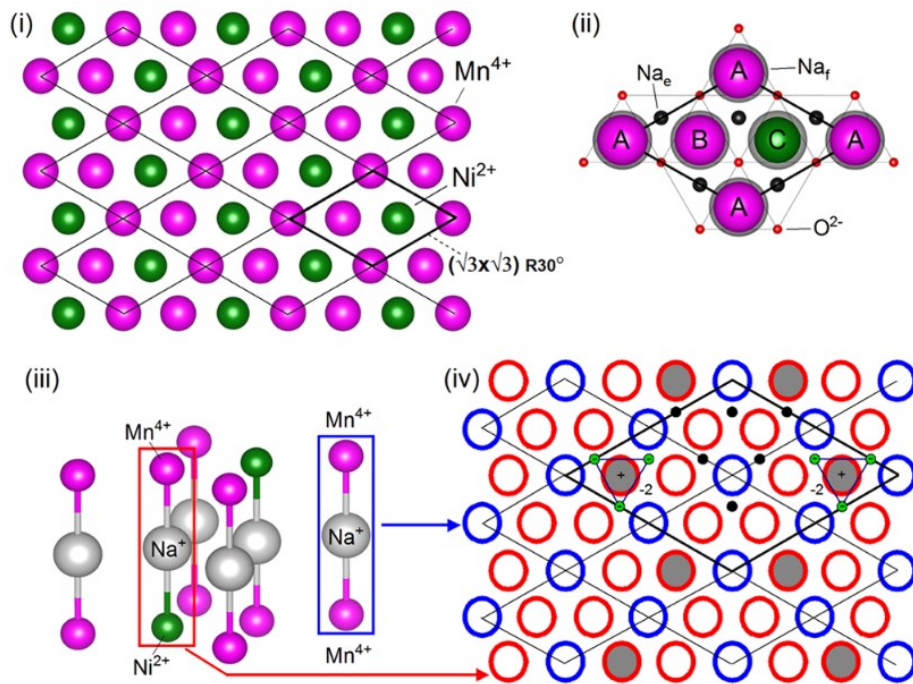


Figure 4.2 – Illustration of a honeycomb type  $\text{Na}^+/\square$  ordering with  $\text{Mn}^{4+}$  in magenta and  $\text{Ni}^{2+}$  in green (i), a diamond type  $\text{Na}^+/\square$  ordering with  $\text{Na}_f$  in grey and  $\text{Na}_e$  in black and oxygen in red (ii), a row type  $\text{Na}^+/\square$  ordering showing Mn-Mn dumbbells in a red box and Mn-Ni dumbbells in a red box (iii) and a large zigzag type  $\text{Na}^+/\square$  ordering (iv) [14]

(i) Transition metal plane in  $\text{Na}_{0.67}\text{Mn}_{0.67}\text{Ni}_{0.33}$  showing the  $\text{Mn}^{4+}$  (magenta) and  $\text{Ni}^{2+}$  (green) ordering described by the  $(\sqrt{3} \times \sqrt{3})\text{-R}30^\circ$  (black diamond; also called large hexagonal unit cell) of the underlying hexagonal plane. (ii) Schematic of the large hexagonal unit cell showing: three unique transition metal sites (*i.e.*, A, B and C), face-sharing sodium ( $\text{Na}_f$ ; grey) underneath each transition metal and edge-sharing sodium ( $\text{Na}_e$ ; black), and oxygen (iii) oblique view of the large hexagonal unit cell ( $\text{Na}_e$  and oxygen omitted) showing the Mn-Mn (blue box) and Mn-Ni (red box) dumbbells formed with  $\text{Na}_f$  sites (iv)  $(\sqrt{3} \times \sqrt{3})\text{R}30^\circ$  from (i) reconstructed to indicate the two unique  $\text{Na}_f$  sites (Mn-Mn or Mn-Ni) matching the box colours used in (iii). Fluorescent green dots indicate three  $\text{Na}_e$  vacancies surrounding one filled  $\text{Na}_f$  site forming a  $(\text{V}_3\text{Na}_f)_2^-$  cluster.

A large difference in the ionic radii of the *TM* is favourable to forming an ordered arrangement. In contrast, small differences in the ionic radii of *TM* are favourable to a disordered arrangement of  $\text{Na}^+$  and  $\square$ . In Johnson, *et al.*, it was found that if a difference between the ionic radii in sodium and transition-metal layered oxides is higher than 15 %, an ordered structure is expected. [14]

A critical area of research within these materials is the effect of cationic dopants when they replace elements in the transition metal layer. These dopants can significantly influence the structural stability, electrochemical performance, and overall efficiency of the cathode. [15] Figure 4.3, illustrates the beneficial effect of smoothing the *plateaux* and decreasing capacity fading when  $\text{Na}_x\text{CoO}_2$  is doped with manganese resulting in  $\text{Na}_x\text{Co}_{2/3}\text{Mn}_{1/3}\text{O}_2$ . [11]

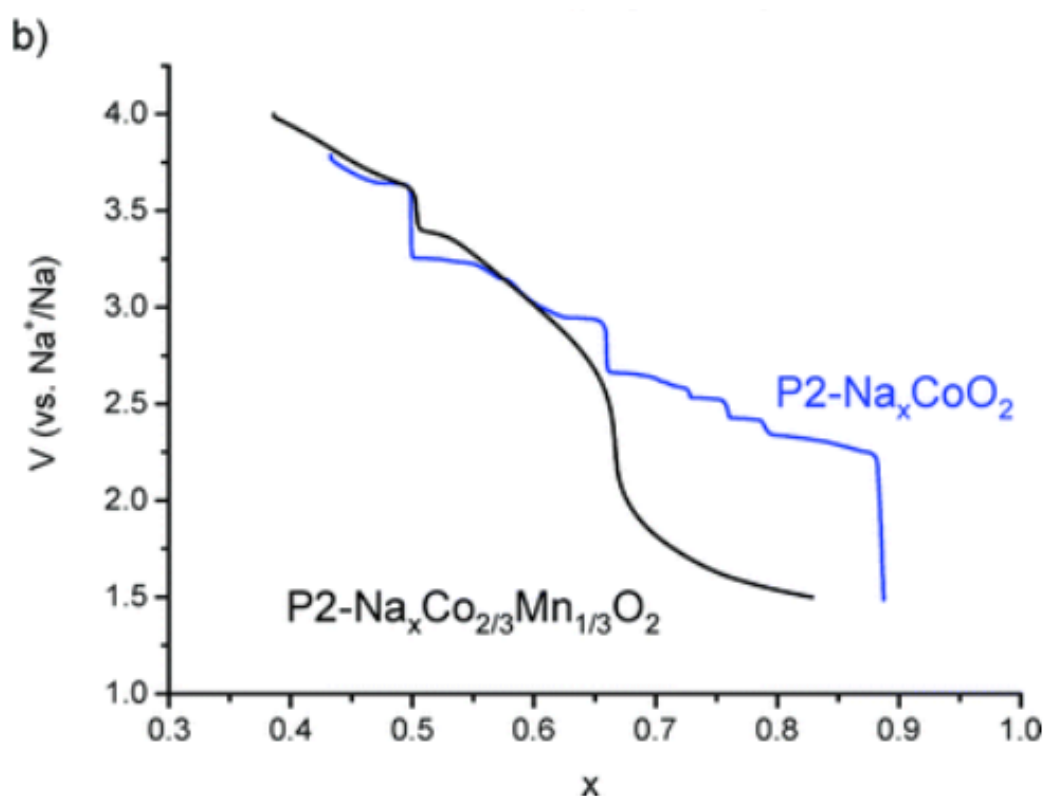


Figure 4.3 – Comparison between the first discharge galvanostatic curve of  $\text{P2-Na}_x\text{CoO}_2$  (●) and  $\text{P2-Na}_x\text{Co}_{2/3}\text{Ni}_{1/3}\text{O}_2$  (●) [11]

Cationic doping involves substituting a portion of the transition metal ions in the cathode material with other metal ions. This substitution can lead to substantial improvements in the performance of *P2*-type manganese-rich layered oxides used as cathodes in sodium-ion batteries. The choice of dopant, its concentration, and the specific site it occupies within the structure are crucial factors that determine the extent of these improvements. [16]

One of the primary effects of cationic dopants is the enhancement of structural stability. Manganese-rich cathodes often suffer from phase transitions and structural degradation during repeated charge-discharge cycles. [17] Dopants such as nickel, cobalt, magnesium, and aluminium can help stabilise the structure by mitigating the Jahn-Teller distortion associated with  $Mn^{3+}$  ions. [18], [19] Another significant impact of cationic doping is the improvement in electrochemical performance.

Research has also focused on the synergistic effects of multiple dopants. For example, co-doping with nickel and cobalt can simultaneously enhance the structural integrity and electrochemical performance, resulting in cathode materials with superior overall characteristics. [20]

### **4.3. Titanium, iron and copper as doping agents**

Transition metal oxides are pivotal in the development of high-performance cathodes for sodium-ion batteries. Specifically, titanium, iron, and copper dopants have shown promising effects in improving the performance of these materials. [10]

Titanium doping in transition metal oxides is particularly advantageous due to its ability to enhance structural stability.  $Ti^{4+}$  ions are known for their strong bond formation and can substitute for other transition metals in the oxide lattice, reducing structural distortion during electrochemical cycling. [21] This stabilisation is crucial for maintaining capacity over extended cycles. Titanium's high valence state also helps in reducing the Jahn-

Teller distortion commonly associated with manganese-based cathodes, thereby preserving the structural integrity of the material. [18], [22]

Iron is another effective dopant for transition metal oxides in NIBs cathodes. Fe(III) and Fe(IV) can participate in redox reactions, contributing to the overall capacity of the battery. [23] Iron doping can also improve electronic conductivity, which is beneficial for enhancing rate capability. [24] The versatility of iron in multiple oxidation states enables it to effectively enhance the redox activity and stability of the cathode material. [24], [25]

Copper doping in transition metal oxides offers unique benefits, particularly in enhancing electronic conductivity and reducing polarisation during cycling. Cu(II) ions can substitute for other transition metals, leading to a more conductive network within the cathode material. [26] This enhanced conductivity leads to improved rate performance and higher power densities. Copper's capacity to transition between multiple oxidation states,  $\text{Cu(II)} \rightleftharpoons \text{Cu(III)}$ , contributes to additional redox processes, thereby further enhancing the energy density of the cathode. [10], [26]

Moreover, combining these dopants can lead to synergistic effects. For instance, co-doping with Ti and Fe or Cu can simultaneously stabilise the structure and enhance electronic conductivity, resulting in cathode materials with superior overall performance. Such multi-doping strategies are being explored to maximise the benefits of each dopant and achieve a balanced enhancement of all critical battery parameters. [27]

#### 4.4. Synthesis and characterisation

In this chapter, *P2*-type  $\text{Na}_{0.67}\text{Mn}_{0.8}\text{Ni}_{0.2}\text{O}_2$  (NMNO),  $\text{Na}_{0.67}\text{Mn}_{0.8}\text{Ni}_{0.15}\text{Ti}_{0.05}\text{O}_2$  (NMNTO),  $\text{Na}_{0.67}\text{Mn}_{0.8}\text{Ni}_{0.15}\text{Fe}_{0.05}\text{O}_2$  (NMNFO), and  $\text{Na}_{0.67}\text{Mn}_{0.8}\text{Ni}_{0.15}\text{Cu}_{0.05}\text{O}_2$  (NMNCO) were synthesised via the solid-state method, which was optimised for the environmental conditions and equipment available, so that the material was obtained without secondary phases or detectable impurities.

After obtaining pure materials, these were characterised structurally, morphologically, and chemically *via* X-ray diffractometry, scanning electron microscopy and energy-dispersive X-ray spectroscopy and, their electrochemical performance was studied and compared using galvanostatic charge and discharge methods, cyclic-voltammetry, galvanostatic intermittent titration technique and *ex-situ* X-ray diffraction. The resistance of these materials to air and water exposure was also evaluated by exposing them to atmospheric air over one month and by stirring them in water for one and 24 hours.

#### 4.4.1. Synthesis

In this work, we intend to prepare a pure phase of *P2*-type  $\text{Na}_{0.67}\text{Mn}_{0.8}\text{Ni}_{0.15}\text{Ti}_{0.05}\text{O}_2$ ,  $\text{Na}_{0.67}\text{Mn}_{0.8}\text{Ni}_{0.15}\text{Fe}_{0.05}\text{O}_2$  and,  $\text{Na}_{0.67}\text{Mn}_{0.8}\text{Ni}_{0.15}\text{Cu}_{0.05}\text{O}_2$ . In the development of *P2* and *O2*-type transition-metal oxides, manganese, nickel, iron, and, to a certain extent, copper can be adopted as the redox-active elements to provide capacity at a relatively low cost. [28]

One effective strategy to encourage the formation of a *P2*-type phase is the reduction of sodium content (Figure 4.4a). [29] Another pivotal approach involves the utilisation of *P2*-promoting transition metals such as manganese (Figure 4.4b). [30] Notably, when manganese constitutes 80% of the total transition metal content, it significantly promotes the arrangement in a *P2* phase. [31]

However, introducing other elements, such as titanium, iron, or copper, may lead to promoting an *O3* phase. [30], [31] This potential shift necessitates careful consideration to achieve the desired phase during the synthesis process.

To synthesise  $\text{Na}_{0.67}\text{Mn}_{0.8}\text{Ni}_{0.15}\text{Ti}_{0.05}\text{O}_2$  (NMNTO),  $\text{Na}_{0.67}\text{Mn}_{0.8}\text{Ni}_{0.15}\text{Fe}_{0.05}\text{O}_2$  (NMNFO), and  $\text{Na}_{0.67}\text{Mn}_{0.8}\text{Ni}_{0.15}\text{Cu}_{0.05}\text{O}_2$  (NMNCO), the procedure outlined in Chapter 2 was followed. Following this synthesis, it is essential to verify the presence of a pure *P2*-type phase. Accurate phase identification post-synthesis is critical to confirm the successful

formation of the intended *P2*-type structure and to understand the influence of any elemental substitutions on the phase stability.

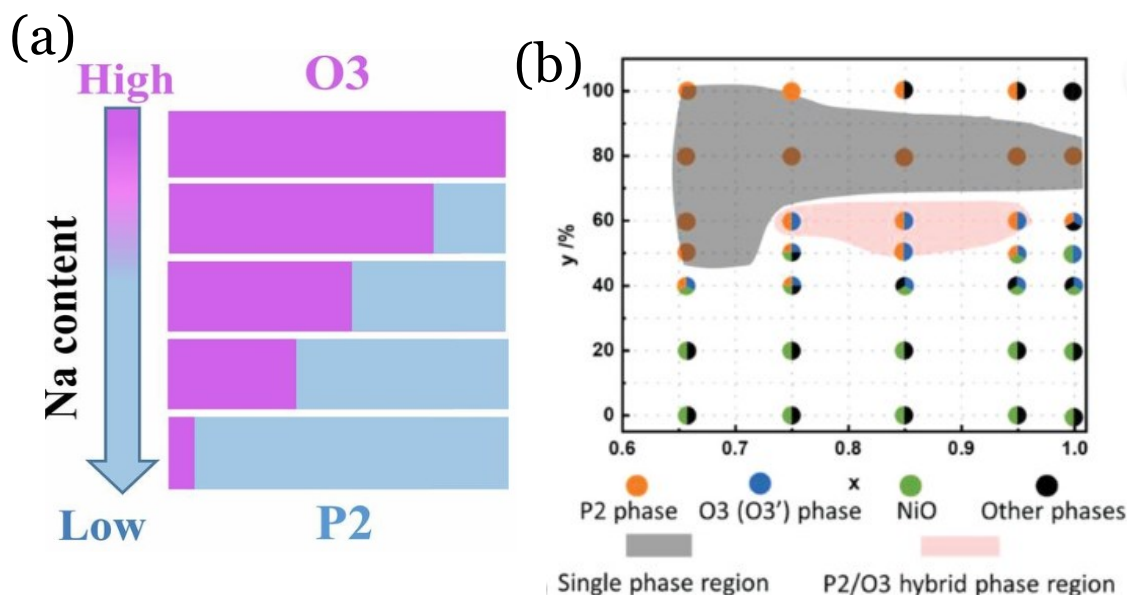


Figure 4.4 – Influence of Na content in the formation of an *O3* or *P2*-type structure (a) and influence of Mn and Ni content in the formation of an *O3* or *P2*-type structure, where the x-axis is the sodium content and the y-axis is the manganese content. (b) [30], [31]

To obtain pure  $\text{Na}_{0.67}\text{Mn}_{0.8}\text{Ni}_{0.15}\text{Ti}_{0.05}\text{O}_2$  (NMNTO),  $\text{Na}_{0.67}\text{Mn}_{0.8}\text{Ni}_{0.15}\text{Fe}_{0.05}\text{O}_2$  (NMNFO),  $\text{Na}_{0.67}\text{Mn}_{0.8}\text{Ni}_{0.15}\text{Cu}_{0.05}\text{O}_2$  (NMNCO) belonging to the space group  $P 6_3/mmc$ . Figure 4.4a shows a scheme of the effect of the sodium content on stabilising the *O3* and *P2* phases. The lower the sodium content, the more likely the stabilisation of a *P2* phase is caused by the electrostatic repulsion of  $\text{O}_2$  in the transition metal layers. [30] Figure 4.4b, shows how 80 % of manganese content in the transition metal layers, can stabilise the *P2*-phase regardless of the sodium content in the structure, showing that, apart from the sodium content, some transition metals may promote a *P2* or an *O3*-phase. [31] The calcination temperature was 900 °C for 12 hours as used in literature. [31] Further experimental details can be found in section 2. In Figure 4.5, the diffractograms of all NMNTO, NMNFO, and

NMNCO are shown and compared with the *O3*-type and *P2*-type  $\text{Na}_{0.67}\text{Mn}_{0.8}\text{Ni}_{0.2}\text{O}_2$ . After synthesis, no traces of the *O3*-type phase or other impurity are detected. The reference material diffractograms were obtained from the ICSD. [32]

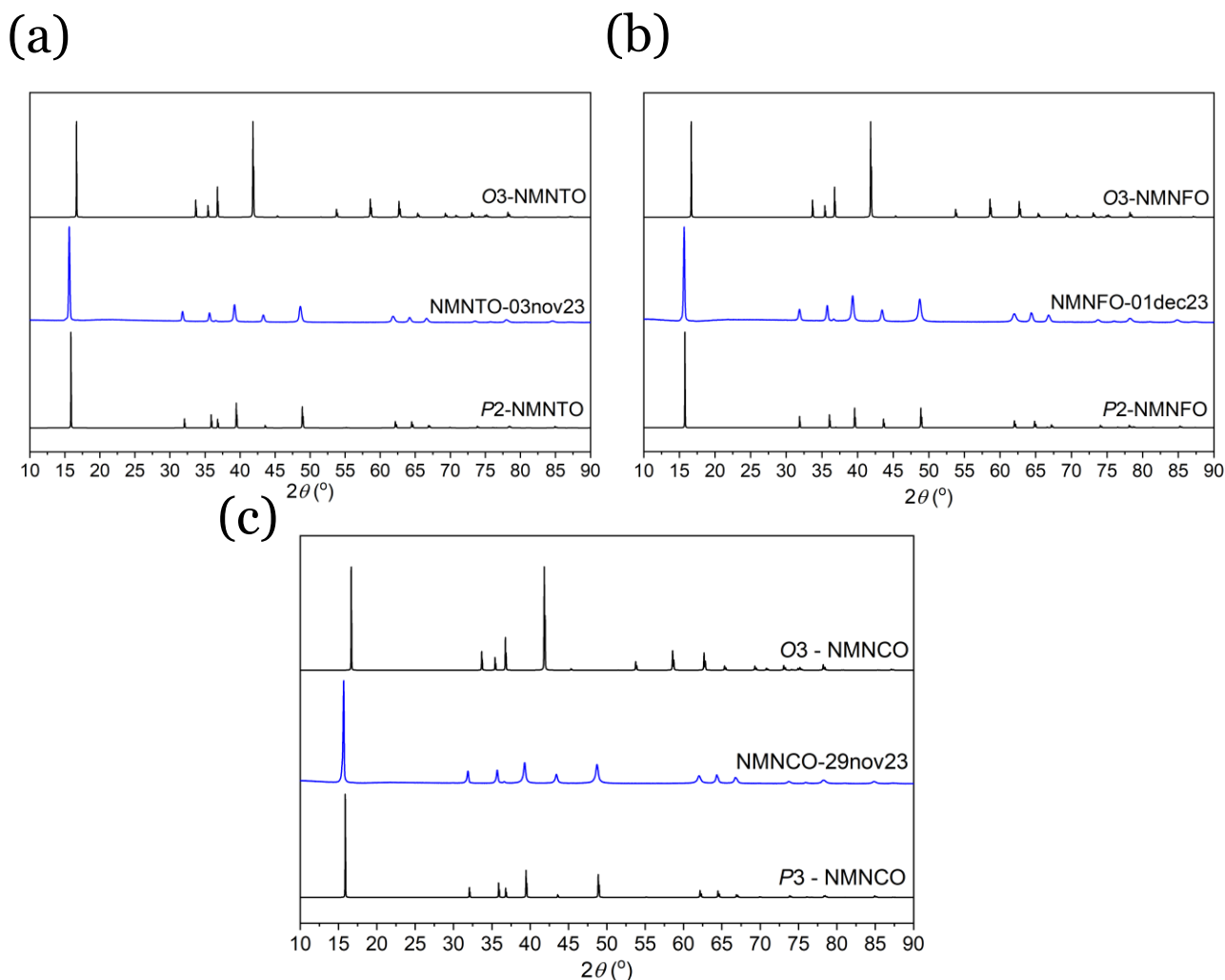


Figure 4.5 – X-ray diffractograms of all NMNTTO, NMNFO, and NMNCO are shown and compared with the *O3*-type and *P2*-type  $\text{Na}_{0.67}\text{Mn}_{0.8}\text{Ni}_{0.2}\text{O}_2$  obtained from ICSD [32]

#### 4.4.2. Rietveld refinements

All NMNTTO, NMNFO and NMNCO, result from the replacement of nickel (II) 6-coordinated octahedral (83 pm) for titanium (II) 6-coordinated octahedral (81 pm), iron (III) 6-coordinated octahedral (78.5 pm), and copper (II) 6-coordinated octahedral (87 pm),

respectively. [33] A schematic representation of NMNO is shown in Figure 4.6, which has a similar structure to NMNTO, NMNFO and, NMNCO except for unit cell parameters.

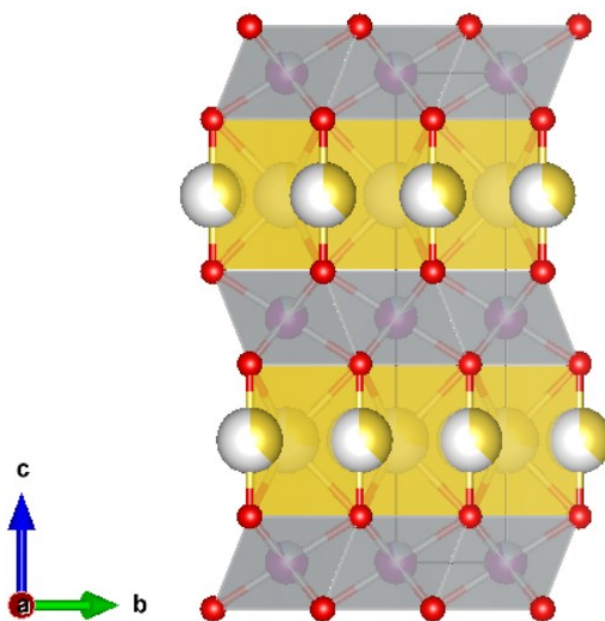


Figure 4.6 – Structure of  $\text{Na}_{0.67}\text{Mn}_{0.8}\text{Ni}_{0.2}\text{O}_2$  obtained with VESTA where oxygen is represented in red, sodium is represented in yellow, manganese is represented in purple and nickel is represented in dark grey.

The lattice parameters of NMNTO were obtained using Rietveld refinement (Figure 4.7). The refined parameters included the zero, lattice, and profile parameters, atomic positions, and isotropic displacement parameters ( $U_{iso}$ ). The lattice parameters were determined to be  $a = b = 2.8905(8) \text{ \AA}$ ,  $c = 11.1700(6) \text{ \AA}$ ,  $\alpha = 90^\circ$ ,  $\beta = 90^\circ$  and  $\gamma = 120^\circ$ , which are in agreement with the unit cell parameters reported in the literature. [34] The refined parameters can be found in Table 4.1. The goodness-of-fit,  $\chi^2$ , was found to be 7.73 and the  $R$  factors such as weighted profile  $R$ -factor,  $R_{wp}$ , and expected  $R$  factor,  $R_{exp}$ , were found to be 3.600 and 2.1553 %, respectively. In this case, the data was collected in a lab diffractometer in reflection mode using conventional Cu  $K_{\alpha 1}$  and Cu  $K_{\alpha 2}$  sources which influenced the goodness of the refinement.

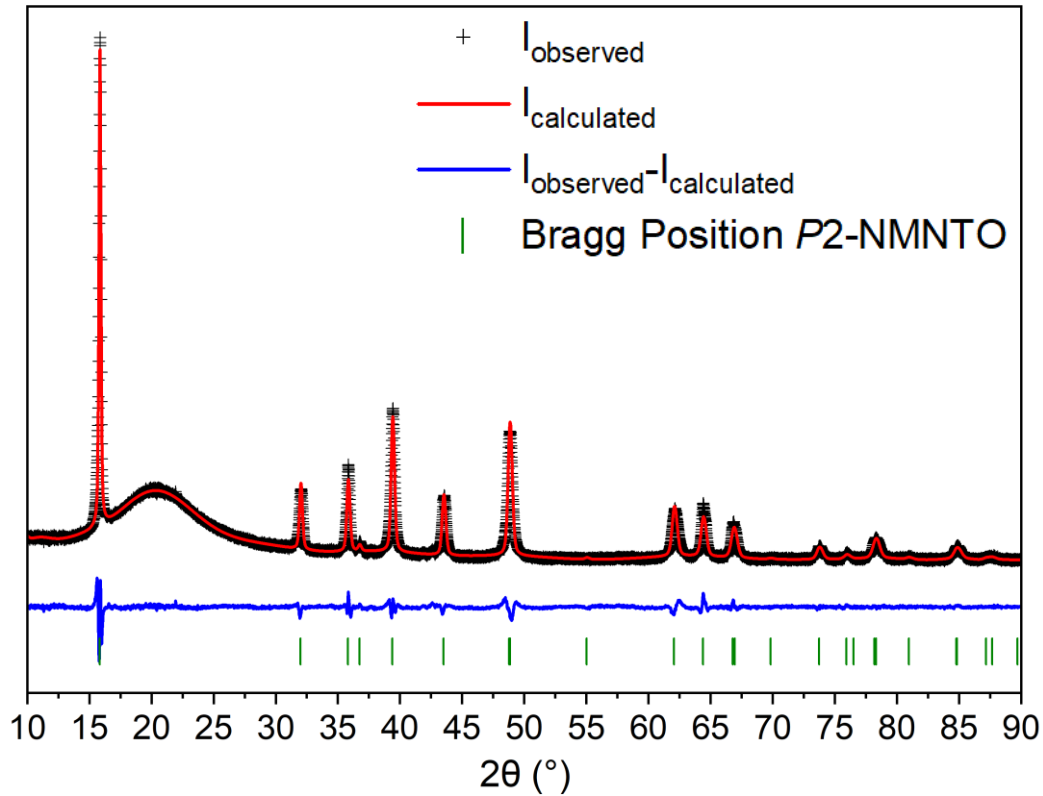


Figure 4.7 – Rietveld refinement of P2-NMNTiO

Table 4.1 - Cell parameters, goodness-of-fitness parameters and phase composition of P2-NMNTiO, obtained from Rietveld refinements on lab XRD data.

Atom	<i>x</i>	<i>y</i>	<i>z</i>	Multiplicity	Occupancy	<i>U</i> <sub>iso</sub> (Å <sup>2</sup> )
Na1	0.3333	0.6667	0.2500	2	0.3400	0.730(3)
Na2	0.0000	0.0000	0.2500	2	0.3300	0.166(6)
Ni1	0.0000	0.0000	0.0000	2	0.1500	0.704(6)
Mn1	0.0000	0.0000	0.0000	2	0.8000	0.601(8)
Ti1	0.0000	0.0000	0.0000	2	0.0500	0.132(5)
O1	0.3333	0.6667	0.1030(2)	4	1.0000	0.251(6)

**Na<sub>0.67</sub>Mn<sub>0.8</sub>Ni<sub>0.15</sub>Ti<sub>0.05</sub>O<sub>2</sub> – space group *P* 6<sub>3</sub>/*m m c***

***a* = *b* = 2.8905(8) Å; *c* = 11.1700(6) Å; *α* = 90 °; *β* = 90 °; *γ* = 120 °**

***χ*<sup>2</sup> = 7.76; *R*<sub>wp</sub> = 3.600 %; *R*<sub>exp</sub> = 2.1553 %**

The lattice parameters of NMNFO were obtained using Rietveld refinement (Figure 4.8). The refined parameters included the zero, lattice, and profile parameters, atomic positions, and isotropic displacement parameters ( $U_{\text{iso}}$ ). The lattice parameters were determined to be  $a = b = 2.8853(5)$  Å,  $c = 11.1692(6)$  Å,  $\alpha = 90^\circ$ ,  $\beta = 90^\circ$ , and  $\gamma = 120^\circ$ , as expected. These refined parameters are detailed in Table 4.2. The goodness-of-fit ( $\chi^2$ ) was calculated to be 6.930, with the weighted profile R-factor ( $R_{\text{wp}}$ ) and expected R-factor ( $R_{\text{exp}}$ ) being 3.222 % and 3.718 %, respectively. The data was collected in reflection mode using conventional Cu  $K_{\alpha 1}$  and Cu  $K_{\alpha 2}$  sources, which influenced the refinement quality.

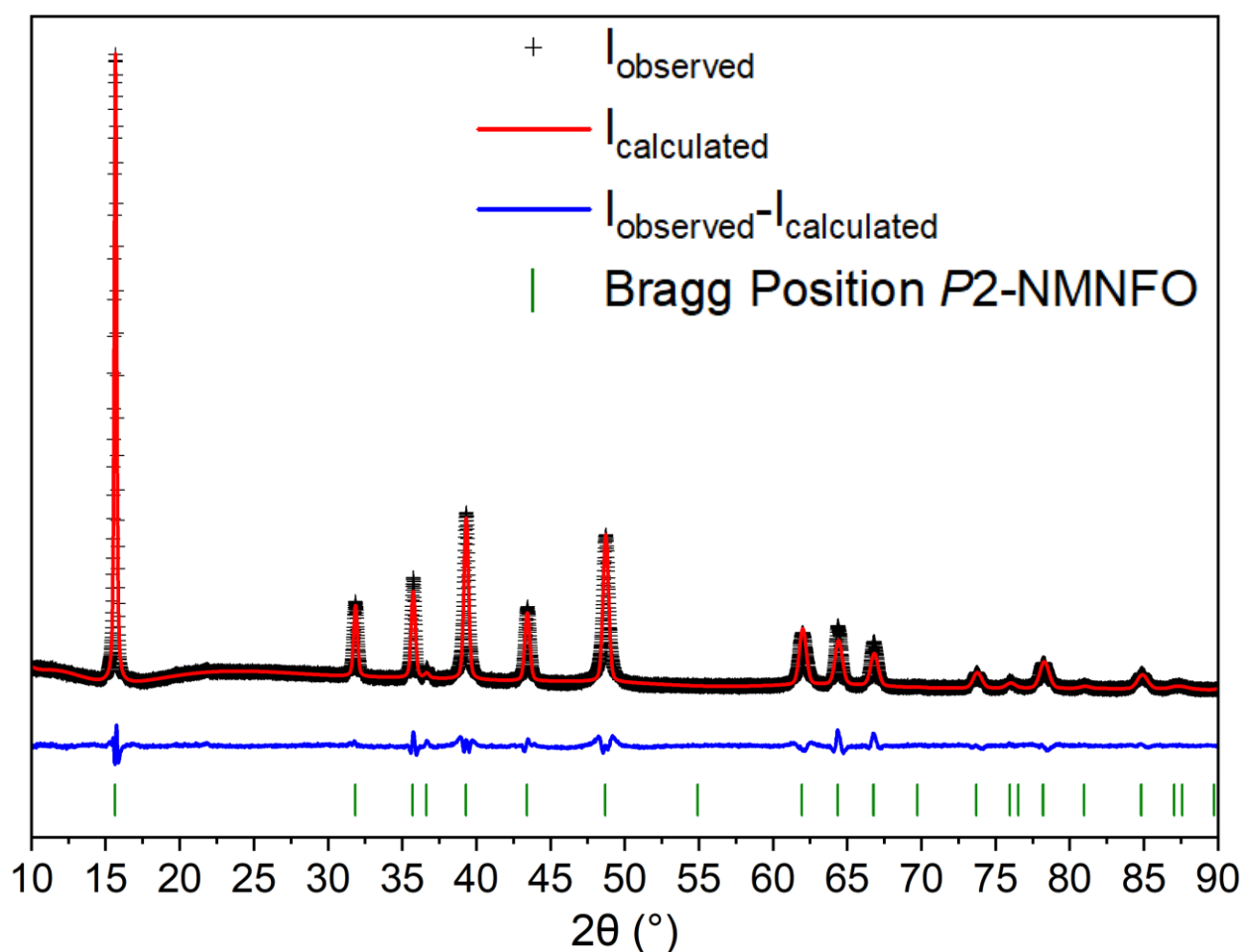


Figure 4.8 - Rietveld refinement of P2-NMNFO

Table 4.2 - Cell parameters, goodness-of-fitness parameters and phase composition of P2-NMNFO, obtained from Rietveld refinements on lab XRD data.

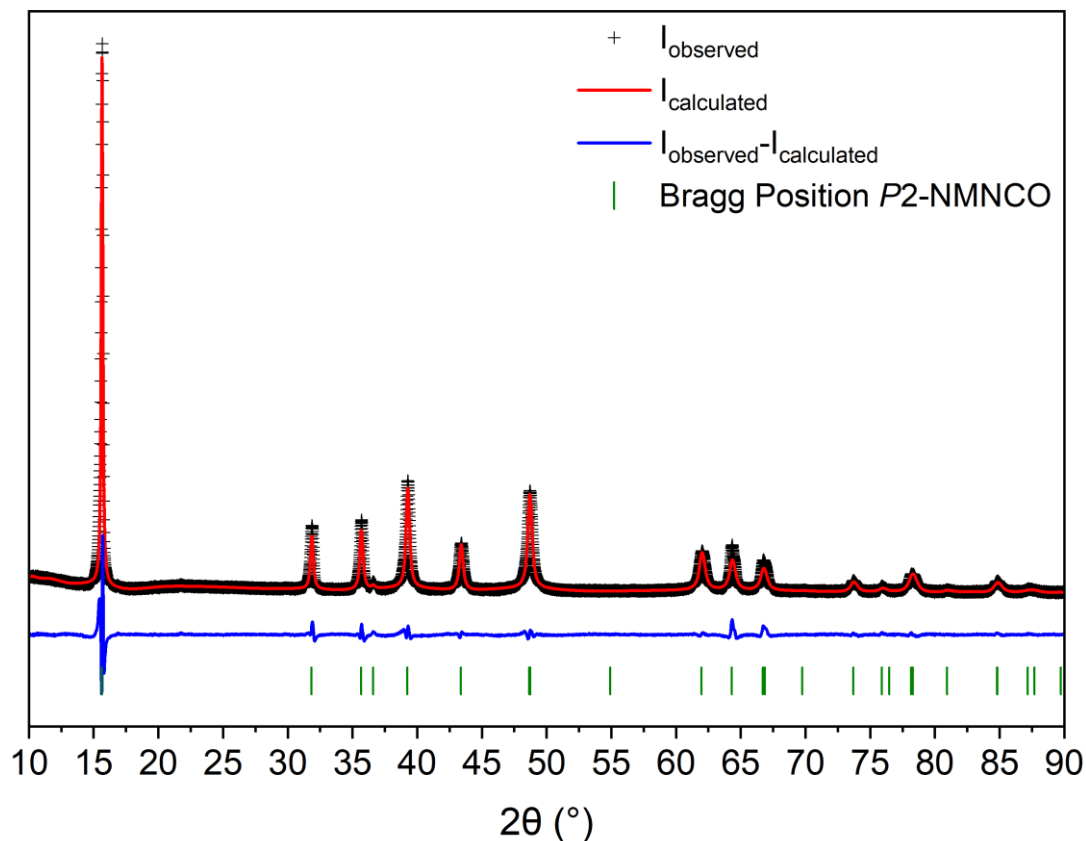
Atom	<i>x</i>	<i>y</i>	<i>z</i>	Multiplicity	Occupancy	<i>U</i> <sub>iso</sub> (Å <sup>2</sup> )
Na1	0.3333	0.6667	0.7500	2	0.3400	0.730(3)
Na2	0.0000	0.0000	0.2500	2	0.3300	0.166(6)
Ni1	0.0000	0.0000	0.0000	2	0.1500	0.704(6)
Mn1	0.0000	0.0000	0.0000	2	0.800	0.701(8)
Fe1	0.0000	0.0000	0.0000	2	0.050	0.132(5)
O1	0.3333	0.6667	0.1029(7)	4	1.000	0.201(7)

<b>Na<sub>0.67</sub>Mn<sub>0.8</sub>Ni<sub>0.15</sub>Fe<sub>0.05</sub> – space group <i>P 6<sub>3</sub>/m m c</i></b>						
<b><i>a</i> = <i>b</i> = 2.8853(5) Å; <i>c</i> = 11.1692(6) Å; α = 90 °; β = 90 °; γ = 120 °</b>						
<b>χ<sup>2</sup> = 7.760; <i>R</i><sub>wp</sub> = 3.600 %; <i>R</i><sub>exp</sub> = 3.000 %</b>						

The lattice parameters of NMNCO were determined using Rietveld refinement, as shown in Figure 4.9. The refined parameters included the graphic's zero error, lattice parameters, profile parameters, atomic positions, and isotropic displacement parameters (*U*<sub>iso</sub>), ensuring a comprehensive and detailed analysis. The lattice parameters were calculated to be *a* = *b* = 2.8853 Å, *c* = 16.13789 Å, and α = β = γ = 90°, indicating a cubic crystal structure. These refined parameters are fully detailed in Table 4.3 for reference and further comparison.

The goodness-of-fit (χ<sup>2</sup>) was calculated to be 14.74, with the weighted profile R-factor (*R*<sub>wp</sub>) and the expected R-factor (*R*<sub>exp</sub>) found to be 4.815 and 7.52 %, respectively, reflecting the quality of the refinement. Data collection was performed in reflection mode, employing conventional Cu K<sub>α1</sub> and Cu K<sub>α2</sub> X-ray sources, which had a significant influence on the refinement quality and the reliability of the results obtained. These results confirm the accuracy and consistency of the structural parameters derived for NMNCO.

Figure 4.9 - Rietveld refinement of *P2*-NMNCOTable 4.3 - Cell parameters, goodness-of-fitness parameters and phase composition of *P2*-NMNCO, obtained from Rietveld refinements on lab XRD data.

Atom	<i>x</i>	<i>Y</i>	<i>z</i>	Multiplicity	Occupancy	$U_{iso}$ (Å <sup>2</sup> )
Na1	0.3333	0.6667	0.7500	2	0.3400	0.1019(4)
Na2	0.0000	0.0000	0.2500	2	0.3300	0.0672(8)
Ni1	0.0000	0.0000	0.0000	2	0.1500	0.0202(8)
Mn1	0.0000	0.0000	0.0000	2	0.8000	0.0138(6)
Cu1	0.0000	0.0000	0.0000	2	0.0500	0.0972(3)
O1	0.3333	0.6667	0.0959(8)	4	1.0000	0.0518(7)

**Na<sub>0.67</sub>Mn<sub>0.8</sub>Ni<sub>0.15</sub>Cu<sub>0.05</sub> – space group *P* 6<sub>3</sub>/*m m c***

***a* = *b* = 2.8854(4) Å; *c* = 11.1508(8) Å;  $\alpha$  = 90 °;  $\beta$  = 90 °;  $\gamma$  = 120 °**

**$\chi^2$  = 7.74;  $R_{wp}$  = 3.815 %;  $R_{exp}$  = 3.52 %**

Both NMNTO and NMNFO exhibit relatively similar unit cell dimensions, which are reflected in their comparable (0 0 2) interlayer distances. The unit cell parameters of NMNTO are  $a = b = 2.8905(8) \text{ \AA}$ ,  $c = 11.1700(6) \text{ \AA}$ , and  $d(0\ 0\ 2) = 5.5851 \text{ \AA}$ . By comparison, NMNFO has  $a = b = 2.8854(4) \text{ \AA}$ ,  $c = 11.1508(8) \text{ \AA}$ , and  $d(0\ 0\ 2) = 5.5846 \text{ \AA}$ . This similarity is likely attributed to the comparable ionic radii of 6-coordinated Ti(III) (81 pm) and Fe(III) (78.5 pm) present in pristine NMNTO and NMNFO, respectively. [33]

In contrast, the unit cell parameters of NMNCO are  $a = b = 3.02169 \text{ \AA}$ ,  $c = 16.13789 \text{ \AA}$ , and  $d(0\ 0\ 2) = 5.5754 \text{ \AA}$ . The expansion of the unit cell in NMNCO may be associated with the larger ionic radius of Cu(II) (73 pm). In its pristine state, copper predominantly exists as a bivalent ion, whereas titanium and iron appear as trivalent ions in their respective pristine phases. The lower oxidation state of copper contributes to the elongation of the Cu-O bonds, which in turn leads to an elongation of the c-axis dimension. [35]

In all cases, the occupancy was fixed during refinement as it was observed to converge to negative values, which lack any physical significance. Additionally, it was anticipated that the thermal vibration values ( $U_{iso}$ ) of atoms with similar masses and comparable local environments would remain consistent, as this is a characteristic of such systems. This refinement approach ensures the reliability of the structural data obtained for these materials.

#### 4.4.3. Morphology and composition

The morphology of NMNTO was assessed with field emission electron microscopy (FESEM). The morphology of NMNTO consists of highly agglomerated particles with approximately 1  $\mu\text{m}$  diameter. This is in agreement with the previously reported data in the literature. [36]–[38] Elemental analysis with EDS, shown in Figure 4.10 confirms that Na, Mn, and Ni elements are present in the sample but not titanium.

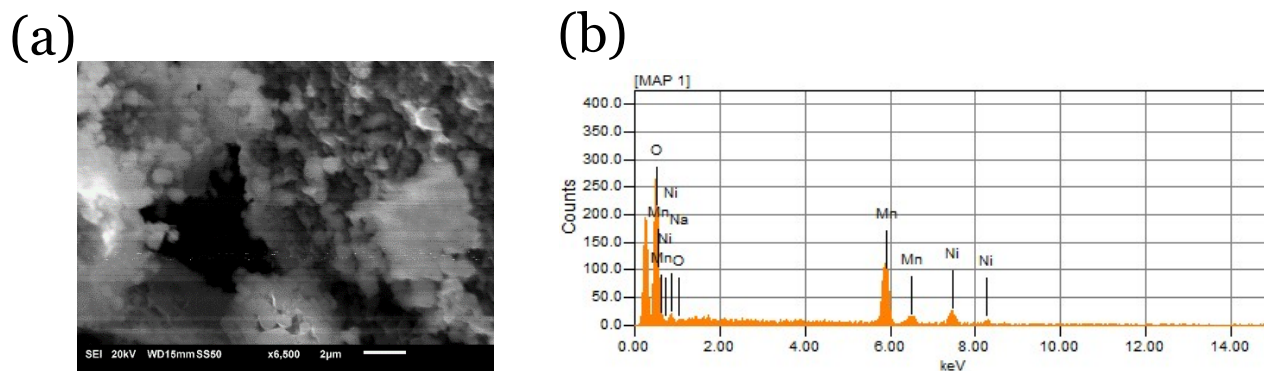


Figure 4.10 – (a) SEM image of NMNTO taken at a magnification of  $\times 6500$ , (b) EDS elemental analysis.

Field emission electron microscopy (FESEM) was carried out in the NMNFO sample (Figure 4.11). The morphology of NMNFO also consists of platelets with approximately 500 nm diameter. Elemental analysis with EDS confirms that Na, Mn, Ni and O elements are present in the sample but not iron.

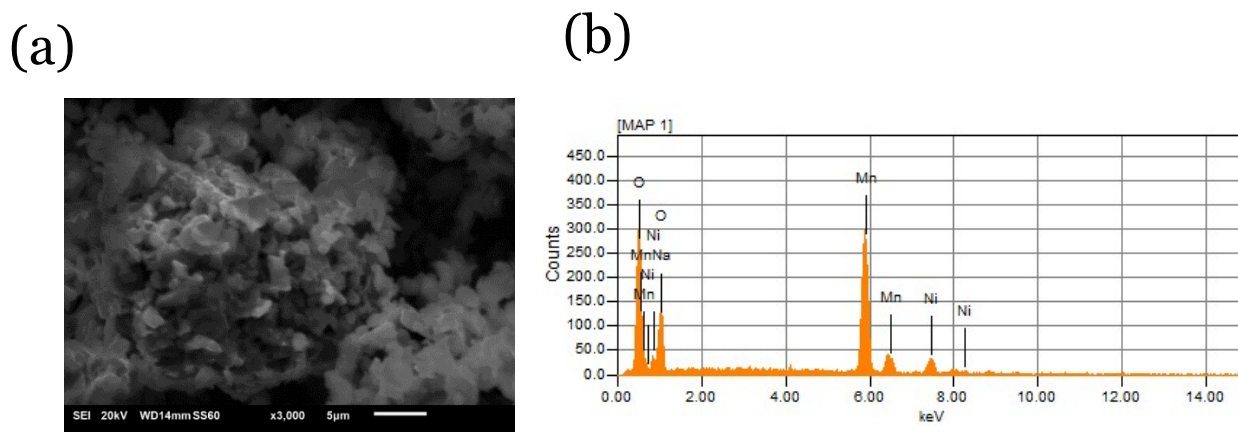


Figure 4.11 – (a) SEM image of NMNFO taken at a magnification of  $\times 6500$ , (b) EDS elemental analysis.

The morphology of NMNCO consists of platelets with approximately 2.5  $\mu\text{m}$  nm diameter, with larger blocks, probably caused by poor grinding (Figure 4.12). Elemental analysis with EDS confirms that Na, Mn, Ni and O elements are present in the sample, but not copper. [39]

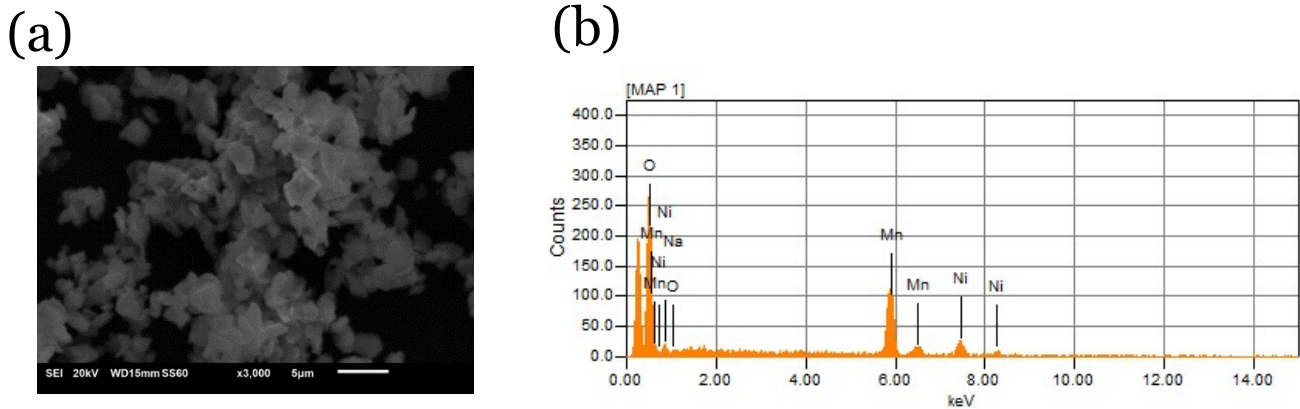


Figure 4.12 – (a) SEM image of NMNTO taken at a magnification of  $\times 6500$ , (b) EDS elemental analysis.

The primary reason titanium, iron, and copper are not detected in these materials using EDS is likely due to their low concentrations in the structure. Additionally, the X-ray emission peaks of iron and copper are close to those of nickel, making it challenging to distinguish these elements under the given conditions. Table 4.4 identifies each element's main X-ray emission peaks in the study. [40]

Table 4.4 – Main emission peaks of all elements used in this chapter, adapted from the EDAX peak identification chart. [40]

(keV)	Z	$K_{\alpha}$	$K_{\beta}$	$K_{ab}$	$L_{\alpha}$	$L_{llab}$	$L_{llab}$	$L_{lab}$
<b>Mn</b>	25	5.898	6.489	6.536	0.637	0.0639	0.650	0.762
<b>Ni</b>	28	7.477	8.263	8.330	0.851	0.853	0.870	1.015
<b>Ti</b>	22	4.510	4.931	4.964	0.452	0.454	0.460	0.530
<b>Fe</b>	26	6.403	7.648	7.708	0.776	0.707	0.721	0.849
<b>Cu</b>	29	8.040	8.904	8.979	0.930	0.933	0.953	1.100
<b>O</b>	8	0.523	0.532	-	-	-	-	-

Adding to the smaller content in the structure, titanium, iron and copper may have not been detected using EDS due to the proximity of the emission peak, mainly  $K_{\alpha}$  of iron (6.403 keV) and copper (8.040 keV) to nickel (7.477 keV). [40] In the case of titanium, the reason

why no emissions are detected can only be justified by the low concentration of titanium in the structure.

#### 4.4.4. Structural stability in contact with air and water

To assess the resilience of the materials to atmospheric conditions, especially, contact with air, these materials were subjected to air exposure for one month with monitoring after 1 hour, 1 week, 2 weeks and a month. To assess the stability when in contact with water, these materials were also stirred in water for 1 hour and 24 hours and dried under vacuum at room temperature. Figure 4.13, shows the X-ray diffractograms of NMNTO before being put in contact with air or water, after one hour, 1 week, 2 weeks and one month in air and 1 hour stirring in water.

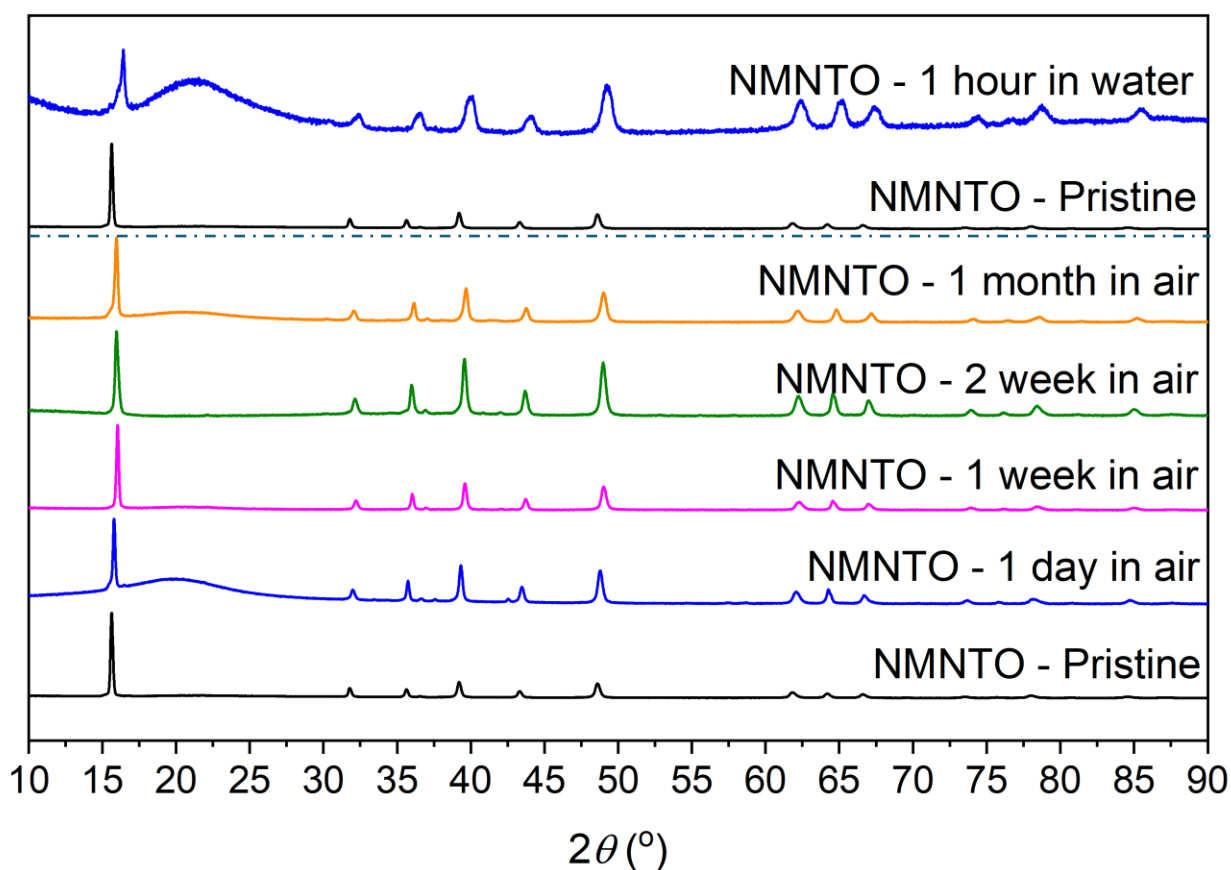


Figure 4.13 - X-ray diffractograms of NMNTO before being put in contact with air or water, after one hour, 1 week, 2 weeks and one month in air and 1 hour stirring in water

Despite some misalignment of the peaks, caused by different sample heights, NMNTO seems to go through very little degradation in contact with the atmosphere. However, NMNTO is not very stable in water as most of the phase with the space group  $P 6_3/m m c$  appears to almost disappear to give place to a busserite phase ( $C 2/m$ ). [41] This degradation is caused by the infiltration of water in the alkali-metal layer of NMNTO. [41] The most intense peak of the busserite diffractogram is below  $2\theta = 10^\circ$ , hence, it is occulted in this diffractogram. [41] A similar process occurs in  $\text{Na}_{0.67}\text{MnO}_2$ . In Figure 4.14, a diffractogram of the *P2*-type  $\text{Na}_{0.67}\text{MnO}_2$  compared with the hydration phase (birnessite) and busserite as well as, a diagram of the hydration and degradation of  $\text{Na}_{0.67}\text{MnO}_2$ , is shown.

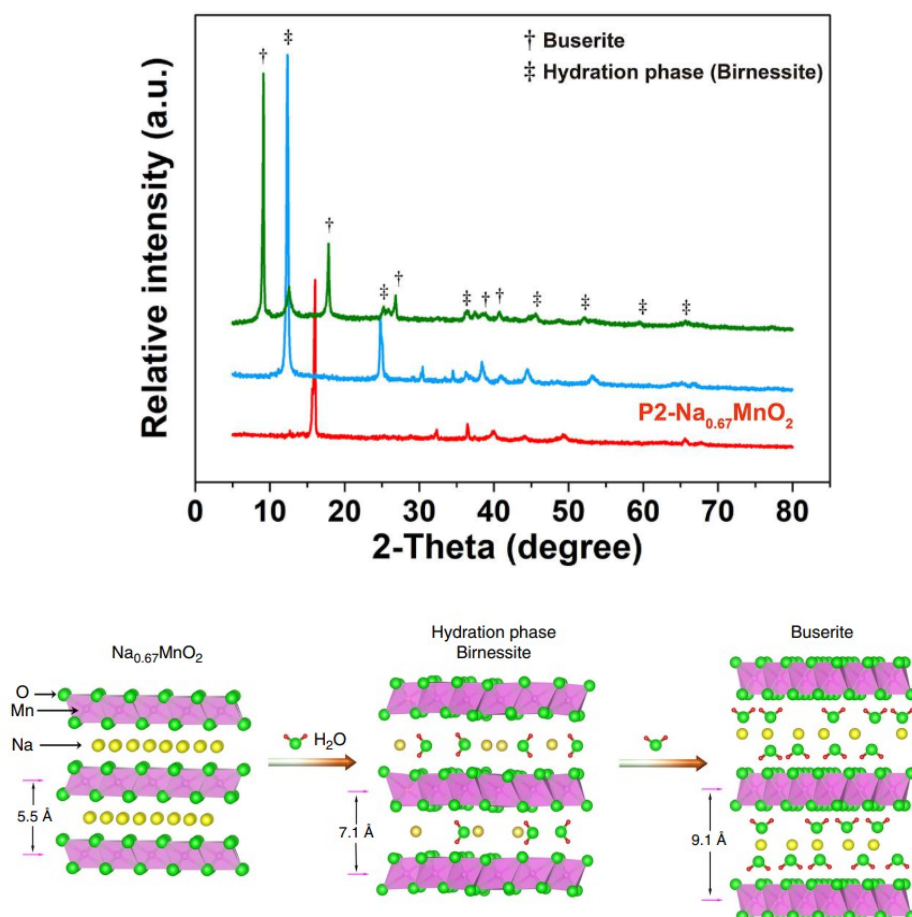


Figure 4.14 - diffractogram of the *P2*-type  $\text{Na}_{0.67}\text{MnO}_2$  compared with the hydration phase (birnessite) and busserite as well as, a diagram illustrating the hydration and degradation process of  $\text{Na}_{0.67}\text{MnO}_2$  [41], [42]

Figure 4.15, shows the X-ray diffractograms of NMNFO before being put in contact with air or water, after one hour, 1 week, 2 weeks and one month in air and 1 hour stirring in water.

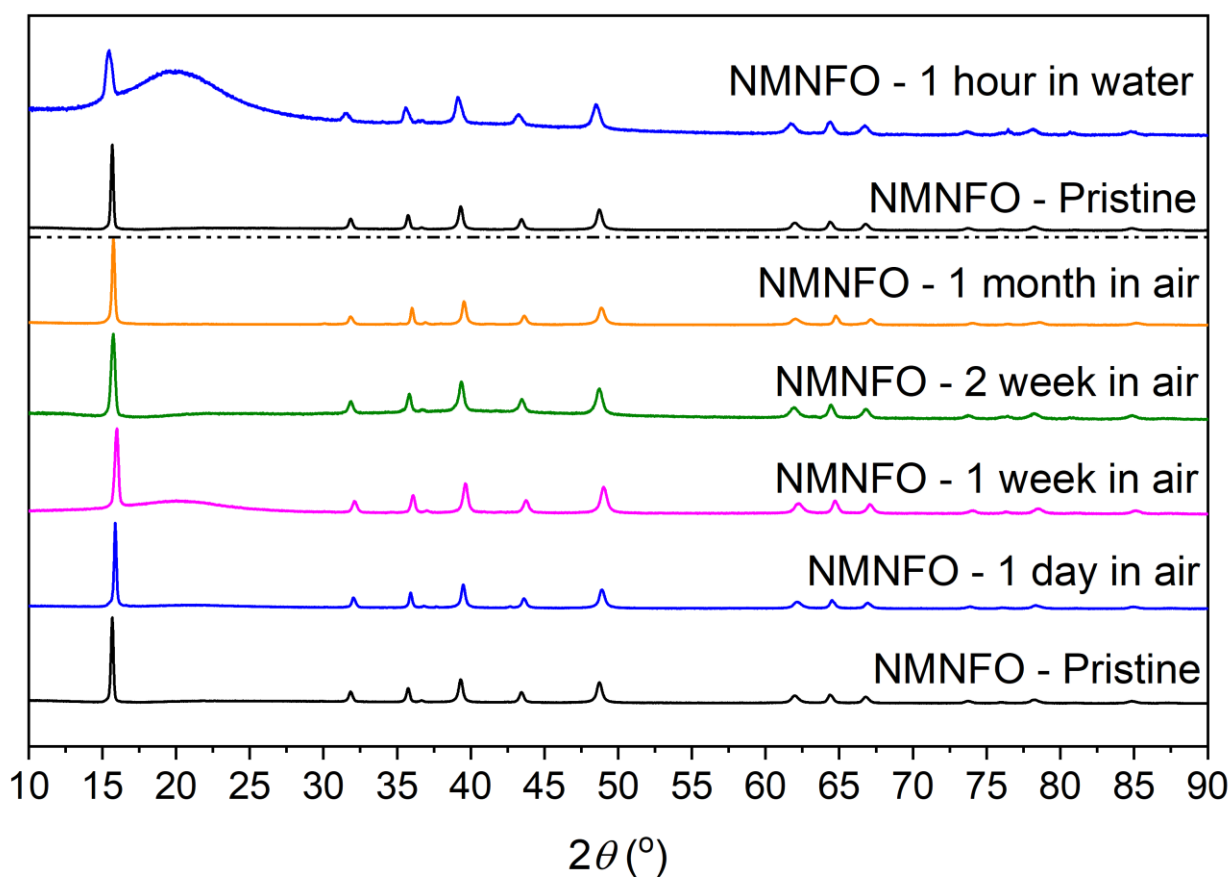


Figure 4.15 - X-ray diffractograms of NMNFO before being put in contact with air or water, after one hour, 1 week, 2 weeks and one month in air and 1 hour stirring in water

Contrary to NMNTO, NMNFO is very stable in water, showing little to no degradation in contact with air or water. As a general rule, for *P2*-type  $\text{Na}_{0.67}\text{TMO}_2$  materials with a higher electrochemical redox potential, the harder it is for sodium to be chemically extracted from the lattice (*i.e.*, when in contact with  $\text{H}_2\text{O}$ ,  $\text{CO}_2$ , *etc.*). Because Fe(III)/Fe(IV) redox potential

(2.75-4.0 V *vs.* Na<sup>+</sup>/Na) is higher than that of Ti(III)/Ti(IV) redox potential (< 1.5 V *vs.* Na<sup>+</sup>/Na), it is expected that NMNFO will be more stable than NMNTO. [41], [42]

In Figure 4.16, the X-rays of the as-synthesised NMNCO and that exposed to air for 1 hour, 1 week, 2 weeks and 1 month, as well as that stirred in water for 1 hour and 24 hours are shown.

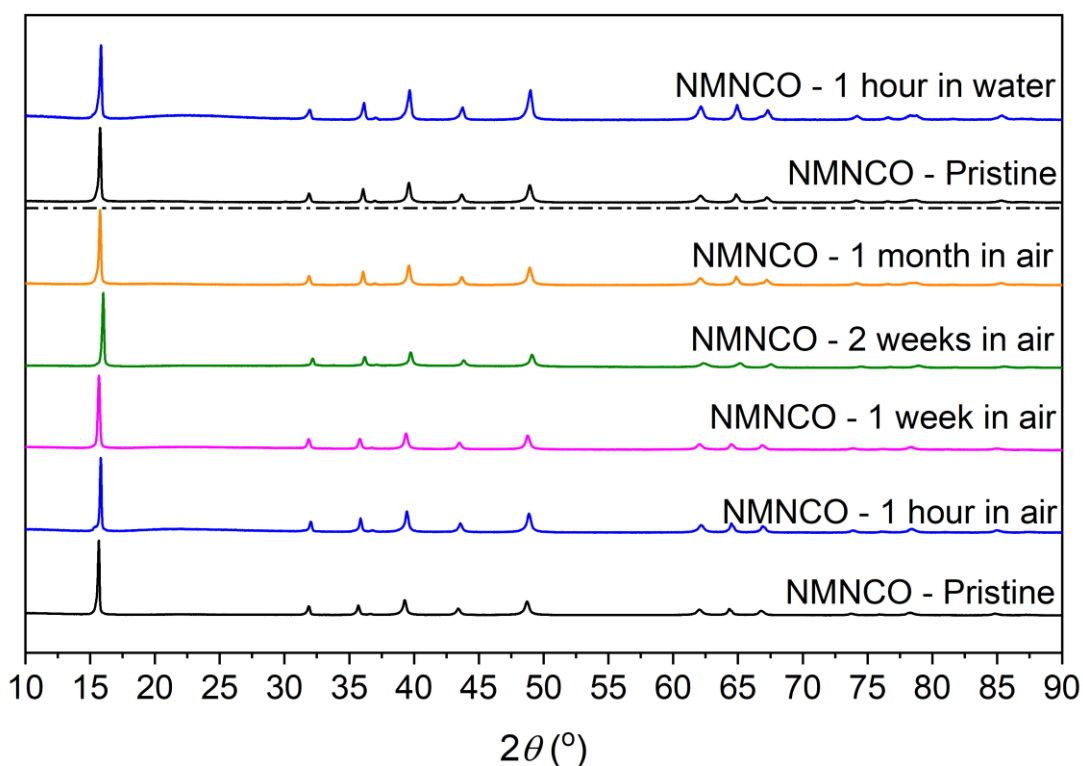


Figure 4.16 - X-ray diffractograms of NMNCO before being put in contact with air or water, after one hour, 1 week, 2 weeks and one month in air and 1 hour stirring in water

As in the case of the other *P2*-type materials studied in the thesis, NMNCO does not show any clear degradation or structure change when exposed to air for 1 month or after 1 hour of stirring in water.

This resilience to degradation in contact with air and water is expected, following the same rationale that the higher the electrochemical redox potential of the transition metal is, the harder it is for sodium to be chemically extracted from the lattice. The redox potential of Cu(II)/Cu(III) is 3.5-4.4 V *vs.* Na<sup>+</sup>/Na hence, it was expected that NMNCO would be relatively stable in contact with the atmosphere and water. Figure 4.17, compared the redox potential of various transition metals and  $O_2 + H_2O + 2e^- \rightarrow 2\cdot OH^-$ . [3], [42]–[49]

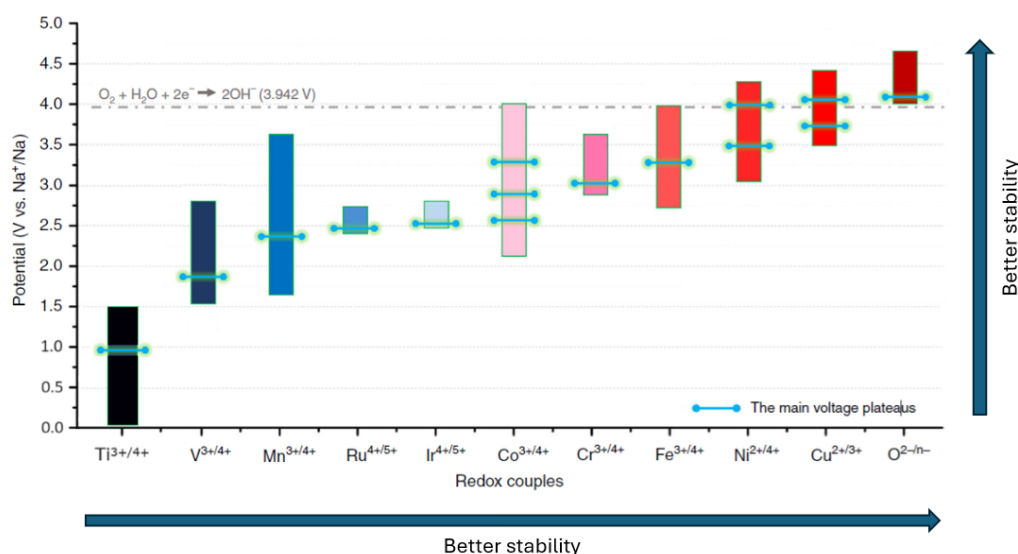


Figure 4.17 – Redox potentials of various transition metals, compared with the  $O_2 + H_2O + 2e^- \rightarrow 2\cdot OH^-$ . adapted from [3], and built with information from [28], [42]–[48]

## 4.5. Electrochemical performance

In this section, various electrochemical techniques were applied to investigate the electrochemical performance of the *P2*-type NMNTO, NMNFO, and NMNCO as cathodes for sodium batteries. These included galvanostatic measurements, cyclic-voltammetry, *post-mortem* X-ray diffraction, and galvanostatic intermittent titration technique. As for the *O3*-type  $\alpha$ -NaFeO<sub>2</sub> series, studied in Chapter 3, the composition of the electrodes was 80 wt% active material, 10 wt% carbon super-P conductor and, 9.9 wt% PVDF binder.

The remaining 0.1 wt% is oxalic acid. Oxalic acid is added to the mixture to avoid the elimination reaction, which may form cross-links between the PVDF chains, causing gelation which affects the quality of the electrodes produced. A slurry pH higher than 8 promotes this H-F elimination reaction and the formation of cross-links. [50]

#### 4.5.1. Galvanostatic measurements

The prepared electrodes of  $\text{Na}_{0.67}\text{Mn}_{0.8}\text{Ni}_{0.15}\text{Ti}_{0.05}$ ,  $\text{Na}_{0.67}\text{Mn}_{0.8}\text{Ni}_{0.15}\text{Fe}_{0.05}$ , and  $\text{Na}_{0.67}\text{Mn}_{0.8}\text{Ni}_{0.15}\text{Cu}_{0.05}$ , were tested in coin-cells between 2.0 and 4.5 V vs.  $\text{Na}^+/\text{Na}$  for 200 cycles at a 0.1 C rate and rate performance for 10 cycles at 0.1 C, 0.2 C, 0.5 C, 1 C, 2 C, 5 C, 10 C, and back to 0.1 C, totalling 80 cycles. In Figure 4.18, the performance, Coulombic efficiency, mean potential, 1<sup>st</sup> cycle galvanostatic curves and cycling at different rates of  $\text{Na}_{0.67}\text{Mn}_{0.8}\text{Ni}_{0.15}\text{Ti}_{0.05}$  (●),  $\text{Na}_{0.67}\text{Mn}_{0.8}\text{Ni}_{0.15}\text{Fe}_{0.05}$  (●), and  $\text{Na}_{0.67}\text{Mn}_{0.8}\text{Ni}_{0.15}\text{Cu}_{0.05}$  (●), is shown.

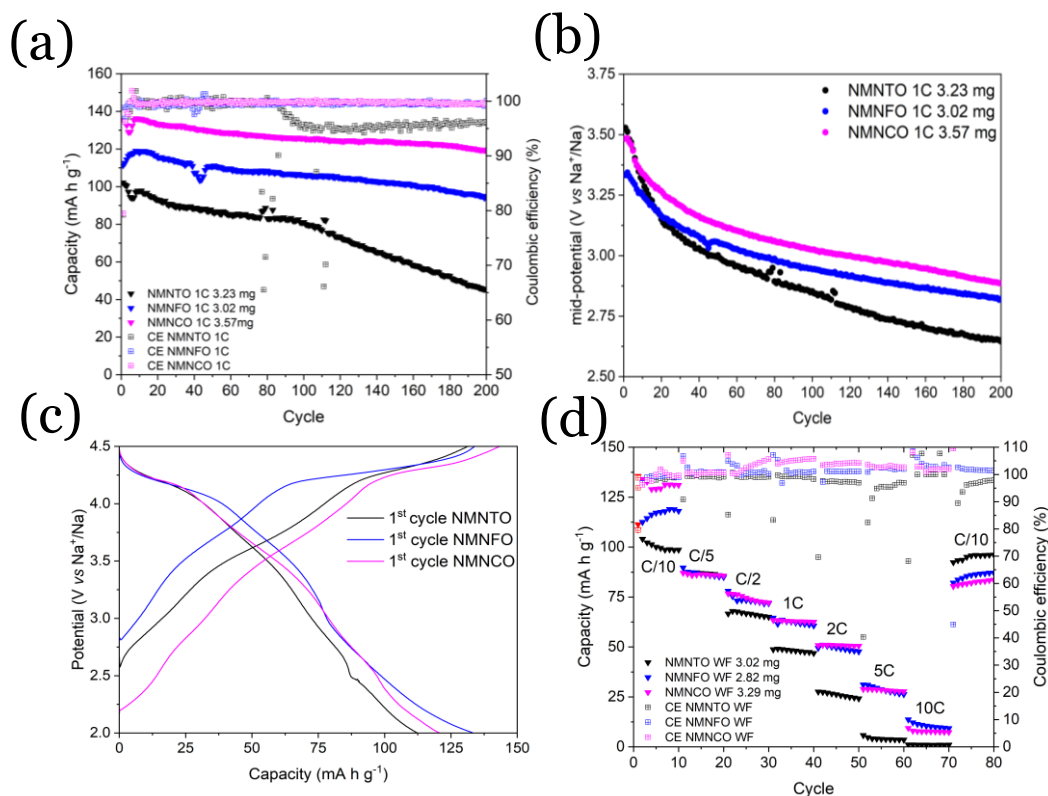


Figure 4.18 – Capacity over 200 cycles of NMNTO, NMNFO and NMNCO (a), evolution of mean-potential over 200 cycles of NMNTO, NMNFO and NMNCO (b), galvanostatic curves of the 1<sup>st</sup> cycle of NMNTO, NMNFO and NMNCO (c), rate capability of NMNTO, NMNFO and NMNCO at 0.1, 0.2, 0.5, 1, 2, 5 and 10 C (d)

The initial capacity of NMNTO, NMNFO and NMNCO is 102, 111 and 136 mA h g<sup>-1</sup>, respectively, as shown in Figure 4.18. The theoretical capacities of NMNTO, NMNFO and NMNCO are 261.353, 260.343, and 259.370 mA h g<sup>-1</sup>, respectively. As the higher theoretical extracted capacity is that of NMNTO, followed by NMNFO and then, NMNCO, it would be expectable that NMNTO would have the higher initial capacity. For this matter, we must take into consideration that, at this potential range, titanium does not undergo any redox reaction. [42], [51] Furthermore, iron undergoes a redox reaction at approximately 3.3 V *vs.* Na<sup>+</sup>/Na, transferring one electron per mole, and copper has its major redox *plateaux* occurring at 3.5 and 4.0 V *vs.* Na<sup>+</sup>/Na, transferring two electrons per mole. [43], [52] Regarding their performance, all materials have a relatively high capacity retention rate up to the 100<sup>th</sup> cycle of, 79.41, 95.45 and 92.42 % for NMNTO, NMNFO and NMNCO. After 200 cycles, the capacity retention is 44.32, 84.90 and 87.96 % for NMNTO, NMNFO and NMNCO. All materials maintain a Coulombic efficiency between 99.5 and 99.8 % for all 200 cycles except NMNTO, which decreases Coulombic efficiency to approximately 94 % after progressively from the 80<sup>th</sup> to the 120<sup>th</sup> cycle. The causes of the decrease in Coulombic efficiency in NMNTO after the 80<sup>th</sup> cycle are not yet known.

Regarding cycling at faster rates, NMNTO consistently has a poorer capacity when using a higher current than the NMNFO and NMNCO. NMNTO has a capacity and C/10 of 102 mA h g<sup>-1</sup>, which decreases to 87, 63, 49, 26, 6, 0 mA h g<sup>-1</sup> at C/5, C/2, 1C, 2C, 5C and 10C. Compared to NMNFO and NMNCO showing capacities at C/10, C/5, C/2, 1C, 2C, 5C, and 10 C of 111, 66, 76, 62, 51, 31, 15 mA h g<sup>-1</sup> and 136, 65, 74, 61, 51, 29, 12 mA h g<sup>-1</sup> for NMNFO and NMNCO respectively. However, NMNTO has a better capacity recovery when returning to slower cycling rates. Upon return to cycling at C/10, has a capacity of 92 mA h g<sup>-1</sup>, while

NMNFO and NMNCO show a lower capacity of 74 and 72 mA h g<sup>-1</sup>. This may indicate that the iron and copper doped are more susceptible to degradation at faster rates, probably because all elements in the transition-metal layer suffer redox reaction while NMNTO has titanium does not undergo any redox reaction. [31], [34], [44]

Furthermore, studies have shown that in *P2*-type Na<sub>x</sub>Mn<sub>(1-y)</sub>M<sub>y</sub>O<sub>2</sub>, where *M* = Li, Mg, Ni, **Ti**, Al, V, Co, Fe, Cr and Mn, that titanium is the transition metal that results in the lower structural deformation when charged. [53]. In Figure 4.19, The lattice distortion of *P2*-type Na<sub>x</sub>Mn<sub>(1-y)</sub>M<sub>y</sub>O<sub>2</sub> upon charge, where *M* = Li, Mg, Ni, **Ti**, Al, V, Co, Fe, Cr and Mn. [53]

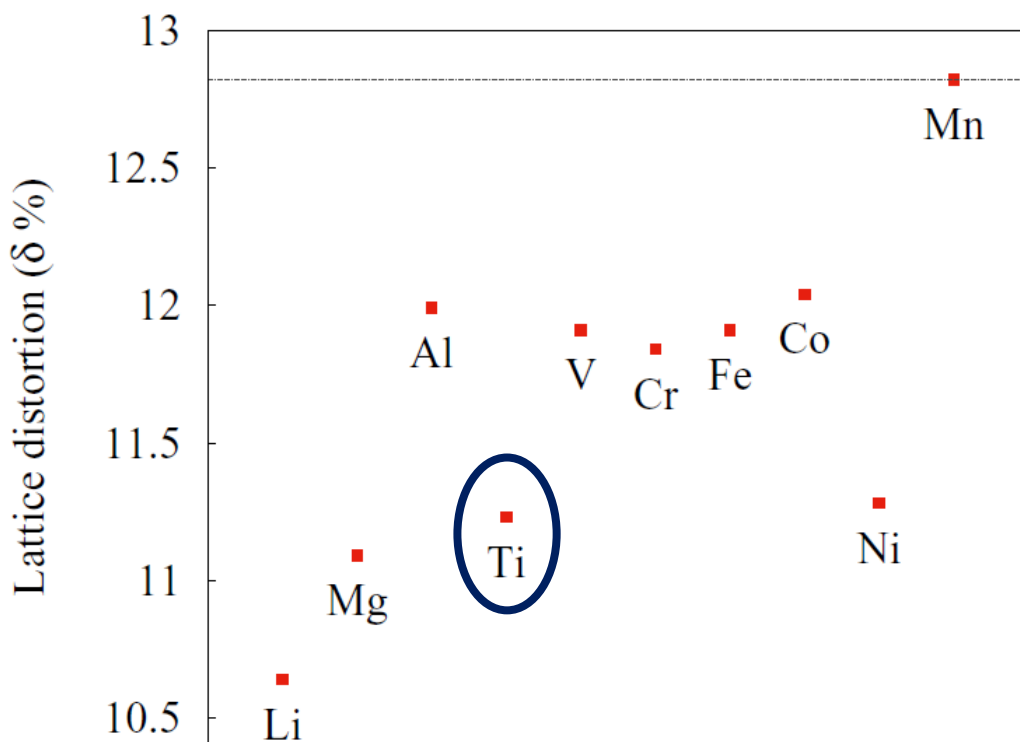


Figure 4.19 – lattice distortion of *P2*-type Na<sub>x</sub>Mn<sub>(1-y)</sub>M<sub>y</sub>O<sub>2</sub>, where *M* = Li, Mg, Ni, **Ti**, Al, V, Co, Fe, Cr and Mn upon charge [53]

Figure 4.20 shows the galvanostatic curves of NMNFO, NMNCO and NMNTO at the 1<sup>st</sup>, 2<sup>nd</sup>, 80<sup>th</sup>, 120<sup>th</sup>, and 200<sup>th</sup> cycles.

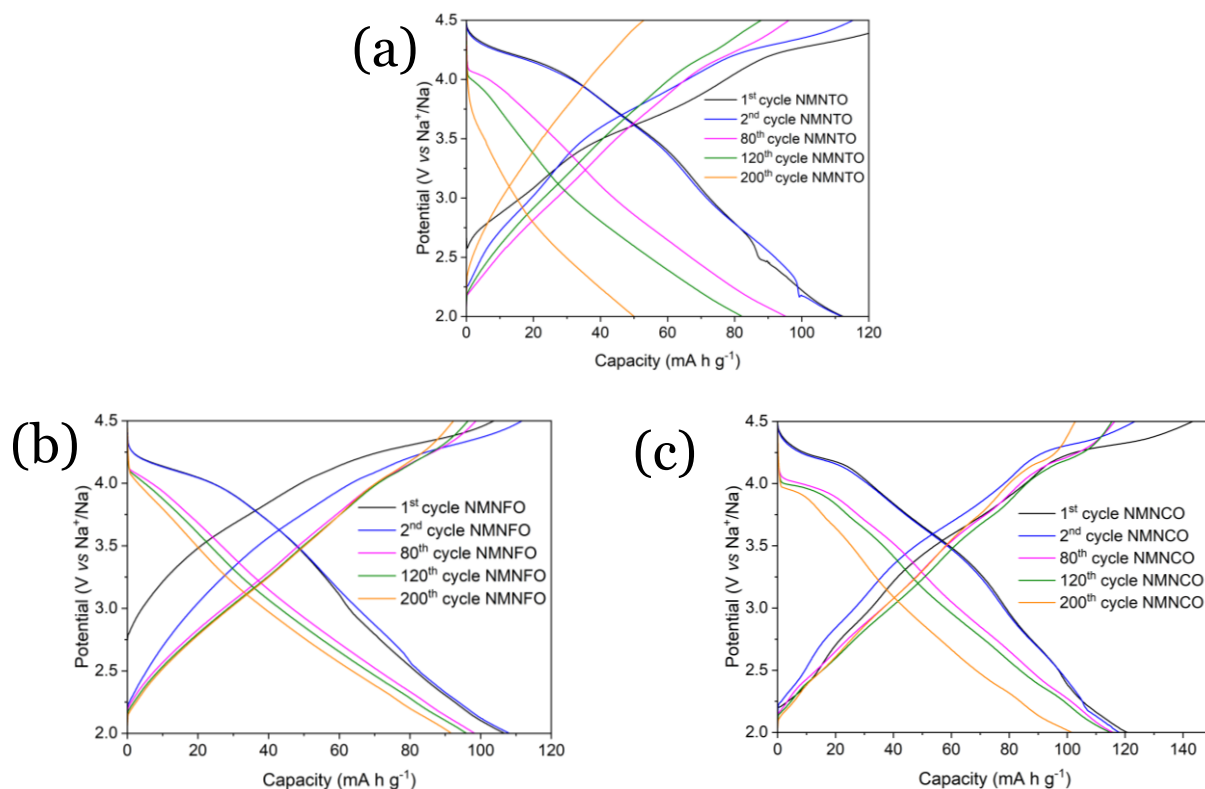


Figure 4.20 – galvanostatic curves of the 1<sup>st</sup>, 2<sup>nd</sup>, 80<sup>th</sup>, 120<sup>th</sup>, and 200<sup>th</sup> cycles of (a) NMNTO, (b) NMNFO and (c) NMNCO.

The instability seen in NMNTO charge and discharge capacity, between 2.0 and 2.75 V *vs.* Na<sup>+</sup>/Na of the 1<sup>st</sup> and 2<sup>nd</sup> cycles may be responsible for the accelerated capacity loss after the 80<sup>th</sup> cycle. This might have been caused by some reactions with the electrolyte or other unknown effects, which should be further investigated.

The initial mean potential is 3.58, 3.33, and 3.48 V *vs.* Na<sup>+</sup>/Na for NMNTO, NMNFO, and NMNCO. The mean potential of all materials decreases with cycling being that NMNTO had a faster mean potential decay, an indication of a faster degradation, followed by a poorer capacity retention rate. NMNTO shows *plateaux* at 2.3 V *vs.* Na<sup>+</sup>/Na, from Mn(III) ↔ Mn(IV), and 3.5 and, 4.1 V *vs.* Na<sup>+</sup>/Na, from Ni(II) ↔ Ni(III) ↔ Ni(IV), ascribed based on other studies of transition metal oxides containing manganese and nickel. [54], [55] Titanium is inactive in this potential range. [56] The presence of a varied number of elements in the transition metal layer causes disorder between sodium and vacancies, which helps smooth the galvanostatic curves and improves capacity retention. [8] The same phenomenon occurs

in the other materials where NMNFO is expected a *plateau* at 3.33 V vs. Na<sup>+</sup>/Na and NMNCO two *plateaux* at 3.75 and 4.1 V vs. Na<sup>+</sup>/Na adding to those appearing in NMNTO, comparing to other transition metal oxides containing iron and copper. [26], [57]

#### 4.5.2. Cyclic-voltammetry

As for the *O3*-type materials in Chapter 3, cyclic-voltammetry was run in Na<sub>0.67</sub>Mn<sub>0.8</sub>Ni<sub>0.15</sub>Ti<sub>0.05</sub>, Na<sub>0.67</sub>Mn<sub>0.8</sub>Ni<sub>0.15</sub>Fe<sub>0.05</sub>, and Na<sub>0.67</sub>Mn<sub>0.8</sub>Ni<sub>0.15</sub>Cu<sub>0.05</sub>, at, 0.1, 0.2, 0.5, and 1.0 mV s<sup>-1</sup> for five cycles, to evaluate the stability and sodium diffusion. In Figure 4.21, the voltammogram of the first five cycles of pristine NMNTO at 0.1 mV s<sup>-1</sup> and the second cycles of all measured rates is shown.

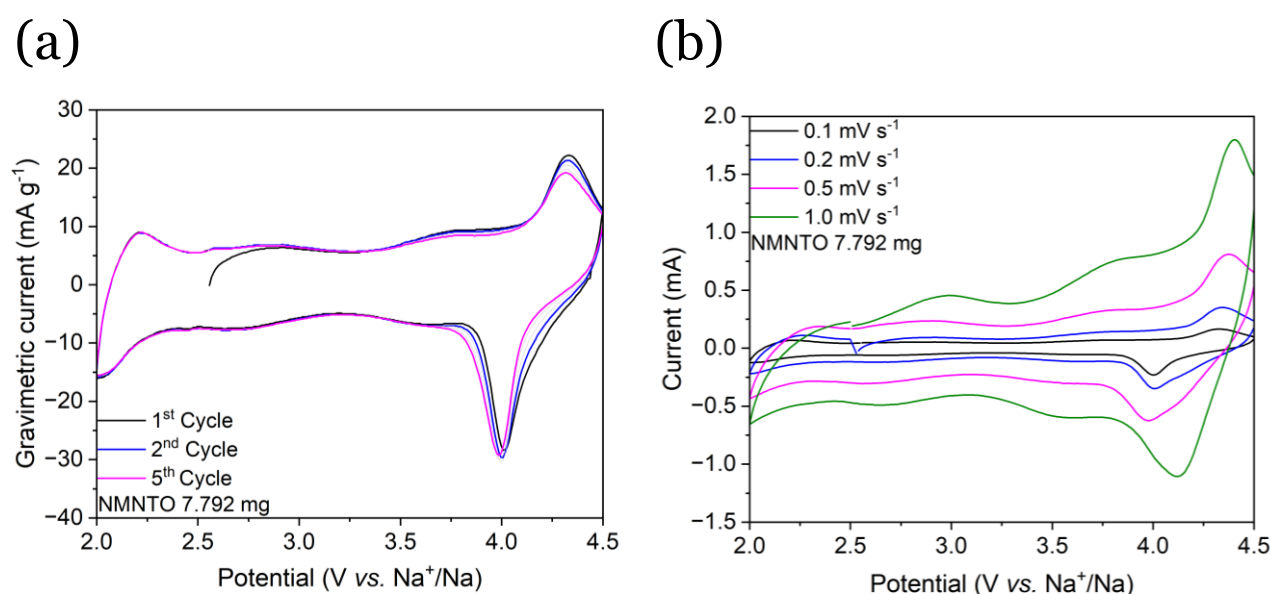


Figure 4.21 – Cyclic-voltammogram of (a) NMNTO at 0.1 mV s<sup>-1</sup> over 5 cycles and the (b) 2<sup>nd</sup> cycles of NMNTO at 0.1, 0.2, 0.5 and 1.0 mV s<sup>-1</sup>.

The voltammogram of NMNTO, run at 0.1 mV s<sup>-1</sup>, shows a negligible decay of the maximum anodic and cathodic current with cycling, which is expected from the galvanostatic information. The cyclic-voltammogram at 0.1 mV s<sup>-1</sup> shows a pair of peaks at 2.25 and 2.0 V,

corresponding to the  $\text{Mn(III)} \rightleftharpoons \text{Mn(IV)}$ , a pair of peaks at approximately 2.9 and 2.75 V, corresponding to  $\text{Ni(II)} \rightleftharpoons \text{Ni(III)}$  and 3.75 and 3.6 V from  $\text{Ni(III)} \rightleftharpoons \text{Ni(IV)}$ . [31], [34], [44], [58] The pair of peaks at approximately 4.2 and 4.0 V, which corresponds to an anionic redox reaction, appears to have great reversibility. Titanium is not redox active at this potential range. [27], [47]

The cyclic-voltammograms at different scan rates still maintain the same peaks as in  $0.1 \text{ mV s}^{-1}$  however, the  $\Delta E^o$  (peak separation) increases, which is the expected behaviour of the mass transport-dependent reaction. In Figure 4.22, the current maxima of each anodic and cathodic peak at different scan rates are compared with the square root of each scan rate,  $\nu^{1/2}$ .

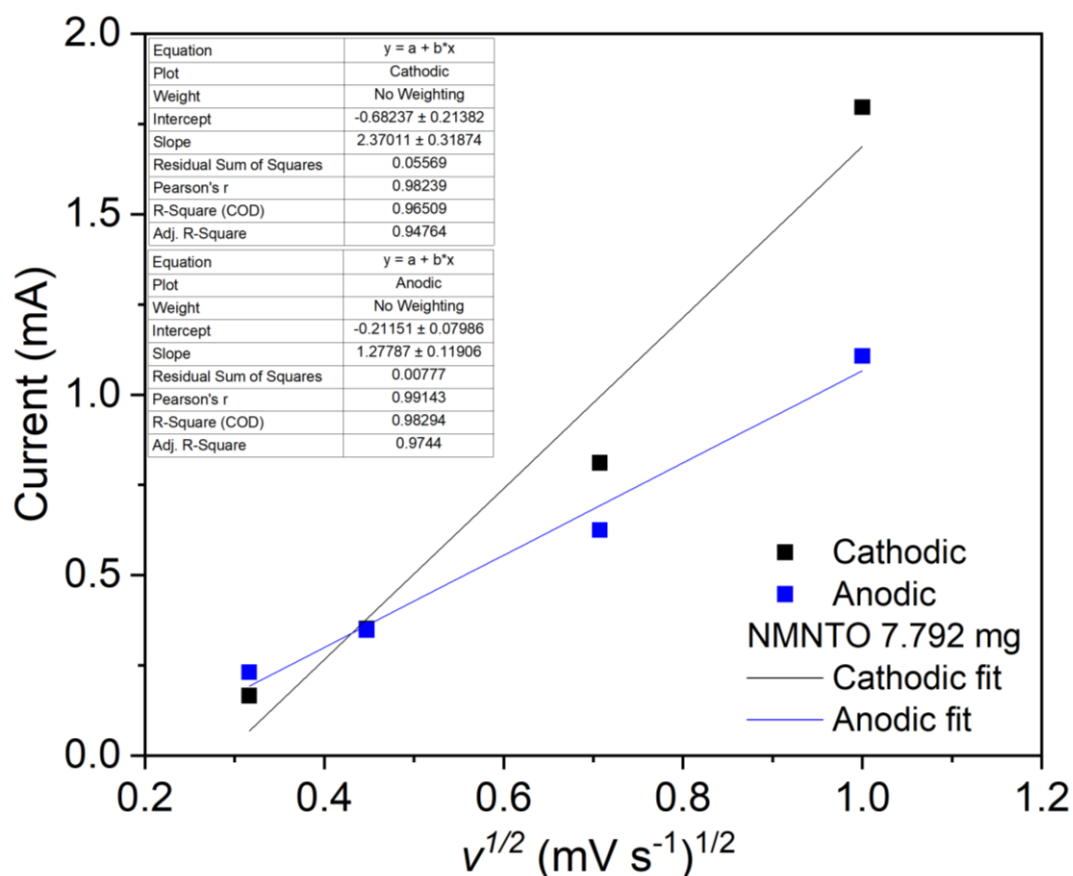


Figure 4.22 - Maxima of the anodic and the cathodic peaks at different scan rates, related to  $\nu^{1/2}$  with the cathodic and anodic linear regressions of NMNTO

The anodic and the cathodic current maxima show a good correlation with the  $v^{1/2}$ , with a correlation coefficient, of  $r^2 = 0.98294$  and  $0.96509$ , respectively. The anodic and cathodic  $\text{Na}^+$  diffusion coefficient was calculated using this method to be  $6.048 \times 10^{-9} \text{ cm}^2 \text{ s}^{-1}$  and  $1.122 \times 10^{-8} \text{ cm}^2 \text{ s}^{-1}$ , respectively.

In Figure 4.23, the voltammogram of the first five cycles of pristine NMNFO at  $0.1 \text{ mV s}^{-1}$  and the second cycles of all measured rates are shown.

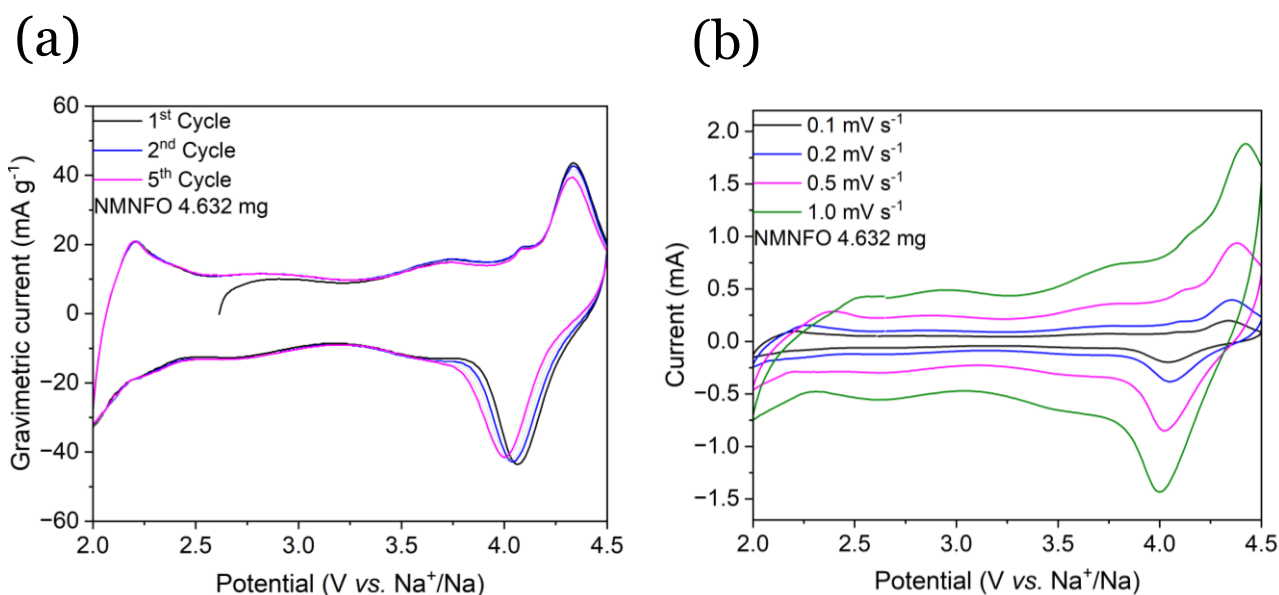


Figure 4.23 – Cyclic-voltammogram of (a) NMNFO at  $0.1 \text{ mV s}^{-1}$  over 5 cycles and the (b) 2<sup>nd</sup> cycles of NMNFO at  $0.1, 0.2, 0.5$  and  $1.0 \text{ mV s}^{-1}$ .

As in the NMNTO, the voltammogram of NMNFO, run at  $0.1 \text{ mV s}^{-1}$ , shows a negligible decay of the maximum anodic and cathodic current with cycling, which is expected from the galvanostatic information. Adding to the peaks in NMNTO corresponding to manganese and nickel, the cyclic-voltammogram of NMNFO at  $0.1 \text{ mV s}^{-1}$  shows a cathodic peak at  $4.1 \text{ V}$  which we could not ascribe to any phenomenon. This is probably related to an extra step in desodiation or iron migration to the alkali-metal layer. [49] The peaks associated with Fe(III)

$\rightleftharpoons$  Fe(IV) are probably occulted by Ni(III)  $\rightleftharpoons$  Ni (IV) as this is expected to occur between 3.0 and 3.5 V *vs.* Na<sup>+</sup>/Na. [37], [59] At approximately 4.2 and 4.0 V, which corresponds to an anionic redox reaction, appears to have great reversibility similar to the NMNTO.

The cyclic-voltammograms at different scan rates still maintain the same peaks as in 0.1 mV s<sup>-1</sup> however, the  $\Delta E^o$  (peak separation) increases, which is the expected behaviour of the mass transport-dependent reaction. [60] In Figure 4.24, the current maxima of each anodic and cathodic peak at different scan rates are compared with the square root of each scan rate,  $v^{1/2}$ .

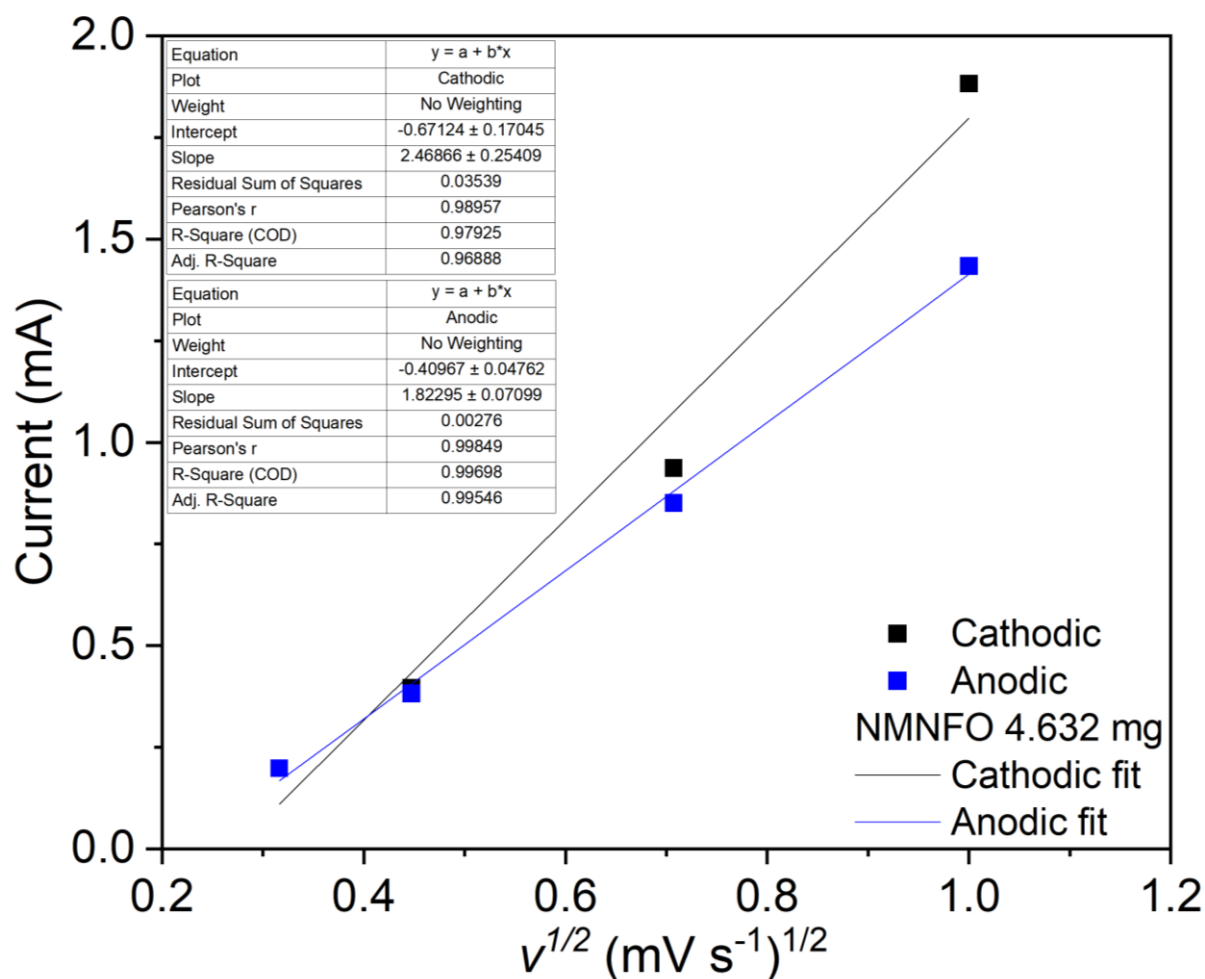


Figure 4.24 - Maxima of the anodic and the cathodic peaks at different scan rates, related to  $v^{1/2}$  with the cathodic and anodic linear regressions of NMNFO

The anodic and the cathodic current maxima show a good correlation with the  $v^{1/2}$ , with a correlation coefficient, of  $r^2 = 0.99698$  and  $0.97925$ , respectively. The anodic and cathodic  $\text{Na}^+$  diffusion coefficient was calculated using this method to be  $8.628 \times 10^{-9} \text{ cm}^2 \text{ s}^{-1}$  and  $1.168 \times 10^{-8} \text{ cm}^2 \text{ s}^{-1}$ , respectively.

In Figure 4.25, the voltammogram of the first five cycles of pristine NMNCO at  $0.1 \text{ mV s}^{-1}$  and the second cycles of all measured rates is shown.

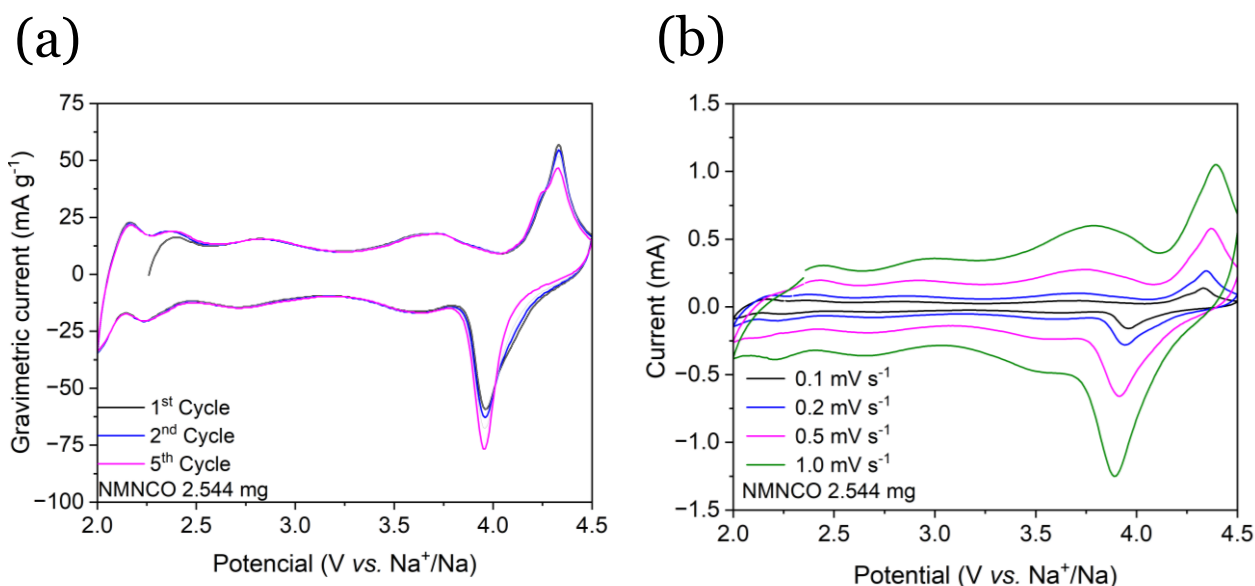


Figure 4.25 - Cyclic-voltammogram of NMNCO at  $0.1 \text{ mV s}^{-1}$  over 5 cycles (a) and the 2<sup>nd</sup> cycles of NMNFO at  $0.1, 0.2, 0.5$  and  $1.0 \text{ mV s}^{-1}$  (b)

As observed in both the NMNTO and NMNFO, identical peaks for manganese, nickel, and the anionic reduction appear at the same potential values. A small cathodic peak at approximately  $4.25 \text{ V}$  can be attributed to the  $\text{Cu(II)} \rightleftharpoons \text{Cu(III)}$  transition, with its anodic pair obscured by the anionic reduction peaks. Additionally, there is an extra redox pair at  $2.4$  and  $2.25 \text{ V}$ , which may suggest a two-step  $\text{Mn(III)} \rightleftharpoons \text{Mn(IV)}$  reduction and oxidation process. This implies a possible multi-step electron transfer mechanism involving Mn species. The

cyclic voltammograms recorded at various scan rates still exhibit the same peaks as those at  $0.1 \text{ mV s}^{-1}$ ; however, the  $\Delta E_0$  (peak separation) increases, which aligns with the expected behaviour of a mass transport-dependent reaction. This is indicative of diffusion-controlled processes occurring during the voltammetric measurements. In Figure 4.26, the current maxima of each anodic and cathodic peak at different scan rates are compared with the square root of each scan rate,  $v^{1/2}$ , which allows for the determination of the mass transport characteristics and provides insight into the electrochemical kinetics.

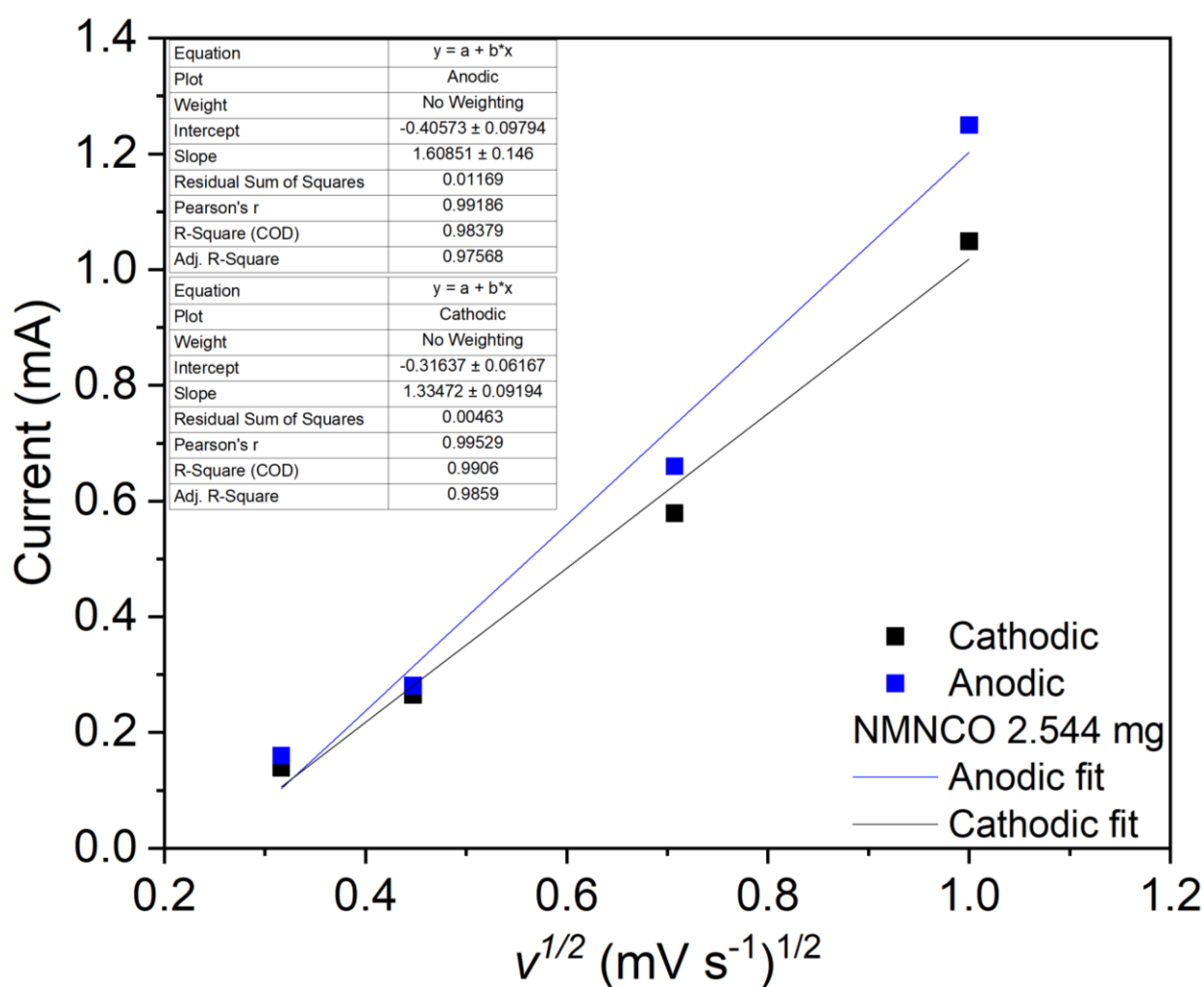


Figure 4.26 - Maxima of the anodic and the cathodic peaks at different scan rates, related to  $v^{1/2}$  with the cathodic and anodic linear regressions of NMNCO

The anodic and the cathodic current maxima show a good correlation with the  $v^{1/2}$ , with a correlation coefficient, of  $r^2 = 0.99060$  and  $0.98379$ , respectively. The anodic and cathodic  $\text{Na}^+$  diffusion coefficient was calculated using this method to be  $7.613 \times 10^{-9} \text{ cm}^2 \text{ s}^{-1}$  and  $6.318 \times 10^{-9} \text{ cm}^2 \text{ s}^{-1}$ , respectively.

Table 4.5, shows the anodic and cathodic diffusion rates of NMNTO, NMNFO and NMNCO.

Table 4.5 – Anodic and cathodic sodium diffusion rates of NMNTO, NMNFO, and NMNFO

	NMNTO	NMNFO	NMNCO
<b>Anodic (<math>\text{cm}^{-2} \text{ s}^{-1}</math>)</b>	$6.048 \times 10^{-9}$	$8.628 \times 10^{-9}$	$7.613 \times 10^{-9}$
<b>Cathodic (<math>\text{cm}^{-2} \text{ s}^{-1}</math>)</b>	$1.122 \times 10^{-8}$	$1.168 \times 10^{-8}$	$6.318 \times 10^{-9}$

In all three materials, the cathodic diffusion rates are higher than the anodic diffusion rates, indicating that, generally, it is easier to remove sodium ions than to reinsert them, which is expected for *P2*-type materials. [61] During charge, it is easier to remove sodium from NMNFO, followed by NMNTO, and finally NMNCO. This ordering remains consistent during discharge. This variation in sodium mobility may be related to the *c*-axis and, more specifically, to the sodium interlayer distance,  $d(0\ 0\ 2)$ . The  $d(0\ 0\ 2)$  was determined via Rietveld refinements earlier in this chapter as 5.5851, 5.5846, and 5.5754 Å for NMNTO, NMNFO, and NMNCO, respectively. This suggests a direct proportionality between the  $d(0\ 0\ 2)$  and the sodium diffusion rates, implying that the tighter the  $\text{Na}^+$  pathway, the more challenging it is to remove a  $\text{Na}^+$  ion. The results further highlight the critical role of structural parameters in determining the ease of sodium ion mobility and the overall electrochemical performance of these materials

### 4.5.3. Galvanostatic intermittent titration technique

The galvanostatic intermittent titration technique was run for all materials. These measurements were conducted at potentials between 2.0 and 4.5 V *vs.* Na<sup>+</sup>/Na. Current equivalent to a 0.1 C rate was applied for 10 minutes followed by a period of relaxation of 30 minutes, while the evolution of the potential was monitored. In Figure 4.27, the galvanostatic curves of NMNTO during GITT analysis and the sodium diffusion coefficient *versus* potential.

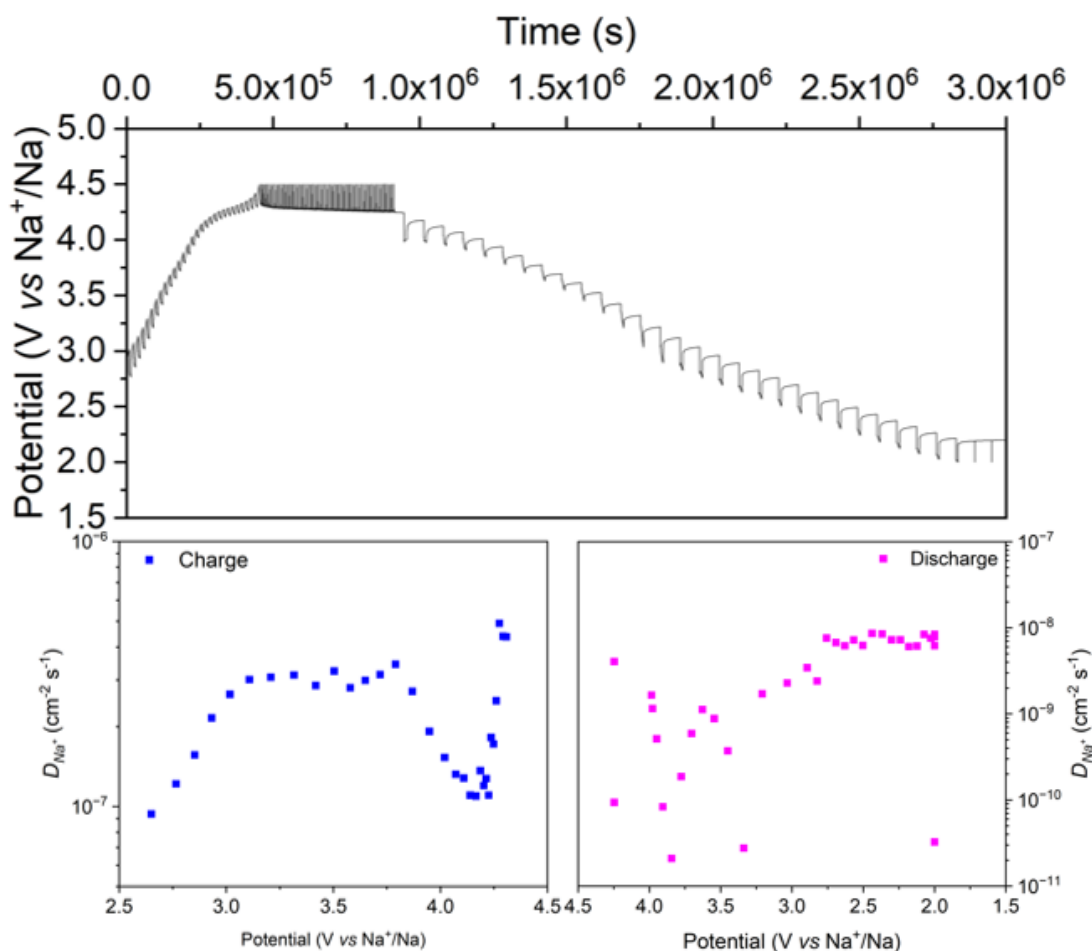


Figure 4.27 - galvanostatic curves of NMNTO during GITT analysis and the sodium diffusion coefficient versus potential

During charge, NMNTO shows a sodium diffusion coefficient between  $10^{-7}$  and  $10^{-6}$   $\text{cm}^2 \text{s}^{-1}$  with a maximum at approximately 2.5 and 4.25V *vs.*  $\text{Na}^+/\text{Na}$ , approximately during the oxidation of manganese and during oxygen oxidation. During discharge, the diffusion rate varies from  $10^{-11}$  to  $10^{-8}$   $\text{cm}^2 \text{s}^{-1}$  with higher values between 4.25 and 3.25 V *vs.*  $\text{Na}^+/\text{Na}$ , approximately during oxygen reduction. This is within the range of the diffusion rates measured using cyclic-voltammetry at different scan rates.

In Figure 4.28, the galvanostatic curves of NMNFO during GITT analysis and the sodium diffusion coefficient *versus* potential.

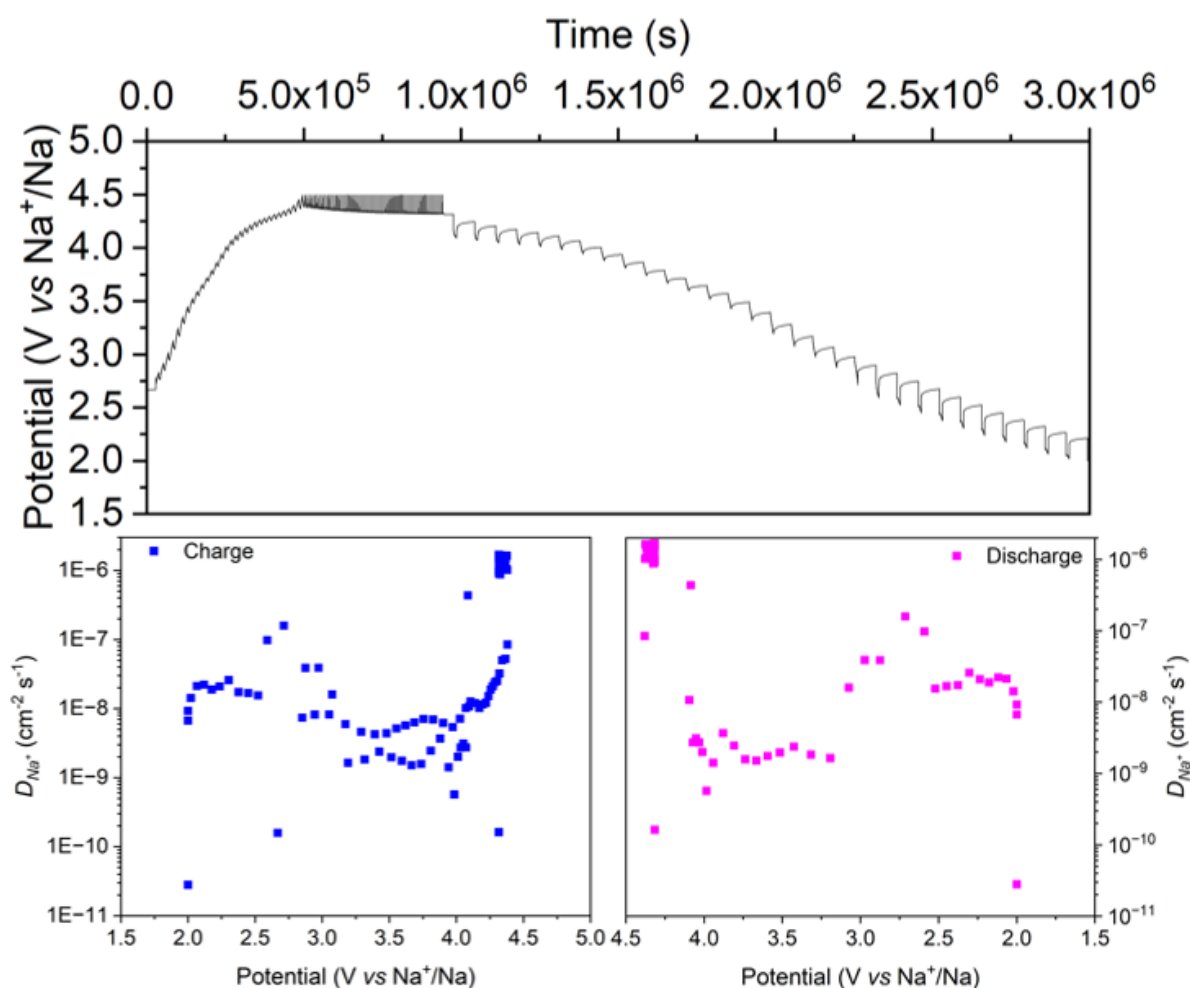


Figure 4.28 – galvanostatic curves of NMNFO during GITT analysis and the sodium diffusion coefficient versus potential

During charge, NMNFO shows a sodium diffusion coefficient between  $10^{-9}$  and  $10^{-7}$   $\text{cm}^2 \text{s}^{-1}$  with a maximum at approximately 2.5 and 4.25V *vs.*  $\text{Na}^+/\text{Na}$ , approximately during the oxidation of manganese and during oxygen oxidation. During discharge, the diffusion rate varies from  $10^{-9}$  to  $10^{-8}$   $\text{cm}^2 \text{s}^{-1}$  with the higher value 4.25 V *vs.*  $\text{Na}^+/\text{Na}$ , approximately during oxygen reduction. This is within the range of the diffusion rates measured using cyclic-voltammetry at different scan rates.

In Figure 4.29, the galvanostatic curves of NMNCO during GITT analysis and the sodium diffusion coefficient *versus* potential.

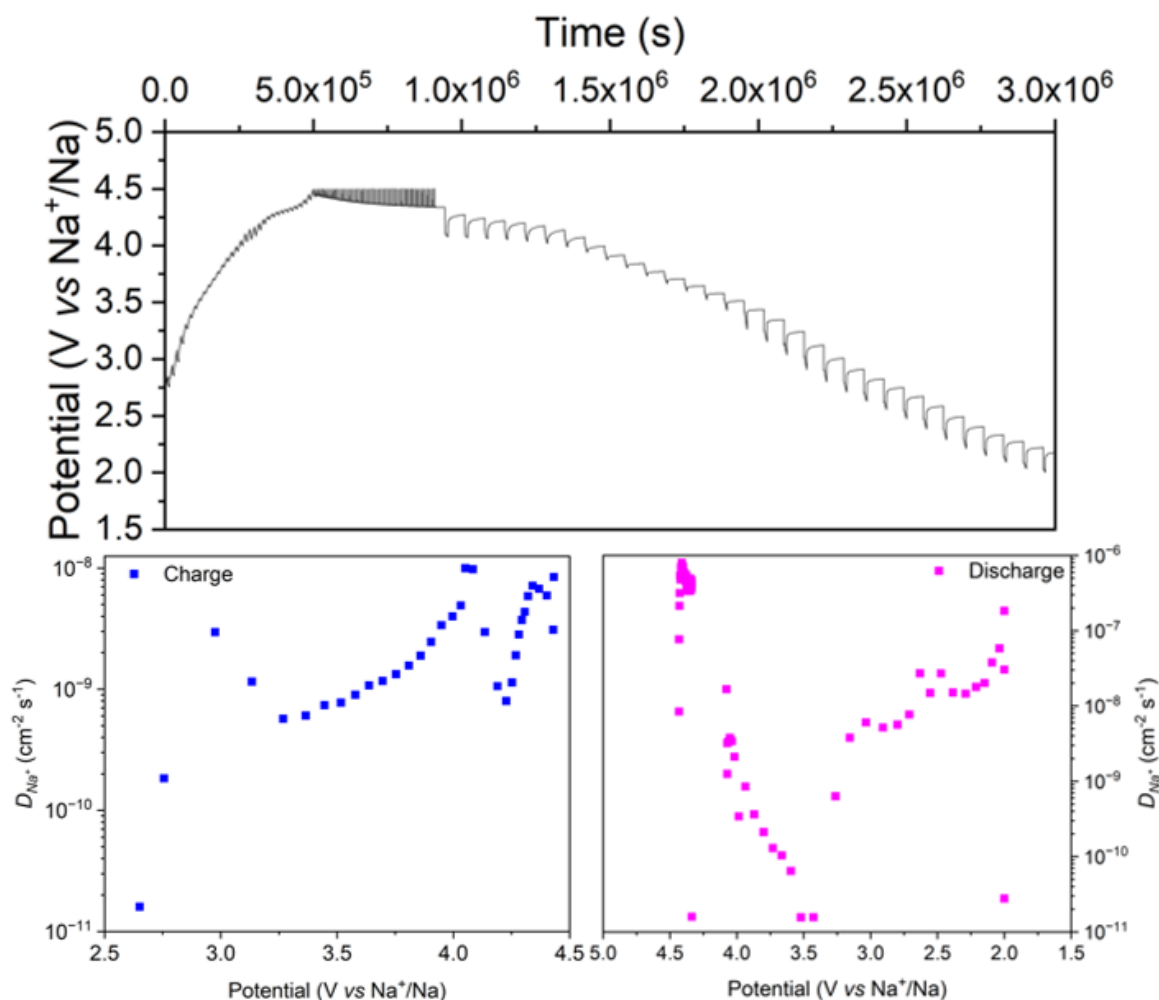


Figure 4.29 - galvanostatic curves of NMNCO during GITT analysis and the sodium diffusion coefficient versus potential

During charge, NMNCO shows a sodium diffusion coefficient between  $10^{-9}$  and  $10^{-8}$   $\text{cm}^2 \text{s}^{-1}$  with a maximum at approximately 2.5 and 4.25V *vs.*  $\text{Na}^+/\text{Na}$ , approximately during the oxidation of manganese and during oxygen oxidation. During discharge, the diffusion rate varies from  $10^{-6}$  to  $10^{-11}$   $\text{cm}^2 \text{s}^{-1}$  with the higher values 4.25 and 3.25 *vs.*  $\text{Na}^+/\text{Na}$ , approximately during oxygen reduction and nickel. This is within the range of the diffusion rates measured using cyclic-voltammetry at different scan rates.

The sodium diffusion rate measured with cyclic-voltammetry at different scan rates falls within the range of sodium diffusion rate measured with GITT. Compared with the results in Chapter 3, this indicated the characteristics of the surface of NMNTO, NMNFO and NMNCO particles have similar characteristics as the bulk. [47], [62] This also corroborates the relation between the  $d(0\ 0\ 2)$  and  $\text{Na}^+$  mobility.

#### 4.5.4. *Ex-situ XRD diffraction*

This section aims to identify any structural changes occurring during cycling. For that, coin-cells were assembled, cycled to a specific potential and then disassembled. The electrodes were then washed with diethyl carbonate, dried at room temperature under vacuum and analysed using X-ray diffractometry. The X-ray diffractograms of NMNTO, NMNFO and NMNCO were taken at 3.0, 4.3, 4.5 and 2.0 V *vs.*  $\text{Na}^+/\text{Na}$ . A measurement of an as-prepared electrode and an electrode left in contact with all the components of the cell but in open circuit potential was also taken and marked as “pristine” and “OCV” respectively. All manipulation of opened cells and electrodes took place in an argon-filled glovebox ( $\text{O}_2 < 0.1$  ppm;  $\text{H}_2\text{O} < 0.1$  ppm) and all diffractometry took place in a nitrogen-filled glovebox ( $\text{O}_2 < 0.5$  ppm;  $\text{H}_2\text{O} < 0.5$  ppm). All X-ray diffractograms were collected with the condition described in Chapter 2. In Figure 4.30, the *ex-situ* diffractograms of NMNTO are shown.

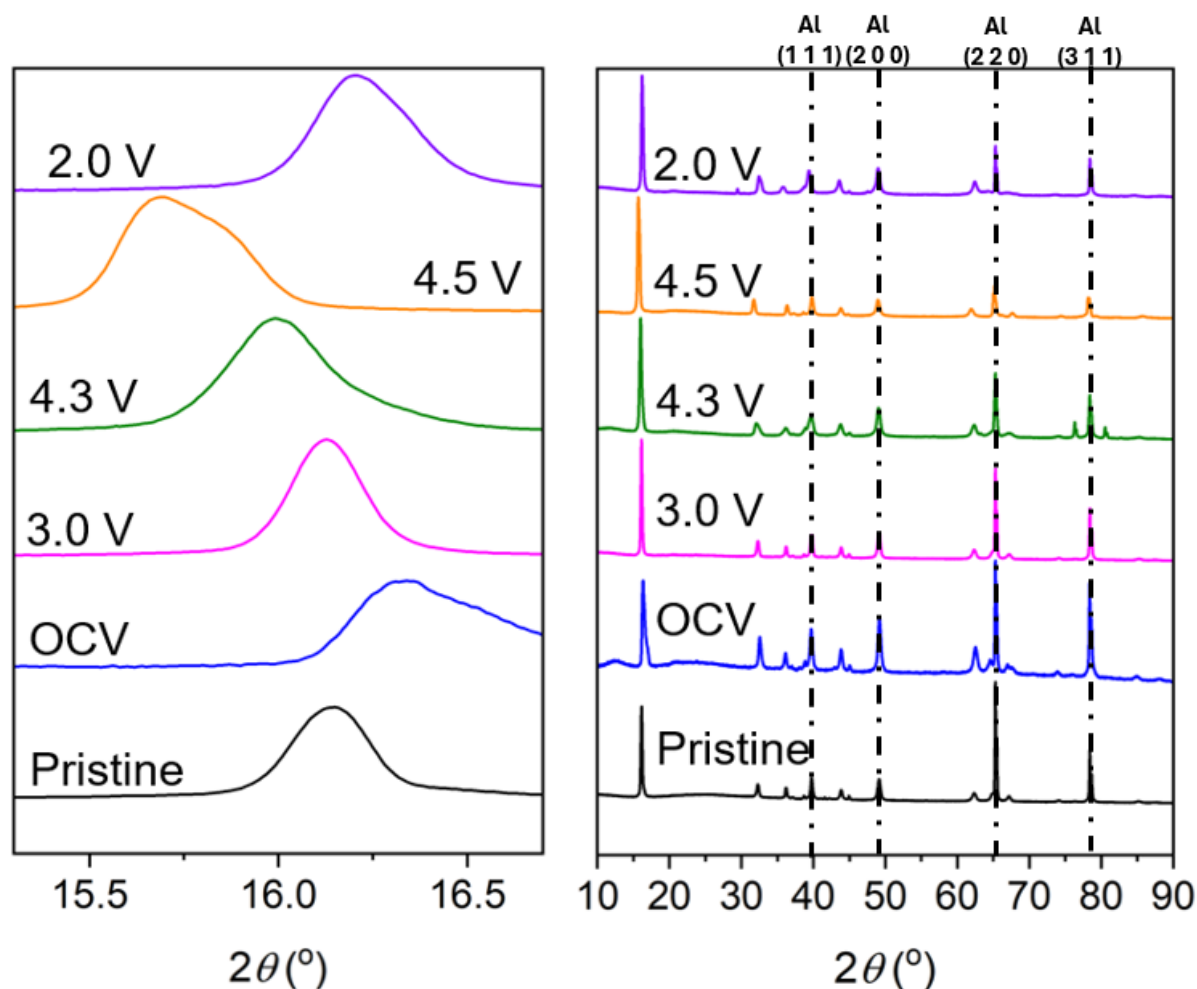


Figure 4.30 – Ex-situ diffractograms of NMNTO at the pristine state, OCV, 3.0, 4.3, 4.5 and 2.0 V vs.  $\text{Na}^+/\text{Na}$ , with detail of the peak (0 0 2) of NMNTO

During the entire charge and discharge process of NMNTO, all peaks that are not indexed to the aluminium current collector, correspond to the  $P6_3/mmc$  space groups.

These results denote that the  $P2$  phase is maintained throughout all charges and discharges. The peak at  $2\theta = 16^\circ$ , ascribed to the (0 0 2) in the pristine stage moves to lower angles during charge, indicating an expansion of the  $c$ -axis of the unit cell from the removal of  $\text{Na}^+$  ions. This phenomenon is illustrated in Figure 4.31, from a study by Hou *et al.*, where the (0 0 2) migrated to lower angles, indicating an expansion of the  $c$ -axis. [63]

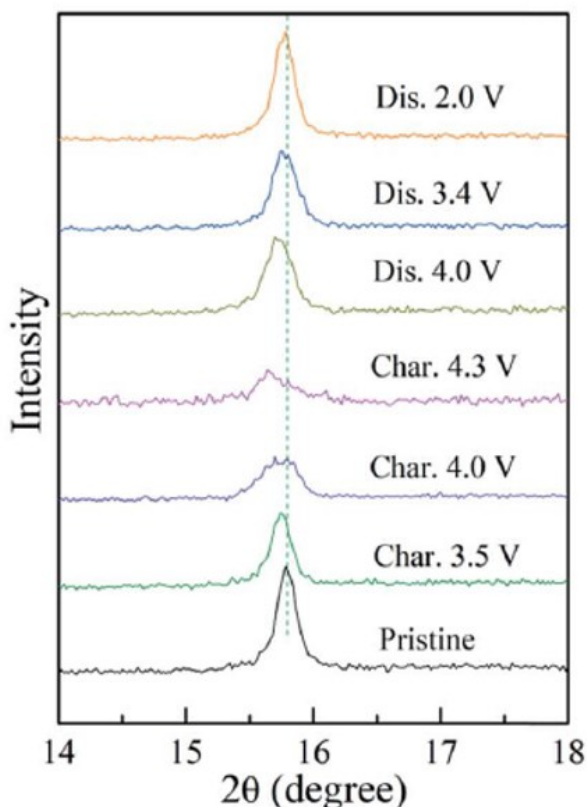


Figure 4.31 – Detail of the (0 0 2) peak of the ex-situ XRD analysis of the gradient  $\text{Co}^{3+}$  substituted *P2*-NaNMO electrode tested at various discharge/ charge states from Hou *et al.* [63]

From 4.5 to 2.0 V *vs.*  $\text{Na}^+/\text{Na}$  returned to the original pristine position, indicating a full reversibility of the structural expansion. This shows that titanium doping helps prevent any deleterious structure transformation.

In the material charged to 4.5 V *vs.*  $\text{Na}^+/\text{Na}$ , a peak emerges at  $2\theta = 15.8^\circ$  next to the peak ascribed previously to the (0 0 2) peak. This peak is according to Cao *et al.*, associated with the formation of the (0 0 4) plane of the *OP4* phase. [64] In OCV, a peak appears at approximately  $2\theta = 16.5^\circ$ . This peak could not be ascribed to any phenomenon or phase occurring upon cell assembly. This can be related to issues preparing the electrolyte after disassembling (*i.e.*, washing, transportation).

In Figure 4.32, the *ex-situ* diffractograms of NMNFO are shown.

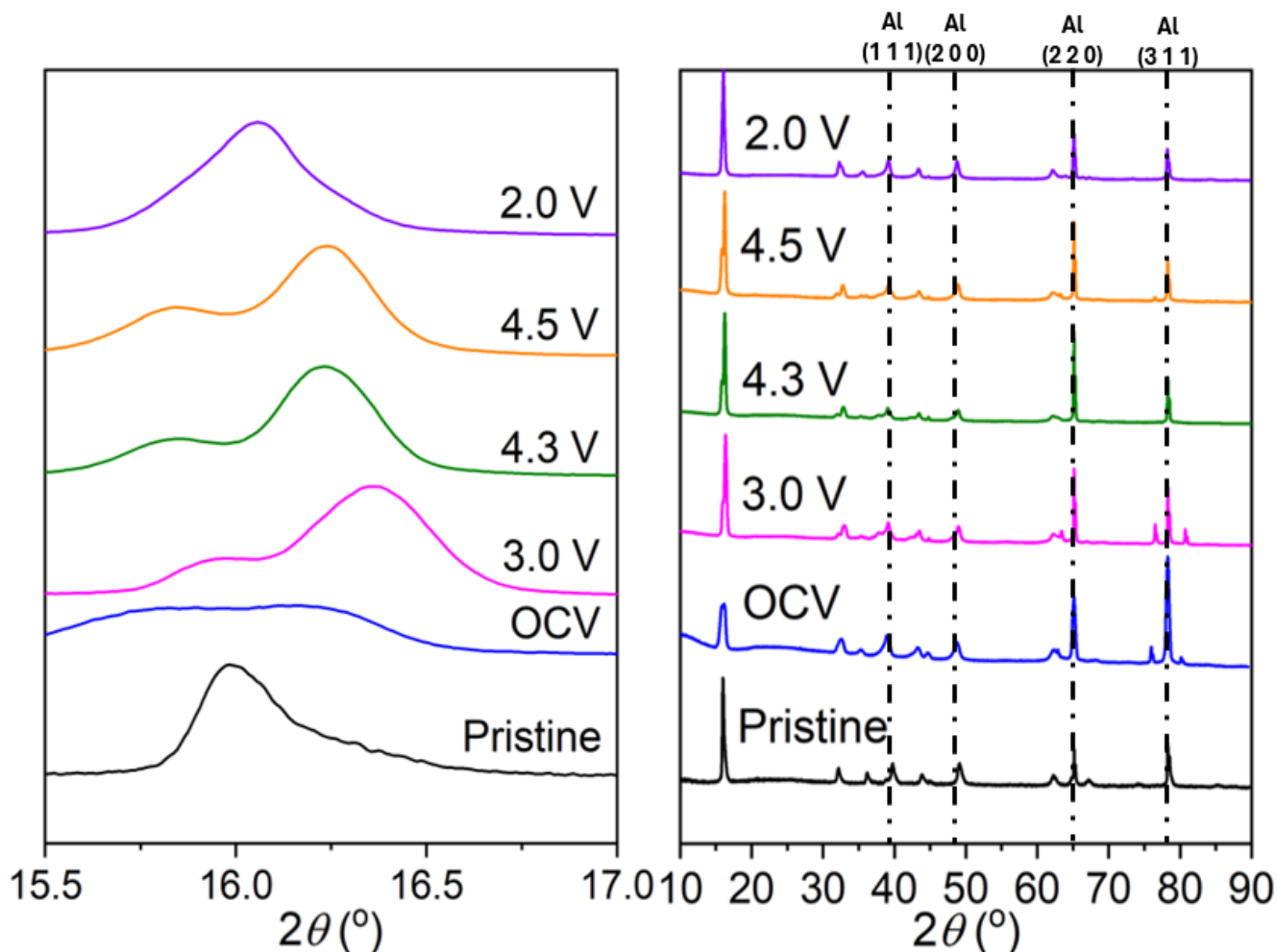


Figure 4.32 – Ex-situ diffractograms of NMNFO at the pristine state, OCV, 3.0, 4.3, 4.5 and 2.0 V vs  $\text{Na}^+/\text{Na}$ , with detail of the peak (0 0 2) of NMNFO

In NMNFO, *ex-situ* XRD shows a structural transformation from a  $P2$  phase to an intermediate phase. Starting from 3.0 V vs.  $\text{Na}^+/\text{Na}$ , the peak at (0 0 2) splits, which may indicate the formation of an  $OP4$  phase, as shown in Figure 4.33. [23], [65] This observation is further supported by a detailed study conducted by Liu, Schumacher, Winter, Li et al. [23], which provides additional evidence of this phase transition. The results suggest that the transformation is associated with significant changes in the material's structural configuration during cycling.

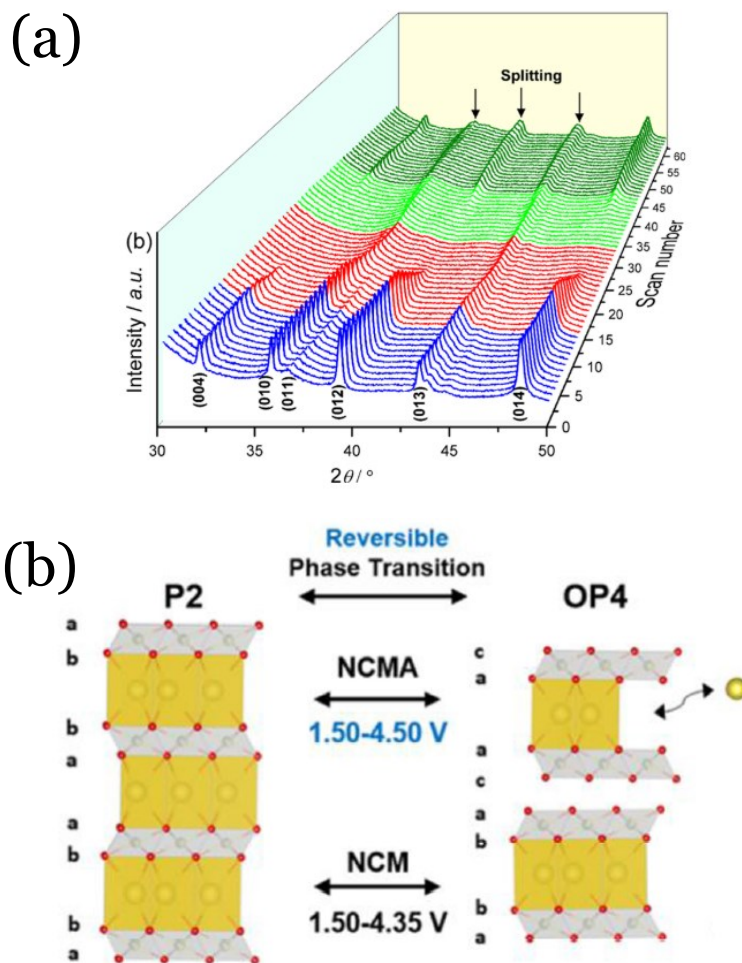


Figure 4.33 – (a) Operando XRD analysis of the  $\text{Na}_{0.67}\text{Fe}_{0.5}\text{Mn}_{0.5}\text{O}_2$  positive electrode and (b) schematic representation of the *P2* to *OP4* transition.

The *OP4* structure is composed of octahedral and prismatic layers stacked alternately along the *c*-axis and the oxygen atoms are aligned in an ABCD form, compared to a *P2* structure where sodium is coordinated in a prismatic form and the oxygen atoms are aligned in an ABBA form. From 4.5 to 2.0 V vs.  $\text{Na}^+/\text{Na}$ , it returned to the original pristine position, indicating full reversibility of the structural transformation in the first cycle. The transformation from *P2* to *OP4* may have a nefarious effect on rate capability, which is lower in NMNFO than in NMNTO.

In Figure 4.34, the *ex-situ* diffractograms of NMNCO are shown.

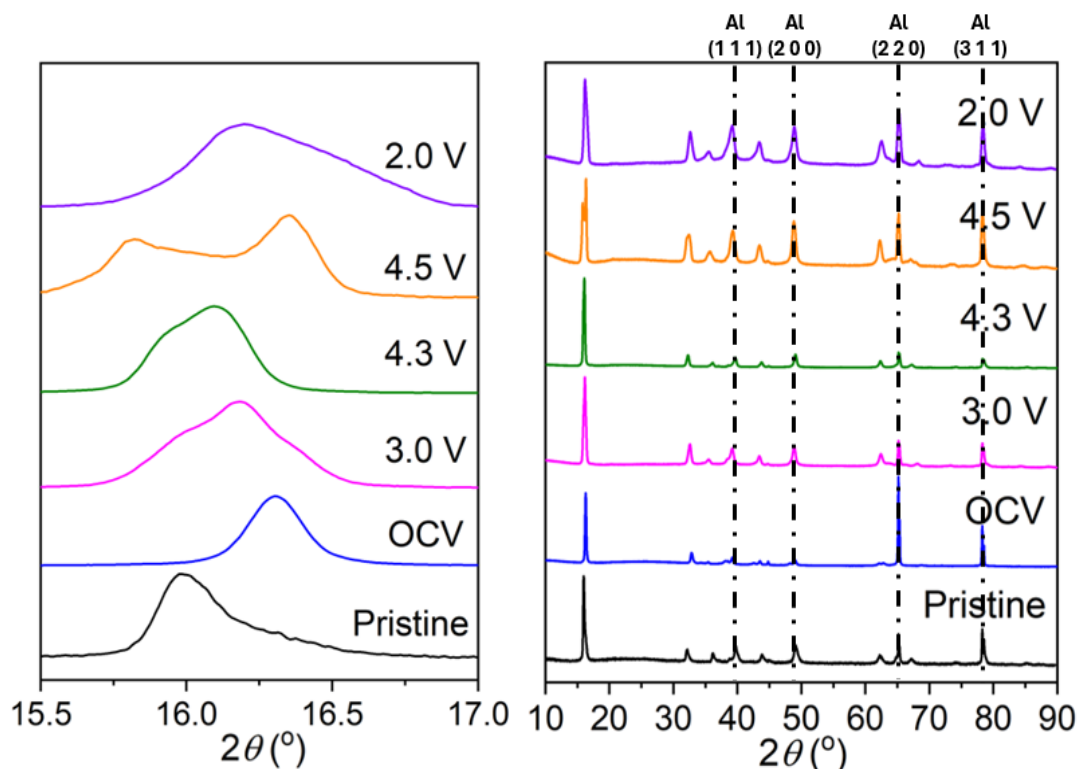


Figure 4.34 - Ex-situ diffractograms of NMNCO at the pristine state, OCV, 3.0, 4.3, 4.5 and 2.0 V va  $\text{Na}^+/\text{Na}$ , with detail of the peak (0 0 2) of NMNCO

In the case of NMNCO, we see an increase of  $2\theta$  in the most intense peak from the pristine to OCV from  $16^\circ$  to  $16.3^\circ$  (Figure 4.34). The reason for this phenomenon is not known, however, this increase of  $2\theta$  indicates a contraction of the *c*-axis. [34], [36] This suggests an intercalation of  $\text{Na}^+$  from the electrolyte intercalates into the alkali-metal layer, occupying the available spaces in the *P2*-type  $\text{Na}_{0.67}\text{Mn}_{0.8}\text{Ni}_{0.15}\text{Cu}_{0.05}\text{O}_2$  structure. [36] Upon charge, the (0 0 2) peak tends to lower  $2\theta$ , which suggests an increase in the interlayer space, an indication of an increase of the electrostatic repulsion of the  $\text{O}^{2-}$  in the structure with the removal of  $\text{Na}^+$ . [36]

Finally, in the case of NMNCO, the results show an evolution from the *P2* phase to an *OP4* intermediate phase. However, this intermediate phase seems to evolve slower than in the case of NMNFO. This may indicate that copper stabilised the *P2* phase better than iron

but, worse than titanium. The ability of the dopant in the transition-metal layer to prevent the formation of the *OP4* intermediate phase appears to significantly contribute to the stability of *P2*-type materials under fast cycling conditions. NMNTO maintains a higher capacity after cycling at faster rates and does not exhibit the intermediate *OP4* phase at higher potentials. In contrast, NMNFO shows a stronger signal associated with the *OP4* phase at higher potentials and recovers the least capacity after fast cycling.

## 4.6. Conclusion

In conclusion, this study successfully synthesised *P2*-type  $\text{Na}_{0.67}\text{Mn}_{0.8}\text{Ni}_{0.15}\text{Ti}_{0.05}\text{O}_2$  (NMNTO),  $\text{Na}_{0.67}\text{Mn}_{0.8}\text{Ni}_{0.15}\text{Fe}_{0.05}\text{O}_2$  (NMNFO), and  $\text{Na}_{0.67}\text{Mn}_{0.8}\text{Ni}_{0.15}\text{Cu}_{0.05}\text{O}_2$  (NMNCO) *via* the ceramic method. The *P2* pure phase was easily obtained by calcining the precursors at 900 °C for 12 hours. The attaining of a pure phase was confirmed by various characterisation techniques including X-ray diffractometry, scanning electron microscopy, and energy-dispersive X-ray spectroscopy.

Upon obtaining the pure materials, their structural, morphological, and chemical properties were thoroughly examined. The structural characterisation, involving Rietveld refinement, confirmed the successful formation of the intended *P2*-type structures. The lattice parameters obtained were in agreement with those reported in the literature, indicating the reliability and accuracy of the synthesis method used.

Morphologically, the materials demonstrated distinct characteristics: NMNTO exhibited highly agglomerated particles, NMNFO consisted of platelets, and NMNCO displayed a combination of platelets and larger blocks. Elemental analysis confirmed the presence of the expected elements in each material, although some discrepancies were observed, such as the absence of titanium in NMNTO, iron in NMNFO, and copper in NMNCO due to low element concentration.

The stability of these materials when exposed to air and water was also a key focus. NMNTO showed minimal degradation when exposed to air but significant instability in water, leading to the formation of a busenite phase. In contrast, NMNFO and NMNCO demonstrated remarkable stability in both air and water, attributed to the higher electrochemical redox potentials of iron and copper compared to titanium, in decreasing order. [53] This finding underscores the importance of selecting appropriate transition metals to enhance the environmental stability of sodium-ion battery cathode materials.

Electrochemical performance was evaluated using various techniques, including galvanostatic charge-discharge methods, cyclic voltammetry, and the galvanostatic intermittent titration technique. The initial capacities of NMNTO, NMNFO, and NMNCO were 102, 111, and 136 mA h g<sup>-1</sup>, respectively. NMNTO exhibited the highest initial capacity despite its theoretical capacity being lower than NMNCO and NMNFO. This is explained by the non-redox active nature of titanium at the potential range studied. Capacity retention rates up to the 100th cycle were 79.41% for NMNTO, 95.45% for NMNFO, and 92.42% for NMNCO. After 200 cycles, the retention rates were significantly lower for NMNTO at 44.32%, compared to 84.90% and 87.96% for NMNFO and NMNCO, respectively.

The mean potential decay and Coulombic efficiency trends provided further insights into the materials' long-term performance. NMNTO showed faster mean potential decay, indicating rapid degradation, which aligned with its poorer capacity retention.

Cyclic-voltammetry revealed detailed redox behaviour of the materials. NMNTO displayed multiple redox peaks corresponding to manganese and nickel redox reactions, with titanium remaining inactive. The voltammograms of NMNFO and NMNCO indicated similar redox processes with additional peaks attributable to iron and copper, respectively. The diffusion coefficients for sodium ions were calculated, showing a good correlation with the square root of the scan rate, confirming the mass transport-dependent nature of the

reactions. A direct correlation between the *c*-axis and the  $d(0\ 0\ 2)$  and the ionic diffusion rate was also found.

This comprehensive study highlights the successful synthesis and characterisation of *P2*-type sodium-ion battery cathode materials, demonstrating their potential for high performance and stability. The findings suggest that NMNFO and NMNCO are particularly promising due to their superior electrochemical stability and performance. However, NMNTO's instability in water and its faster degradation during cycling point to the need for further optimisation. Future research should focus on enhancing the stability and performance of these materials, possibly through doping strategies or surface modifications, to realise their full potential in sodium-ion battery applications.

## 4.7. References

- [1] Y. Cao, M. Xiao, X. Sun, W. Dong, and F. Huang, “Recent Advances on High-Capacity Sodium Manganese-Based Oxide Cathodes for Sodium-ion Batteries,” *Chem. - A Eur. J.*, vol. 29, no. 12, 2023, doi: 10.1002/chem.202202997.
- [2] K. Tang *et al.*, “The effects of dual modification on structure and performance of P2-type layered oxide cathode for sodium-ion batteries,” *Chem. Eng. J.*, vol. 384, no. October 2019, p. 123234, 2020, doi: 10.1016/j.cej.2019.123234.
- [3] W. Zuo *et al.*, “Structure-Performance Relationship of Zn<sup>2+</sup> Substitution in P2-Na<sub>0.66</sub>Ni<sub>0.33</sub>Mn<sub>0.67</sub>O<sub>2</sub> with Different Ni/Mn Ratios for High-Energy Sodium-Ion Batteries,” *ACS Appl. Energy Mater.*, vol. 2, no. 7, pp. 4914–4924, 2019, doi: 10.1021/acsaem.9b00614.
- [4] R. J. Clément, P. G. Bruce, and C. P. Grey, “Review—Manganese-Based P2-Type Transition Metal Oxides as Sodium-Ion Battery Cathode Materials,” *J. Electrochem. Soc.*, vol. 162, no. 14, pp. A2589–A2604, 2015, doi: 10.1149/2.0201514jes.
- [5] B. Sayahpour, H. Hirsh, S. Parab, L. H. B. Nguyen, M. Zhang, and Y. S. Meng, “Perspective: Design of cathode materials for sustainable sodium-ion batteries,” *MRS Energy Sustain.*, vol. 9, no. 2, pp. 183–197, 2022, doi: 10.1557/s43581-022-00029-9.
- [6] K. Kang, Y. S. Meng, J. Bréger, C. P. Grey, and G. Ceder, “Electrodes with High Power and High Capacity for Rechargeable Lithium Batteries,” *Science (80-. )*, vol. 311, no. 5763, pp. 977–980, 2006, doi: 10.1126/science.1122152.
- [7] C. Delmas, A. Maazaz, C. Fouassier, J.-M. Réau, and P. Hagemuller, “Influence de l’environnement de l’ion alcalin sur sa mobilité dans les structures à feuillets Ax(LxM<sub>1-x</sub>)O<sub>2</sub>,” vol. 14, pp. 329–335, 1979.

- [8] P.-F. Wang *et al.*, “Na<sup>+</sup>/vacancy disordering promises high-rate Na-ion batteries,” *Sci. Adv.*, vol. 4, no. 3, p. eaar6018, 2018, doi: 10.1126/sciadv.aar6018.
- [9] S. Sun, J. Li, C. Xu, T. Zhai, and H. Xia, “Manganese-based layered oxides for electrochemical energy storage: a review of degradation mechanisms and engineering strategies at the atomic level,” *J. Mater. Chem. A*, vol. 10, no. 37, pp. 19231–19253, 2022, doi: 10.1039/d2ta02242g.
- [10] Y. Li, M. Chen, B. Liu, Y. Zhang, X. Liang, and X. Xia, “Heteroatom Doping: An Effective Way to Boost Sodium Ion Storage,” *Adv. Energy Mater.*, vol. 10, no. 27, pp. 1–36, 2020, doi: 10.1002/aenm.202000927.
- [11] D. Carlier *et al.*, “The P2-Na<sub>2/3</sub>Co<sub>2/3</sub>Mn<sub>1/3</sub>O<sub>2</sub> phase: structure, physical properties and electrochemical behavior as positive electrode in sodium battery,” *Dalt. Trans.*, vol. 40, no. 36, pp. 9306–9312, 2011.
- [12] D. W. Hoffman, “No 主観的健康感を中心とした在宅高齢者における健康関連指標に関する共分散構造分析Title.”
- [13] R. Berthelot, D. Carlier, and D. Claude, “Electrochemical Investigation of the P2–Na<sub>x</sub>CoO<sub>2</sub> Phase Diagram,” *Nat. Mater.*, vol. 10, pp. 74–80, 2011, doi: 10.1038/nmat2920.
- [14] A. Gutierrez *et al.*, “On Disrupting the Na<sup>+</sup>-Ion/Vacancy Ordering in P2-Type Sodium-Manganese-Nickel Oxide Cathodes for Na<sup>+</sup>-Ion Batteries,” *J. Phys. Chem. C*, vol. 122, no. 41, pp. 23251–23260, 2018, doi: 10.1021/acs.jpcc.8b05537.
- [15] W. Zuo and Y. Yang, “Synthesis, Structure, Electrochemical Mechanisms, and Atmospheric Stability of Mn-Based Layered Oxide Cathodes for Sodium Ion Batteries,” *Accounts Mater. Res.*, vol. 3, no. 7, pp. 709–720, 2022, doi:

10.1021/accountsmr.2c00058.

- [16] J. Liu *et al.*, “Entropy Tuning Stabilizing P2-Type Layered Cathodes for Sodium-Ion Batteries,” *Adv. Funct. Mater.*, vol. 34, no. 24, pp. 1–9, 2024, doi: 10.1002/adfm.202315437.
- [17] Y. Li *et al.*, “Native Vacancy Enhanced Oxygen Redox Reversibility and Structural Robustness,” *Adv. Energy Mater.*, vol. 9, no. 4, Jan. 2019, doi: 10.1002/aenm.201803087.
- [18] P. L. W. Tregenna-Piggott, S. P. Best, M. C. M. O’Brien, K. S. Knight, J. B. Forsyth, and J. R. Pilbrow, “Cooperative Jahn-Teller Effect in Titanium Alum,” *J. Am. Chem. Soc.*, vol. 119, no. 14, pp. 3324–3332, 1997, doi: 10.1021/ja963509w.
- [19] W. Kong *et al.*, “Simultaneously tuning cationic and anionic redox in a P2-Na<sub>0.67</sub>Mn<sub>0.75</sub>Ni<sub>0.25</sub>O<sub>2</sub> cathode material through synergic Cu/Mg co-doping †,” 2019, doi: 10.1039/c9ta00968j.
- [20] A. D. A. Bin Abu Sofian *et al.*, “Nickel-rich nickel–cobalt–manganese and nickel–cobalt–aluminum cathodes in lithium-ion batteries: Pathways for performance optimization,” *J. Clean. Prod.*, vol. 435, no. October 2023, 2024, doi: 10.1016/j.jclepro.2023.140324.
- [21] “Small - 2021 - Cho - Critical Role of Ti<sup>4+</sup> in Stabilizing High-Voltage Redox Reactions in Li-Rich Layered Material.pdf.crdownload.” .
- [22] A. Nagasubramanian, “Studies of manganese based oxides as alternative electrode materials for lithium based energy storage devices.” 2016, doi: 10.32657/10356/67015.
- [23] J. Wang *et al.*, “Insights into P2-Type Layered Positive Electrodes for Sodium Batteries: From Long-Range Order to Short-Range Order,” *ACS Appl. Mater. Interfaces*, vol. 12, no. 4, pp.

5017–5024, 2020, doi: 10.1021/acsami.9b18109.

- [24] W. Zuo, A. Innocenti, M. Zarrabeitia, D. Bresser, Y. Yang, and S. Passerini, “Layered Oxide Cathodes for Sodium-Ion Batteries: Storage Mechanism, Electrochemistry, and Techno-economics,” *Acc. Chem. Res.*, vol. 56, no. 3, pp. 284–296, 2023, doi: 10.1021/acs.accounts.2c00690.
- [25] J. Hu *et al.*, “Interstitial Water Improves Structural Stability of Iron Hexacyanoferrate for High-Performance Sodium-Ion Batteries,” *ACS Appl. Mater. Interfaces*, vol. 14, no. 10, pp. 12234–12242, 2022, doi: 10.1021/acsami.1c23762.
- [26] W. Kang *et al.*, “Copper substituted P2-type  $\text{Na}_{0.67}\text{Cu}_x\text{Mn}_{1-x}\text{O}_2$ : A stable high-power sodium-ion battery cathode,” *J. Mater. Chem. A*, vol. 3, no. 45, pp. 22846–22852, 2015, doi: 10.1039/c5ta06371j.
- [27] Q. Liu *et al.*, “Sodium transition metal oxides: the preferred cathode choice for future sodium-ion batteries?,” *This J. is Cite this Energy Environ. Sci*, vol. 14, p. 158, 2021, doi: 10.1039/d0ee02997a.
- [28] R. J. Clément *et al.*, “Structurally stable Mg-doped P2- $\text{Na}_{2/3}\text{Mn}_{1-\text{Y}}\text{Mg}_y\text{O}_2$  sodium-ion battery cathodes with high rate performance: Insights from electrochemical, NMR and diffraction studies,” *Energy Environ. Sci.*, vol. 9, no. 10, pp. 3240–3251, 2016, doi: 10.1039/c6ee01750a.
- [29] C. Lin *et al.*, “P2/O3 biphasic integration promoting the enhancement of structural stability for sodium layered oxide cathode,” *Chem. Eng. J.*, vol. 480, no. August 2023, pp. 1–8, 2024, doi: 10.1016/j.cej.2023.147964.
- [30] B. Xiao *et al.*, “A general strategy for batch development of high-performance and cost-effective sodium layered cathodes,” *Nano Energy*, vol. 89, no. PA, p. 106371, 2021, doi: 10.1016/j.nanoen.2021.106371.

- [31] T. Zhang *et al.*, “Promoting the performances of P2-type sodium layered cathode by inducing Na site rearrangement,” *Nano Energy*, vol. 100, no. June, 2022, doi: 10.1016/j.nanoen.2022.107482.
- [32] “Home | ICSD,” *FIZ Karlsruhe GmbH*, 2024. <https://icsd.products.fiz-karlsruhe.de/> (accessed Apr. 10, 2024).
- [33] “WebElements Periodic Table » Bromine » radii of atoms and ions.” [https://webelements.com/bromine/atom\\_sizes.html](https://webelements.com/bromine/atom_sizes.html).
- [34] L. Yang *et al.*, “Structural Aspects of P2-Type Na<sub>0.67</sub>Mn<sub>0.6</sub>Ni<sub>0.2</sub>Li<sub>0.2</sub>O<sub>2</sub> (MNL) Stabilization by Lithium Defects as a Cathode Material for Sodium-Ion Batteries,” *Adv. Funct. Mater.*, vol. 31, no. 38, 2021, doi: 10.1002/adfm.202102939.
- [35] S. Åsbrink and L.-J. Norrby, “A refinement of the crystal structure of copper(II) oxide with a discussion of some exceptional e.s.d.’s,” *Acta Crystallogr. Sect. B*, vol. 26, no. 1, pp. 8–15, Jan. 1970, doi: 10.1107/S0567740870001838.
- [36] B. na SilvánSilv, E. Gonzalo, L. Djuandhi, N. Sharma, F. Fauth, and D. Saurel, “On the dynamics of transition metal migration and its impact on the performance of layered oxides for sodium-ion batteries: NaFeO<sub>2</sub> as a case study †,” 2018, doi: 10.1039/c8ta02473a.
- [37] M. Tabuchi and R. Kataoka, “Structure and Electrochemical Properties of  $\alpha$ -NaFeO<sub>2</sub> Obtained under Various Hydrothermal Conditions,” *J. Electrochem. Soc.*, vol. 166, no. 10, pp. A2209–A2214, 2019, doi: 10.1149/2.1411910jes.
- [38] J. Kugai, H. Mine, S. Seino, T. Nakagawa, T. A. Yamamoto, and H. Yamada, “Effects of sodium nitrate and heat treatment atmosphere on the synthesis of  $\alpha$ -NaFeO<sub>2</sub> layered oxide,” *Mater. Chem. Phys.*, vol. 249, Jul. 2020, doi: 10.1016/J.MATCHEMPHYS.2020.122948.

- [39] D. Yusupov *et al.*, “Fluorite Formation in Poplar Leaves (*Populus balsamifera* L.) in an HF-Polluted Area,” *Water, Air, Soil Pollut.*, vol. 232, 2021, doi: 10.1007/s11270-021-05279-w.
- [40] C. Structures, “www.EDAX.com,” vol. 99, no. 251. .
- [41] W. Zuo *et al.*, “The stability of P2-layered sodium transition metal oxides in ambient atmospheres,” *Nat. Commun.*, vol. 11, no. 1, pp. 1–12, 2020, doi: 10.1038/s41467-020-17290-6.
- [42] P. Díaz-Carrasco, A. Kuhn, N. Menéndez, and F. García-Alvarado, “Reversible Fe<sup>3+</sup>/Fe<sup>2+</sup> and Ti<sup>4+</sup>/Ti<sup>3+</sup> redox couple in Fe-substituted LiTi<sub>2</sub>O<sub>4</sub> ramsdellite and its electrochemical properties as electrode material in lithium ion batteries,” *J. Alloys Compd.*, vol. 968, no. September, 2023, doi: 10.1016/j.jallcom.2023.172027.
- [43] C. Delmas, J. J. Braconnier, C. Fouassier, and P. Hagenmuller, “Electrochemical intercalation of sodium in Na<sub>x</sub>CoO<sub>2</sub> Bronzes,” *Solid State Ionics*, vol. 3/4, pp. 165–169, 1981, doi: 10.1016/0167-2738(88)90351-7.
- [44] S. Kumakura, Y. Tahara, K. Kubota, K. Chihara, and S. Komaba, “Sodium and Manganese Stoichiometry of P2-Type Na<sub>2/3</sub>MnO<sub>2</sub>,” *Angew. Chemie - Int. Ed.*, vol. 55, no. 41, pp. 12760–12763, 2016, doi: 10.1002/anie.201606415.
- [45] W. Kang *et al.*, “Copper substituted P2-type Na<sub>0.67</sub>Cu<sub>x</sub>Mn<sub>1-x</sub>O<sub>2</sub>: A stable high-power sodium-ion battery cathode,” *J. Mater. Chem. A*, vol. 3, no. 45, pp. 22846–22852, 2015, doi: 10.1039/c5ta06371j.
- [46] B. Mortemard De Boisse *et al.*, “Intermediate honeycomb ordering to trigger oxygen redox chemistry in layered battery electrode,” *Nat. Commun.*, vol. 7, pp. 1–9, 2016, doi: 10.1038/ncomms11397.

- [47] A. J. Perez *et al.*, “Strong oxygen participation in the redox governing the structural and electrochemical properties of Na-rich layered oxide  $\text{Na}_2\text{IrO}_3$ ,” *Chem. Mater.*, vol. 28, no. 22, pp. 8278–8288, 2016, doi: 10.1021/acs.chemmater.6b03338.
- [48] S. Komaba, “Electrochemical intercalation activity of layered  $\text{NaCrO}_2$  vs.  $\text{LiCrO}_2$ ,” *Electrochem. Commun.*, vol. 12, no. 3, 2010.
- [49] N. Yabuuchi, H. Yoshida, and S. Komaba, “Crystal structures and electrode performance of alpha- $\text{NaFeO}_2$  for rechargeable sodium batteries,” *Electrochemistry*, vol. 80, no. 10, pp. 716–719, 2012, doi: 10.5796/electrochemistry.80.716.
- [50] S. Roberts, L. Chen, B. Kishore, C. E. J. Dancer, M. J. H. Simmons, and E. Kendrick, “Mechanism of gelation in high nickel content cathode slurries for sodium-ion batteries,” *J. Colloid Interface Sci.*, vol. 627, pp. 427–437, 2022, doi: 10.1016/j.jcis.2022.07.033.
- [51] S. H. Song, K. Ahn, M. G. Kanatzidis, J. A. Alonso, J. G. Cheng, and J. B. Goodenough, “Effect of an internal electric field on the redox energies of  $\text{ALnTiO}_4$  ( $A = \text{Na}$  or  $\text{Li}$ ,  $\text{Ln} = \text{y}$  or Rare-Earth),” *Chem. Mater.*, vol. 25, no. 19, pp. 3852–3857, 2013, doi: 10.1021/cm401814z.
- [52] N. Yabuuchi, K. Kubota, M. Dahbi, and S. Komaba, “Research development on sodium-ion batteries,” *Chem. Rev.*, vol. 114, no. 23, pp. 11636–11682, 2014, doi: 10.1021/cr500192f.
- [53] H. D. Luong, H. Momida, V. A. Dinh, and T. Oguchi, “Understanding doping effects on  $P2$  Formula Presented (Formula Presented, Mg, Al, Ti, V, Cr, Fe, Co, Ni) cathode materials for Na-ion batteries,” *Phys. Rev. Mater.*, vol. 6, no. 1, pp. 1–10, 2022, doi: 10.1103/PhysRevMaterials.6.015802.
- [54] L. Wang *et al.*, “Unravelling the origin of irreversible capacity loss in  $\text{NaNiO}_2$  for high

- voltage sodium ion batteries,” *Nano Energy*, vol. 34, no. January, pp. 215–223, 2017, doi: 10.1016/j.nanoen.2017.02.046.
- [55] M. A. Khan, D. Han, G. Lee, Y. Il Kim, and Y. M. Kang, “*P2*/*O3* phase-integrated  $\text{Na}_{0.7}\text{MnO}_2$  cathode materials for sodium-ion rechargeable batteries,” *J. Alloys Compd.*, vol. 771, pp. 987–993, 2019, doi: 10.1016/j.jallcom.2018.09.033.
- [56] L. Zhang *et al.*, “Lithium lanthanum titanate perovskite as an anode for lithium ion batteries,” *Nat. Commun.*, vol. 11, no. 1, pp. 1–8, 2020, doi: 10.1038/s41467-020-17233-1.
- [57] M. Kim, H. Kim, M. Cho, and D. Kim, “Theoretical understanding of oxygen stability in Mn-Fe binary layered oxides for sodium-ion batteries,” *J. Mater. Chem. A*, pp. 11101–11109, 2022, doi: 10.1039/d2ta01747d.
- [58] W. Kang *et al.*, “Tunable Electrochemical Activity of  $\text{P2-Na}_{0.6}\text{Mn}_{0.7}\text{Ni}_{0.3}\text{O}_{2-x}\text{F}_x$  Microspheres as High-Rate Cathodes for High-Performance Sodium Ion Batteries,” *ACS Appl. Mater. Interfaces*, vol. 13, no. 13, pp. 15333–15343, Apr. 2021, doi: 10.1021/acsaami.1c02216.
- [59] I. Hasa, D. Buchholz, S. Passerini, and J. Hassoun, “A comparative study of layered transition metal oxide cathodes for application in sodium-ion battery,” *ACS Appl. Mater. Interfaces*, vol. 7, no. 9, pp. 5206–5212, 2015, doi: 10.1021/am5080437.
- [60] Z. Zhao, B. Huang, M. Wang, X. Yang, and Y. Gu, “Facile synthesis of fluorine doped single crystal Ni-rich cathode material for lithium-ion batteries,” *Solid State Ionics*, vol. 342, Dec. 2019, doi: 10.1016/j.ssi.2019.115065.
- [61] M. D. Slater, D. Kim, E. Lee, and C. S. Johnson, “Sodium-ion batteries,” *Adv. Funct. Mater.*, vol. 23, no. 8, pp. 947–958, 2013, doi: 10.1002/adfm.201200691.

- [62] B. Kang and G. Ceder, “Battery materials for ultrafast charging and discharging,” *Nature*, vol. 458, no. 7235, pp. 190–193, 2009, doi: 10.1038/nature07853.
- [63] P. Hou, F. Li, Y. Wang, J. Yin, and X. Xu, “Mitigating the P2-O2 phase transition of high-voltage P2-Na  $2/3$  [Ni  $1/3$  Mn  $2/3$  ]O<sub>2</sub> cathodes by cobalt gradient substitution for high-rate sodium-ion batteries,” *J. Mater. Chem. A*, vol. 7, no. 9, pp. 4705–4713, 2019, doi: 10.1039/c8ta10980j.
- [64] D. Yuan *et al.*, “P2-type Na<sub>0.67</sub>Mn<sub>0.65</sub>Fe<sub>0.2</sub>Ni<sub>0.15</sub>O<sub>2</sub> Cathode Material with High-capacity for Sodium-ion Battery,” *Electrochim. Acta*, vol. 116, pp. 300–305, 2014, doi: 10.1016/j.electacta.2013.10.211.
- [65] S. Eom, S. H. Jeong, S. J. Lee, Y. H. Jung, and J. H. Kim, “Mitigating the P2–O2 phase transition of Ni–Co–Mn based layered oxide for improved sodium-ion batteries via interlayered structural modulation,” *Mater. Today Energy*, vol. 38, p. 101449, 2023, doi: 10.1016/j.mtener.2023.101449.

## **5. Layered perovskite oxides as anodes for LIBs and NIBs**



5. Layered perovskite oxides as anodes for LIBs and NIBs .....	2099
5.1. Introduction.....	21313
5.1.2. Titanium-based Perovskites .....	21313
5.1.3. Layered Perovskites .....	2188
5.2. Synthesis optimisation and characterisation .....	22627
5.2.1. Calcination temperature optimisation .....	22727
5.2.2. Sodium Excess Optimisation .....	2289
5.2.3. Structure .....	23031
5.2.4. Morphology and composition .....	23435
5.2.5. Chemical deviation of structural sodium .....	23738
5.2.6. Optic behaviour .....	2389
5.3. Electrochemical performance <i>versus</i> lithium .....	24041
5.3.1. Galvanostatic measurements.....	24041
5.3.2. Cyclic-voltammetry .....	24243
5.3.3. Structural changes during operation .....	24445
5.4. Electrochemical performance <i>versus</i> sodium .....	24546
5.4.1. Galvanostatic measurements.....	24546
5.4.2. Cyclic-voltammetry .....	24849
5.4.3. Carbon super-P electrochemical performance .....	24950
5.4.4. Sodium mobility and diffusion coefficient by electrochemical impedance spectroscopy .....	25253
5.5. Conclusion.....	25657

5.6. References ..... 2589

## 5.1. Introduction

### 5.1.2. Titanium-based Perovskites

Throughout the years, many structures have been studied to be used as electrodes for LIB, NIB, or other types of high-performance batteries. In recent years, the properties of perovskite structured materials were found to be interesting for the application of novel materials for LIB high-performance anodes. These structures allow a wide variety of elements to integrate in their structure. This helps capitalise on the hidden variety of properties of different combinations of elements.

Perovskites were first discovered in the Russian Ural Mountains by Gustav Rose in 1839 and named after the Russian mineralogist Lev Perovski. The perovskite found naturally by Gustav Rose is a mineral of calcium, titanium, and oxygen, forming  $\text{CaTiO}_3$ , with a cubic crystal structure, as shown in Figure 5.1. Non-layered perovskites have a general formula of  $\text{ABX}_3$ , where  $A$  is typically an s-block or f-block element (alkali, alkaline-earth, internal transition metals) or an organic monovalent cation,  $B$  is a  $3d$ ,  $4d$ , or  $5d$  transition metal and  $X$  is oxygen or a halide, with a schematic shown in Figure 5.1. [1]–[3]

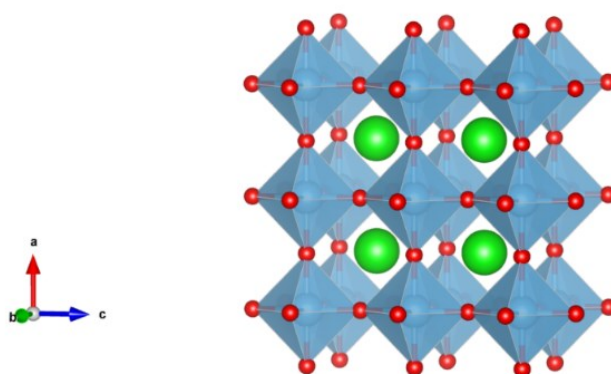


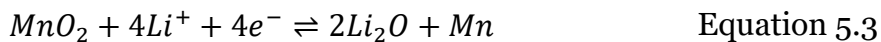
Figure 5.1 – Schematic representation of  $\text{CaTiO}_3$  perovskite obtained from VESTA with Materials Project database (mp-5827) where the  $\text{TiO}_6$  octahedra are represented in grey-blue, the oxygen on the tips of the octahedra in red and calcium in green.

CaTiO<sub>4</sub> structure is cubic, belonging to the space group  $Pm\bar{3}m$ . The structure consists of corner sharing BO<sub>6</sub> octahedra in all three crystallographic directions, forming a packed array. [4] With the substitution of elements, some distortions of this perovskite structure occur. [4], [5] With the substitution of atoms in the structure, perovskites exhibit impressive properties including, magnetoresistance – changes in electrical resistance when subjected to magnetic fields –, superconductivity, charge ordering, spin-dependant transport, *etc.* The applications may include, sensors, catalyst electrodes, fuel cells, solar cells, lasers, memory devices, and spintronics applications – the study of the intrinsic spin of the electron and its associated magnetic moment. [1], [2], [6]

A large number of metallic elements can be tolerated in a perovskite structure. The tolerance of elements in a perovskite is given by the Goldschmidt ratio of tolerance. [4] If the ratio of tolerance,  $t$ , is in the range of 0.75-1, the structure is stable. [2], [4] The  $t$  value is given by the expression in Equation 5.1, where  $R_A$ ,  $R_B$ , and  $R_O$ , represent the radii of the elements A and B, and oxygen, respectively. [2], [4]

$$t = \frac{R_A + R_O}{\sqrt{2} \cdot (R_B + R_O)} \quad \text{Equation 5.1}$$

Recently, the use of perovskite materials as anodes for LIB caught the interest of some researchers. [5] Calcium manganese oxide (CaMnO<sub>3</sub>) perovskite was studied as a novel anode material for LIB by Chan *et al.* [7] The electrochemical capacity of this material relies on the redox pair Mn(IV) to Mn metal hence, it is predicted that four electrons will intervene in the reaction. Given that information, the theoretical capacity of this CaMnO<sub>3</sub> is 749.624 mA·h·g<sup>-1</sup>. The predicted decomposition of the CaMnO<sub>3</sub> perovskite is shown in Equations 5.2 and 5.3. [7]



The process involves the irreversible decomposition of  $\text{CaMnO}_3$  to  $\text{CaO}$  and  $\text{MnO}_2$ . Accompanying the reduction process and the formation of manganese nanoparticles, the process involves the formation of  $\text{Li}_2\text{O}$ . As shown in

Figure 5.2 on the first cathodic scan, a peak appeared at 0.89 V and a sharp peak from 0.3 to 0.01 V that corresponds to the irreversible conversion from  $\text{CaMnO}_3$  to  $\text{MnO}_2$ , the decomposition of the electrolyte and formation of the SEI film on electrode surface as well as reduction of  $\text{MnO}_2$  to  $\text{Mn}$ . [7]

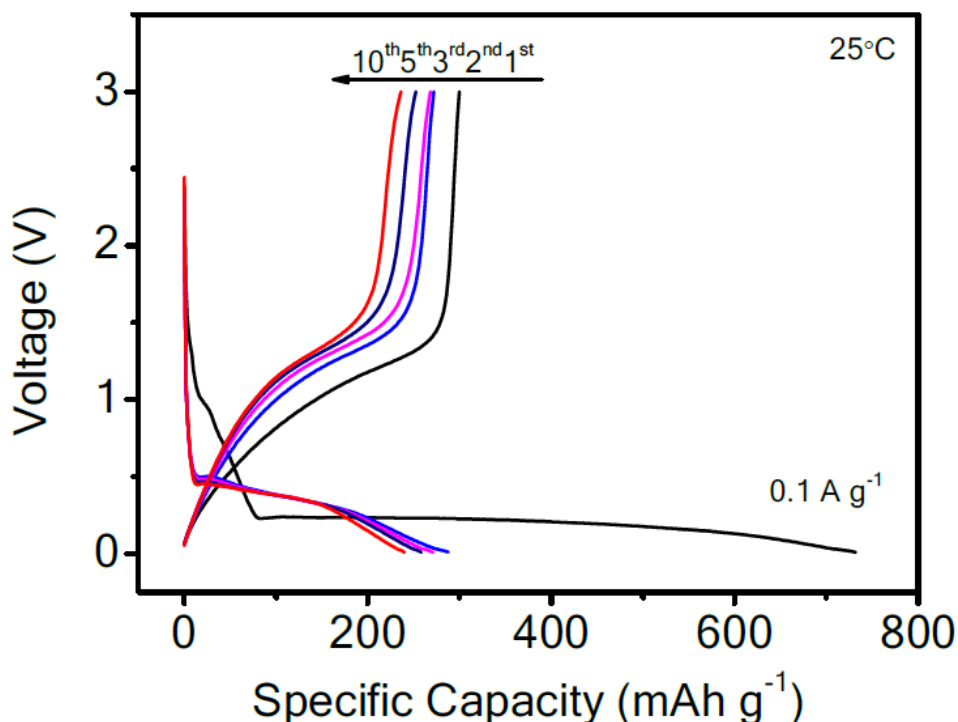


Figure 5.2 - Charge/discharge curves of  $\text{CaMnO}_3$  at  $0.1 \text{ A g}^{-1}$  in the 1<sup>st</sup>, 2<sup>nd</sup>, 3<sup>rd</sup>, 5<sup>th</sup> and 10<sup>th</sup> cycles at the current density of  $0.1 \text{ A g}^{-1}$ [7]

The formation of an inert CaO matrix serves as a buffer to enhance its electrochemical performance by mitigating mechanical and structural stress caused by volume changing. During the charging process, the oxidation peak at 1.24 V corresponds to the  $\text{Li}^+$ , corresponding to the deintercalation process. In the following cycle 2nd cycle, the curves gradually stabilised and the redox potential pairs stabilised at 0.16/1.39 V *vs.*  $\text{Li}^+/\text{Li}$ , indicating the excellent stability of the  $\text{CaMnO}_3$  material. [7]

The discharge capacity is 293.0 mA h  $\text{g}^{-1}$  at 0.1 A  $\text{g}^{-1}$ . The material exhibits an initial discharge capacity is 726.1 mA h  $\text{g}^{-1}$  on the first cycle, decreasing to 254.1 mA h  $\text{g}^{-1}$  after the 11<sup>th</sup> cycle, and can maintain a capacity of 225.4 mA h  $\text{g}^{-1}$  after the 90<sup>th</sup> cycle. [7] This material has a theoretical discharge capacity of 743.64 mA h  $\text{g}^{-1}$ , relatively close to the discharge capacity on the first cycle.

The above-mentioned perovskite-like material gets its electrochemical capacity uniquely from the redox capacity of the manganese. [7] Other studies investigate the electrochemical capacities of perovskite materials by the insertion of lithium or sodium. [7], [8] A study by Yan *et al.*, investigates the capacity of  $[(\text{Bi}, \text{Na})_{1/5}(\text{La}, \text{Li})_{1/5}(\text{Ce}, \text{K})_{1/5}\text{Ca}_{1/5}\text{Sr}_{1/5}]\text{TiO}_3$ , here referred to as high-entropy perovskite oxide (HEPO). HEPO was found to provide an initial discharge capacity of 125.9 mA h  $\text{g}^{-1}$  with a reversible capacity of 120.4 mA h  $\text{g}^{-1}$ , after the 300<sup>th</sup> cycle at 1000 mA  $\text{g}^{-1}$ . [8]

XRD was used to investigate the stability of the material during the charge/discharge process. The diffractograms in Figure 5.3 show a comparison between the pristine HEPO, HEPO after discharge and HEPO after 300 cycles. During discharge, a shift of the peak from 34.7 ° to 34.2 ° occurs. This shift is concomitant with the insertion of lithium in the structure by increasing the interlayer distance with the increase of electrostatic repulsion. Upon recharge, the peak shifts back to the original position, showing a highly reversible

insertion/disinsertion reaction and a highly stable structure with little but reversible distortions. [8]

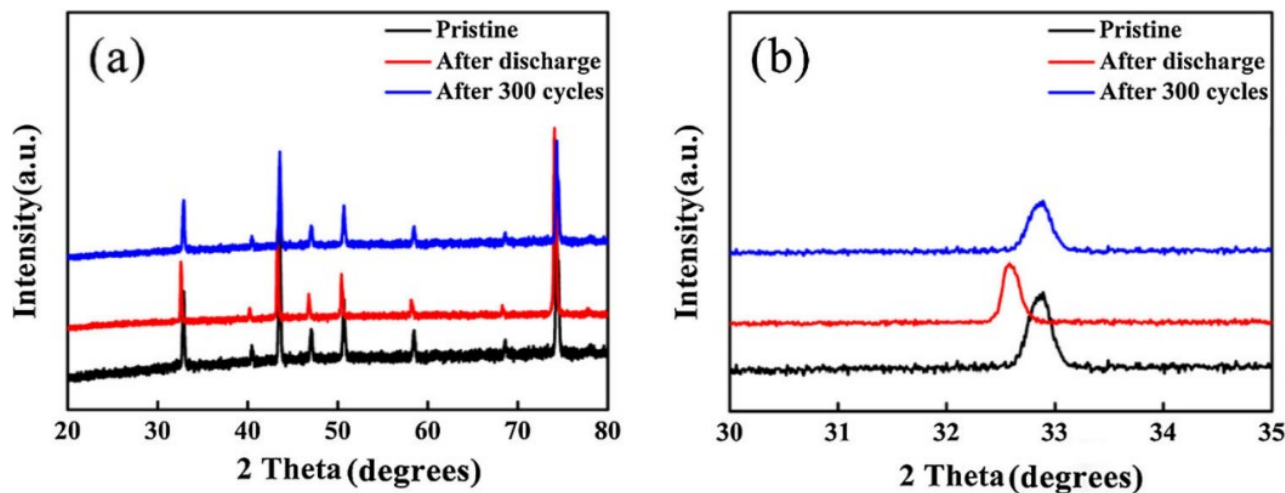


Figure 5.3 – (a) Phase structures of the pristine, after discharge and after 300 cycles of HEPO, and (b) enlargement of the diffractogram between  $2\theta$  values of  $30^\circ$  and  $35^\circ$  [8].

The most common insertion sites for  $\text{Li}^+$  ions include the octahedral sites ( $\text{BO}_6$ ) and the A-positive dipole. Given the tightly packed structure, the insertion of ions into the octahedral sites is very difficult, as it requires overcoming significant steric and electrostatic barriers. [8] Figure 5.4 presents a charge/discharge curve of HEPO over a potential range from 0.01 to 3.00 V vs.  $\text{Li}/\text{Li}^+$ , with a current of  $100 \text{ mA g}^{-1}$ . The charge/discharge plateaux are observed near 0.67 and 0.37 V, respectively. The discharge and charge capacities in the first cycle are 125.9 and  $69.6 \text{ mA h g}^{-1}$ , respectively. This results in a Coulombic efficiency (CE) of 55.3% on the first cycle. This relatively low CE can be attributed to the irreversible formation of the solid electrolyte interphase (SEI) layer, which consumes some capacity. From the second cycle onwards, the CE increases significantly to 98.2 %, showing a marked

improvement and a tendency to approach 100 %. This behaviour indicates high reversibility and suggests a stable electrochemical performance in subsequent cycles. [8]

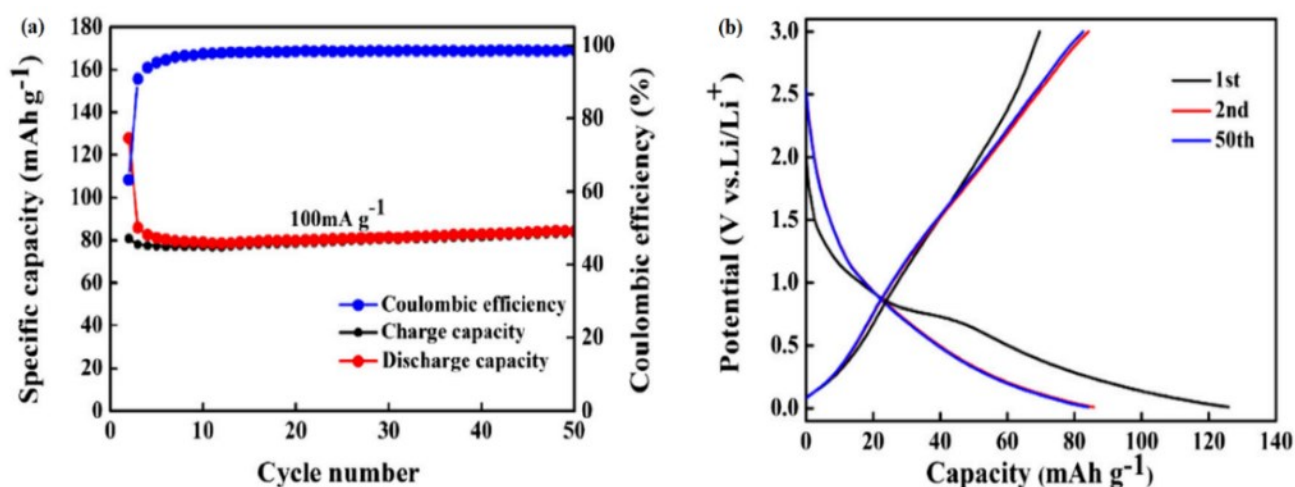


Figure 5.4 – (a) cycling performance and Coulombic efficiency of HEPO at  $100 \text{ mA}\cdot\text{g}^{-1}$  and (b) galvanostatic charge/discharge profiles of the selected cycles at the current density of  $100 \text{ mA}\cdot\text{g}^{-1}$  [8]

HEPO materials not only show great electrochemical performance but also excellent cyclability and stability. This excellent cyclability is attributed to the entropy-stabilised structures offered by mixed low and high radii cations. High-entropy oxide perovskites offer new options and opportunities for tailoring materials with high electrochemical performance. [8]

### 5.1.3. Layered Perovskites

The requirements to achieve a cubic structure are very rigorous so, a slight distortion can produce less symmetric versions, where the coordination numbers of the *A* and *B* atoms are reduced. Complex perovskite structures contain two different *B* cations. [2] This results in the possibility of ordered and disordered variants. This may result in perovskites structured in layers, with the above  $ABO_3$  separated by thin sheets of other materials. In perovskites, different forms of intrusions are based on the chemical composition of the intrusion or interpenetration and are defined as: [2]

- **Sillén-Aurivillius Phase** was discovered by Bengt Aurivillius in 1949, this is a layered perovskite with interlayers of bismuth oxide. The general formula is  $(M_2O_2)(A_{n-1}B_nO_{3n+1})$  and can have up to five perovskite layers ( $n-1$ ) per  $(M_2O_2)^{2+}$  sheet. The  $A$  ion can have a coordination number up to 12 and the  $B$  ion can hold up to 6 coordination bonds. Typical  $A$  ions are,  $Na^+$ ,  $K^+$ ,  $Ca^+$ ,  $Sr^{2+}$ ,  $Ba^{2+}$  and rare earth elements, while  $B$  ions are typically  $Fe^{3+}$ ,  $Ti^{4+}$ ,  $Nb^{5+}$ ,  $W^{6+}$ , *etc.* The bismuth oxide layer can be exchanged using a strong acid to create a proton layer in its place. [4], [6]
- **Dion-Jacobson** and **Ruddlesden-Popper (RP)** phases are similar to Aurivillius. By having a general formula of  $A_2[A_{m-1}B_mO_{3m+1}]$  where  $m$  can go from 1 to 3. [9] The same rules apply for assigning ions to the  $A$  and  $B$  sites in the perovskite layer. The main difference is in the interlayer which, for Dion-Jacobson is a monovalent cation, and for Ruddlesden-Popper a divalent cation or two monovalent cations. The interlayer of the Ruddlesden-Popper oxide has a slightly larger charge, leading to a thicker interlayer than the Dion-Jacobson structure. Usually, these cations are alkali or alkali-earth cations. These oxides are easily ion-exchanged with protons using strong acids. [4], [6]

The RP phases arise from a cut of the cubic perovskite  $ABO_3$  along its (1 0 0) direction followed by the insertion of additional oxygen. The oxides of the RP-type perovskite are usually more familiar because they are known for many different  $B$  cations. As previously mentioned, the layering of the perovskite structure is caused by slight distortions in the  $BO_6$  octahedra. The distortion of the octahedra is the largest at the boundary of the layers because the deviation from a perovskite structure is the greatest. On the other hand, moving to the inner region of the layers, the distortion of the  $BO_6$  octahedra decreases. [3]

If the  $A$  or  $B$  elements in the structure have different valences, then the elements with the higher valence tend to occupy the boundary of the layers while the smallest occupy the centre of the layers. Compared to non-layered perovskites, the amount of oxygen ( $O^{2-}$ )

accessible is relatively large. This results in a significant amount of negative charges at the boundary of the layers. This will create a tendency for the cations with higher valence to accumulate at the boundary of the layers. In Figure 5.5 a sketch of the various types of layered perovskites, compared to the pristine form is shown. [3]

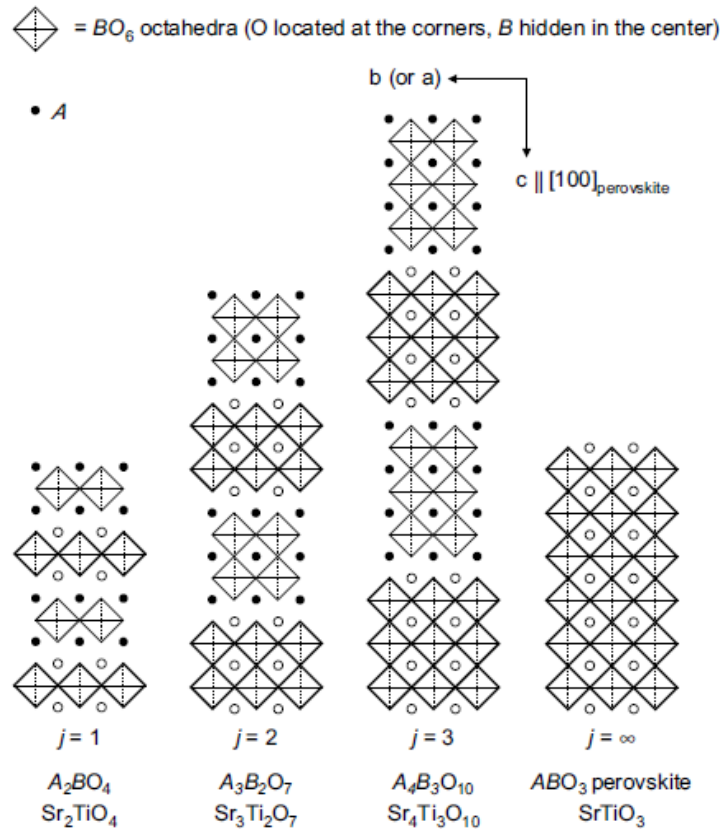


Figure 5.5 – Sketch of the idealised crystal structure of the  $n = 1, 2, 3,$  and  $N$  members of the perovskite-related layered homologous series  $A_2[A_{m-1}B_mO_{3m+1}]$  (RP phases) projected along with the  $a$  and  $b$  axes.[3]

The RP phase of  $CaTiO_3$  ( $Ca_2TiO_4$ ) has a favourable formation enthalpy ( $\Delta_f H$ ) and entropy ( $S$ ) of  $-2373.7 \text{ kJ mol}^{-1}$  ( $CaTiO_3$ ) and  $124.0 \text{ J K}^{-1} \text{ mol}^{-1}$  ( $Ca_2TiO_4$ ), respectively. However, as mentioned above, not all  $Ca_2MO_4$  RP structures can be prepared. [4] Considering the relaxation of the RP structure to the pristine structure to be  $A_2MO_4 \rightarrow AMO_3 + AO$ , the Gibbs energy changes with the component oxides are given by Equation 5.4 [4]

$$\Delta_r G^0 = \Delta_f G^0(AMO_3) - \Delta_f G^0(A_2MO_4) \quad \text{Equation 5.4}$$

Where  $\Delta_r G^0$  is the relaxation Gibbs energy,  $\Delta_f G^0(AMO_3)$  is the formation Gibbs energy of the cubic non-layered perovskite, and  $\Delta_f G^0(A_2MO_4)$  is the formation Gibbs energy of the  $n=1$  layered perovskite. If  $\Delta_r G^0$  is positive, the RP structure will not be stable, which might happen in some circumstances. It is known that a large radius transition metal ( $M$ ) should be accompanied by larger radii alkali, alkali-earth, or internal transition metals, that better match for packing. These relations between elements can be described by the above-mentioned Goldschmidt ratio of tolerance. [4]

Ruddlesden-Popper (RP) perovskite structures caught the attention of the development of electrodes for various applications (*e.g.*, *Li*-ion batteries, fuel cells, etc.) for their relatively high ion mobility and relatively high conductivity. [10], [11] Studies on  $\text{NaLaTiO}_4$  by Qu *et al.*, report  $\text{Na}^+$  mobility of  $4.66 \times 10^{-11} \text{ cm}^2 \text{ s}^{-1}$  and a conductivity of  $0.26 \text{ S} \cdot \text{cm}^{-1}$ . Unfortunately, not many studies on layered perovskites as anodes for NIB have been conducted. [10] In Figure 5.6 a schematic representation of a Ruddlesden-Popper-type layered perovskite ( $\text{NaLaTiO}_4$ ) is shown.

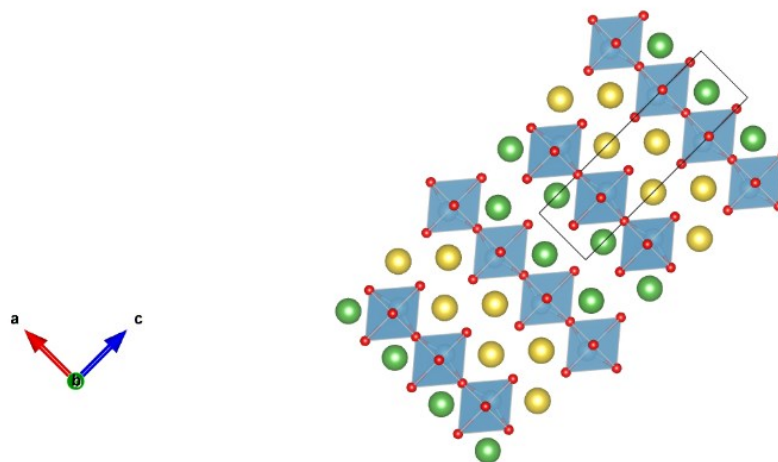


Figure 5.6 – Schematic representation of a Ruddlesden-Popper type layered perovskite obtained from VESTA with Materials Project database (mp-6514) where the titanium octahedra are represented in

grey-blue, lanthanum in dark green, the oxygen on the tips of the octahedra in red and sodium in yellow.

The  $\text{NaLaTiO}_4$  has an interlayer distance of 13.21 Å (Predicted using VESTA), compared with 3.4 and 7.8 Å of graphene and  $\text{Na}_2\text{Ti}_3\text{O}_7$ , respectively. [12] [13] This, together with the flexibility of perovskites, permits a wide range of structural modifications by intercalation.[4]

In 2013, Song *et al.* studied several RP-layered perovskites as LIB anode materials with the general formula of  $\text{NaLnTiO}_4$ , where  $Ln$  is a lanthanide. [14] These materials were synthesised *via* a solid-state reaction and they exhibit an orthorhombic crystal structure. [14] As mentioned above, this corresponds to a distortion of a cubic crystal structure that leads to other phases of perovskites. [2], [4], [6], [14] In this work the lanthanides used were yttrium, terbium, gadolinium, europium, samarium, neodymium, praseodymium and lanthanum. In Figure 5.7 the cycling performances of various RP layered perovskites are shown.

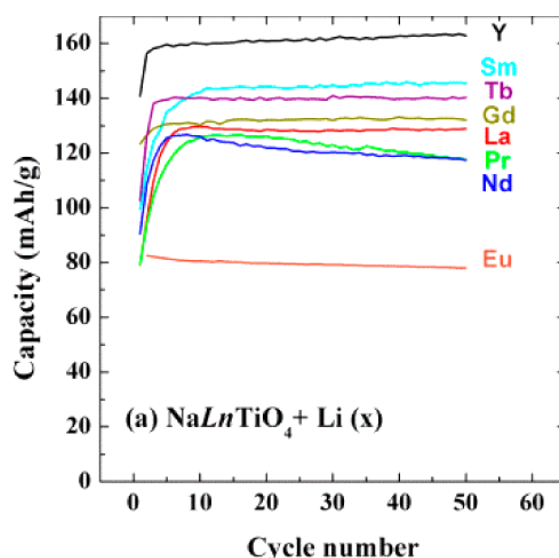


Figure 5.7 – Cycling performances to the 50<sup>th</sup> cycle at 0.2 C of  $\text{NaLnTiO}_4$ , where  $Ln = \text{Y, Tb, Gd, Eu, Sm, Nd, Pr, La}$  [14]

All these materials, except  $\text{NaEuTiO}_4$ , were able to maintain a capacity above 100 mA h g<sup>-1</sup> at 2 C, after 50 cycles. To evaluate whether a certain material is promising, the costs

of production should be taken into consideration. In Table 5.1 the prices of 10 g of the sources of yttrium, terbium, gadolinium, europium, samarium, neodymium, praseodymium, and lanthanum are compared. The substances' prices were obtained from Sigma-Aldrich®.

Table 5.1 – Prices of some rare earth element oxides

SUBSTANCE	£ g <sup>-1</sup>	SUBSTANCE	£ g <sup>-1</sup>	SUBSTANCE	£ g <sup>-1</sup>
Y <sub>2</sub> O <sub>3</sub>	2.76	Eu <sub>2</sub> O <sub>3</sub>	110	La <sub>2</sub> O <sub>3</sub>	2.72
Nd <sub>2</sub> O <sub>3</sub>	9.70	Gd <sub>2</sub> O <sub>3</sub>	21.8	Sm(NO <sub>3</sub> ) <sub>3</sub>	9.24
Pr <sub>2</sub> O <sub>3</sub>	19.80	Tb <sub>2</sub> O <sub>3</sub>	44.45	TiO <sub>2</sub>	0.44

Both substitutions with lanthanum, samarium, and gadolinium show very promising properties, whilst having relatively inexpensive precursors. For that, NaLaTiO<sub>4</sub>, NaSmTiO<sub>4</sub>, and NaGdTiO<sub>4</sub> seem to be the most promising RP-layered perovskites for NIB anode materials.

Another study by Hwang *et al.*, reports on the properties of LiEuTiO<sub>4</sub> as an anode for Li-ion batteries. [15] In this study, the electrochemical performance was studied. The reported specific capacity on the second discharge is 219.2 mA h g<sup>-1</sup> at a rate of 100 mA g<sup>-1</sup>. The intercalation potential is 0.75 V *vs.* Li/Li<sup>+</sup>, corresponding to the galvanostatic profile *plateaux* observed in Figure 5.8. [16]

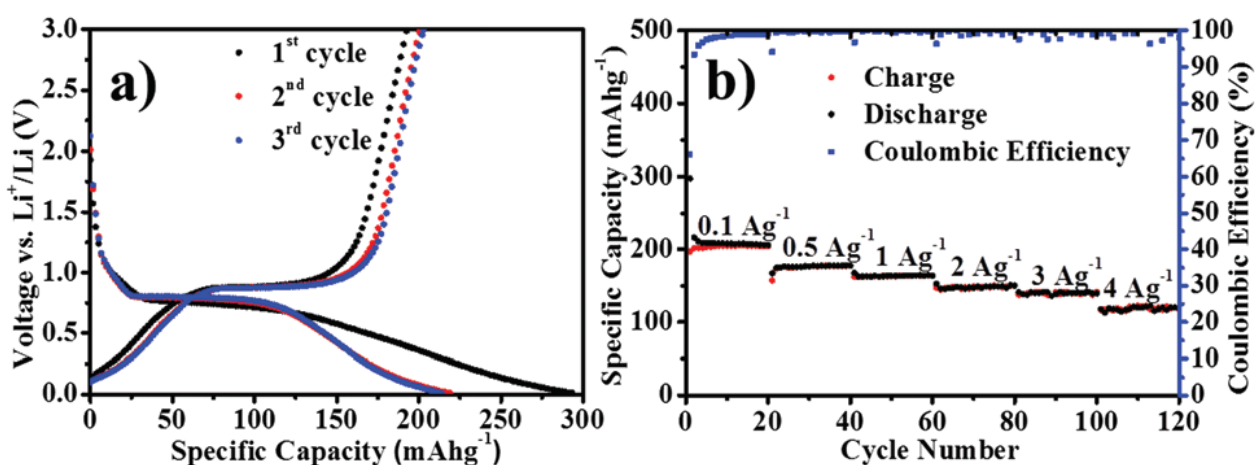


Figure 5.8 - (a) Galvanostatic discharge/charge voltage profiles of LiEuTiO<sub>4</sub> for the first three cycles at 100 mA·g<sup>-1</sup>, (b) Rate performance and Coulombic efficiency at various current densities ranging from 0.1 to 4 A·g<sup>-1</sup>. [16]

The small deviance on the charge and discharge *plateaux* shows and small polarisation of approximately 100 mV. As expected, the irreversible capacity on the first cycle is related to the reductive decomposition of the electrolyte to form the SEI. The resulting Coulombic efficiency is 67 %. Upon cycling, CE suffers a sharp increase well above 99 %. At the 500<sup>th</sup> cycle, the discharge capacity of 217 mA h g<sup>-1</sup>, represents a Coulombic efficiency of 99.2 %. This shows great cyclability and indicates minimal expansion during discharge. [16]

The X-ray diffractograms of LiEuTiO<sub>4</sub> in the middle of the discharge process, full discharge, middle of the charging process, and full charge are used to compare the lithium storage behaviour. The first cycle was selected for this study whose results are shown in Figure 5.9. [16]

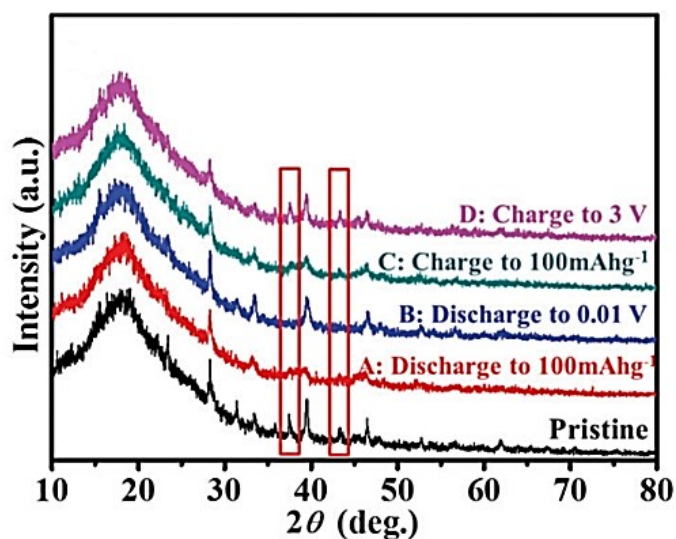


Figure 5.9 – X-rays diffractograms of NaEuTiO<sub>4</sub> at four different charge states: Pristine; A – Discharge to 100 mA·h·g<sup>-1</sup>; B – Discharge to 0.01 V; C – Charge to 100 mA·h·g<sup>-1</sup> and; D – Charge to 3 V.[16]

The peaks at  $2\theta$  equal to 38 and 42.8 ° gradually disappear upon discharge and reappear during the charging process. This peak disappearance a reappearance shows the reversibility of lithium into the LiEuTiO<sub>4</sub>. When lithium intercalates into transition metal oxides, the oxidation state of some elements within the structure will change to keep the

overall structure's electrical neutrality. This process leads to the acceptance of one electron per  $\text{Li}^+$  intercalated. Both titanium and europium can change their valence to accommodate the  $\text{Li}^+$ . XPS analysis was used to evaluate the redox processes occurring in the material. In Figure 5.10 the XPS spectra of europium and titanium are shown. [16]

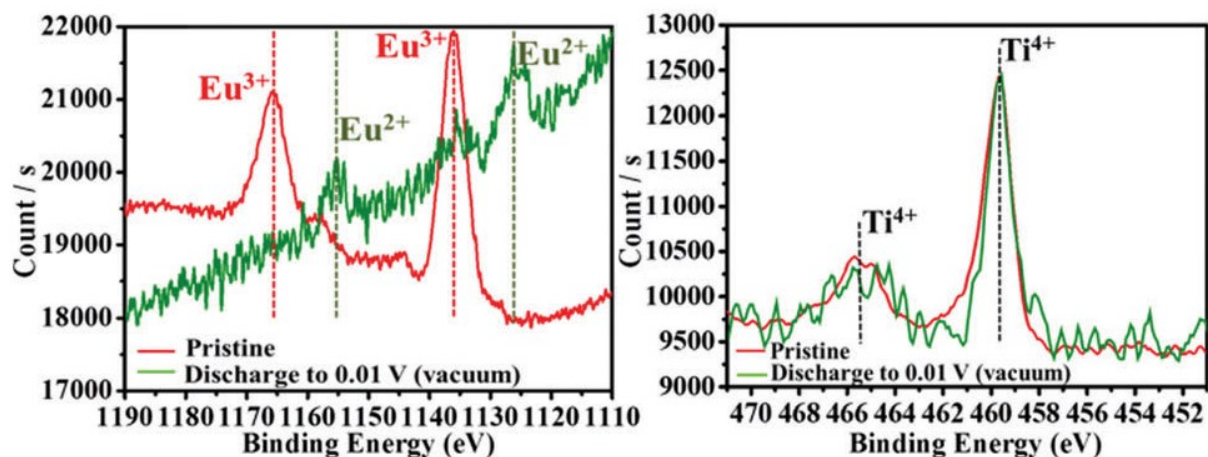


Figure 5.10 - XPS spectra of Eu and Ti of two electrode samples (pristine and after 1<sup>st</sup> discharge to 0.01 V [16]

Referring to the study of the oxidation state of europium, one can see a notable difference between the spectra of the pristine and the sample after the first discharge to 0.01 V. The spectrum of europium in the pristine sample shows clear peaks at 1165 and 1135 eV, corresponding to  $\text{Eu}(\text{III})$ . The fully discharged spectrum of Eu shows weak peaks at 1156 and 1125 eV, corresponding to  $\text{Eu}(\text{II})$ . This indicates that  $\text{Eu}(\text{III})$  has been reduced to  $\text{Eu}(\text{II})$ , upon lithium intercalation into  $\text{LiEuTiO}_4$ . [16] Concerning titanium, the two main peaks in the XPS spectra appear at 465.4 and 459.6 eV, corresponding to  $\text{Ti}(\text{IV})$ . After full discharge, no significant changes are noticeable indicating that during this process, no reduction of titanium occurred. [16]

In summary, unlike other titanium-based intercalation materials, including other  $\text{NaLnTiO}_4$ ,  $\text{NaEuTiO}_4$  relies on the reduction of  $\text{Eu}(\text{III})$  to  $\text{Eu}(\text{II})$  as well as  $\text{Ti}(\text{IV})$  to  $\text{Ti}(\text{III})$ . The proposed mechanism for lithium intercalation is as shown in Equation 5.5. [16]



This study does not provide any value for the moles of  $\text{Li}^+$  that intercalate for every stoichiometric molar amount of  $\text{LiEuTiO}_4$ . This material has a theoretical capacity for 98.985, 197.970, 296.955, and 395.940  $\text{mA h g}^{-1}$  for  $x$  equal to 1, 2, 3, and 4, this being, the intercalation of 1, 2, 3, and 4 moles of  $\text{Li}^+$  per stoichiometric molar amount of  $\text{LiEuTiO}_4$ . The first cycle of the discharge process at 1000  $\text{mA g}^{-1}$  has a capacity of around 170  $\text{mA h g}^{-1}$ . This experimental result is closer to the theoretical capacity for 197.970  $\text{mA h g}^{-1}$ , indicating intercalation of two moles of  $\text{Li}^+$  per stoichiometric molar amount of  $\text{LiEuTiO}_4$  or  $x$  equals two. [16]

These studies describe the application of this type of material as anodes for LIB. As mentioned, these materials present a very wide range of possibilities on what concerns properties manipulation by element substitution. By replacing some elements and synthesis methods, the structures can be manipulated to be used as efficient anodes for NIB.

## 5.2. Synthesis optimisation and characterisation

During this chapter, the synthesis method of  $\text{NaLaTiO}_4$  and  $\text{NaYTiO}_4$  *via* the solid-state method was optimised to the environmental conditions and equipment existent in the lab in a way that the material was obtained with the least amount possible of the secondary phase. This was accomplished by manipulating the calcination temperature and the excess sodium added to compensate for its volatilisation. Some variations of this material were synthesised by Goodenough *et al.* hence, the synthesis of these materials will be based on this work. [14]

After the optimisation of the synthesis method, the electrochemical performance was determined *via* galvanostatic charge and discharge methods, cyclic-voltammetry, and *operando* X-ray diffraction.

### 5.2.1. Calcination temperature optimisation

In this work, the synthesis of  $\text{NaLaTiO}_4$  was first attempted. For that, the calcination temperature to obtain the desired final product was calcined at 800, 840, 900, and 1000 °C, to investigate the effect of temperature in the formation of  $\text{NaLaTiO}_4$ . The experimental details are described in Section 2.1.1. In Figure 5.11, the diffractograms of the material obtained from calcination at 800, 840, 900, and 1000 °C are compared with a reference of  $\text{NaLaTiO}_4$  and one of the most common impurities  $\text{Na}_2\text{La}_2\text{Ti}_3\text{O}_{10}$  obtained from the ICSD. [17]

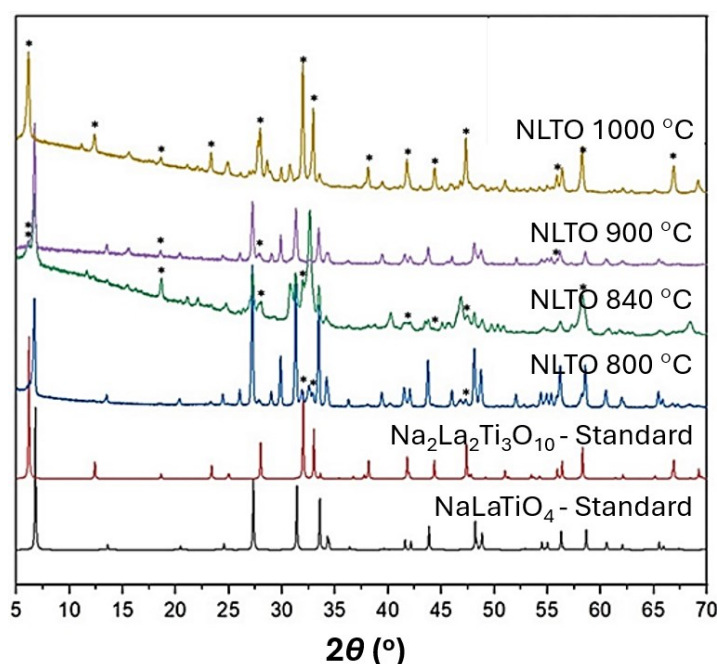


Figure 5.11 – X-ray diffractograms of the samples synthesised at temperatures of 800, 840, 900, and 1000 °C with the standards of  $\text{NaLaTiO}_4$  and  $\text{Na}_2\text{La}_2\text{Ti}_3\text{O}_{10}$  obtained from the ICSD. [17] The peaks attributed only to the  $\text{Na}_2\text{La}_2\text{Ti}_3\text{O}_{10}$  phase are indicated with an asterisk (\*).

The secondary phase,  $\text{Na}_2\text{La}_2\text{Ti}_3\text{O}_{10}$  is detected in all the temperatures tried in experiments to obtain a  $\text{NaLaTiO}_4$ . However, comparing the diffractograms obtained at all temperatures of calcination, the calcination temperature that leads to the least amount of the secondary phase is 800 °C, which is lower than the reported in previous studies. [14], [18] Most peaks are ascribed, either to the primary phase ( $\text{NaLaTiO}_4$ ) or the main secondary phase ( $\text{Na}_2\text{La}_2\text{Ti}_3\text{O}_{10}$ ). Those peaks that are not ascribed to any of these phases are likely to come

from other products of degradation such as  $\text{La}_2\text{Ti}_3\text{O}_7$  and  $\text{TiO}_2$ . [19] The stability of the  $n=1$  layered titanate relies on the stoichiometric balance between Na and La. [14], [20] Sodium has a boiling point of around  $883^\circ\text{C}$  hence since the calcination temperatures studies in this work are close or higher than this value, some sodium is likely lost due to volatilisation. [21] This imbalance between the sodium and lanthanum layers may lead to the collapse and agglomeration of the  $\text{TiO}_6$  layers forming the  $\text{Na}_2\text{La}_2\text{Ti}_3\text{O}_{10}$  ( $n=3$ ) and other lanthanum and titanium-rich impurities. [3], [19], [22] Adding to this phenomenon, the increased temperature may also destabilise the  $\text{TiO}_4$  monolayers, inducing a parallel reaction leading to the agglomeration of layers. [23] For this reason, it was decided that further optimisation of the synthesis of  $\text{NaLaTiO}_4$  will be conducted at  $800^\circ\text{C}$ .

### 5.2.2. Sodium Excess Optimisation

The Na-La-Ti-O system has two main phases that appear during a ceramic reaction. To keep the necessary balance between lanthanum and sodium, an excess of sodium, which is the sodium source, should be added to the mix. Different works on this material specify that different molar percentages of sodium excess will result in at least number of secondary phases, which is highly dependent on the calcination temperature. Qu *et al.*, reported the synthesis of  $\text{NaLaTiO}_4$  at  $800^\circ\text{C}$  with no excess of sodium, whereas Byeon *et al.*, reports the synthesis of  $\text{NaLaTiO}_4$  with a 20 % excess sodium at the same calcination temperature. [10], [19] Adding the this, Goodenough *et al.*, reported that a pure  $\text{NaLaTiO}_4$  phase was obtained with a 30 % excess of sodium at  $900^\circ\text{C}$ . [14]

Following the condition described in section 2.1.1., an excess of 20, 30, 40, and 50 % (mol) of sodium from sodium carbonate was added to the precursor mixture. The precursor was calcined at  $800^\circ\text{C}$ , as it was previously defined as the optimal calcination temperature for the primary phase. The diffractograms shown in Figure 5.12, compare the structures obtained by adding a 20, 30, 40, and 50 % sodium excess.

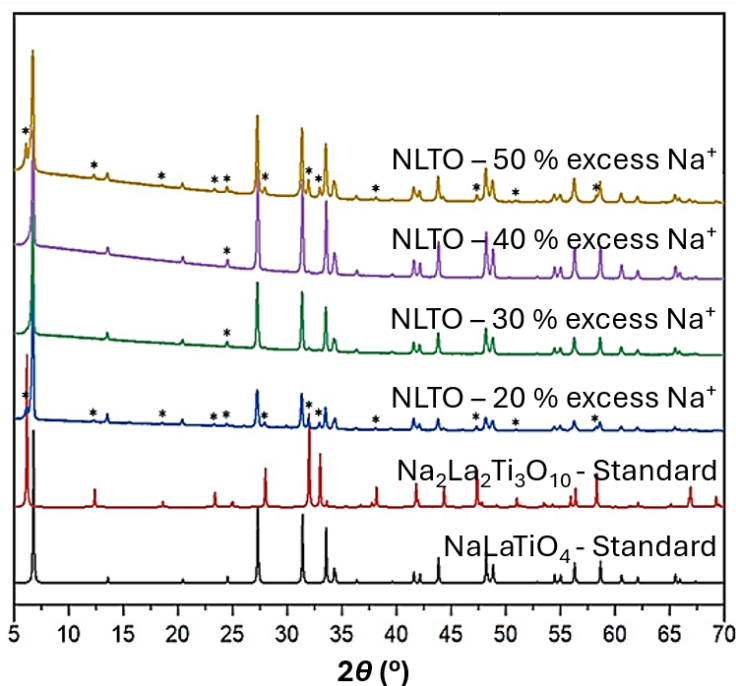


Figure 5.12 – X-ray diffractograms of the samples synthesised with an excess of 20, 30, 40, and 50 % sodium compared with the standards of  $\text{NaLaTiO}_4$  and  $\text{Na}_2\text{La}_2\text{Ti}_3\text{O}_{10}$  obtained from ICSD. The peaks attributed only to the  $\text{Na}_2\text{La}_2\text{Ti}_3\text{O}_{10}$  phase are highlighted with an asterisk (\*).

The precursors with an excess of sodium of 30 and 40 % show the lowest amount of  $\text{Na}_2\text{La}_2\text{Ti}_3\text{O}_{10}$  after calcination. However, this secondary phase could not be completely avoided. The precursors containing 20 and 50 % excess sodium show a higher presence of the secondary phase. This was qualitatively assessed by counting the number of peaks that can be ascribed to the secondary phase *versus* those that can be ascribed to the primary phase.

These experiments reflect the careful control needed upon heating and Na/La balance to avoid the secondary phase. At the temperatures of calcination required for the synthesis of this material,  $\text{Na}_2\text{CO}_3$  is volatilised from the mixture, leading to the agglomeration of  $\text{TiO}_6$  layers to form  $\text{Na}_2\text{La}_2\text{Ti}_3\text{O}_{10}$  and on the other hand, too much excess sodium will equally promote the formation of the  $\text{Na}_2\text{La}_2\text{Ti}_3\text{O}_7$  phase. [19]  $\text{NaYTiO}_4$  was synthesised under the same conditions.

### 5.2.3. Structure

The lattice parameters of  $\text{NaLaTiO}_4$  were obtained using Rietveld refinement (Figure 5.13). The refined parameters included the zero, lattice, and profile parameters, atomic positions, and isotropic displacement parameters ( $U_{iso}$ ). The lattice parameters were found to be  $a = b = 3.77965(5) \text{ \AA}$ ,  $c = 13.04530(6) \text{ \AA}$ ,  $\alpha = 90^\circ$ ,  $\beta = 90^\circ$  and  $\gamma = 90^\circ$ , which are in agreement with the unit cell parameters reported in the literature. [14] The refined parameters can be found in Table 5.2. The goodness-of-fit,  $\chi^2$ , was found to be 6.0000 and the R factors such as weighted profile R-factor,  $R_{wp}$ , and expected R factor,  $R_{exp}$ , were found to be 13.1 and 5.33 %, respectively. In this case, the data was collected in reflection mode using conventional  $\text{Cu K}\alpha_1$  and  $\text{Cu K}\alpha_2$  sources which influenced the goodness of the refinement. As expected, the material used for these and the following experiments has a purity of 92.16 % and an impurity of  $\text{Na}_2\text{La}_2\text{Ti}_3\text{O}_{10}$ , corresponding to 7.84 % of the total amount of material. This impurity content contributes to a higher weighted profile R-factor of 13.13 %.

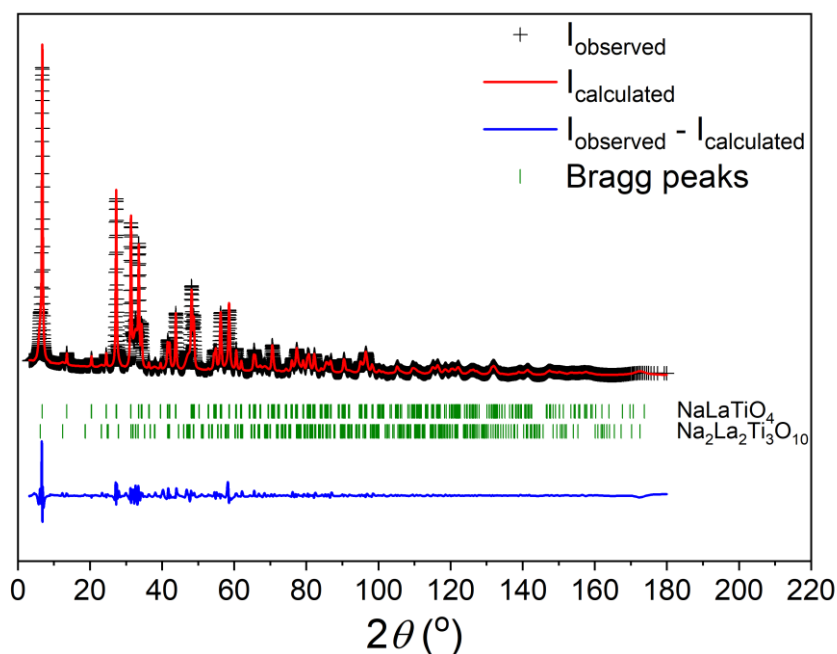


Figure 5.13 – Rietveld fit of XRD data of NLTO. (+) corresponds to the observed data, the solid red line indicates the calculated profile and the solid blue line corresponds to the difference between the two profiles. (|) indicate Bragg reflections of  $\text{NaLaTiO}_4$  (ICSD 73323) and  $\text{Na}_2\text{La}_2\text{Ti}_3\text{O}_{10}$ .

Table 5.2 – Atomic positions, isotropic displacement parameters, occupancies, and reliability factors of NaLaTiO<sub>4</sub> determined by the Rietveld refinement method from the PXRD data acquired at room temperature.

Atom	x	y	z	Multiplicity	Occupancy	U <sub>iso</sub> (Å <sup>2</sup> )
<b>Na1</b>	0.0000	0.5000	0.5850(1)	2	0.5	0.15(2)
<b>La1</b>	0.0000	0.5000	0.8890(2)	2	0.5	0.10(4)
<b>Ti1</b>	0.0000	0.5000	0.2755(1)	2	0.5	0.10(6)
<b>O1</b>	0.0000	0.0000	0.2430(4)	2	0.5	0.30(9)
<b>O2</b>	0.0000	0.5000	0.0720(1)	2	0.5	0.20(1)
<b>O3</b>	0.0000	0.5000	0.4060(2)	2	1.0	0.60(9)

NaLaTiO<sub>4</sub> – space group *P 4/n m m*

*a* = *b* = 3.77965(5) Å; *c* = 13.04530(6) Å; α = 90 °; β = 90 °; γ = 90 °

χ<sup>2</sup> = 6.000; R<sub>wp</sub> = 13.1 %; R<sub>exp</sub> = 5.33 %

%(NaYTlO<sub>4</sub>) = 92.16 %; %(Na<sub>2</sub>CO<sub>3</sub>) = 7.84 %

In the same way, the lattice parameters of NaYTlO<sub>4</sub> were obtained using Rietveld refinement (Figure 5.14). The refined parameters included the zero, lattice, and profile parameters, atomic positions, and isotropic displacement parameters (*U*<sub>iso</sub>). The lattice parameters were found to be *a* = 12.26130(9) Å; *b* = 5.35611(3) Å; *c* = 5.34070(9) Å; α = 90 °; β = 90 ° and; γ = 90 °. The refined parameters can be found in Table 5.3. The goodness-of-fit, χ<sup>2</sup>, was found to be 5.4480 and the R factors such as weighted profile *R*-factor, *R*<sub>wp</sub>, and expected *R* factor, *R*<sub>exp</sub>, were found to be 10.3 and 4.42 %, respectively. In this case, the data was collected in reflection mode using conventional Cu K<sub>α1</sub> and Cu K<sub>α2</sub> sources which influenced the goodness of the refinement. As expected, the material used for these and the following experiments has a purity of 96.2 % and an impurity of Na<sub>2</sub>CO<sub>3</sub>, corresponding to 3.8 % of the total amount of material. The lower amount of impurities is concomitant with the lower weighted profile *R*-factor of 10.3 % when compared to NaLaTiO<sub>4</sub>.

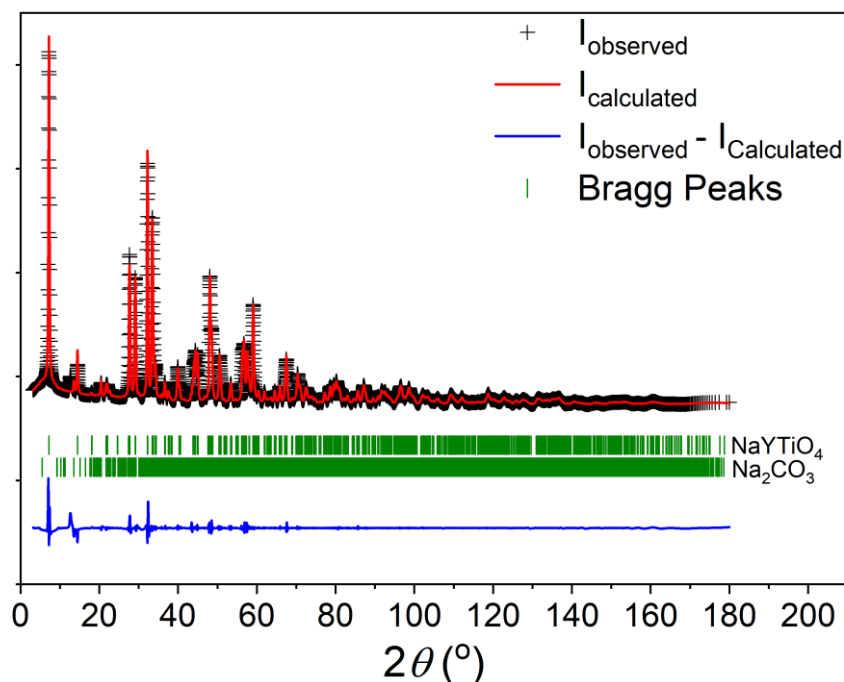


Figure 5.14 – Rietveld fit of XRD data of  $\text{Ta-WTe}_2$ . (+) corresponds to the observed data, the solid red line indicates the calculated profile and the solid blue line corresponds to the difference between the two profiles. (|) indicate Bragg reflections of  $\text{NaLaTiO}_4$  (ICSD 73323) and  $\text{Na}_2\text{La}_2\text{Ti}_3\text{O}_{10}$ .

Table 5.3 – Atomic positions, isotropic displacement parameters, occupancies, and reliability factors of  $\text{NaYTlO}_4$  determined by the Rietveld refinement method from the PXRD data acquired at room temperature.

Atom	x	y	z	Multiplicity	Occupancy	$U_{\text{iso}}$ ( $\text{\AA}^3$ )
<b>Na1</b>	0.5905(2)	0.0154(2)	0.2500	2	0.5	2.30(1)
<b>Y1</b>	0.8931(3)	0.0298(3)	0.2500	2	0.5	0.40(1)
<b>Ti1</b>	0.2610(3)	0.0111(1)	0.2500	2	0.5	0.50(1)
<b>O1</b>	0.2062(2)	0.2500	0.0000	2	0.5	1.00(1)
<b>O2</b>	0.7571(4)	0.2500	0.0000	2	0.5	1.00(2)
<b>O3</b>	0.07030(3)	-0.0809(1)	0.2500	2	0.5	1.20(2)
<b>O4</b>	0.3980(2)	0.0568(1)	0.2500	2	0.5	1.10(1)

$\text{NaYTlO}_4$  – space group  $Pbcm$

$a = 12.26130(9) \text{ \AA}$ ;  $b = 5.35611(3) \text{ \AA}$ ;  $c = 5.340709 \text{ \AA}$ ;  $\alpha = 90^\circ$ ;  $\beta = 90^\circ$ ;  $\gamma = 90^\circ$

$\chi^2 = 5.448$ ;  $R_{\text{wp}} = 10.3 \%$ ;  $R_{\text{exp}} = 4.42 \%$

$\%(\text{NaYTlO}_4) = 96.2 \%$ ;  $\%(\text{Na}_2\text{CO}_3) = 3.8 \%$

The structure of  $\text{NaLaTiO}_4$  and  $\text{NaYTiO}_4$  belong, is illustrated in Figure 5.15. This figure shows that alternate NaO and  $\text{LnO}$  double layers are arranged with a sequence of  $(\text{NaO})_2\text{-TiO}_2\text{-}(\text{LnO})_2\text{-TiO}_2\text{-}$  along the  $c$ -axis. Note that in naming the axes, the attributed name to the abovementioned  $c$ -axis is named as  $a$ -axis in the  $\text{NaYTiO}_4$  model. The titanium atoms are displaced out of the plane towards the NaO double layers, leading to a considerable distortion of the  $\text{TiO}_2$  layers. The distortion of the  $\text{LnO}$  layers is also observed whilst the NaO layers seem to be almost flat. [23]

The  $c$  parameter of  $\text{NaLaTiO}_4$  was calculated as 13.045306 Å while the  $c$  parameter of  $\text{NaYTiO}_4$  ( $a$  parameter), is 12.261309 Å. This variation is in good agreement with the previously reported, stating that the  $c$  parameter decreases as the atomic radii of the lanthanide ( $\text{Ln}$ ) decrease. [23] La = 240 pm; Y = 219 pm.

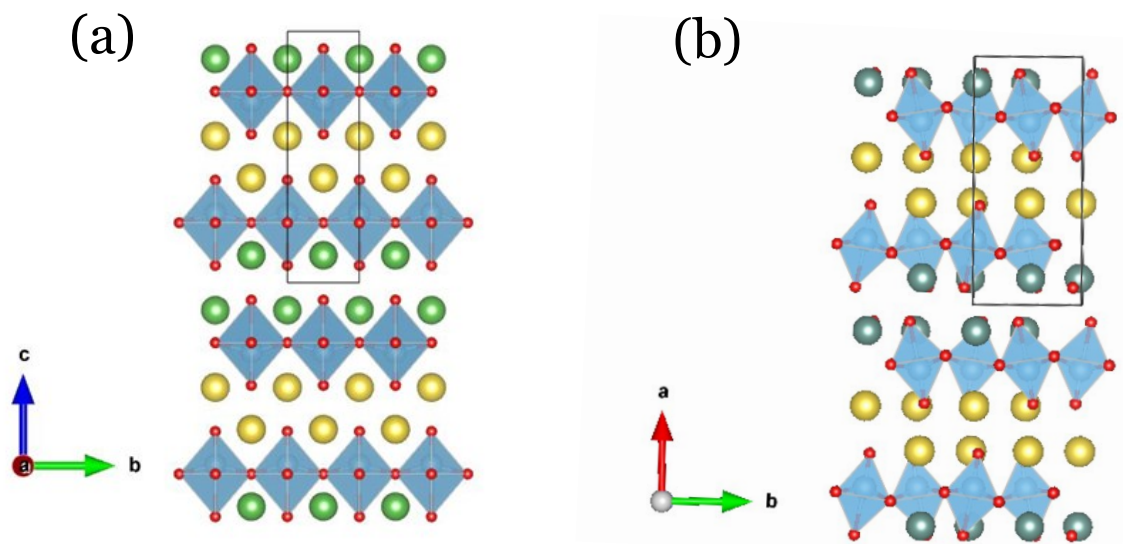


Figure 5.15 – Schematic representation of (a) NLTO and (b) NYTO, where sodium is represented in yellow, lanthanum in green, yttrium in grey-blue, titanium in blue and oxygen in red.

### 5.2.4. Morphology and composition

To assess and compare the morphology of both NLTO and NYTO, FESEM analysis was carried out. The morphology of both NLTO and NYTO consists of shard-like platelets; however, the platelets appear more distinct and well-defined in NYTO than in NLTO (Figure 5.16). The size of the NLTO particles ranges from 0.1 to 1  $\mu\text{m}$ , whilst the size range of NYTO particles extends from 0.1 to 2  $\mu\text{m}$ , indicating a broader distribution. Elemental analysis using EDS, shown in Figure 5.17 and Figure 5.18, confirms that Na, Ti, La, Y, and O elements are uniformly and evenly distributed throughout the sample. These findings align with those previously reported in the literature, where the solid-state reaction method was employed for synthesis. [10], [14], [24], [25]

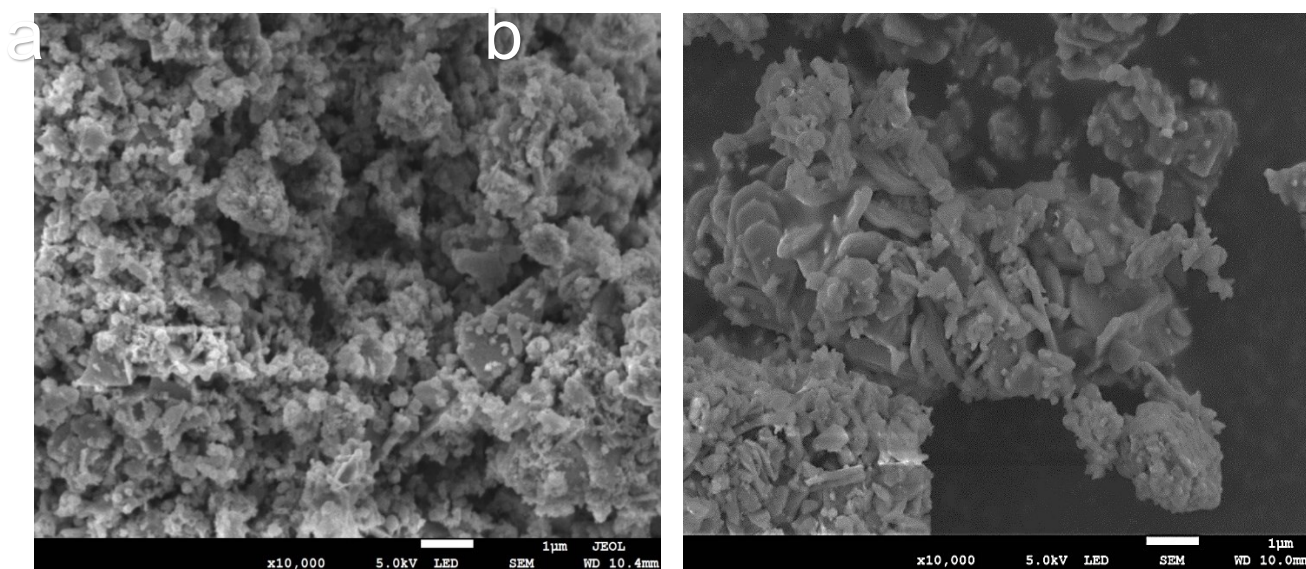


Figure 5.16 – FESEM images of as-synthesised (a) NLTO and (b) NYTO after calcination at 800 °C for 12 hours

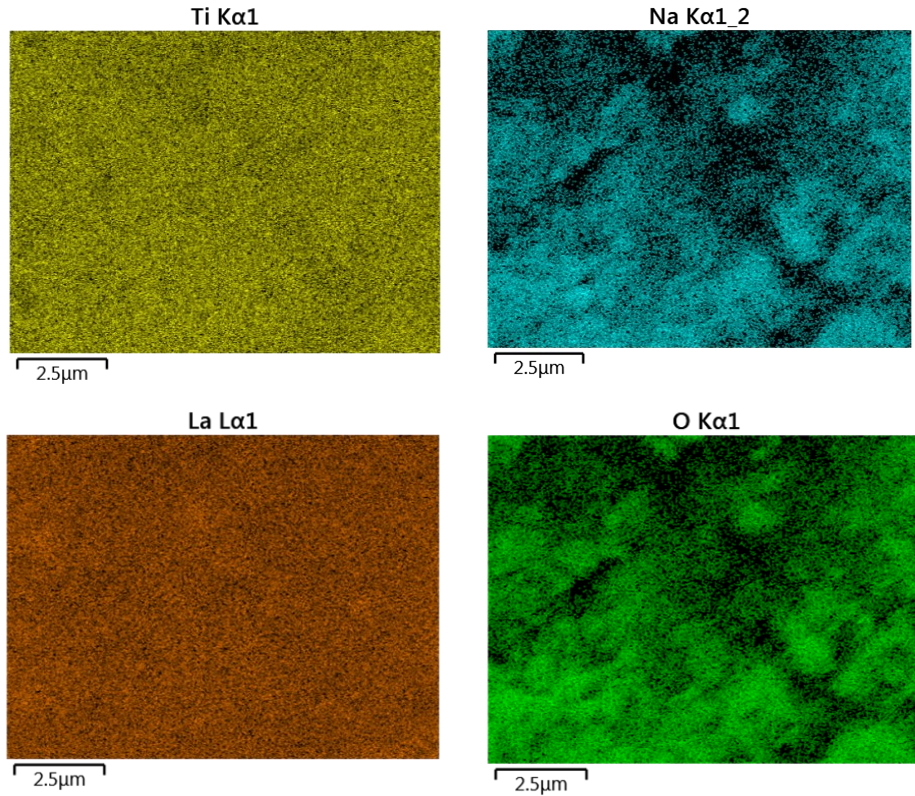


Figure 5.17 – EDS mapping of Na, Ti, La, and O elements in the as-synthesised NLTO after calcination at 800 °C for 12 hours .

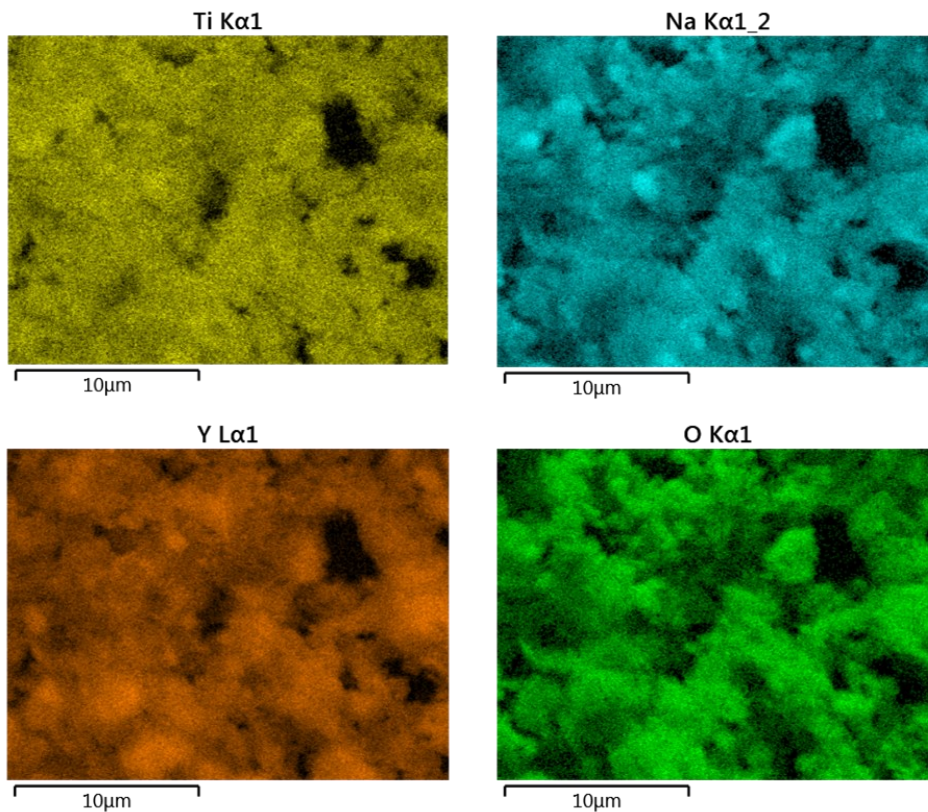


Figure 5.18 – EDS mapping of Na, Ti, Y, and O elements in the as-synthesised NYTO after calcination at 800 °C for 12 hours.

TEM images of NLTO were taken by Dr Robert Crewe and Dr Layla Mahdi at the University of Liverpool. This image was captured in the (1 1 0) direction, which is the direction the material slides and breaks, parallel to TiO<sub>6</sub> growth. The obtained images confirm the layered structure of this material in the (1 1 0) direction with a 2.66 Å interplanar distance, compared to theoretical values from Vesta of 2.67 Å. In Xu et al., the layered stacks were determined to grow in the (0 0 1) direction, allowing visualisation of the stack. The interlayer distance of approximately 13.0 Å matches the 13.014 Å value obtained from Vesta. [25] Figure 5.19 shows a TEM image from Xu et al., with the interlayer distance marked in red in the (0 0 1) direction.

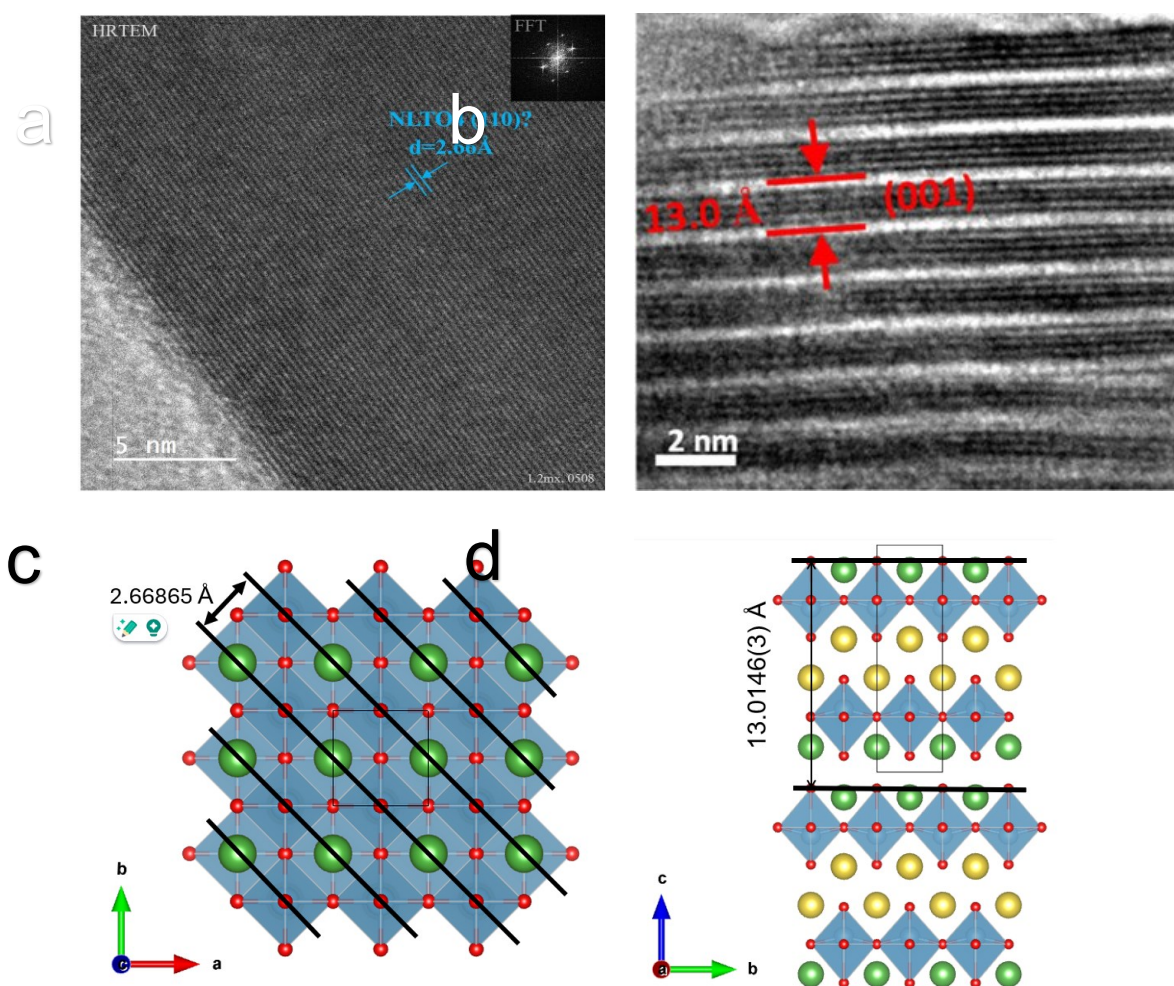


Figure 5.19 – (a) TEM images of NLTO taken from the (1 1 0) taken at the University of Liverpool, (b) TEM image of NLTO taken from the (0 0 1) from Xu, et al., (c) diagram of the material seen from the (1 1 0) and (d) a diagram for the material seen from the (0 0 1) (d)

### 5.2.5 Chemical deviation of structural sodium

Solid-state  $^{23}\text{Na}$  nuclear magnetic resonance analysis was used in this section to distinguish the different electronic vicinity and shielding of sodium in the structures of  $\text{NaLaTiO}_4$  and  $\text{NaYTlO}_4$ . These analyses were performed by Dr Valerie Seymour of Lancaster University. Figure 5.20 shows a 2D solid-state  $^{23}\text{Na}$  NMR of  $\text{NaLaTiO}_4$  and  $\text{Na}_2\text{La}_2\text{Ti}_3\text{O}_{10}$ .

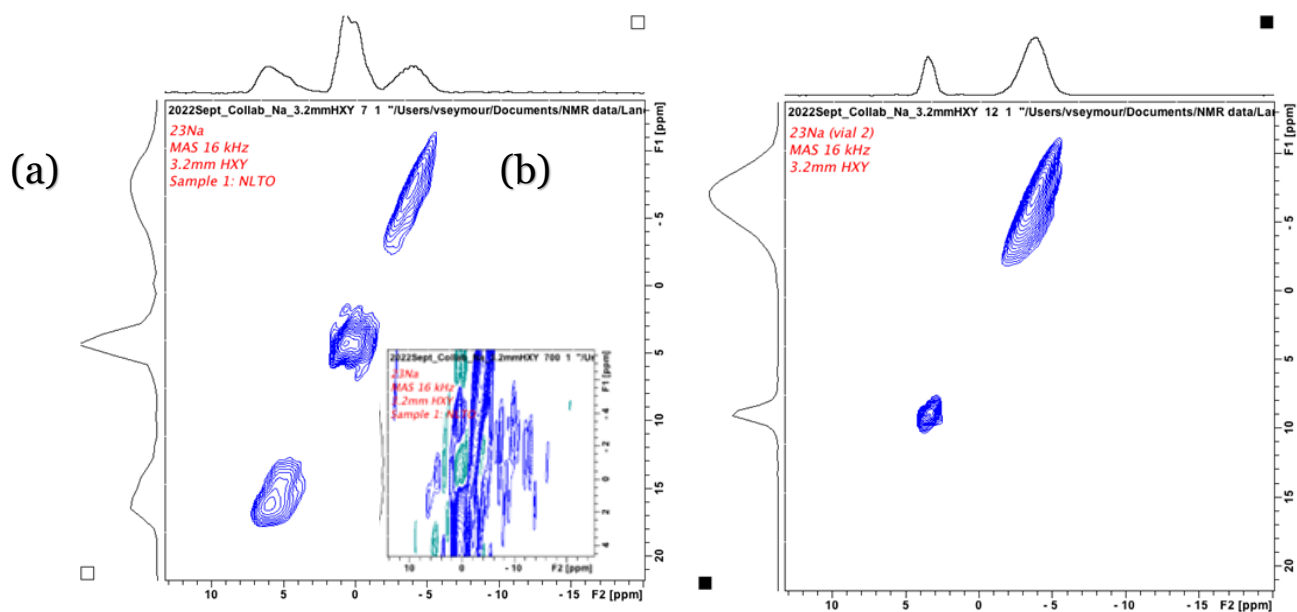


Figure 5.20 – (a) 2D  $^{23}\text{Na}$  solid-state NMR of as-synthesised  $\text{NaLaTiO}_4$  and (b)  $\text{Na}_2\text{La}_2\text{Ti}_3\text{O}_{10}$ .

The 2D NMR spectra with the chemical deviations of  $\text{NaLaTiO}_4$  show three sodium sites located on a diagonal, which indicates a highly ordered structure. Note that one of the sites originates from the main impurity,  $\text{Na}_2\text{La}_2\text{Ti}_3\text{O}_{10}$ , detected with Rietveld refinements. The protrusions on the peaks associated with the main phase indicate that the main phase's sodium location has some disorder. The inset detects some broad peaks associated with  $\text{Na}_2\text{CO}_3$ , which may indicate a small amount of  $\text{Na}_2\text{CO}_3$  impurity.

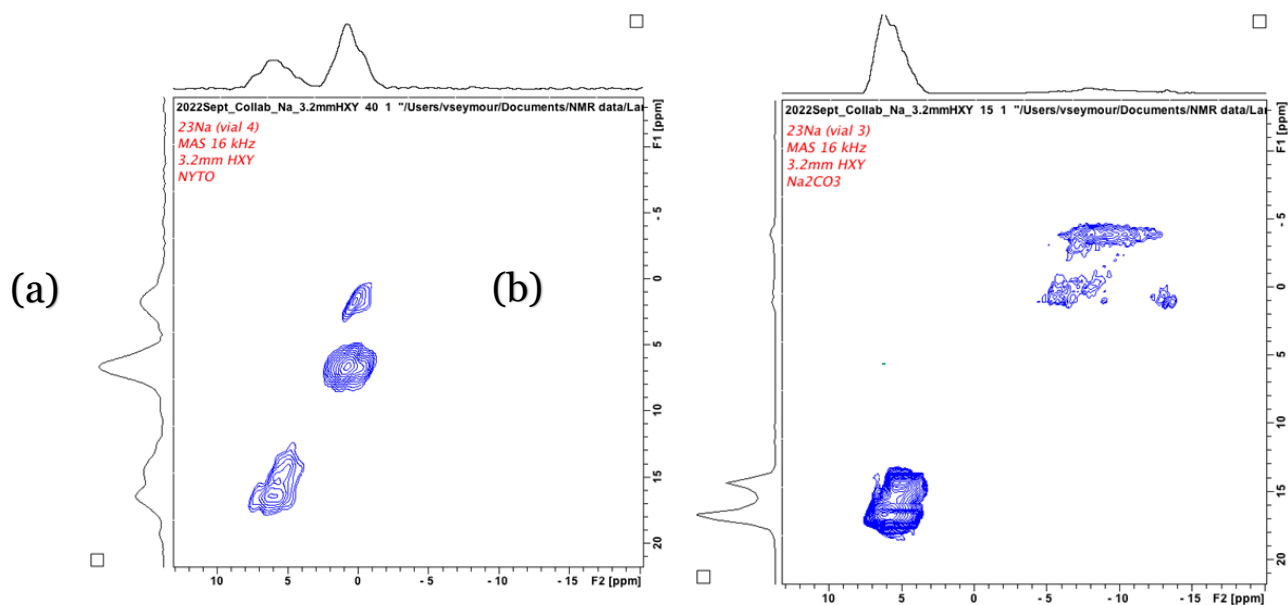


Figure 5.21 – 2D  $^{23}\text{Na}$  NMR of as-synthesised NaYTiO<sub>4</sub> (a) and Na<sub>2</sub>CO<sub>3</sub> precursor (b)

The 2D NMR spectra, with the chemical deviations of NaYTiO<sub>4</sub> shows three sodium sites located on a diagonal, which indicates a highly ordered structure, similar to NaLaTiO<sub>4</sub> (Figure 5.21). Like NLTO, NYTO shows two sodium sites however, these are less shielded, indicating that the distance between sodium and other electrophilic atoms, such as titanium is smaller, concomitant with the lower  $c$  parameter, calculated previously in the Rietveld refinements. There is also a strong signal associated with the Na<sub>2</sub>CO<sub>3</sub> impurity, also previously detected by Rietveld refinements.

### 5.2.6 Optic behaviour

The bandgap plays a crucial role in determining the performance of an anode in sodium-ion batteries. The bandgap refers to the energy difference between the valence band, where electrons are bound, and the conduction band, where electrons are free to move. [26]–[28] For an anode material, a suitable bandgap ensures efficient sodium insertion and extraction during charging and discharging cycles. [29]

A narrow bandgap allows for easier movement of electrons between the valence and conduction bands, facilitating rapid sodium-ion diffusion within the anode material. [28] This promotes faster charging and discharging rates, crucial for high-performance batteries used in applications like electric vehicles or portable electronics. [30]

A wide bandgap might hinder electron mobility, slowing down the charging/discharging process and reducing the battery's overall efficiency. [31] Therefore, selecting an anode material with an appropriate bandgap is essential for achieving desired battery performance characteristics, including energy density, power density, cycle life, and safety. [29], [31] In Figure 5.22, the UV-vis diffuse reflectance spectra of NLTO and NYTO are shown.

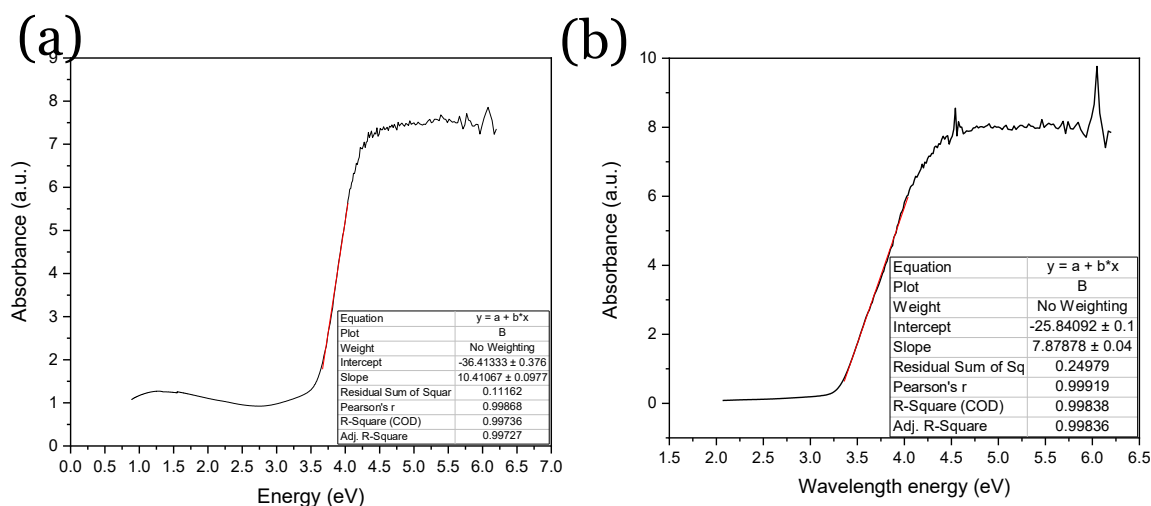


Figure 5.22 – (a) Diffuse reflectance spectra of NLTO and (b) NYTO with the calculations of each material's bandgaps marked in red.

The bandgap of NLTO was calculated to be  $3.49987 \pm 0.0048834$  eV and NYTO was calculated as  $3.27981 \pm 0.00195$  eV. The narrowed bandgap of NYTO suggests that this material has a higher electron mobility compared to NLTO. [27], [28] A narrowed bandgap generally allows for a more efficient electron transfer between the valence and conduction band, which can enhance the charging and discharging performance of a battery. [32]

Consequently, NYTO might exhibit faster kinetics during the sodium insertion and extraction processes, leading to faster charging and higher power density. [32] However, the wider bandgap of NLTO indicated improved stability and reduced susceptibility to side reactions. [33] A wider bandgap is often correlated with a higher energy threshold for unwanted chemical reactions, thereby enhancing the battery's cycle life and overall safety. [33] NLTO may thus have better long-term performance and durability, particularly in demanding applications. Furthermore, the bandgap values influence the compatibility of these materials with different electrode potentials. NLTO's higher bandgap implies a larger energy difference between its valence and conduction bands, potentially allowing it to operate over a wider voltage range without undergoing undesirable electrochemical reactions. [34] On the other hand, NYTO's narrower bandgap might limit its voltage stability, requiring careful voltage management to prevent degradation and ensure safety.

### 5.3. Electrochemical performance *versus* lithium

In this section, various electrochemical techniques were applied to investigate the electrochemical performance of NLTO and NYTO as anodes for lithium batteries. These included galvanostatic measurements, cyclic-voltammetry, *operando* X-ray diffraction, and electrochemical impedance spectroscopy. The composition of the electrodes was 70 % NLTO or NYOT, 20 % carbon super-P conductor and, 10 % PVDF binder.

#### 5.3.1. Galvanostatic measurements

The galvanostatic cycling measurements were carried out in the potential range of 0.01 to 0.60 V *vs.* Li<sup>+</sup>/Li with a current density of 0.1 C, which corresponds to 9.79 mA g<sup>-1</sup> and 11.98 mA g<sup>-1</sup> for NLTO and NYTO, respectively. As shown in Figure 5.23, the initial capacity of NLTO is 225 mA h g<sup>-1</sup> and the initial capacity of NYTO is 270 mA h g<sup>-1</sup>. From the first to the second cycle, the capacity decreases to 150 mA h g<sup>-1</sup> for NLTO and 180 mA h g<sup>-1</sup>. This

irreversible initial capacity is likely associated with the formation of a solid-electrolyte interphase (SEI). After the 10<sup>th</sup> cycle, both materials have their capacities stabilised at 130 mA h g<sup>-1</sup> for NLTO and 160 mA h g<sup>-1</sup> with little to no losses in the following 30 cycles. These results superseded the previously reported in the literature by 20 mA h g<sup>-1</sup>. [14]

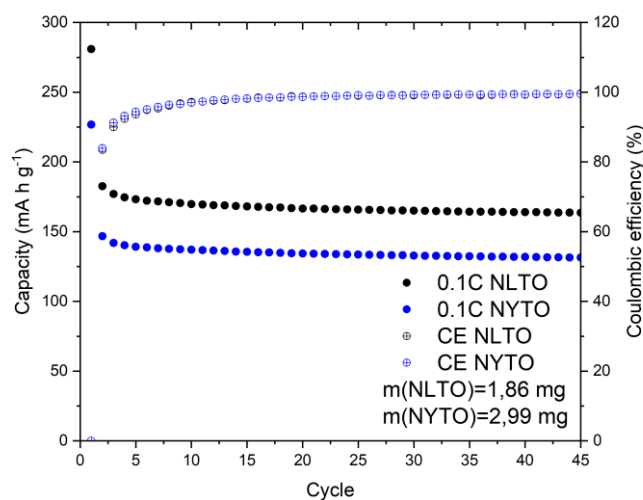


Figure 5.23 – Capacity of NLTO (●) and NYTO (●) over 45 cycles at a 0.1 C rate and Coulombic efficiency of NLTO (⊕) and NYTO (⊕), over a potential window between 0.01 and 0.60 V vs. Li<sup>+</sup>/Li.

Figure 5.24 shows the potential profiles of the NaLaTiO<sub>4</sub> and NaYTiO<sub>4</sub> versus lithium under a constant current of 0.1 C, over the potential range of 0.01 to 0.60 V vs. Li<sup>+</sup>/Li. A solid-electrolyte interface was formed in the 1st discharge at a potential below 1.0 V vs. Li<sup>+</sup>/Li. Both materials show reversible *plateaux* at a potential below 0.5 V vs. Li<sup>+</sup>/Li. The pair of *plateaux* at 0.1 V vs. Li<sup>+</sup>/Li correspond to the Ti(IV)/Ti(III) redox couple and not to the Ln(III)/Ln(II) redox couple as these *plateaux* occur in both NLTO and NYTO at the same potential. On the other hand, NYTO shows an extra *plateau* at ~0.3 V vs. Li<sup>+</sup>/Li, which indicates the access to the Y(III)/Y(II) redox pair as well as the Ti(IV)/Ti(III) redox pair. [14], [35] This may help explain the extra capacity the NYTO delivers. About 30 mA h g<sup>-1</sup> can be attributed to the Y(II)/Y(III) redox couple, and the rest of the capacity from the Ti(IV)/Ti(III) redox couple.

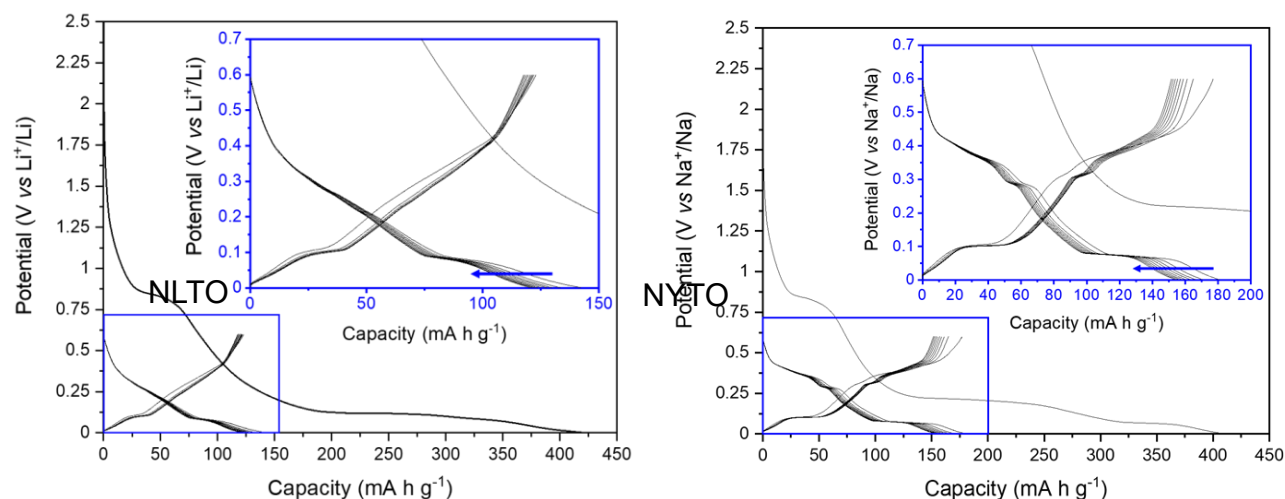


Figure 5.24 – Galvanostatic curves of NLTO and NYTO at a 0.1 C rate over a potential window of 0.01 to 0.60 V vs. Li<sup>+</sup>/Li with a detail on the 2<sup>nd</sup> cycle onwards shown in the inset.

### 5.3.2. Cyclic-voltammetry

To probe the lithium intercalation and deintercalation into NLTO and NYTO, cyclic-voltammetric studies were performed using lithium half-cells in the potential range of 0.01 to 0.60 V vs. Li<sup>+</sup>/Li at a scan rate of 0.1 mV s<sup>-1</sup> and 1.0 mV s<sup>-1</sup> for 10 cycles, shown in Figure 5.25 and Figure 5.26.

The first anodic peak shows a peak at approximately 0.7 V vs. Li<sup>+</sup>/Li for both materials at a scan rate of 0.1 mV s<sup>-1</sup>. This is concomitant with a *plateau* at approximately the same potential, attributed to the formation of an SEI. At a scan rate of 1.0 mV s<sup>-1</sup>, the peak appears at 0.6 V vs. Li<sup>+</sup>/Li. This phenomenon appears at a lower potential probably due to lithium transport kinetics.

NLTO at a scan rate of 0.1 mV s<sup>-1</sup> shows a pair of peaks close to 0.1 V vs. Li<sup>+</sup>/Li, which become clearer towards the 10<sup>th</sup> cycle, these are commonly associated with the Ti(IV)/Ti(III) redox pair. These peaks are less clear due to the increase of pseudo-capacitive phenomena at higher scan rates. [36] There are two pairs of peaks at 0.4 and 0.6 V vs. Li<sup>+</sup>/Li, which are not ascribed to any phenomenon in any of the studies where this material or other titanates are

part. These however may be assigned to lithium ordering processes, as discussed in Chapters 3 and 4. [37]

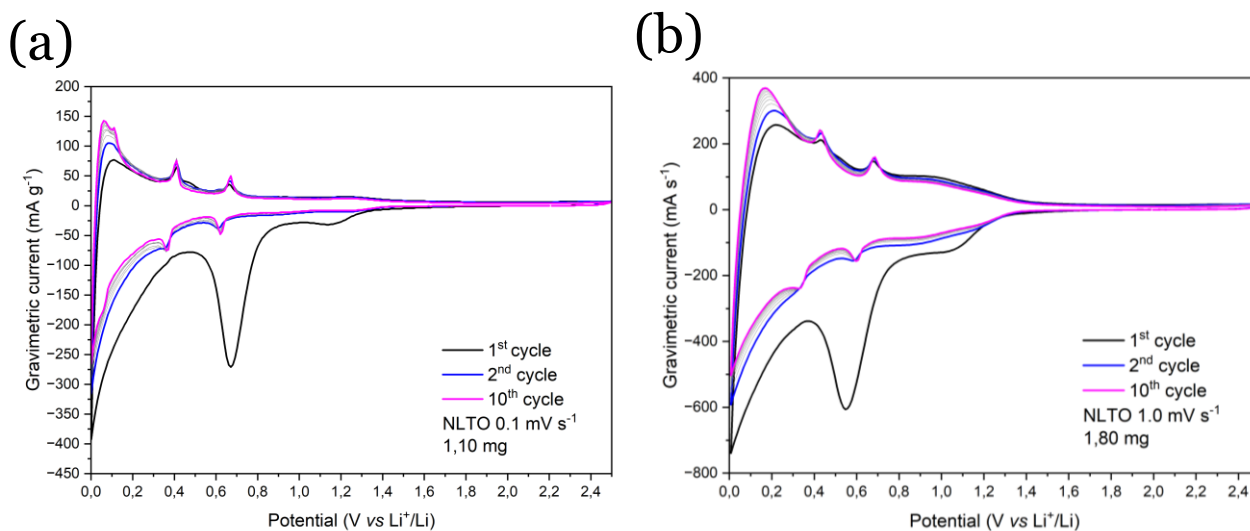


Figure 5.25 – Cyclic-voltammetry of NLTO at 0.1 mV s<sup>-1</sup> (a) and at 1.0 mV s<sup>-1</sup> (b) over 10 cycles.

Like the case of NLTO, NYTO also shows a pair of peaks approximately at 0.1 V *vs.* Li<sup>+</sup>/Li that can be ascribed to the Ti(IV)/Ti(III) redox pair. These redox peaks are more separated than NLTO, 0.05 V in NLTO compared to 0.10 V in NYTO. This is usually associated with lower lithium mobility within the material interlayer. This is in agreement with the tighter spacing between the (0 0 1) planes of NYTO of 12.23 Å compared to the 13.01 Å of NLTO, calculated from the Rietveld refinements using Bragg's law. [38] Adding to the previously mentioned peaks, NYTO cyclic-voltammetry also shows an extra reversible peak pair at approximately 0.40 V *vs.* Li<sup>+</sup>/Li which can be ascribed to a Y(III)/Y(II) redox pair. [35] A peak pair at approximately 0.3 V *vs.* Li<sup>+</sup>/Li also appears which, similarly to NLTO can be ascribed to lithium ordering, being that the second peak at overlapped by the Y(III)/Y(II) peaks. [39] As in the case of NLTO, at a faster scan rate of 1.0 mV s<sup>-1</sup>, the redox and ordering peaks are less well-defined when compared to 0.1 mV s<sup>-1</sup>, probably related to a higher contribution of pseudo-capacitance at a higher rate. [39]

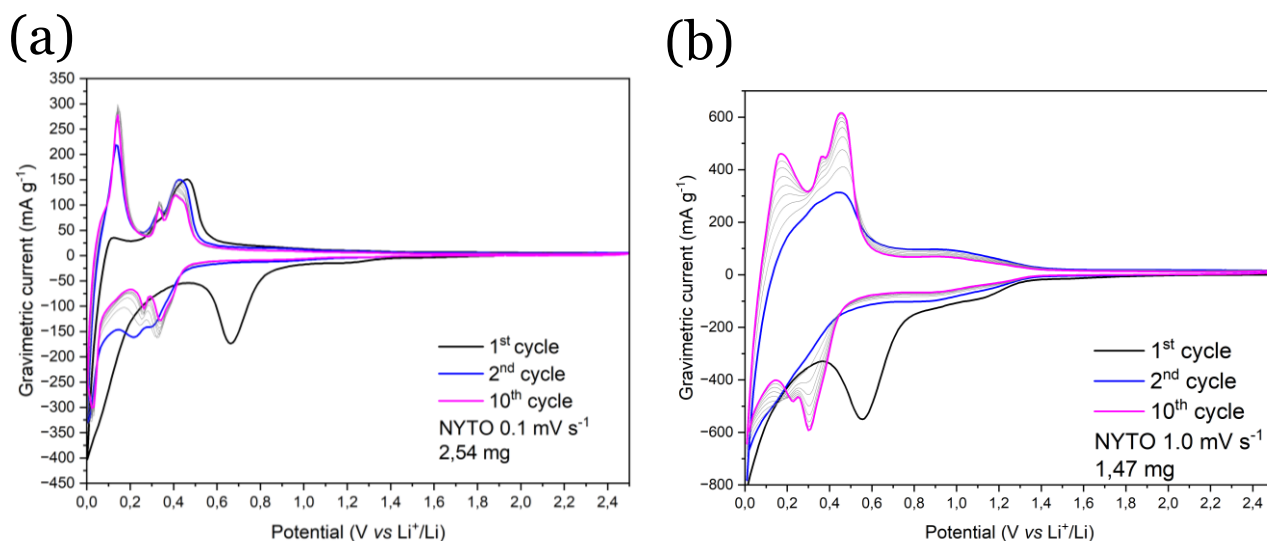


Figure 5.26 – Cyclic-voltammetry of NYTO at  $0.1 \text{ mV s}^{-1}$  (a) and  $1.0 \text{ mV s}^{-1}$  (b) over 10 cycles

### 5.3.3. Structural changes during operation

For probing structural changes, synchrotron *operando* XRD was collected for both materials. In Figure 5.27, the heatmaps with the structural variation on the NLTO and NYTO in relation to time and state-of-charge.

For NLTO there is a shift of the (0 0 1) reflection upon discharge from  $Q = 0.5 \text{ \AA}^{-1}$  to  $0.55 \text{ \AA}^{-1}$  indicating a decrease of the interlayer space due to intercalation of lithium in the  $\text{Na}_2\text{O}_2$  that caused an increase of the electrostatic attraction between  $\text{Na}^+$  and  $\text{Li}^+$  and the  $\text{O}^{2-}$  of the  $(\text{TiO})_2$  layer. We can also observe a shift in (0 0 4) from  $Q = 1.8 \text{ \AA}^{-1}$  to  $2.0 \text{ \AA}^{-1}$  indicating a decrease of the interlayer space due intercalation of Li into both the  $(\text{Na}_2\text{O}_2)$  and  $(\text{La}_2\text{O}_2)$  layers, which increases the electrostatic forces between  $\text{Na}^+$ ,  $\text{Li}^+$ , and  $\text{La}^{2+}$  with the  $\text{O}^{2-}$  of the  $(\text{TiO})_2$ . Similarly, we observed shifts of the peaks at  $Q=2.1 \text{ \AA}^{-1}$  to  $2.19 \text{ \AA}^{-1}$  and  $Q=2.2 \text{ \AA}^{-1}$  to  $2.22 \text{ \AA}^{-1}$  in the (4 0 0) and (3 1 1) reflections, respectively in NYTO. This indicates that during discharge, lithium intercalated into the  $\text{Na}_2\text{O}_2$  and  $\text{Y}_2\text{O}_2$ , causing a contraction of these layers due to the increased electrostatic forces within the  $\text{Na}_2\text{O}_2$  and  $\text{Y}_2\text{O}_2$  caused by inserting  $\text{Li}^+$

into them. This phenomenon is recurrent in other layered materials, especially cathodes for LIB and NIB. [40]

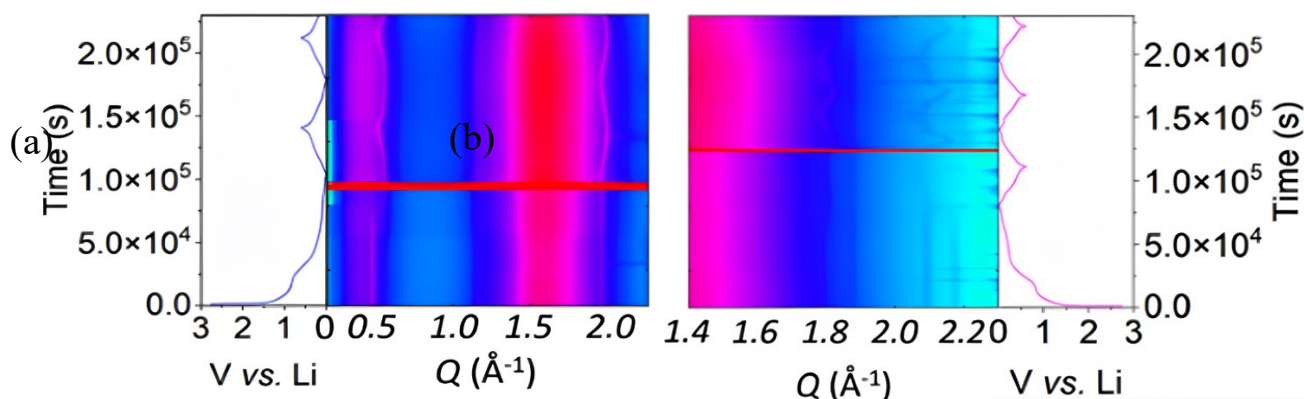


Figure 5.27 – (a) Heatmap of the operando X-ray diffraction on NLTO, between  $0.5 \leq Q \leq 2 \text{ \AA}^{-1}$  and (b) NYTO, between  $1.4 \leq Q \leq 2.2 \text{ \AA}^{-1}$ . Electrochemical cycling occurred between 0.01 and 0.60 V vs. Li<sup>+</sup>/Li.

## 5.4. Electrochemical performance *versus* sodium

In the section, as in Section 5.3, various electrochemical techniques were applied to investigate the electrochemical performance of NLTO and NYTO as anodes for sodium batteries. These were then compared with the electrochemical performance of carbon super-P to ensure the origin of electrochemical performance. These included galvanostatic measurements, cyclic-voltammetry, *operando* X-ray diffraction, and electrochemical impedance spectroscopy. As for Section 5.3, the composition of the electrodes was 70 % NLTO or NYTO, 20 % carbon super-P conductor and, 10 % PVDF binder

### 5.4.1. Galvanostatic measurements

The galvanostatic cycling measurements were carried out in the potential range of 0.01 to 2.50 V *vs.* Na<sup>+</sup>/Na with a current density of 0.1 C, which corresponds to 9.79 mA g<sup>-1</sup> and 11.98 mA g<sup>-1</sup> for NLTO and NYTO, respectively. As shown in Figure 5.28, the initial capacity of NLTO is 274 mA h g<sup>-1</sup> and the initial capacity of NYTO is 243 mA h g<sup>-1</sup>. From the first to the

second cycle, the capacity decreases to  $119 \text{ mA h g}^{-1}$  for NLTO and  $98 \text{ mA h g}^{-1}$ . The substantially lower reversible capacity can result from the nature of sodium, being a heavier and bulkier element than lithium, or from a dramatic change in the chemical behaviour of these materials when they are cycled versus sodium.

The irreversible initial capacity is likely associated with the formation of a solid-electrolyte interphase (SEI), as in the case of lithium. After the 20<sup>th</sup> cycle, both materials have their capacities stabilised at  $100 \text{ mA h g}^{-1}$  for NLTO and  $76 \text{ mA h g}^{-1}$  with little to no losses in the following 80 cycles.

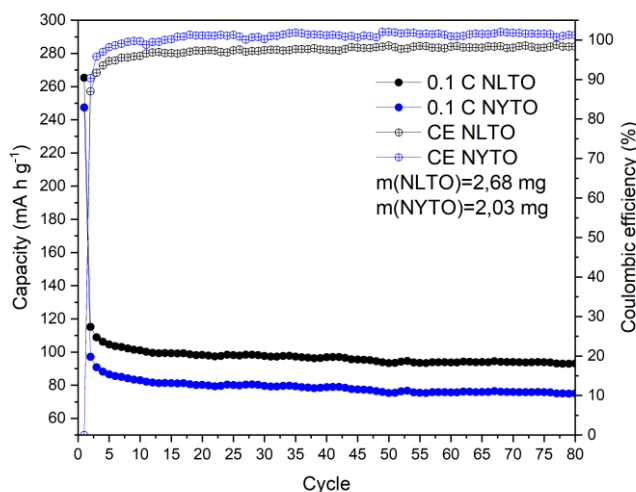


Figure 5.28 – Capacity of NLTO (●) and NYTO (●) over 80 cycles at a 0.1 C rate and Coulombic efficiency of NLTO (⊕) and NYTO (⊕), over a potential window between 0.01 and 2.50 V vs.  $\text{Na}^+/\text{Na}$ .

Figure 5.29 shows the potential profiles of the  $\text{NaLaTiO}_4$  and  $\text{NaYTlO}_4$  versus sodium under a constant current of 0.1 C, over the potential range of 0.01 to 2.50 V vs.  $\text{Na}^+/\text{Na}$ . A solid-electrolyte interface was formed in the 1st discharge at a potential below 0.4 V vs.  $\text{Na}^+/\text{Na}$ . Both materials show reversible plateaux at a potential below 0.05 V vs.  $\text{Na}^+/\text{Na}$ . The pair of plateaux at 0.05 V vs.  $\text{Na}^+/\text{Na}$  does not seem to be associated with any redox-active element. However, both potential profiles are similar to a carbon-based anode similar to hard carbon. In both cases, until approximately  $60 \text{ mA h g}^{-1}$  indicates a behaviour similar to sodium adsorption in the surface

of the active material and carbon conductors, from 60 mA h g<sup>-1</sup> to 100 mA h g<sup>-1</sup> shows a behaviour similar to sodium insertion into hard carbon. [41]

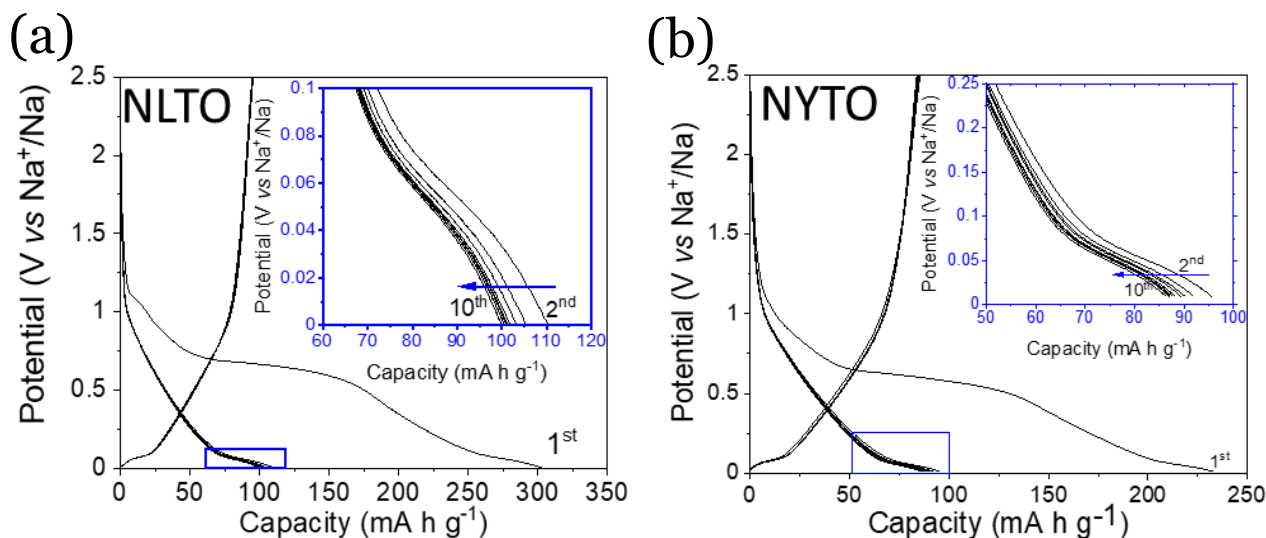


Figure 5.29 – (a) Galvanostatic curves of NLTO and (b) NYTO at a 0.1 C rate over a potential window of 0.01 to 2.50V vs. Na<sup>+</sup>/Na with a detail on the 2<sup>nd</sup> cycle onwards shown in the inset.

Figure 5.30 shows the galvanostatic measurements run at 1 C, 2 C and 5 C, corresponding to 97.9 mA g<sup>-1</sup>, 195.8 mA g<sup>-1</sup>, and 489.5 mA g<sup>-1</sup> respectively for NLTO and, 119.8 mA g<sup>-1</sup>, 239.6 mA g<sup>-1</sup>, and 599.0 mA g<sup>-1</sup> respectively, for NYTO. At 1 C, the initial capacity of NLTO is 208 mA h g<sup>-1</sup> and the initial capacity of NYTO is 190 mA h g<sup>-1</sup>. From the first to the second cycle, the capacity decreases to 91 mA h g<sup>-1</sup> for NLTO and 82 mA h g<sup>-1</sup>. At 2 C, the initial capacity of NLTO is 180 mA h g<sup>-1</sup> and the initial capacity of NYTO is 160 mA h g<sup>-1</sup>. From the first to the second cycle, the capacity decreases to 65 mA h g<sup>-1</sup> for NLTO and 47 mA h g<sup>-1</sup>. At 5 C, the initial capacity of NLTO is 167 mA h g<sup>-1</sup> and the initial capacity of NYTO is 145 mA h g<sup>-1</sup>. From the first to the second cycle, the capacity decreases to 59 mA h g<sup>-1</sup> for NLTO and 38 mA h g<sup>-1</sup>.

The irreversible initial capacity is likely associated with the formation of a solid-electrolyte interphase (SEI), as in the case of lithium. After the 10<sup>th</sup> cycle for 1 C, the 20<sup>th</sup> cycle

for 2 C, and the 40<sup>th</sup> for 5 C. The Coulombic efficiency after the 20<sup>th</sup> cycle stabilised at approximately 98 % for NLTO and 102 % for NYTO, indicating a good reversibility. These materials have an expected behaviour at higher rates and show that this material is not ideal for fast charging. [42]

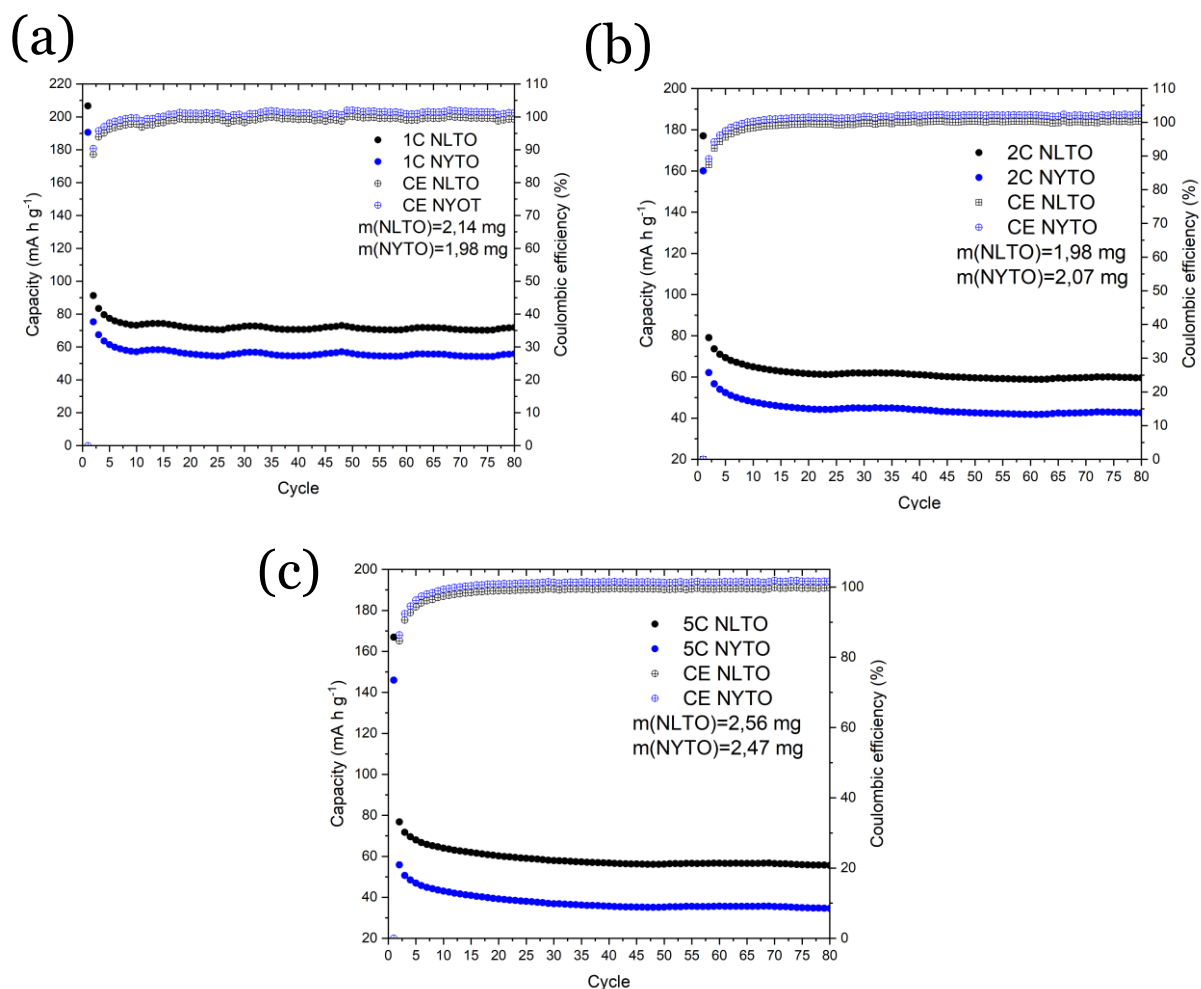


Figure 5.30 – Capacity of NLTO (●) and NYTO (●) over 80 cycles at a 1 C rate (a), 2 C rate (b), and 5 C rate, as well as the respective Coulombic efficiency of NLTO (⊕) and NYTO (⊕) for each scan rate, over a potential window between 0.01 and 0.60 V vs. Na<sup>+</sup>/Na.

### 5.4.2. Cyclic-voltammetry

Figure 5.31 shows a cyclic-voltammetry of NLTO and NYTO *versus* sodium at 0.2 mV s<sup>-1</sup>. Both NLTO and NYTO have a strong peak at approximately 0.45 V *vs.* Na<sup>+</sup>/Na, likely associated with the formation of a SEI. Both materials also show a strong peak pair at

0.05 V *vs.* Na<sup>+</sup>/Na which is most likely not associated with any redox-active element but rather the intercalation of sodium into the layers of and inorganic carbon like hard carbon or carbon super-P. [42] Throughout the rest of the potential window analysed, it seems that most of the processes are pseudo-capacitive or surface adsorption being that NYTO seems to have a higher contribution due to its more well-defined platelet-shaped particles. [43]

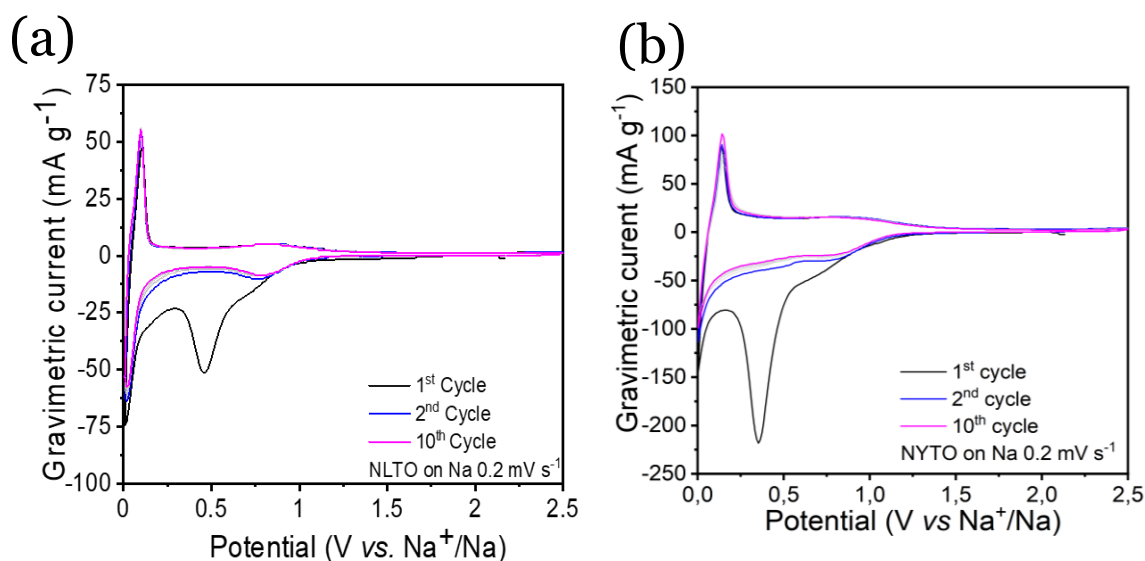


Figure 5.31 – Cyclic-voltammetry of NYTO (a) and NYTO (b) at 0.2 mV s<sup>-1</sup> over 10 cycles

### 5.4.3. Carbon super-P electrochemical performance

Since the behaviour of NLTO and NYTO *versus* sodium is very similar to that of carbon super-P *versus* sodium, it is important to examine the electrochemical behaviour of carbon super-P to assess whether the capacity of the previously studied electrodes does not come from carbon super-P instead of the previously considered “active material”. Figure 5.32(a), shows a comparison between NLTO, NYTO and carbon super-P electrodes at the 2<sup>nd</sup> cycle, and Figure 5.32(b), shows the capacity of NLTO and NYTO electrodes when the weight of carbon super-P is considered, instead of the weight of NLTO or NYTO at the 2<sup>nd</sup> cycle.

These electrodes were measured at a potential range of 0.01 to 2.50 V *vs.* Na<sup>+</sup>/Na at a rate of 0.1 C. The carbon super-P electrode has a reversible capacity of 162 mA h g<sup>-1</sup> as the reversible capacity of NLTO and NYTO is 112 and 98 mA h g<sup>-1</sup>, respectively. The potentiostatic curves between the three materials do not show any different features that allow us to make a clear distinction. This indicated that the electrochemically active material in all cases is carbon super-P. In addition, Wu, *et al.*, describe the behaviour of carbon super-P to be very similar to the one reported in this work for NLTO and NYTO. [44]

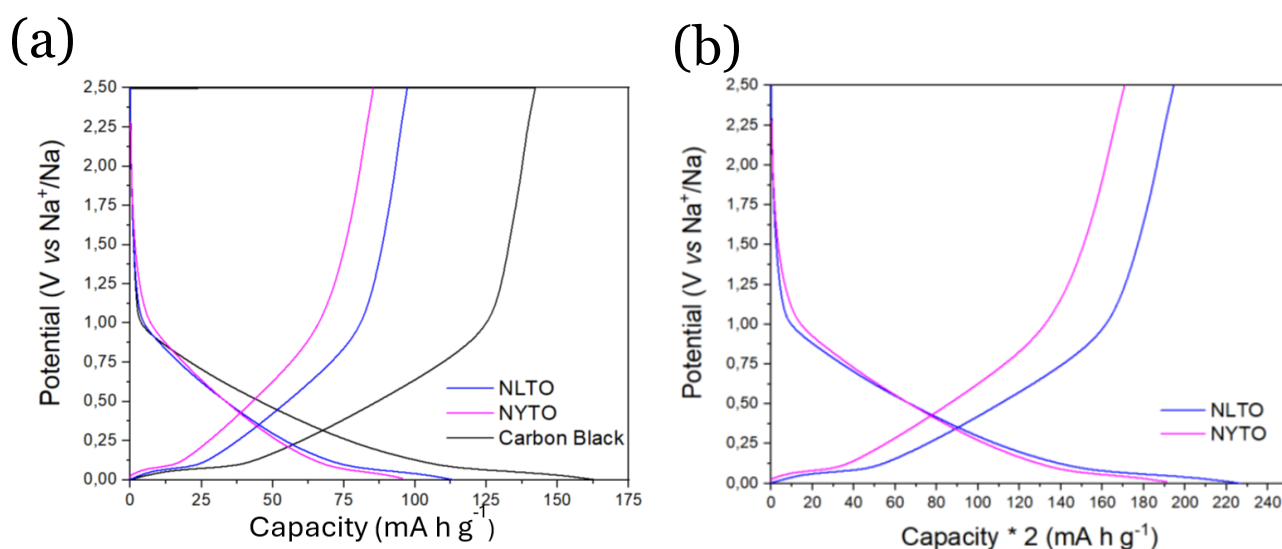


Figure 5.32 - Galvanostatic curves of NLTO and NLTO compared with carbon super-P at a 0.1 C rate over a potential window of 0.01 to 2.50V *vs.* Na<sup>+</sup>/Na (a) and NLTO and NYTO where the capacity is normalised to the mass of carbon super-P (b).

When the capacity of the NLTO and NYTO electrodes is normalised to the weight of the carbon super-P, we obtain a reversible capacity of 225 mA h g<sup>-1</sup> and 191 mA h g<sup>-1</sup> whilst the electrode containing carbon super-P and PVDF binder is 162 mA h g<sup>-1</sup>. This indicates that about 31 mA h g<sup>-1</sup> in the case of NLTO and 14 mA h g<sup>-1</sup> in the case of NYTO comes from these materials, probably from surface adsorption and some intercalation however, this should be further investigated.

Figure 5.33 shows a cyclic-voltammetry of a carbon super-P electrode *versus* sodium at  $0.2 \text{ mV s}^{-1}$  between the potential window of 0.01 and 2.50 V *vs.*  $\text{Na}^+/\text{Na}$ . As in the case of NLTO and NYTO, this electrode shows a strong peak at approximately 0.45 V *vs.*  $\text{Na}^+/\text{Na}$ , likely associated with the formation of a SEI. Carbon super-P also shows a strong peak pair at 0.05 V *vs.*  $\text{Na}^+/\text{Na}$  which is most likely the intercalation of sodium into the layers of inorganic carbon like hard carbon or carbon super-P similar to those reported in Wu, *et al.* [42], [44] Throughout the rest of the potential window analysed, it seems that most of the processes are pseudo-capacitive or surface adsorption. [43]

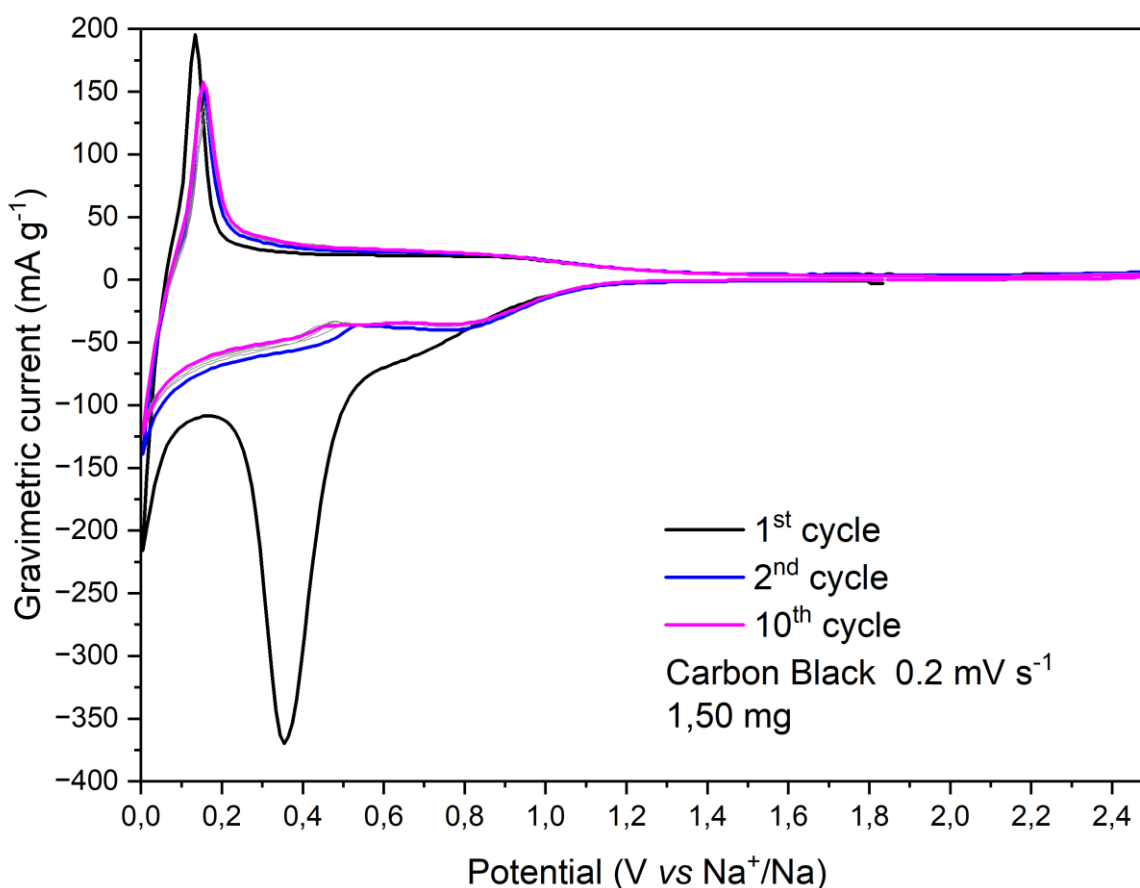


Figure 5.33 – Cyclic-voltammetry of carbon super-P at  $0.2 \text{ mV s}^{-1}$  over 10 cycles

The redox potential of  $\text{Na}^+ \leftrightarrow \text{Na}$  is  $-2.713 \text{ V vs. SHE}$  while  $\text{Li}^+ \leftrightarrow \text{Li}$  is  $3.040 \text{ V vs. SHE}$ . Since the redox potential of the  $\text{Na}^+/\text{Na}$  is  $0.33 \text{ V}$  higher than  $\text{Li}^+/\text{Li}$  meaning that all redox

processes occurring below 0.33 V vs. Li<sup>+</sup>/Li are not accessible when cycling against sodium. Furthermore, sodium tends to coordinate in a rock-salt while lithium coordinates in an antiferroite.

Figure 5.34 shows a potentiostat curve of NYTO *versus* lithium with the area below 0.3 V shaded and a schematic representation of NaLnTiO<sub>4</sub> and LiLnTiO<sub>4</sub>, showing the preferential coordination manner of sodium and lithium on layered perovskite oxides. [47]

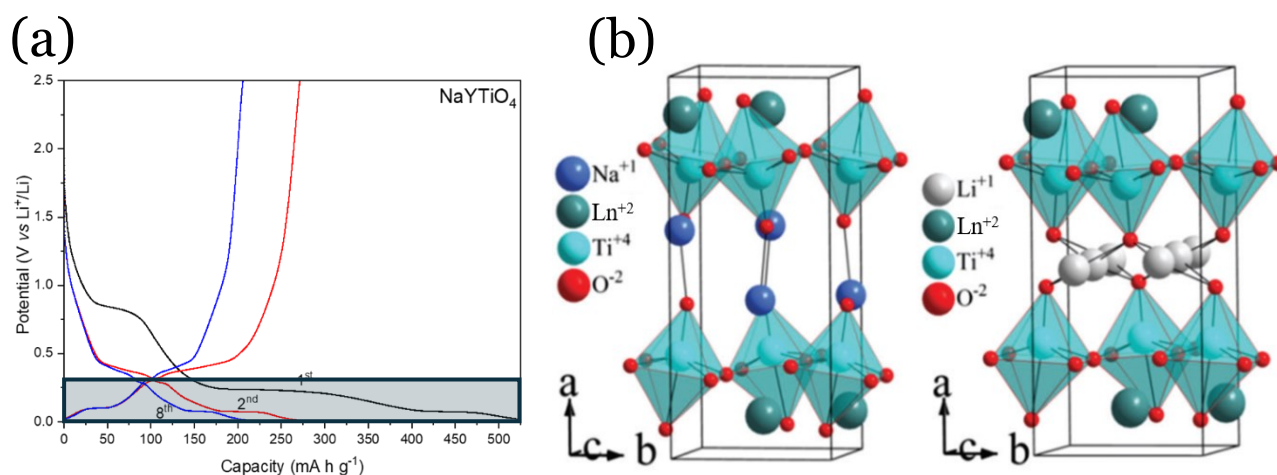


Figure 5.34 – Potentiostatic curve of NYTO versus lithium with the area below 0.3 V shaded to illustrate the area inaccessible when cycling versus sodium (a) and schematic representation of NaLnTiO<sub>4</sub> and LiLnTiO<sub>4</sub> adapted from Hirano, et al. [48]

NaLnTiO<sub>4</sub> has the antiferroite location free for lithium intercalation while the rocksalt position is not available and may not allow further incorporation of sodium. [48] The possibility for other structural changes, like exfoliation or doping can be explored to gift these materials the adequacy to be used in sodium-ion batteries.

#### 5.4.4. Sodium mobility and diffusion coefficient by electrochemical impedance spectroscopy

To measure the sodium diffusion rate for the use of these materials for sodium electrolytes, EIS measurements were performed in 1 mm thick pellets. Dr Wei Zhixuan performed the EIS measurements from the Justus Liebig University – Gießen.

Figure 5.35 shows the Nyquist plots of NLTO before and after activation and the variation of conductivity with temperature, before and after activation. In this context, activation energy is the energy needed to  $\text{Na}^+$  migration. [45]

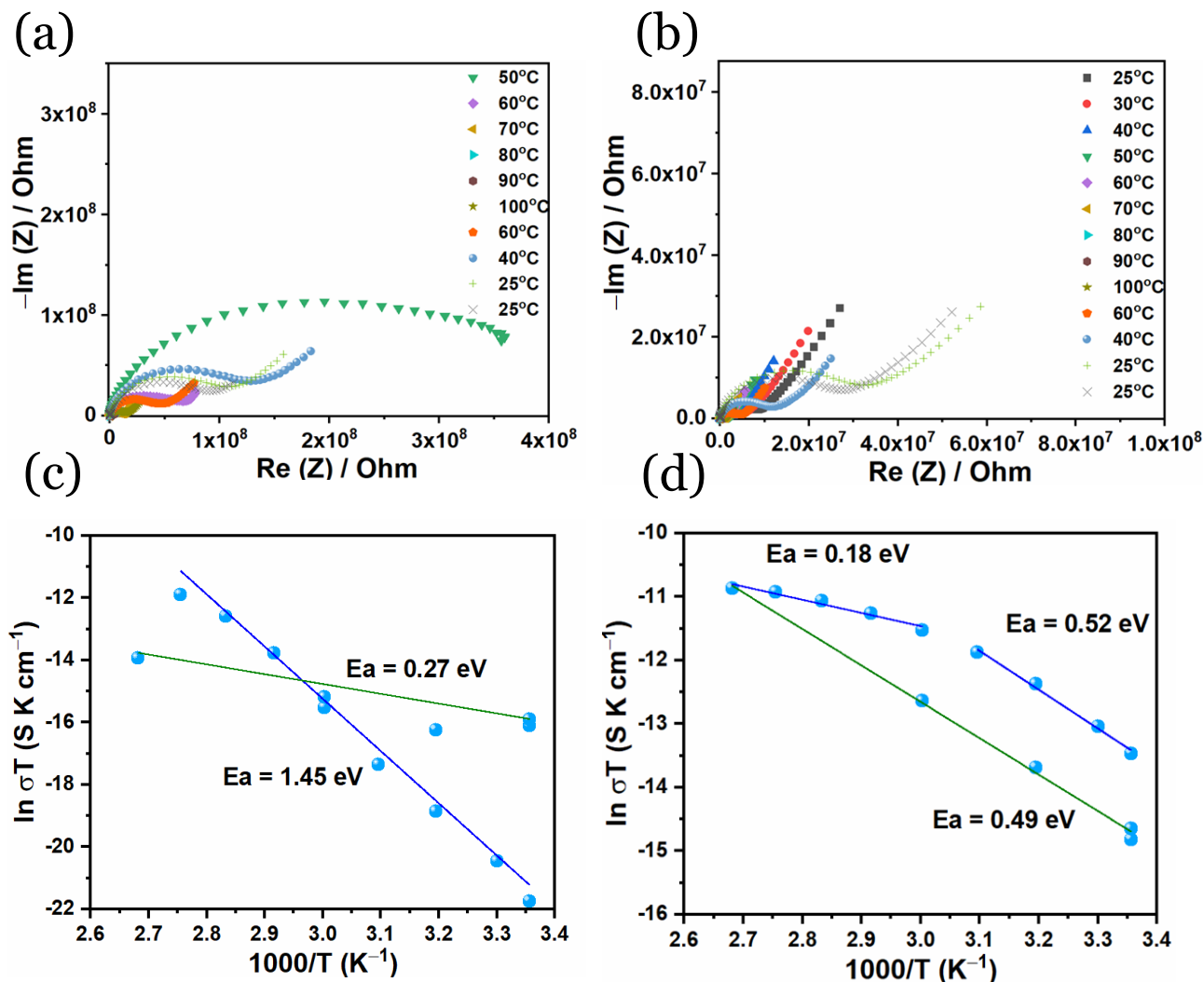


Figure 5.35 – (a) Nyquist plot of NLTO before and (b) after activation between 1 MHz and 1 mHz and (c) variation of conductivity before and (d) after activation with the calculated activation energy for each step.

The impedance was measured at 25, 30, 40, 50, 60, 70, 80, 90, 100, 60, 40 and 25 °C, twice. At 25 °C has a conductivity of  $1.21 \times 10^{-12} \text{ S cm}^{-1}$  and increases to  $1.89 \times 10^{-8} \text{ S cm}^{-1}$  at 90 °C at cooling the material back to 25 °C, the material has a conductivity of  $4.15 \times 10^{-10} \text{ S cm}^{-1}$ , retaining a higher conductivity than initially. On the second heating cycle, the material

reaches the maximum conductivity at 40 °C of  $1.35 \times 10^{-8} \text{ S cm}^{-1}$ , going to  $1.45 \times 10^{-9} \text{ S cm}^{-1}$  at 25 °C. NLTO has a property change at temperatures ranging from 50 to 60 °C because, during heating, until 50 °C, NLTO has an activation energy of 0.18 eV and beyond 60 °C, NLTO has an activation energy of 0.52 eV. During cooling, NLTO has an activation energy of 0.49 eV.

Figure 5.36 shows the Nyquist plots of NYTO before and after activation and the variation of conductivity with temperature, before and after activation.

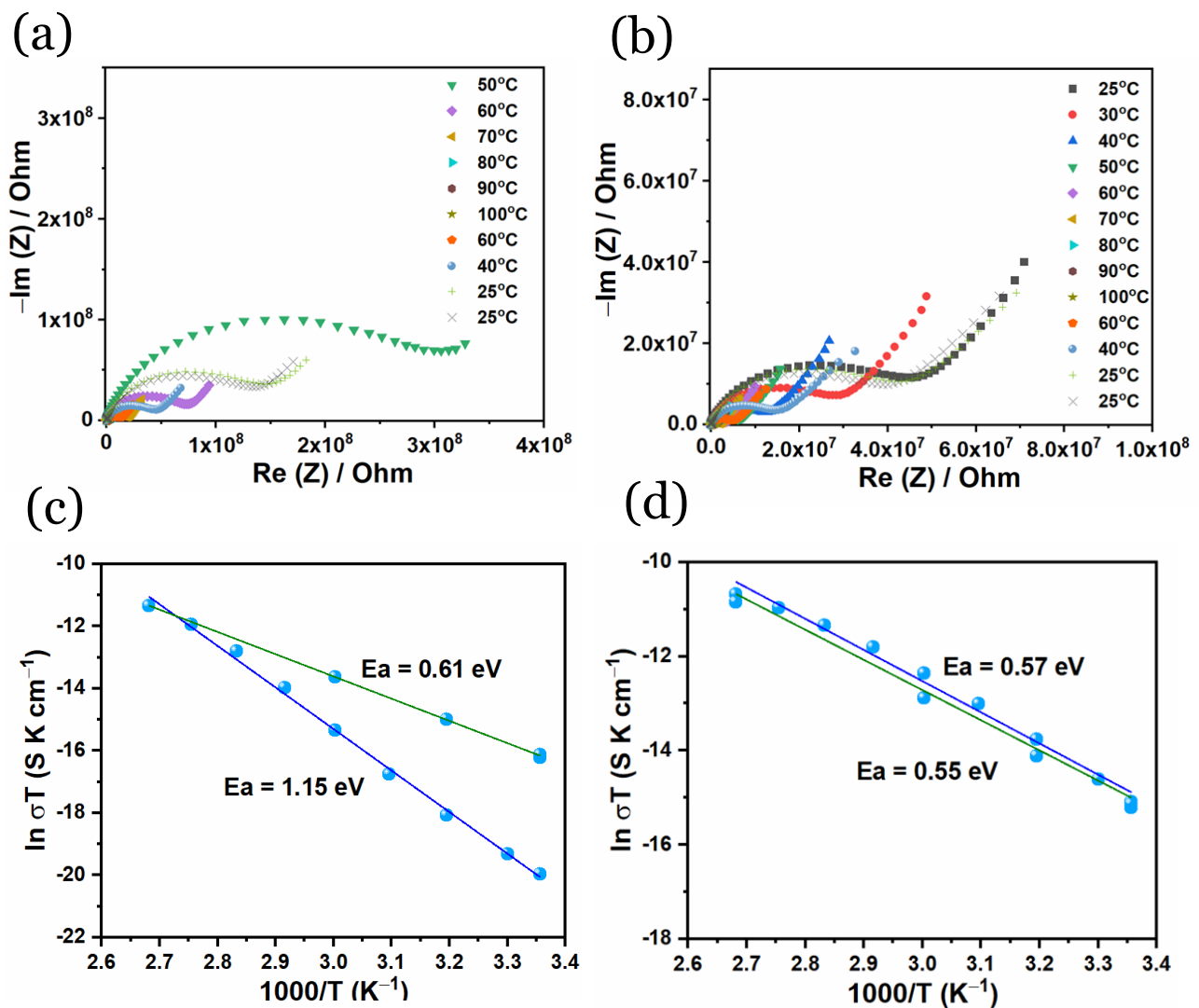


Figure 5.36 – Nyquist plot of NYTO before (a) and after (b) activation between 1 MHz and 1 mHz and variation of conductivity before (c) and after (d) activation

Like in the case of NLTO, the impedance of NYTO was measured at 25, 30, 40, 50, 60, 70, 80, 90, 100, 60, 40 and 25 °C, twice. At 25 °C has a conductivity of  $7.16 \times 10^{-12} \text{ S cm}^{-1}$  and increases to  $3.14 \times 10^{-8} \text{ S cm}^{-1}$  at 90 °C after cooling the material back to 25 °C, the material has a conductivity of  $3.30 \times 10^{-10} \text{ S cm}^{-1}$ . On the second heating cycle, the material reaches the maximum conductivity at 60 °C of  $1.28 \times 10^{-8} \text{ S cm}^{-1}$ , going to  $1.285 \times 10^{-8} \text{ S cm}^{-1}$ . Unlike NLTO, NYTO has no change in behaviour during heating. During cooling, NYTO has an activation energy of 0.57 eV and during heating has an activation energy of 0.55 eV.

Ideally, a good material to be used as a solid-state electrolyte has a conductivity of  $10^{-4} \text{ S cm}^{-1}$  and an activation energy of  $10^{-3} \text{ eV}$  hence, these materials are not ideal for the use as solid-state electrolytes. [46]

## 5.5. Conclusion

The study described herein investigates the synthesis and electrochemical performance of NaLaTiO<sub>4</sub> and NaYTiO<sub>4</sub> as potential anode materials for sodium-ion batteries. The focus is on optimising the synthesis process to minimise the formation of undesirable secondary phases and characterising the electrochemical behaviour of these materials.

First, the synthesis method for NaLaTiO<sub>4</sub> and NaYTiO<sub>4</sub> was optimised using ceramic processing techniques. By carefully controlling the calcination temperature and adjusting the sodium excess in the precursor mixtures, the formation of secondary phases, particularly Na<sub>2</sub>La<sub>2</sub>Ti<sub>3</sub>O<sub>10</sub>, was minimised. The optimal calcination temperature was determined to be 800 °C for NaLaTiO<sub>4</sub> synthesis, which was lower than previously reported. Excessive sodium was found to promote secondary phase formation, emphasising the importance of precise stoichiometry in the synthesis process.

Structural characterisation *via* X-ray diffraction (XRD) and Rietveld refinement confirmed the formation of the desired NaLnTiO<sub>4</sub> and NaYTiO<sub>4</sub> phases with lattice parameters consistent with literature values. Microscopic analysis (FESEM and TEM) revealed the morphology and particle size distribution of the synthesised materials, providing insights into their physical properties. Moreover, solid-state <sup>23</sup>Na nuclear magnetic resonance (NMR) spectroscopy elucidated the local electronic environments in NaLaTiO<sub>4</sub> and NaYTiO<sub>4</sub>. The presence of distinct sodium sites and their shielding effects were indicative of the materials' structural integrity and potential ion transport pathways.

The study further explored the bandgap properties of NaLaTiO<sub>4</sub> and NaYTiO<sub>4</sub>, which play a crucial role in determining their electrochemical performance as anode materials. UV-vis diffuse reflectance spectroscopy revealed different bandgap energies for the two materials, influencing their electron mobility and charge transfer kinetics during battery cycling.

The electrochemical performance of NaLaTiO<sub>4</sub> and NaYTiO<sub>4</sub> as anodes for lithium-ion batteries was evaluated through galvanostatic charge-discharge tests, cyclic voltammetry, and *operando* XRD studies. Both materials exhibited reversible sodium insertion and extraction processes with stable cycling performance over multiple charge-discharge cycles. NaYTiO<sub>4</sub> demonstrated higher initial capacity and improved rate capability compared to NaLaTiO<sub>4</sub>, attributed to its narrower bandgap facilitating faster electron transport and to the participation of the Y(II)/Y(III) redox pair.

Importantly, impedance spectroscopy measurements provided insights into the sodium diffusion rates and ionic conductivity of the materials, essential for assessing their suitability as battery solid-state electrolytes. The study highlighted the influence of temperature on conductivity, underscoring the importance of understanding ion transport mechanisms under different operating conditions.

Unfortunately, these materials were shown not to be adequate for use in sodium-ion batteries, either as anodes or as solid-state electrolytes.

## 5.6. References

- [1] M. L. Perovskite-Info, “No Title,” 2018. <https://www.perovskite-info.com/perovskite-introduction>.
- [2] Hrishit Banerjee, “STUDY OF ELECTRONIC STRUCTURE OF ORGANIC AND INORGANIC COMPLEXES,” University of Calcutta, 2006.
- [3] F. Lichtenberg, A. Herrnberger, and K. Wiedenmann, “Synthesis, structural, magnetic and transport properties of layered perovskite-related titanates, niobates and tantalates of the type  $A_nB_nO_{3n+2}$ ,  $A'A_k-1B_kO_{3k+1}$  and  $A_mB_m-1O_{3m}$ ,” *Prog. Solid State Chem.*, vol. 36, no. 4, pp. 253–387, 2008, doi: 10.1016/j.progsolidstchem.2008.10.001.
- [4] L. Glasser, “Systematic Thermodynamics of Layered Perovskites: Ruddlesden-Popper Phases,” *Inorg. Chem.*, vol. 56, no. 15, pp. 8920–8925, 2017, doi: 10.1021/acs.inorgchem.7b00884.
- [5] J. Y. Hwang *et al.*, “Sodium and sodium-ion energy storage batteries,” *Chem. Soc. Rev.*, vol. 3, no. 3, pp. 1867–1875, 2019, doi: 10.1039/c5ta03181h.
- [6] V. L. Blair, “ENGINEERING METHODS FOR IMPROVED WATER SPLITTING BY PHOTOCATALYTIC LAYERED PEROVSKITES BY A THESIS SUBMITTED TO THE FACULTY OF ALFRED UNIVERSITY IN PARTIAL FULFILLMENT OF THE REQUIREMENTS FOR THE DEGREE OF DOCTOR OF PHILOSOPHY IN CERAMICS ALFRED , NEW YOR,” no. April, 2014.
- [7] L. Chang *et al.*, “Perovskite-type  $CaMnO_3$  anode material for highly efficient and stable lithium ion storage,” *J. Colloid Interface Sci.*, 2020, doi: 10.1016/j.jcis.2020.04.014.
- [8] J. Yan *et al.*, “A high-entropy perovskite titanate lithium-ion battery anode,” *J. Mater.*

- Sci.*, vol. 55, no. 16, pp. 6942–6951, 2020, doi: 10.1007/s10853-020-04482-0.
- [9] J. Qu *et al.*, “ScienceDirect ScienceDirect ScienceDirect ScienceDirect A New Sodium-ion-conducting Layered Perovskite Oxide as Highly A New Sodium-ion-conducting Layered Perovskite Oxide as Highly Active and Sulfur Tolerant Electrocatalyst for Solid Oxide Fuel Active an,” *Energy Procedia*, vol. 158, pp. 1660–1665, 2019, doi: 10.1016/j.egypro.2019.01.387.
- [10] J. Qu *et al.*, “A New Sodium-ion-conducting Layered Perovskite Oxide as Highly Active and Sulfur Tolerant Electrocatalyst for Solid Oxide Fuel Cells,” *Energy Procedia*, vol. 158, pp. 1660–1665, 2019, doi: 10.1016/j.egypro.2019.01.387.
- [11] J. Y. Hwang, S. T. Myung, and Y. K. Sun, “Sodium-ion batteries: Present and future,” *Chem. Soc. Rev.*, vol. 46, no. 12, pp. 3529–3614, 2017, doi: 10.1039/c6cs00776g.
- [12] H. Kang *et al.*, “Update on anode materials for Na-ion batteries,” *J. Mater. Chem. A*, vol. 3, no. 35, pp. 17899–17913, 2015, doi: 10.1039/c5ta03181h.
- [13] Q. Chen, W. Zhou, G. H. Du, and L. M. Peng, “Trititanate nanotubes made via a single alkali treatment,” *Adv. Mater.*, vol. 14, no. 17, pp. 1208–1211, 2002, doi: 10.1002/1521-4095(20020903)14:17<1208::AID-ADMA1208>3.0.CO;2-0.
- [14] S. H. Song, K. Ahn, M. G. Kanatzidis, J. A. Alonso, J. G. Cheng, and J. B. Goodenough, “Effect of an internal electric field on the redox energies of  $ALnTiO_4$  ( $A = Na$  or  $Li$ ,  $Ln = y$  or Rare-Earth),” *Chem. Mater.*, vol. 25, no. 19, pp. 3852–3857, 2013, doi: 10.1021/cm401814z.
- [15] J. Y. Hwang, S. T. Myung, and Y. K. Sun, “Sodium-ion batteries: Present and future,” *Chem. Soc. Rev.*, vol. 46, no. 12, pp. 3529–3614, 2017, doi: 10.1039/c6cs00776g.
- [16] J. Huang, K. Yang, Z. Zhang, L. Yang, and S. Hirano, “Layered perovskite  $LiEuTiO_4$  as

- a 0.8 V lithium intercalation electrode,” pp. 7800–7803, 2017, doi: 10.1039/c7cc03933f.
- [17] “Home | ICSD,” *FIZ Karlsruhe GmbH*, 2024. <https://icsd.products.fiz-karlsruhe.de/> (accessed Apr. 10, 2024).
- [18] M. Tabuchi and R. Kataoka, “Structure and Electrochemical Properties of  $\alpha$ -NaFeO<sub>2</sub> Obtained under Various Hydrothermal Conditions,” *J. Electrochem. Soc.*, vol. 166, no. 10, pp. A2209–A2214, 2019, doi: 10.1149/2.1411910jes.
- [19] S. Byeon and K. Park, “Structure and Ionic Conductivity of Na Ln TiO<sub>4</sub>; Comparison with Those of Na<sub>2</sub>Ln<sub>2</sub>Ti<sub>3</sub>O<sub>10</sub> (Ln = La, Nd, Sm, and Gd),” vol. 436, no. 121, pp. 430–436, 1996.
- [20] A. L. Patterson, “The scherrer formula for X-ray particle size determination,” *Phys. Rev.*, vol. 56, no. 10, pp. 978–982, 1939, doi: 10.1103/PhysRev.56.978.
- [21] “Sodium - Melting Point - Boiling Point,” *Nuclear Power*, 2024. <https://www.nuclear-power.com/sodium-melting-point-boiling-point/> (accessed Apr. 26, 2024).
- [22] G. G. Eshetu *et al.*, “Electrolytes and Interphases in Sodium-Based Rechargeable Batteries: Recent Advances and Perspectives,” *Adv. Energy Mater.*, vol. 10, no. 20, 2020, doi: 10.1002/aenm.202000093.
- [23] S. Byeon, J.-J. Yoon, and S.-O. Lee, “A New Family of Protonated Oxides HLnTiO<sub>4</sub> (Ln = La, Nd, Sm and Gd),” *J. Sol-Gel Sci. Technol.*, vol. 127, pp. 119–122, 1996.
- [24] D. K. Pradhan, B. K. Samantaray, R. N. P. Choudhary, and A. K. Thakur, “Complex impedance analysis of NaLaTiO<sub>4</sub> electroceramics,” *J. Mater. Sci. Mater. Electron.*, vol. 17, no. 3, pp. 157–164, 2006, doi: 10.1007/s10854-006-6756-0.
- [25] X. Xu, R. Wang, X. Sun, M. Lv, and S. Ni, “Layered Perovskite Compound NaLaTiO<sub>4</sub>

- Modified by Nitrogen Doping as a Visible Light Active Photocatalyst for Water Splitting,” *ACS Catal.*, vol. 10, no. 17, pp. 9889–9898, 2020, doi: 10.1021/acscatal.0c02626.
- [26] S. Banerjee, S. Neihisial, and S. K. Pati, “First-principles design of a borocarbonitride-based anode for superior performance in sodium-ion batteries and capacitors,” *J. Mater. Chem. A*, vol. 4, no. 15, pp. 5517–5527, 2016, doi: 10.1039/C6TA01645F.
- [27] Y. Von Lim, X. L. Li, and H. Y. Yang, “Recent Tactics and Advances in the Application of Metal Sulfides as High-Performance Anode Materials for Rechargeable Sodium-Ion Batteries,” *Adv. Funct. Mater.*, vol. 31, no. 10, pp. 1–33, 2021, doi: 10.1002/adfm.202006761.
- [28] Y. Li, M. Chen, B. Liu, Y. Zhang, X. Liang, and X. Xia, “Heteroatom Doping: An Effective Way to Boost Sodium Ion Storage,” *Adv. Energy Mater.*, vol. 10, no. 27, pp. 1–36, 2020, doi: 10.1002/aenm.202000927.
- [29] L. Li, Y. Zheng, S. Zhang, J. Yang, Z. Shao, and Z. Guo, “Recent progress on sodium ion batteries: Potential high-performance anodes,” *Energy Environ. Sci.*, vol. 11, no. 9, pp. 2310–2340, 2018, doi: 10.1039/c8ee01023d.
- [30] J. Xu *et al.*, “High-Energy Lithium-Ion Batteries: Recent Progress and a Promising Future in Applications,” *Energy Environ. Mater.*, vol. 6, no. 5, pp. 1–26, 2023, doi: 10.1002/eem2.12450.
- [31] Q. Yao *et al.*, “Theoretical prediction of phosphorene and nanoribbons as fast-charging Li ion battery anode materials,” *J. Phys. Chem. C*, vol. 119, no. 12, pp. 6923–6928, 2015, doi: 10.1021/acs.jpcc.5b02130.
- [32] S. Sarawutanukul, C. Tomon, and S. Duangdangchote, “Rechargeable Photoactive Zn-Air Batteries Using NiCo<sub>2</sub>S<sub>4</sub> as an Efficient Bifunctional Photocatalyst towards OER

- / ORR at the Cathode,” pp. 541–547, 2020, doi: 10.1002/batt.201900205.
- [33] B. Roose, Q. Wang, and A. Abate, “The Role of Charge Selective Contacts in Perovskite Solar Cell Stability,” vol. 1803140, pp. 1–20, 2019, doi: 10.1002/aenm.201803140.
- [34] H. Park, S. Yu, and D. J. Siegel, “Predicting Charge Transfer Stability between Solid Electrolytes and Li Metal Anodes,” pp. 0–7, 2021, doi: 10.1021/acseenergylett.0c02372.
- [35] N. B. Mikheev, S. A. Kulyukhin, A. N. Kamenskaya, I. A. Rumer, and N. A. Konovalova, “Lower oxidation states of f elements: II. Physicochemical characteristics of actinides and lanthanides in lower oxidation states,” *Radiochemistry*, vol. 46, no. 6, pp. 521–535, 2004, doi: 10.1007/s11137-005-0022-9.
- [36] S. Y. Vassiliev, E. E. Levin, and V. A. Nikitina, “Kinetic analysis of lithium intercalating systems: Cyclic voltammetry,” *Electrochim. Acta*, vol. 190, pp. 1087–1099, 2016, doi: 10.1016/j.electacta.2015.12.172.
- [37] T. Kim *et al.*, “Applications of voltammetry in lithium ion battery research,” *J. Electrochem. Sci. Technol.*, vol. 11, no. 1, pp. 14–25, 2020, doi: 10.33961/jecst.2019.00619.
- [38] M. Yashima *et al.*, “Size effect on the crystal structure of barium titanate nanoparticles,” *J. Appl. Phys.*, vol. 98, no. 1, 2005, doi: 10.1063/1.1935132.
- [39] K. Tang, X. Yu, J. Sun, H. Li, and X. Huang, “Kinetic analysis on LiFePO<sub>4</sub> thin films by CV, GITT, and EIS,” *Electrochim. Acta*, vol. 56, no. 13, pp. 4869–4875, 2011, doi: 10.1016/j.electacta.2011.02.119.
- [40] B. na SilvánSilv, E. Gonzalo, L. Djuandhi, N. Sharma, F. Fauth, and D. Saurel, “On the dynamics of transition metal migration and its impact on the performance of layered

- oxides for sodium-ion batteries:  $\text{NaFeO}_2$  as a case study †,” 2018, doi: 10.1039/c8ta02473a.
- [41] X. Dou *et al.*, “Hard carbons for sodium-ion batteries: Structure, analysis, sustainability, and electrochemistry,” *Mater. Today*, vol. 23, no. March, pp. 87–104, 2019, doi: 10.1016/j.mattod.2018.12.040.
- [42] Y. Li *et al.*, “Dual-Functionalized Ca Enables High Sodiation Kinetics for Hard Carbon in Sodium-Ion Batteries,” *ACS Appl. Mater. Interfaces*, vol. 16, no. 2, pp. 2397–2407, 2024, doi: 10.1021/acsami.3c16484.
- [43] L. Zhang *et al.*, “Lithium lanthanum titanate perovskite as an anode for lithium ion batteries,” *Nat. Commun.*, vol. 11, no. 1, pp. 1–8, 2020, doi: 10.1038/s41467-020-17233-1.
- [44] C. M. Wu *et al.*, “The mechanism of the sodiation and desodiation in Super P carbon electrode for sodium-ion battery,” *J. Power Sources*, vol. 340, pp. 14–21, 2017, doi: 10.1016/j.jpowsour.2016.11.048.
- [45] H. Pan *et al.*, “Sodium Storage and Transport Properties in Layered  $\text{Na}_2\text{Ti}_3\text{O}_7$  for Room-Temperature Sodium-Ion Batteries,” *Adv. Energy Mater.*, vol. 3, no. 9, pp. 1186–1194, Sep. 2013, doi: 10.1002/aenm.201300139.
- [46] Y. Lu, L. Li, Q. Zhang, Z. Niu, and J. Chen, “Electrolyte and Interface Engineering for Solid-State Sodium Batteries,” *Joule*, vol. 2, no. 9, pp. 1747–1770, 2018, doi: 10.1016/j.joule.2018.07.028.
- [47] W. L. Pang *et al.*, “P2-type  $\text{Na}_{2/3}\text{Mn}_{1-x}\text{Al}_x\text{O}_2$  cathode material for sodium-ion batteries: Al-doped enhanced electrochemical properties and studies on the electrode kinetics,” *J. Power Sources*, vol. 356, pp. 80–88, 2017, doi: 10.1016/j.jpowsour.2017.04.076.

- [48] J. Huang, K. Yang, Z. Zhang, L. Yang, and S. I. Hirano, “Layered perovskite LiEuTiO<sub>4</sub> as a 0.8 v lithium intercalation electrode,” *Chem. Commun.*, vol. 53, no. 55, pp. 7800–7803, 2017, doi: 10.1039/c7cc03933f.



## **6. Conclusion**



6. Conclusion.....	267
6.1. Dual calcium and fluorine-doping in <i>O</i> <sub>3</sub> -type iron-rich transition layered oxides for cathodes for sodium-ion batteries .....	270
6.2. Transition-metal doping in manganese-rich <i>P</i> <sub>2</sub> -type layered oxides .....	272
6.3. Layered perovskite oxides as anodes for LIBs and NIBs .....	273
6.4. Future work.....	274

In this thesis, the synthesis optimisation, structural, chemical, and morphological characterisation of various  $O_3$ -type and  $P_2$ -type transition metal oxides and titanium-based layered perovskite oxides, have been conducted and described. The electrochemical behaviour as cathodes for sodium-ion oxides ( $O_3$ -type and  $P_2$ -type) and as anodes and solid electrolytes for sodium-ion oxides (titanium-based layered perovskite oxide) was studied.

The morphology, crystal parameters, and purity are key factors, as they may affect the electrochemical performance, as these influence the  $\text{Na}^+$  mobility and charge transfer. The characterisation of the material in this study PXRD, SEM, TEM, EDS,  $^{23}\text{Na}$  NMR and UV-vis spectroscopy techniques were used. The electrochemical behaviour of the materials synthesised in this work was studied using electrochemical methods such as galvanostatic cycling, cyclic-voltammetry, GITT, and EIS. Furthermore, the electrochemical and structural behaviour of these materials was studied using hybrid techniques such as *operando* and *ex-situ* XRD were also used to understand the structural evolution with ion extraction and reinsertion.

## 6.1. Dual calcium and fluorine-doping in $O_3$ -type iron-rich transition layered oxides for cathodes for sodium-ion batteries

Chapter 3 consisted of the study of the  $O_3$ -type  $\alpha\text{-NaFeO}_2$  belonging to the  $R\bar{3}m$  space group and the effect of sodium substitution with calcium and dual sodium and oxygen substitution with calcium and fluorine, respectively, as cathodes for sodium-ion batteries. Structured refinement shows the presence of small amounts of impurities in all doping iterations. These, consisting mostly of the  $\beta\text{-NaFeO}_2$ , belonging to the space group  $Pna2_1$ . XRD measurements also show a contraction of the crystal unit cell on the  $c$ -axis with the increase

of  $\text{Ca}^{2+}$  in the structure, a result of the stronger electrostatic attraction between  $\text{Ca}^{2+}$  and  $\text{O}^{2-}$ . With the incorporation of fluorine, the unit cell tends to expand on the *c*-axis. SEM imaging shows that  $\text{O}_3$ -type  $\alpha\text{-NaFeO}_2$  particles tend to be highly agglomerated nanospheres with approximately 500 nm diameter.

Preliminary studies have shown that going above 3.5 V vs  $\text{Na}^+/\text{Na}$  triggers irreversible anionic reduction, which hinders capacity retention. Undoped  $\alpha\text{-NaFeO}_2$  cycled in the window 2.0-3.5 V vs  $\text{Na}^+/\text{Na}$  had an initial capacity of 91 mA h  $\text{g}^{-1}$  with a capacity retention of 54 % after 100 cycles. Calcium-doping at 5 % had expectedly resulted in an initial capacity decrease to 68 mA h  $\text{g}^{-1}$  due to reduction of available sodium however, the capacity retention has increased to 77 %. This means that, the capacity of the 5% doped  $\alpha\text{-NaFeO}_2$  shows a higher capacity from the 60<sup>th</sup> cycle. Calcium-doping at 3 % had no positive effect on the performance of this material. Dual fluorine and calcium doping had a positive effect on the performance of these materials, especially in the initial capacity. The initial capacity of 3% and 5 % dual fluorine and calcium-doped materials is 68 and 89 mA h  $\text{g}^{-1}$  with a capacity retention of 66 % and 75 %, respectively. In the case of the 5 % dual fluorine and calcium-doped materials, these showed a higher capacity than the pristine after the 15<sup>th</sup> cycle.

The  $\text{Na}^+$  diffusion rate measured with CV at different rates and GITT show an opposite tendency being that, in CV, the tendency is that, with higher doping comes lower  $\text{Na}^+$  diffusion and with GITT, higher doping comes with higher  $\text{Na}^+$  diffusion. As mentioned in Chapter 3, CV at different rates measures the ion diffusion at the particle surface and, GITT measures the measure the ion diffusion at the bulk of the particles. This may indicate that a layer, possibly degradation in contact with oxygen or moisture or CEI may be forming on the surface of the particles with higher doping rates that have a deleterious effect on  $\text{Na}^+$  diffusion. This does not affect the bulk of the materials and shows that an increase of doping

allows for better Na<sup>+</sup> mobility whether by disrupting the Na<sup>+</sup>/□ ordering in the case of calcium doping and the increase of the *c*-axis, allowing better sodium diffusion.

## 6.2. Transition-metal doping in manganese-rich *P2*-type layered oxides

Chapter 4, consisted of the study of nickel substitution with titanium (NMNTO), iron (NMNFO) and copper (NMNCO) in *P2*-type Na<sub>0.67</sub>Mn<sub>0.8</sub>Ni<sub>0.2</sub>O<sub>2</sub>, belonging to the space group *P* 6<sub>3</sub>/*m m c* as cathodes for sodium-ion batteries. XRD and structure refinements detected no impurities. Given the relative proximity of the atomic radii of nickel (II) 6-coordinated octahedral (83 pm), titanium (II) 6-coordinated octahedral (81 pm), iron (III) 6-coordinated octahedral (78.5 pm), and copper (II) 6-coordinated octahedral (87 pm), there were no remarkable changes in the unit cell parameters with nickel substitution.

The initial capacity of NMNTO, NMNFO and NMNCO is 102, 111 and 136 mA h g<sup>-1</sup>, respectively. This was expected given that titanium is not electrochemical active at the potential window of 2.0 to 4.5 V *vs* Na<sup>+</sup>/Na, while iron and copper are. NMNTO also has a lower capacity retention of 49 % after 200 cycles, compared with NMNFO and NMNCO with capacity retentions of 90 % and 86 %, respectively. This is probably related to a better stabilisation of the O – *M* bond, increasing the reversibility of the anionic redox in these materials.

Both CVs and GITT show that the Na<sup>+</sup> diffusion tends to decrease from NMNTO > NMNCO > NMNFO. This indicated that contrary to the *O3*-type, there's no indication of a formation of a layer with deleterious effects in sodium diffusion. Hence, the difference in Na<sup>+</sup> diffusion can be related to phase changes, which are indicated by the higher number of *plateaux* and peak pairs in CVs in NMNCO and NMNFO.

### 6.3. Layered perovskite oxides as anodes for LIBs and NIBs

Chapter 5 of this thesis studies the use of  $\text{NaLaTiO}_4$  and  $\text{NaYTiO}_4$  layered oxides as anodes for sodium and lithium-ion batteries. These materials belong to the space groups  $P4/nmm$  and  $Pbcm$ , respectively.  $\text{NaLaTiO}_4$  synthesis was successfully optimised to reduce the number of unreacted precursors and the  $\text{Na}_2\text{La}_2\text{Ti}_3\text{O}_{10}$  secondary phase. A small amount of this could not be avoided. In the case of  $\text{NaYTiO}_4$ , impurities mostly consisted of unreacted precursors, which were minimised. Both materials show a relatively wide alkali-metal layer of 13.045 and 12.261 Å, for  $\text{NaLaTiO}_4$  and  $\text{NaYTiO}_4$ , respectively, which are thought to have a good impact on ion mobility.

Cycling these materials *versus* sodium has shown that sodium is unable to be inserted in this material and that most of the capacity obtained comes from carbon Super-*P* and some surface adsorption. The capacity thought to come from these materials when cycled on a sodium half-cell does not go beyond 31 mA h g<sup>-1</sup> and 14 mA h g<sup>-1</sup>, for  $\text{NaLaTiO}_4$  and  $\text{NaYTiO}_4$ , respectively, with the rest attributed to carbon Super-*P*. When cycling these materials *versus* lithium, these have shown an initial reversible capacity of 150 and 180 mA h g<sup>-1</sup> for  $\text{NaLaTiO}_4$  and  $\text{NaYTiO}_4$ , respectively. This shows that lithium can be intercalated easily in these materials, whether because of the volume of sodium (102 pm), compared to lithium (76 ppm) and also, the potential difference between  $\text{Na}^+/\text{Na}$  and  $\text{Li}^+/\text{Li}$  or due to a lack of sites that can receive sodium in the structure, these materials are unable to intercalate sodium in the structure.

EIS measurements have reached an activation energy for sodium mobility of 0.52 and 0.49 eV for  $\text{NaLaTiO}_4$  during heating and cooling respectively.  $\text{NaYTiO}_4$  shows an activation energy of 0.57 and 0.55 eV during heating and cooling, respectively. A good solid electrolyte

has an activation energy for sodium mobility in the range of  $10^{-3}$  eV meaning that, these materials are not ideal for use as solid electrolytes.

## 6.4. Future work

Several families of materials were characterised and investigated for use in energy storage as sodium-ion batteries. In this thesis, the materials were characterised with a focus on the initial capacity, capacity retention, cycle life and rate capability. Other performance tests, such as sodium mobility measurements, *operando/ex-situ* structural measurements, and environmental resilience testing were also performed. Other performance parameters such as high-temperature behaviour, thermodynamic properties and theoretical correlations between electrochemical and structural properties have not been investigated. It is therefore suggested that the following efforts should be made to further understand and improve the performances of as-prepared materials:

1. In dual calcium and fluorine-doping of  $O_3$ -type  $\alpha$ - $\text{NaFeO}_2$ :
  - a. Investigation of the structural changes during operation on the calcium-doped and the dual calcium and fluorine-doped material with *operando* XRD.
  - b. Experimental determination of the preferred position of calcium and fluorine *via operando* XPDF analysis.
  - c. Investigation of coating and doping that prevent or delay the degradation of materials in contact with the environmental conditions.
2. In nickel substitution with titanium, iron and copper in P2-type  $\text{Na}_{0.67}\text{Mn}_{0.8}\text{Ni}_{0.2}\text{O}_2$ :
  - a. Investigation of multiple dopant substitution.

- b. Research of predictive strategies to select dopants and substituents.
  - c. Investigation of other dopants such as Mg, K, Zn, Y or Zr.
  - d. Study of deleterious structural changes *via operando* XRD.
  - e. Study of the effect of sodium substitution by calcium and oxygen substitution by fluorine
3. In layered perovskite oxides as anodes:
- a. Determination of all redox events via XPS.
  - b. Investigation of different rare-earth substituents.
  - c. Investigation of layers disordering by exfoliation to allow the intercalation of sodium.

Although several improvements should be made to tune and improve the materials' performance, this work contributes to the quickly growing field of electrode development for sodium-ion batteries and is a timely contribution to the rapidly growing field of electrode development for energy storage technologies by testing different strategies to ameliorate existing materials properties.



## **7. Annexes**



For the extraction of the data to calculate the Na<sup>+</sup> diffusion rate of the materials studied in this thesis, *via* GITT, the following Python script was used:

```
#for files not update, check with sheet number first, start with sheet_name=4,max until 8, for the
next file start wiith 1

import pandas as pd

# File path
file_path = "JC_C2NFO_4_6.72_GITT.xlsx"

try:
    # Read the fifth sheet
    df_fifth_sheet = pd.read_excel(file_path, sheet_name=4) # Indexing starts from 0, so 4
    represents the fifth sheet
    # Part 1: Collecting the last voltage value and its corresponding Step ID
    last_voltage_per_step = {} # Dictionary to store the last voltage value for each Step ID
    for step_id, group in df_fifth_sheet.groupby('Step ID'):
        last_voltage = group.iloc[-1]['Voltage(V)'] # Get the last voltage value for the current
    Step ID
        last_voltage_per_step[step_id] = last_voltage # Store the last voltage value in the
    dictionary
    # Writing Part 1 results to Excel
    df_part1 = pd.DataFrame(last_voltage_per_step.items(), columns=['Step ID', 'Last Voltage(V)'])
    df_part1.to_excel("7part1_results.xls", index=False, engine='openpyxl')
    print("Part 1 results saved to 'part1_results.xls'")
    # Part 2: Initialize variables to store the first Voltage(V) value and Step Name for CC_Chg or
    CC_DChg steps
    first_voltage_per_charging_step = {}
    step_name_per_charging_step = {}
    # Iterate through each step in the dataframe
    for index, row in df_fifth_sheet.iterrows():
        step_id = row['Step ID']
        step_name = row['Step Name']
        voltage = row['Voltage(V)']
        # If the step is a charging step and it's the first occurrence, record its first voltage
    value and step name
        if step_name in ['CC_Chg', 'CC_DChg'] and step_id not in first_voltage_per_charging_step:
            first_voltage_per_charging_step[step_id] = voltage
            step_name_per_charging_step[step_id] = step_name
    # Writing Part 2 results to Excel
    df_part2 = pd.DataFrame({
        'Step ID': list(first_voltage_per_charging_step.keys()),
        'Step Name': list(step_name_per_charging_step.values()),
        'First Voltage(V)': list(first_voltage_per_charging_step.values())
    })
    df_part2.to_excel("7part2_results.xls", index=False, engine='openpyxl')
    print("Part 2 results saved to 'part2_results.xls'")

    print("\nData collection complete.")
except FileNotFoundError:
    print(f"File '{file_path}' not found.")
```

